

Promotors: Prof. dr. ir. Jan G. Pieters
Department of Biosystems Engineering

Prof . dr. ir. Koen Dewettinck
Department of Food Safety and Food Quality

Dean: Prof. dr. ir. Guido Van Huylenbroeck

Rector: Prof. dr. ir. Paul Van Cauwenberge

Wasan DUANGKHAMCHAN

CFD MODELLING OF THE FLUIDISED BED COATING PROCESS

Thesis submitted in fulfillment of the requirements
For the degree of Doctor (PhD) in Applied Biological Sciences

Dutch translation of the title:

CFD-modellering van het wervelbedomhullingsproces

For citation:

Duangkhamchan, W. (2012). CFD modelling of the fluidised bed coating process. PhD thesis, Ghent University, Belgium, 196 p.

ISBN-number: 978-90-5989-503-4

The author and the promotor give the authorisation to consult and to copy parts of this work for personal use only. Every other use is subject to the copyright laws. Permission to reproduce any material contained in this work should be obtained from the author.

Acknowledgements

First of all I wish to thank my parents, who devoted their lives to me, and my family who always gave me courage when I was frustrated.

To my promoters, Prof. Koen Dewettinck and Prof. Jan Pieters, thank you for the guidance and patience over the years. Prof. Frederik Ronsse and Prof. Frédéric Depypere for all the hard work you put into this work.

To all the staff (and former staff) of Biosystems Engineering (Wolter, Eveline, Dieter, Eddy, Kris, Mike, Güray and my all colleagues) and Laboratory of Food Technology and Engineering, you made me feel second home.

Wasan
Ghent, February 2012

Summary

Originally developed for pharmaceutical applications, microencapsulation is now increasingly being applied in the food industry to protect a pure active ingredient or a mixture of ingredients from adverse environmental conditions. The focus in this research work lies solely on the top-spray fluidised bed coating as a feasible microencapsulation method for food applications. In order to control or improve efficiency of the fluidised bed coating process, understanding of mechanisms prevailing in the process is required. Consequently, the aim of this PhD research was to model the complete top-spray fluidised bed coating process by means of computational fluid dynamics (CFD), with the global aim of understanding the process fundamentals and providing the insight for optimising process control and reactor design. The modelling of the complete coating process requires several aspects to be studied in more detail and consequently, the research was split up into four parts, pertaining to the modelling of these aspects. First, a CFD model with an appropriate drag model was constructed to allow the accurate prediction of gas/solid behaviour in tapered fluidised beds. Next, the effect of the release of compressed air – to assist in the atomisation of the coating solution – on the hydrodynamic behaviour of the fluidised bed was studied. The third part dealt with the hydrodynamic modelling of the liquid spray in the gas/solid fluidised bed. Finally, the overall CFD model was concluded by adding the heat and mass transfer (i.e. droplet evaporation).

The first stage of the research involved the selection of a drag coefficient model used to calculate the drag force. A gas-solid fluidised bed in a tapered reactor was simulated by means of an Eulerian CFD model with granular flow extension. The time-averaged solid volume fractions predicted by the CFD model associated with several drag models were compared with experimental data obtained using the Positron Emission Particle Tracking method (PEPT) from Depypere *et al.* (2009).

Initial results using a 2-phase Eulerian model showed poor agreement with experiment results. As a result of the particle size distribution of the materials used in the validation (PEPT) experiment, extending the Eulerian model to include 3 solid phases with different mean particle diameters per phase, provided better qualitative and quantitative consistency of model simulations with experimental data. Furthermore, among several drag models, the so-called modified Gidaspow model gave the best quantitative agreement between CFD simulations and experimental data.

Because of its effect on hydrodynamic properties in the fluidised bed coating, the release of compressed air assisting the atomisation of the coating solution was modelled using the 4-phase Eulerian-Eulerian CFD model together with the modified Gidaspow drag model. Variation of atomisation air pressure was used in order to study the effect on solids concentration in a reactor. The model-predicted results were verified using published experimental data (PEPT) and showed a change in solids concentration with variation of atomisation air pressures. Even though the model-predicted results showed good correlation with the experimental results, discrepancy between simulated values and experimental data were observed. It was shown that the model proved to be highly sensitive to changes in the fluidisation air flow rate regarding the model-predicted solids concentration. A sensitivity analysis of the superficial air velocity boundary condition showed that quantitative improvement of the CFD model could be found with a 10% adjustment of fluidisation air flow rate, which was smaller than the experimental error.

For the next stage, the two-fluid atomisation in a tapered fluidised bed coater was modelled using an Eulerian-Lagrangian CFD model associated with the air-blast/air-assisted atomiser model. In addition, the multi-fluid flow model combined with a population balance model was used as an alternative approach to describe the two-fluid atomisation. For both approaches, not only atomisation was modelled

with and without the solids phase, but the effects of operating conditions on spray cone and liquid mass fraction inside the reactor were also investigated. To verify the gas-liquid CFD model, experimental spray patterns visualised by means of UV illumination at two atomisation air pressures were compared with those obtained from simulations. Moreover, comparison of time-averaged fluidised bed behaviour with the inclusion of sprays showed the consistency between the two approaches.

As a further step, the complete top-spray fluidised bed coating process was modelled using an Eulerian-Lagrangian CFD model, including energy equations describing heat transfer and droplet evaporation. In the last stage of the research work, the solids dynamics, droplets trajectories and droplet evaporation were simulated to account for temperature and air humidity distribution in the fluidised bed coater. The expanded bed height was first determined using a near-wall gas temperature profile and a static pressure profile obtained using a CFD model. The model-predicted expanded bed heights from both methods agreed well with published experimental results. In addition, the temperature distributions of gas and solid phases were simulated in order to investigate the effect of the compressed air release. It was found that the additional atomisation air with a higher pressure resulted in a decrease in gas and solid temperature in the reactor. Furthermore, a gas-solid Lagrangian model was used to simulate the temperature and humidity distribution with variation of process variables.

Finally, the overall CFD model was validated using data from literature. The gas and solid temperature distributions obtained using CFD were consistent with the experimental observation of the different thermal zones: heat transfer zone, isothermal zone and coating zone. However, disagreement between the simulated outlet air temperature and the experimental result could be seen, which could be possibly explained by the underestimation of droplet evaporation because of the omission of droplet deposition onto the surface of solids particles. Consequently, in future work, the global CFD model must include the droplet adhesion on the

fluidised particles and heat and mass transfer between the wet particles and hot fluidising air.

Samenvatting

Oorspronkelijk ontwikkeld voor farmaceutische toepassingen, wordt micro-encapsulatie meer en meer toegepast in de voedingsindustrie om pure ingrediënten of mengsels van ingrediënten te beschermen tegen omgevingsinvloeden of om vrijstelling ervan te sturen. Dit onderzoek legde zich toe op het zgn. *top-spray* wervelbedomhullingsproces als een haalbare techniek voor toepassing in de voedingsindustrie. Om het omhullingsproces te kunnen sturen of om de efficiëntie ervan te kunnen verhogen, is verregaand inzicht vereist in de onderliggende fysische mechanismen die optreden tijdens het wervelbedomhullingsproces. Het doel van dit doctoraatsonderzoek was bijgevolg het modelleren van het volledige *top-spray*-wervelbedomhullingsproces door middel van numerieke stromingsleer (*computational fluid dynamics*, CFD), teneinde de fundamentele fysische mechanismen te doorgronden en tevens ook inzichten te verwerven die nuttig zijn voor processturing en reactorontwerp.

Het modelleren van het volledige omhullingproces vereist dat verschillende deelaspecten in meer detail worden bestudeerd en daarom werd het onderzoek opgesplitst in vier delen, waarvan elk een deelaspect van het omhullingmodel belichtte. Eerst werd een CFD-model met de geschikte keuze van sleepkrachtmodel ontwikkeld met als doel een nauwkeurige voorspelling van het fluïdisatiegedrag in conische wervelbedreactoren. Vervolgens werd het effect van de vrijstelling van perslucht – gebruikt ter ondersteuning van de verneveling van de vloeistof waarin het omhullingsmateriaal is opgelost – op het hydrodynamische gedrag van het wervelbed bestudeerd. Het derde deel handelde over het hydrodynamisch modelleren van de vloeistofnevel in het vast/gas-gefluidiseerde wervelbed. Tenslotte werd het CFD-model vervolledigd door verschillende warmte- en massaoverdrachten toe te voegen.

Het eerste deel van het onderzoek omvatte de keuze van het sleepkrachtmodel om de sleepkracht die vaste deeltjes in het wervelbed ondervinden, te berekenen. Met behulp van een Euleriaans CFD-model uitgebreid met een submodel voor de beschrijving van deeltjesstroming, werd een vast/gas-wervelbed in een conische reactor gesimuleerd. De tijdsgemiddelde vastestofconcentraties, gesimuleerd met behulp van zeven verschillende sleepkrachtmodellen, werden vergeleken met experimentele data bekomen door middel van *Positron Emission Particle Tracking* (PEPT) zoals beschreven door Depypere *et al.* (2009). De initiële resultaten bekomen via een tweefasig (nl. vaste fase en gasfase) Euleriaans model vertoonden een slechte overeenkomst met de experimentele resultaten. Omwille van de deeltjesgrootteverdeling van het materiaal dat werd gebruikt voor de experimentele validatie, werd het Euleriaanse model in een volgende stap uitgebreid tot drie vaste fasen. Iedere vaste fase van het uitgebreide model had een verschillende partikeldiameter, om zo een betere overeenstemming te bekomen met de verdeling van de deeltjesgrootte van het experimenteel gebruikte materiaal. Met het uitgebreide Euleriaanse model werd een betere kwalitatieve en kwantitatieve overeenkomst bereikt tussen de gesimuleerde en de experimentele waarden. Van de verschillende geteste sleepkrachtmodellen werd het zogenaamde gewijzigde Gidaspow-model behouden vermits het resulteerde in de beste kwantitatieve overeenkomst tussen CFD-simulaties en experimentele data.

Omwille van het effect op de hydrodynamische eigenschappen van het wervelbed werd de invloed van perslucht ter ondersteuning van de verneveling van de omhullingsvloeistof, gemodelleerd in het reeds ontwikkelde 4-fasig Euleriaans model (3 vaste + 1 gasfase). Het effect van verschillende persluchtdrukken op de verdeling van de vaste stofconcentratie in de reactor, werd bestudeerd. Opnieuw werden de resultaten, voorspeld door het model, vergeleken met gepubliceerde experimentele (PEPT) meetgegevens. Hoewel een goede overeenkomst werd bekomen tussen de gesimuleerde en de experimentele gegevens, werden nog steeds discrepanties tussen beide vastgesteld. Tevens kon worden aangetoond dat

het ontwikkelde CFD-model vrij gevoelig was voor veranderingen in de randvoorwaarden wat betreft de inlaatluchtsnelheid. Daarom werd een gevoeligheidsanalyse uitgevoerd met betrekking tot de variatie van de inlaatluchtsnelheid en het effect hiervan op de voorspelde vastestofconcentraties in de reactor.

In een derde stap, werd de met perslucht ondersteunde verneveling van de omhullingsvloeistof gemodelleerd aan de hand van een Euleriaans-Lagrangiaans CFD-model waarbij gebruik gemaakt werd van het zogenaamde “*air-blast/air-assisted*” vernevelingsmodel. In een alternatieve aanpak werd het multifasig Euleriaans model gecombineerd met een populatiebalansmodel teneinde de verneveling te beschrijven. In beide aanpakken werd niet alleen de verneveling in af- en aanwezigheid van de vaste fase gemodelleerd, maar ook de effecten van de procesomstandigheden op de sproeikegel en de vloeistofverdeling in de reactor werden bestudeerd. Om het vernevelingsmodel in afwezigheid van de vaste deeltjes experimenteel te verifiëren, werden de vernevelingspatronen gevisualiseerd met behulp van ultraviolette straling, en dit bij verschillende persluchtdrukken. De aldus gevisualiseerde vernevelingspatronen werden vergeleken met de voorspelde tijdsgemiddelde vloeistofverdeling in de reactor en een goede kwalitatieve overeenkomst werd vastgesteld.

Als een laatste stap werd het bestaande model, ontwikkeld in de vorige drie delen, vervolledigd met energievergelijkingen die de warmte- en massaoverdracht, met inbegrip van de verdamping van druppels, beschrijven. Deze toevoeging liet toe om de temperatuur- en luchtvochtigheidsverdeling in het wervelbed te simuleren. De geëxpandeerde bedhoogte werd eerst bepaald aan de hand van het verloop van de wandtemperatuur (Depypere et al., 2009). Een goede overeenkomst werd bekomen tussen de op deze manier gesimuleerde en experimenteel bepaalde bedhoogtes. Vervolgens werden de temperatuursverdelingen van de gas- en de vaste fase gesimuleerd en het effect van de perslucht ter ondersteuning van

verneveling werd bestudeerd. Er werd vastgesteld dat een verhoogde persluchtdruk resulteerde in een bijkomende daling van zowel de gas- als de vastestoftemperatuur in de reactor.

Tenslotte werd het globale CFD-model gevalideerd aan de hand van data beschikbaar in de literatuur. De temperatuursverdelingen van de gasfase en de vaste fase waren consistent met de experimentele vaststelling van de verschillende thermische zones in een wervelbed voor omhullingsprocessen. Deze thermische zones bestaan uit een warmteoverdrachtszone, een isotherme zone en een *coating*-zone. Een discrepantie kon echter worden vastgesteld tussen de voorspelde en de experimenteel bepaalde uitlaatluchttemperatuur, wat mogelijk kan verklaard worden door de onderschatting van de druppelverdamping in het model aangezien het model geen rekening hield met het effect van adhesie van druppeltjes aan het deeltjesoppervlak. Met andere woorden, verdamping in het model werd enkel in rekening gebracht voor de zich vrij bewegende druppeltjes, niet voor de neergeslagen druppeltjes. Dit impliceert dat voor toekomstig onderzoek, dat verder bouwt op de resultaten van dit doctoraatsonderzoek, een globaal CFD-model voor wervelbedomhullingsprocessen ook de fenomenen van adhesie van druppeltjes (met de omhullingsvloeistof) aan de gefluidiseerde vaste deeltjes en van warmte- en massaoverdracht tussen bevochtigde deeltjes en de fluïdisatielucht, mee in rekening dient te brengen. Dergelijke aanpak moet ook toelaten de kwaliteit van de coating door simulatie te kwantificeren en te relateren aan ontwerp en regelstrategie.

Nomenclatures

A, A', A'', E	Image intensity matrices
A_b	cross-section area (m^2)
Ar	Archimedes number (-)
A_d	droplet surface area (m^2)
a, b	coefficients in the Symlal-O'Brien model (-)
B	Birth rate (s^{-1})
C	constant (-)
C_D	drag coefficient (-)
C_{fr}	coefficient of friction (-)
$C_{i,d}$	vapour concentration at the droplet surface ($mol\ m^{-3}$)
$C_{i,l}$	vapour concentration in the bulk gas ($mol\ m^{-3}$)
C_z	porous zone inertial resistance (m^{-1})
c_p	specific heat at constant pressure ($J\ kg^{-1}K^{-1}$)
c_v	specific heat at constant volume ($J\ kg^{-1}K^{-1}$)
D	Death rate (s^{-1})
$D_{l,m}$	diffusion coefficient of vapour in the bulk (m^2s^{-1})
D_z	porous zone impermeability (m^{-2})
d	particle diameter (m)
d_v	diameter of equivalent sphere (m)
d_{sh}	sheet thickness (m)
e	specific internal energy ($kJ\ kg^{-1}$)
e_s	coefficient of restitution (-)
e_{abs}	absolute mean error (-)
F_{drag}	drag force (N)
\vec{F}	external body force (N)
\vec{F}_{lift}	lift force (N)
\vec{F}_{vm}	virtual mass force (N)

f	force per unit mass (N kg^{-1})
f_{drag}	drag force per unit mass (N kg^{-1})
$g(\)$	breakage frequency function (s^{-1})
\bar{g}	acceleration due to gravity (m s^{-2})
g_0	radial distribution coefficient (-)
h	specific enthalpy (kJ/kg)
h_c	heat transfer coefficient ($\text{kJ s}^{-1}\text{m}^{-2}\text{K}^{-1}$)
K	interphase momentum exchange coefficient ($\text{kg m}^{-3}\text{s}^{-1}$)
K'	wave number corresponding to the maximum growth rate (m^{-1})
K_C	mass transfer coefficient (m s^{-1})
k'	heat conductivity ($\text{Wm}^{-1}\text{K}^{-1}$)
L	length (m)
M	mass (kg)
M_d	current droplet mass (kg)
M_{d0}	initial droplet mass (kg)
M_{tot}	total mass in the total region of interest (kg)
M_{vo}	mass fraction of volatile component (-)
\dot{m}	mass flow rate (kg s^{-1})
\dot{m}_{fs}	mass flow rate from fluid phase to solid phase (kg s^{-1})
\dot{m}_{sl}	mass flow rate from solid phase to fluid phase (kg s^{-1})
N	total number of pixels (-)
N_i	molar flux of vapour ($\text{kmol m}^{-2}\text{s}^{-1}$)
Nu	Nusselt number (-)
n	mole
$n(\)$	number density function
n_{pix}	Number of pixels (-)
O_{vox}	voxel occupancy (-)
p	pressure (Pa)
Pr	Prandlt number (-)
$P_{sat,d}$	saturated vapour pressure at droplet temperature (Pa)

q	heat flux ($\text{kJ s}^{-1}\text{m}^{-2}$)
Q	heat exchange rate between phases (kJ s^{-1})
R	Universal gas constant ($\text{J mol}^{-1}\text{K}^{-1}$)
Re	Reynolds number (-)
RMS	root mean square (-)
Sc	Schmidt number (-)
Sh	Sherwood number (-)
SSR	Sum of squared residuals (-)
T	temperature (K)
T_{ref}	reference temperature (K)
t	time (s)
t_{run}	total run time (s)
t_{vox}	total time the tracer spent in the voxel of interest (s)
U_t	terminal velocity (m s^{-1})
U_{mf}	minimum fluidisation velocity (m s^{-1})
u, v, w	velocity component in X, Y and Z direction, respectively (m s^{-1})
V, V'	volume (m^3)
V_{tot}	total volume (m^3)
V_{vox}	volume of the voxel (m^3)
\dot{V}	fluidisation air flow rate (m^3s^{-1})
\vec{v}	velocity vector (m s^{-1})
v_l	axial velocity component of liquid at the nozzle orifice (m s^{-1})
$v_{r,s}$	terminal velocity of particles (m s^{-1})
X_i	local bulk mole fraction of species i

Greek symbols

α	volume fraction (-)
ρ	density (kg m^{-3})
ρ_{app}	apparent density (kg m^{-3})

τ	shear stress ($\text{kg m}^{-1}\text{s}^{-2}$)
$\bar{\bar{\tau}}$	stress-strain tensor ($\text{kg m}^{-1}\text{s}^{-2}$)
μ	shear viscosity (Pa.s)
μ_{app}	apparent viscosity (-)
ν	kinematic viscosity (m^2s^{-1})
λ	latent heat (J kg^{-1})
φ	transition function (-)
ϕ	sphericity coefficient (-)
Ψ	dissipation function (-)
$\beta()$	probability density function (kernel function)
θ	angle (radian)
Ω	maximum growth rate (s^{-1})

Subscripts

<i>at</i>	atomisation
<i>b</i>	initial
<i>d</i>	droplet
<i>eff</i>	effective
<i>exp</i>	experiment
<i>f</i>	fluidisation
<i>g</i>	gas phase
<i>i, j</i>	class or integer
<i>inj</i>	injection
<i>l</i>	fluid phase
<i>lg</i>	ligament
<i>m</i>	solid phase m
<i>p</i>	particle or droplet
<i>q</i>	solid or gas phase

<i>ref</i>	reference
<i>s</i>	solid phase
<i>sh</i>	sheet
<i>sim</i>	simulation
<i>vap</i>	vaporization
<i>bp</i>	boiling point
<i>vox</i>	volume element (voxel) of the occupancy plot

Contents

Introduction	1
0.1 Motivation of research work	1
0.2 Research objectives	2
0.3 Outline of the thesis	2
Chapter 1 Modelling the fluidised bed coating process: state of the art	5
1.1 Microencapsulation in Food industry	5
1.1.1 Introduction	5
1.1.2 Microcapsule materials	7
1.1.3 Release mechanisms	8
1.1.4 Microencapsulation techniques	8
1.2 Fluidised bed coating	9
1.2.1 Introduction	9
1.2.2 Fluidisation	10
1.2.2.1 Description of fluidization	10
1.2.2.2 Powder classification	13
1.2.2.3 Bed properties	14
1.2.3 Phenomena in the fluidised bed coating process	15
1.2.3.1 Droplet atomization	16
1.2.3.2 Particle growth mechanisms	17
1.2.4 Fluidised bed configurations	18
1.3 Computational Fluid Dynamics	20
1.3.1 Introduction	20
1.3.2 Performing CFD analysis	21
1.3.2.1 Pre-processing	21
1.3.2.2 Solving	22
1.3.2.3 Post-processing	22
1.3.3 Overview of Computational Fluid Dynamics	23
1.3.3.1 Governing Equations	24
1.3.3.2 Equation of State	27
1.3.4 Turbulence models	28
1.4 CFD in food industry	29
1.5 CFD in fluidised bed coating process	30

1.5.1	CFD modelling of gas-solid fluidised beds	31
1.5.2	Fluidised bed coating process	32
Chapter 2	Comparison and evaluation of interphase momentum exchange models for simulation of the solids volume fraction in tapered fluidised beds	35
2.1	Introduction	36
2.2	Governing equations	38
2.2.1	Conservation equations of mass and momentum	38
2.2.2	Interphase momentum exchange coefficient (drag coefficient) models	40
2.2.2.1	Symalal-O'Brien drag model	40
2.2.2.2	Wen-Yu drag model	41
2.2.2.3	Gidaspow drag model	41
2.2.2.4	Modified Gidaspow model	42
2.2.2.5	Arastoopour drag model	42
2.3	Materials and methods	43
2.3.1	Numerical setup	43
2.3.2	Experimental setup	47
2.4	Results and Discussion	48
2.4.1	Introduction	48
2.4.2	Voidage contours	50
2.4.2.1	Qualitative analysis	50
2.4.2.2	Quantitative analysis	59
2.4.3	Time-averaged solids volume fraction profiles	61
2.5	Conclusion	65
Chapter 3	CFD study of solids concentration in a fluidised-bed coater with variation of atomisation air pressure	67
3.1	Introduction	68
3.2	Governing equations	68
3.2.1	Conservation equations of mass and momentum	69
3.2.2	Interphase momentum exchange coefficient (drag coefficient) models	69
3.2.2.1	The solid-solid momentum exchange coefficient	69
3.2.2.2	Sphericity coefficient	70
3.3	Materials and methods	71
3.3.1	Numerical setup	71
3.3.2	Experimental setup	74
3.3.3	Validation	76

3.4 Results and Discussion	77
3.4.1 Steady-state results	77
3.4.2 Experimental validation	77
3.4.3 Sensitivity of the model to the fluidisation air flow rate	80
3.5 Conclusions	97
Chapter 4 CFD study of droplet atomisation using a binary nozzle in fluidised bed coating	99
4.1 Introduction	100
4.2 CFD model description	104
4.2.1 Discrete phase model (DPM)	104
4.2.1.1 The Eulerian-Lagrangian approach	104
4.2.1.2 Air-blast/air-assisted atomiser model	106
4.2.2 Multi-fluid flow model combined with population balance model (MFM-PBM)	108
4.3 Materials and methods	111
4.3.1 Overview of the numerical method	111
4.3.2 Modelling the two-fluid atomisation using the DPM	113
4.3.2.1 Two-phase flow model (gas-liquid DPM model)	113
4.3.2.2 Three-phase flow model (gas-solid-liquid DPM model)	114
4.3.3 Modelling the two-fluid atomisation using the MFM-PBM	115
4.3.3.1 Two-phase flow model (gas-liquid MFM-PBM model)	115
4.3.3.2 Three-phase flow model (gas-solid-liquid MFM-PBM model)	115
4.3.4 Experimental spray visualization	116
4.3.4.1 Measurement set-up	116
4.3.4.2 Data processing	117
4.4 Results and Discussion	118
4.4.1 Air-blast/air-assisted atomiser model calibration	118
4.4.2 Two-phase (gas-liquid) model of droplet atomisation in the fluidised bed coater	120
4.4.2.1 Discrete phase model (gas-liquid DPM)	120
4.4.2.2 Multi-fluid flow model combined with population balance model (gas-liquid MFM-PBM)	123
4.4.3 Spray pattern validation (gas-liquid two-phase flow)	125
4.4.4 Three-phase (gas-solid-liquid) model of droplet atomisation in the fluidised bed coater	127
4.4.4.1 Discrete phase model (gas-solid-liquid DPM)	127

4.4.4.2 Multi-fluid flow model combined with population balance model (gas-solid-liquid MFM-PBM)	130
4.5 Conclusions	131
Chapter 5 Conceptual study of heat and mass transfer in a fluidised bed coating process	133
5.1 Introduction	133
5.2 CFD model description	135
5.2.1 Heat transfer between gas and solid phases	135
5.2.2 Heat and mass transfer models for a liquid phase	137
5.2.2.1 Inert heating	137
5.2.2.2 Droplet vaporization	138
5.3 Numerical setup	140
5.4 Simulation circumstances and validation	144
5.4.1 Expanded bed height determination	144
5.4.2 Effect of atomisation air pressure on average bed temperature	145
5.4.3 Droplet evaporation	146
5.4.4 Heat transfer in the fluidised bed coater with the inclusion of all phases	146
5.4.5 Experimental validation	148
5.4.5.1 Expanded bed height determination	148
5.4.5.2 Outlet air temperature measurement	149
5.5 Results and discussion	149
5.5.1 Expanded bed height	149
5.5.2 Effect of atomisation air pressure on bed temperature	153
5.5.3 Droplet evaporation	155
5.5.4 Results of droplet evaporation with the inclusion of gas-solid fluidised bed	159
5.6 Conclusions	165
Chapter 6 General conclusions and future work	167
6.1 Introduction	167
6.2 Drag coefficient models and effect of particle size distribution	167
6.3 Effect of atomisation air on fluidisation behavior	168
6.4 Hydrodynamic of the liquid spray in the gas/solid fluidised bed	169
6.5 Heat and mass transfer in the fluidised bed coating process	170
6.6 Future work	171
References	173

Introduction

0.1 Motivation of the research work

Microencapsulation is a process in which a continuous thin film of usually a polymeric material is formed around an active ingredient or mixture of ingredients for the purpose of controlled release, increased shelf life, taste masking, improved processability. Although microencapsulation has been used in the pharmaceutical industry for years, it is being increasingly applied in the food industry for improved or totally new properties of products. Among the microencapsulation techniques, fluidised bed coating originally developed for pharmaceutical application is increasingly applied in the food industry as an important treatment process.

Fluidised bed coating is often chosen because of its flexibility and its great cost saving potential, because all essential steps of the coating process can be performed in one single apparatus. However, with respect to fluidised bed coating, problems and side-effects: agglomeration resulting from collision of wet particles, spray-drying resulting from premature evaporation of droplets, and attrition caused by inter-particle and particle-to-wall collisions, are still encountered. Many experimental attempts have been made to avoid these problems. To avoid agglomeration, the process controller could increase the kinetic energy of the fluidised particles, increasing the drying capacity of the supplied air, resulting in a decrease of the overall energy efficiency and a higher production time and hence production costs. Process models such as CFD models, with knowledge of the phenomena taking place in a process, could be considered a useful tool in optimising and designing the fluidised bed coating system.

0.2 Research objectives

The research presented in this thesis deals with the numerical study of the fundamental process of top-spray fluidised bed coating by means of Computational Fluid Dynamics. The main objective of the research presented in this thesis is the development and validation of a fundamental hydrodynamic model, which accurately predicts the particle behaviour in a laboratory scale fluidised bed coater. In addition, the two-fluid atomisation and heat and mass transfer processes taking place during the process are also presented. The specific objectives of this research are:

- To study the gas-solid flow in a tapered fluidised bed coater and to find a suitable drag coefficient model.
- To study the particle behaviour in a fluidised bed coater with the inclusion of atomisation air at different pressures.
- To study droplet atomisation using a two-fluid nozzle used in the fluidised bed coating process.
- To study droplet evaporation and heat transfer in the fluidised bed coating process.

0.3 Outline of the thesis

The thesis consists of six chapters.

Chapter 1 describes the application of microencapsulation techniques in the food industry, focussed on fluidised bed coating as a means of producing encapsulated food ingredients. A theoretical background concerning CFD is provided together with its application in the food industry. Finally, a literature review of the use of CFD models in gas-solid fluidised bed flow and its application in fluidised bed coating is given.

Chapter 2 focusses on drag coefficient models used for simulating the gas-solid interaction in a tapered fluidised bed coater. In this chapter, various drag coefficient models are evaluated in order to select a suitable model. Moreover, the extended Eulerian model including 3 solid phases is presented to take the particle size distribution into account.

In Chapter 3, the particle behaviour inside a tapered fluidised bed coater with inclusion of atomisation air is presented. The model-predicted solids volume fractions at different atomisation air pressures were compared with those obtained from published experimental results.

Chapter 4 demonstrates the droplet atomisation of a two-fluid nozzle used in the fluidised bed coating process. This chapter starts with the use of a discrete phase CFD model to describe droplet trajectories with and without inclusion of the solids phase. In addition, a multi-fluid CFD model combined with a population balance model was employed as an alternative approach for modelling the two-fluid atomisation. Finally, model-predicted results obtained from those two approaches were evaluated using experimental data.

Chapter 5 presents the conceptual study of modelling droplet evaporation and heat and mass transfer in the top-spray fluidised bed coater. In order to validate the CFD model, simulated results were compared with experimental literature data.

Finally, the general conclusions of this research are presented, and the prospective approach for modelling heat and mass transfer resulting in particle growth mechanisms in the fluidised bed coating process are suggested.

Chapter 1 Modelling the fluidised bed coating process: state of the art

In this chapter, a brief discussion will be given concerning the application of microencapsulation techniques in the food industry. As this work focusses on fluidised bed coating as a means of producing encapsulated food ingredients, some of the basic physical aspects involved in fluidised bed coating will be discussed, including fluidisation, coating principles and numerical approaches (CFD).

1.1 Microencapsulation in Food industry

Partly adapted and modified after Depypere (2005) and Ronsse (2006).

1.1.1 Introduction

Microencapsulation is defined as a process in which a continuous thin film of usually a polymeric material is formed around solid, liquid droplets, or gas cells for the purpose of shielding the active ingredient from the surrounding environment (Barbosa-Canovas *et al.*, 2005; Wilson and Shah, 2007; Shekhar *et al.*, 2010, Bansode *et al.*, 2010). Extremely tiny ingredients are packed within the miniature sealed capsules ranging in size from one μm to several hundreds of μm . These so-called microcapsules release their content at a later time at controlled rates and under specific conditions by means appropriate to the application (Barbosa-Canovas *et al.*, 2005; Desai and Park, 2005). When their size is below 1 μm , the capsules are called nanocapsules, while the capsules with a size larger than 1 mm are called macrocapsules (Jyothi *et al.*, 2009).

Microencapsulation is a topic of interest in a wide range of scientific and industrial areas, varying from pharmaceuticals to agriculture and from pesticides to enzymes

(Arshady, 1993; Ronsse, 2006). Industrial application of microencapsulation was first commercially applied in 1954 for carbonless copy paper (Dziezak, 1988). Gelatin was used to microencapsulate a colourless dye precursor by means of coacervation (Fanger, 1974; Deasy, 1984; Dziezak, 1988; Jackson & Lee, 1991). Since then, microencapsulation has been constantly improved, modified and adapted for a variety of purposes and areas. This technique has been utilised in the pharmaceutical industry for the past 40 years to offer controlled release of drugs to the body (Rosinski *et al.*, 2002, Bansode *et al.*, 2010). Although the technology of encapsulation and controlled release is undoubtedly most developed in the pharmaceutical industry, it is being increasingly used in the food and fragrance industries (Greenblatt *et al.*, 1993; Dewettinck and Huyghebaert, 1999; Gibbs *et al.*, 1999). As an enabling technology providing tailor-made and fine-tuned ingredients, microencapsulation gains increasing interest demonstrated by the exponential growth in the number of publications and patents covering the use in food applications (Gouin, 2004).

In particular, microencapsulation in food applications is directly related to the coating of tiny particles of ingredients, e.g. acidulants, fats and flavours, providing liquid and solid ingredients with an effective barrier for environmental and/or chemical reactions until release is desired (Barbosa-Canovas *et al.*, 2005). As a result, the retention of the bioactivity of the components during the processing and storage of the formulated product and delivering the desired bioactive components to the target site of the body is maximized (Wilson and Shah, 2007). Microencapsulation has been used to coat fish oil to increase n-3 polyunsaturated fatty acid intake (Higgins *et al.*, 1999), to encapsulate probiotic bacteria in frozen dairy foods (Shah and Ravala, 2000), to encapsulate a major flavour component of aromatic rice to retain this flavour component upon storage (Apintanapong and Noomhorm, 2003), etc.

1.1.2 Microcapsule materials

The microcapsule structure is divided into the ingredients to be coated, referred to as the core – also called fill, encapsulate, substrate or internal phase and the coating material applied to the microcapsule referred to as wall, shell, external phase or membrane (Barbosa-Canovas *et al.*, 2005, Shekhar *et al.*, 2010). Based on structural properties, microcapsules can be distinctly categorised into three classes: single particle structures, aggregate structures, and multi-walled structures (Arshdy, 1993; Gibbs *et al.*, 1999; Barbosa-Canovas *et al.*, 2005). The size and shape of microcapsules depend on the phase (solid, gas, liquid) of the core. If a solid or a crystalline material is used, an irregular shape may be formed, whereas the simple spherical microcapsules may be formed with the use of liquid as the core (Shekhar *et al.*, 2010).

Based on edible polysaccharides (Nisperos-Cariedo, 1994), proteins (Gennadios *et al.*, 1994), lipids and resins (Hernandez, 1994), there are a number of commercially approved coating materials available to produce microencapsulated food ingredients (Shekhar *et al.*, 2010). Not all coating materials meet all the properties needed, so they are often used in combination with other coating materials. As a result, the choice of coating material should be made based on the following (Jackson and Lee, 1991):

- the physicochemical properties of both the core and coating material
- the compatibility between core and coating material
- the type of release mechanism
- the cost of the shell material.

1.1.3 Release mechanisms

Microcapsules release their core's content at a specific time, rate and location by means of four typical mechanisms: mechanical rupture of the capsule wall, dissolution of the wall, melting of the wall and diffusion through the wall (Shekhar *et al.*, 2010). Commonly used mechanisms for controlled release in foods include temperature and moisture release for hydrophilic encapsulants, and thermal release for fat capsules (Risch and Reineccius, 1995; Wilson and Shah, 2007).

1.1.4 Microencapsulation techniques

There is a wide range of techniques for microencapsulation of food ingredients, but no single encapsulation process is adaptable to all core and coating materials. In general, the choice of a specific technique depends on economics, properties of the core and coating materials, the desired size of the microcapsules, the type of application of the encapsulated food ingredients and the controlled release mechanisms (Jackson and Lee, 1991, Ronsse, 2006). Table 1.1 outlines common methods used to produce microencapsulated food ingredients.

Table 1.1 Methods used to produce microencapsulated food ingredients (Wilson and Shah, 2007)

Methods of microencapsulation	Food ingredients
Spray drying	Vitamins, flavours, starter cultures, carotenoids, fats and oils, clouding agents.
Spray cooling and spray chilling	Ferrous sulphate, vitamins, minerals, acidulants
Extrusion	Vitamin C, visible flavour pieces, colours and extension of shelf life
Fluidised bed coating	Vitamin C, citric acid, lactic acid, sorbic acid, sodium bicarbonate in baked goods
Liposome entrapment	Delivery of vaccines, hormones, enzymes and vitamins in to the body
Coacervation	Vitamin A

A number of outstanding reviews covering the variety of microencapsulation techniques and their applicability in the food industry have been published (Wilson and Shah, 2007; Boh and Sumiga, 2008; Jyothi *et al.*, 2009; Shekhar *et al.*, 2010). However, among different techniques, as shown in Table 1.1, only the fluidised bed coating method is focussed on in this research work.

1.2 Fluidised bed coating

1.2.1 Introduction

Depending on the application, there is a wide range of encapsulation techniques of food ingredients or additives (Arshady, 1993). Among them, fluidised bed coating is used as a feasible method when it comes to coating dry solid particles or powders (Teunou and Poncelet, 2002).

Fluidised bed coating, developed by Dale Wurster in the 1950's for coating pharmaceutical tablets, is also referred to as air suspension coating (Arshady, 1993). This type of coating process results in capsules called a reservoir system where particles are surrounded by a single layer or by multiple layers. Fig. 1.1 shows various microcapsule morphologies.

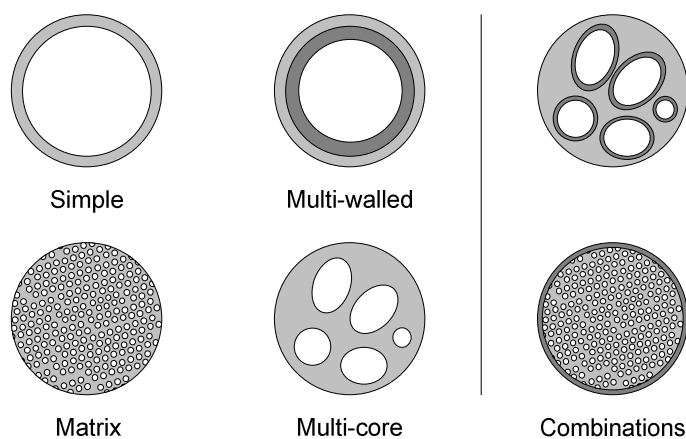


Figure 1.1 Various (idealised) microcapsule morphologies (after Arshady, 1993; Gibbs *et al.*, 1999; Ronsse, 2006).

During recent decades, research and development of fluidised bed coating have yielded an improvement of coating quality based on the same basic working principle, which is the application of the coating material by means of atomising or spraying onto fluidised core particles (Ronsse, 2006). Some of the predominant fluidised bed coating designs will be briefly discussed in the following sections.

1.2.2 Fluidisation

1.2.2.1 Description of fluidisation

Air flowing through a particle bed in upward direction exerts a drag force upon the particles. When the air velocity is less than the minimum fluidisation velocity, the fixed bed regime exists. From this point, increasing gas velocity results in a drag force exerted by the gas upon the particles supporting the weight of the particles in

the bed leading to the onset of fluidisation. Further increase of the air velocity causes the bed to enter the bubbling fluidisation regime and subsequently the bubbles grow so large, nearly or completely filling the vessel cross-section, resulting in a so-called slugging bed regime. Eventually, a pneumatically mobilised bed regime is obtained when the increasing air velocity reaches the particle terminal velocity (Teunou and Poncelet, 2002; 2005; Dixit and Puthli, 2009).

The principle of a fluid bed is to maintain particles in suspension in a specific volume by means of a fluid flow blown through a powder bed. In fluidisation, the fluidising medium is any fluid: gas, liquid, or gas and liquid. However, as the focus in this research work lies solely on gas as the fluid, only air will be mentioned as the fluidising medium. As a result of blowing air through a bed, the state of the fluid bed depends on the air velocity and also on the properties of the particles, resulting in different regimes of fluidisation (Fig. 1.2).

According to the different fluid bed regimes, the main important air velocities are the terminal velocity (U_t), also referred to as free-fall velocity or settling velocity, and the minimum fluidisation velocity (U_{mf}). The former is the air velocity at which dragging or transportation of the particles occurs, for instance, in pneumatic conveying (Fig. 1.2) (Teunou and Poncelet, 2002; 2005; Ronsse, 2006). Therefore, the terminal velocity (Eq. (1.1)) is the maximum allowable air velocity for fluidisation:

$$U_t = \left[\frac{4gd_p(\rho_p - \rho_g)}{3\rho_g C_D} \right]^{0.5} \quad (1.1)$$

where C_D is the drag coefficient which is a function of the particle Reynolds number $\left(\text{Re}_p = \frac{\rho_g d_p v_g}{\mu_g} \right)$, d_p the particle diameter (m), v_g the gas velocity (m s^{-1}), ρ_p the particle density (kg m^{-3}) and ρ_g the gas density (kg m^{-3}).

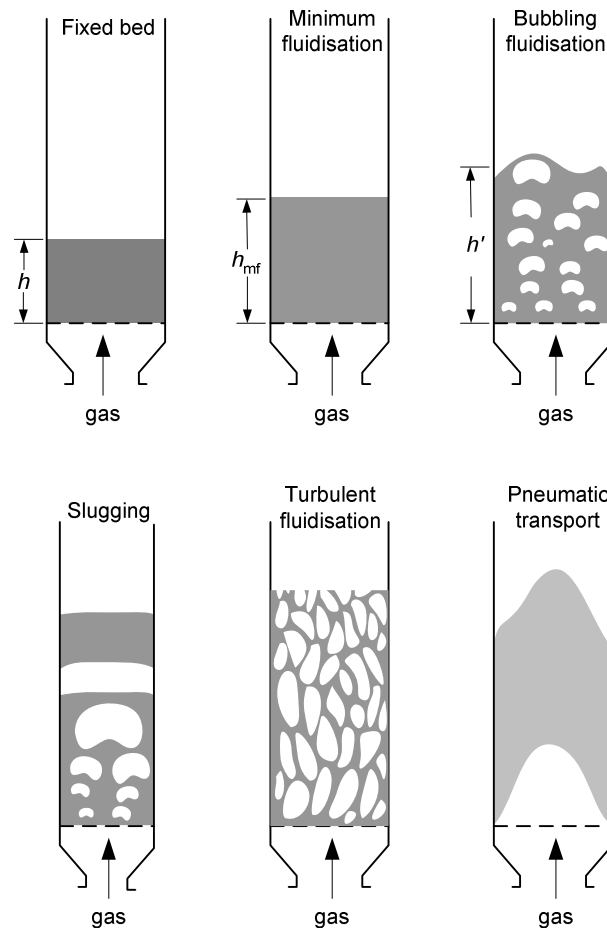


Figure 1.2 Different regimes occurring when a bed of particles is subjected to an increasing air flow rate (after Kunii and Levenspiel, 1991; Ronsse, 2006).

Another important factor in fluidisation technology is the minimum fluidisation velocity, U_{mf} , which is the air velocity at which the powder bed shows fluid-like behaviour. Several authors have proposed empirical correlations for predicting U_{mf} depending on particle properties (Teunou and Poncelet, 2002; 2005; Dixit and Puthli, 2009); such as:

for $d_p < 100 \mu\text{m}$;

$$U_{mf} = \frac{(\rho_p - \rho_g)^{0.934} g^{0.934} d_p^{1.8}}{111 \mu_g^{0.87} \rho_g^{0.066}} \quad (1.2)$$

for $d_p > 100 \mu\text{m}$;

$$U_{mf} = \frac{\mu_g}{\rho_g d_v} \left[(1135.7 + 0.0408 Ar)^{0.5} - 33.7 \right] \quad (1.3)$$

where ρ_g is the gas density (kg m^{-3}), ρ_p the particle density (kg m^{-3}), μ_g the gas viscosity ($\text{kg m}^{-1} \text{s}^{-1}$), d_v the diameter of equivalent sphere (m), based on the volume of the particle and Ar the dimensionless Archimedes number.

1.2.2.2 Powder classification

In a gas fluidised bed, bubbles are formed at the air distributor at the bottom and move through the dense particulate phase, affecting the quality of fluidisation. Consequently, the properties of the gas-solid system play an important role to define the types of fluidisation. Powders can be classified according to Geldart's work (1973) into four different groups based on particle size and density and gas density. Fig. 1.3 shows four groups designated as group A, B, C and D, which are all characterised by the mean particle size and the difference between the particle density and the fluidising gas density.

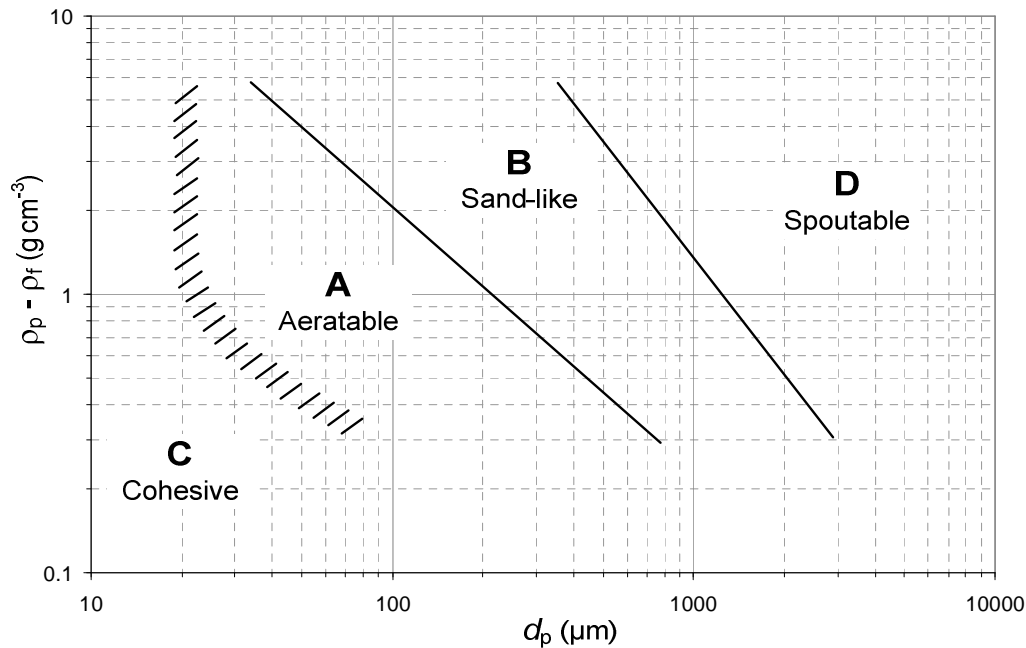


Figure 1.3 The Geldart (1973) powder classification scheme (after Ronsse, 2006).

The chart (Fig. 1.3) is very helpful for quick decisions. For example, particles from group A and B are suitable for the purpose of fluidisation, while powders from group C are difficult to fluidise due to cohesion.

1.2.2.3 Bed properties

Even though the fluid-bed system is a very complex unit operation due to unpredictable particle movements in the fluid bed, it has found many applications due to limited pressure drop, good mixing and optimal heat and mass transfer and easy control of flow rate and reaction kinetics (Teunou and Poncelet, 2002; 2005; Ronsse *et al.*, 2009; Dixit and Puthli, 2009). Having similar properties to a fluid (Teunou and Poncelet, 2002; 2005), fluid bed properties are:

- the density or apparent specific weight, calculated by Eq. (1.4), neglecting the air density:

$$\rho_{app} = (1 - \alpha_g) \rho_p \quad (1.4)$$

where α_g is the voidage,

- the apparent viscosity proposed by Kunii and Levenspiel (1991):

$$\mu_{app} = \frac{1 + 0.5(1 - \alpha_g)}{\alpha_g^4} \cdot \mu_g \quad (1.5)$$

where μ_g is the gas viscosity.

- In the fluidisation state, the pressure drop across the bed is equal to the effective weight of the bed per unit area:

$$\Delta p = \left[\frac{M}{\rho_p A_b} (\rho_p - \rho_g) \right] \times g \quad (1.6)$$

where M is the total mass of the particle bed (kg) and A_b the cross-sectional area of the bed (m²).

1.2.3 Phenomena in the fluidised bed coating process

The principles of fluidised bed coating are schematically described in Fig. 1.4. In this process, three phases can be distinguished in the basic unit: solid (particles), liquid (liquid coating materials) and gas (the fluidising air). At first, in a fluidised bed coating operation, the solid particles at the bottom are fluidised by a continuous air stream blown through an air distributor. A coating solution is pumped and subsequently atomised through a nozzle and sprayed towards the particle bed, resulting in wet particles. With the use of hot fluidising air, drying of the coating solution on the particles takes place. As a result, layer growth or agglomeration mechanisms occur, these phenomena are briefly described in the following sections.

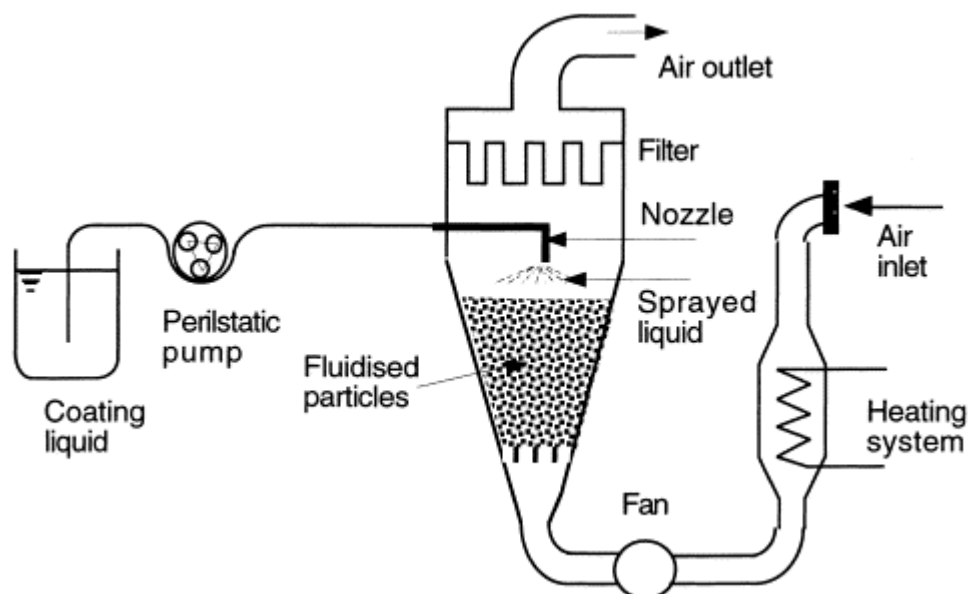


Figure 1.4 Principle of fluidised bed coating (after Teunou and Poncelet, 2002).

1.2.3.1 Droplet atomisation

In order to spread on the particle surface, small droplets containing the coating material are continuously sprayed towards the fluidised bed usually by means of a pneumatic or binary or two-fluid nozzle, which may be submerged in or positioned above the bed (Zank *et al.*, 2001; Nasr *et al.*, 2002; Hede *et al.*, 2008). In the mechanism of the two-fluid atomisation, shown in Fig. 1.5, a high velocity gas impacts a liquid jet issuing from a nozzle orifice creating high shear force over the liquid surface, leading to disintegration into spray droplets with a size ranging from 10 to 40 μm (Lefebvre, 1989; Varga *et al.*, 2003; Hede *et al.*, 2008; Sridhara and Ranghunanandan, 2010).

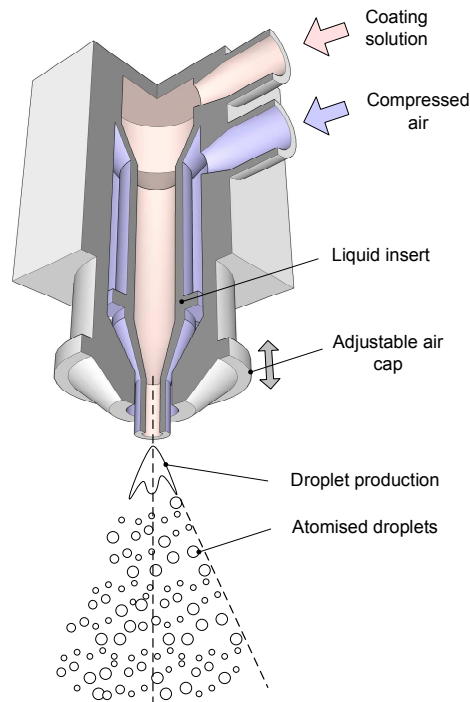


Figure 1.5 The pneumatic or binary nozzle with external liquid/gas mixing (Ronsse, 2006)

1.2.3.2 Particle growth mechanisms

To increase the number of particle droplet collisions, the coating solution is atomised as droplets which collide with and spread on the particle surface, resulting in flattening and adhesion of the droplet on the particle. A layer of coating material does not occur during a single pass through the coating zone, but a continuous film is formed after several wetting and drying cycles, with a controlled thickness and a composition depending on the material used. However, it should be noted that the tendency for agglomeration between two or several particles is high in the case of excessive wetting: liquid bridges form between the core particles, resulting in the formation of large, wet clumps, and eventually, the collapse and defluidisation of the bed (Depypere, 2005).

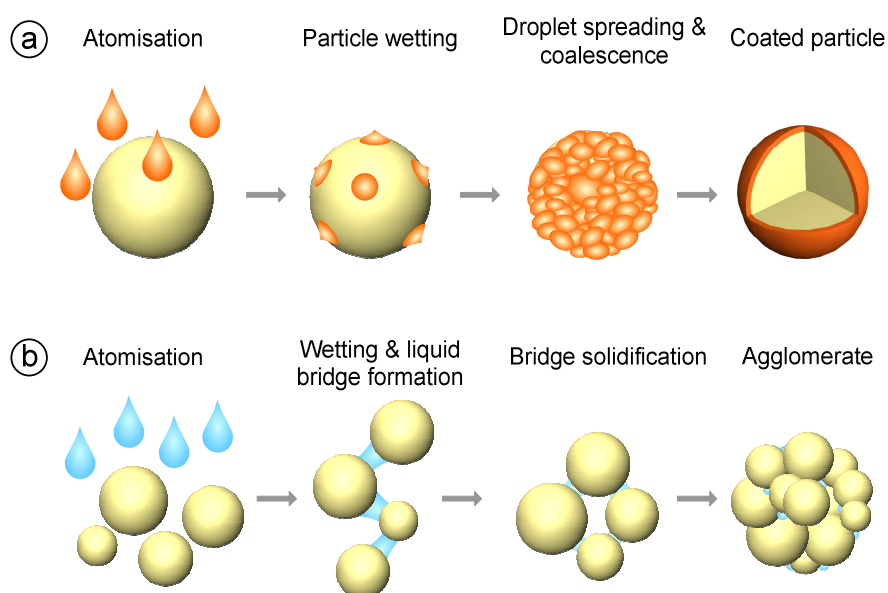


Figure 1.6 Fluidised bed coating (a) and agglomeration (b) mechanisms (Ronsse, 2006)

1.2.4 Fluidised bed configurations

In the fifties, particles as small as 100 μm were coated in a top-spray fluidised bed reactor (Fig. 1.7(a)) in which the nozzle was positioned above the fluid bed. In terms of material deposition and coating quality, the efficiency was poor as a consequence of spray-drying side effects (Teunou and Poncelet, 2002; 2005; Dixit and Puthli, 2009). In order to increase the possibility of particle –droplet collision, the coating material was sprayed from the bottom of the fluid bed, the so-called bottom-spray fluidised bed coating process (Wurster, 1950). As a result, the spray drying of droplets was reduced, resulting in higher coating efficiency. However, the risk of agglomeration was high resulting from the high concentration of wetted particles. Therefore, Wurster decided to guide the particle motion using a cylindrical tube at the bottom (Fig. 1.7(b)), called the Wurster system. Subsequently, a fluidised bed coater was developed providing specific capsule properties such as high spherical shape and density with the use of a rotor system, as shown in Fig. 1.7(c). This system obtained a coating film quality similar to that of the Wurster reactor, but, as a result of the high agitation, the rotor system limits

its application to coating materials which are not too crumbly or friable (Teunou and Poncelet, 2002; 2005, Dixit and Puthli, 2009).

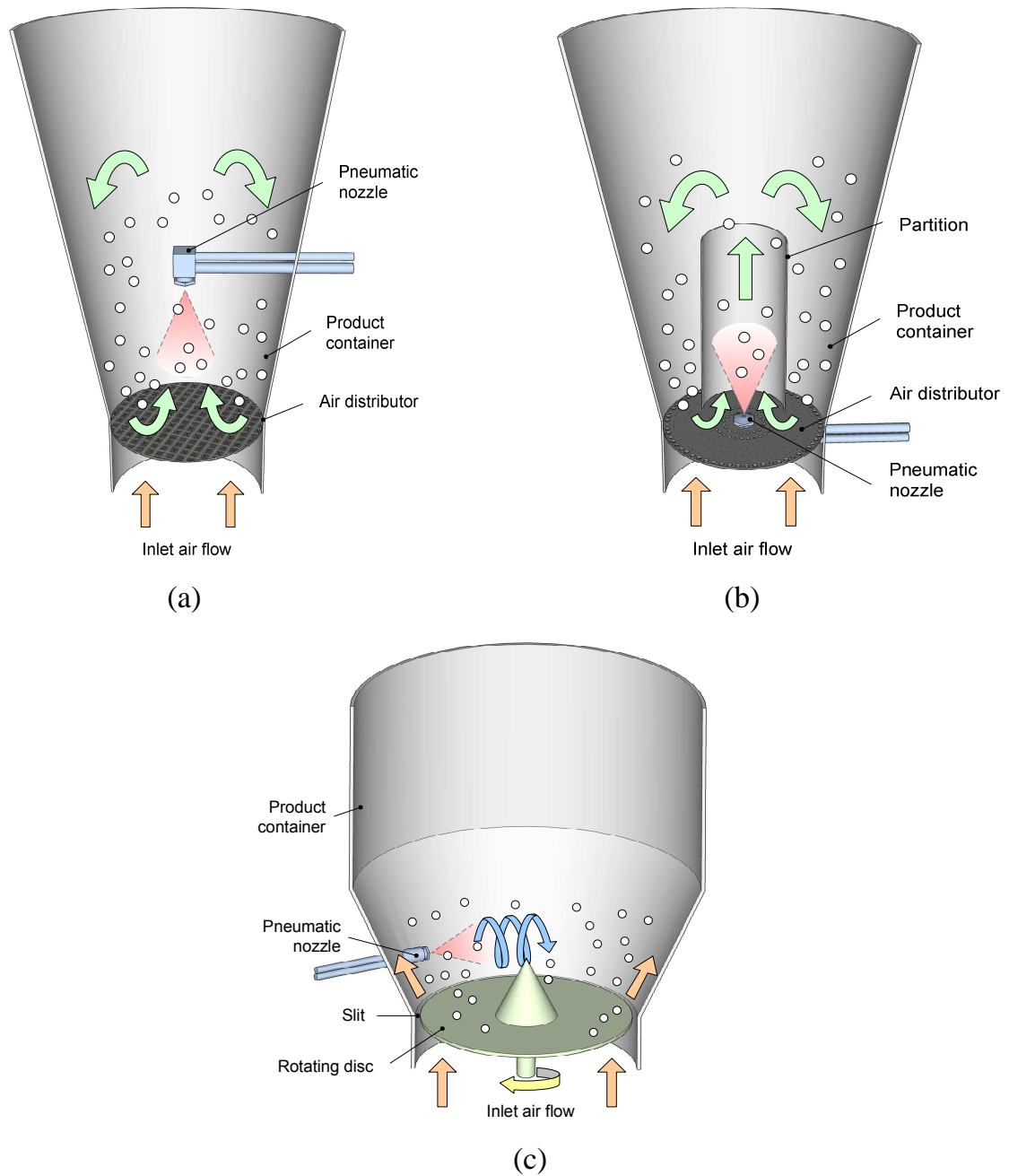


Figure 1.7 Fluidised bed configurations (Ronsse, 2006)

1.3 Computational Fluid Dynamics

Partly taken over from and modified after Versteeg and Malalasekera (2007) and Sun (2007)

1.3.1 Introduction

Computational Fluid Dynamics (CFD), a numerical tool using powerful computers and applied mathematics, is a tool to analyse systems involving fluid flow, heat transfer and associated phenomena such as chemical reactions by means of computer-based simulation (Versteeg and Malalasekera, 2007). This numerical technique has been constantly developed in many applications, both industrial and non-industrial since the 1960s when the aerospace industry began to use this technique in its design and development process of aircraft bodies and engines. The automobile industry has routinely simulated the drag force and air flows with CFD. In addition, the simulation of the combustion process in internal combustion engines is also done with CFD as a result of considerable growth in the development and applications to all aspects of fluid dynamics (Parviz and John, 1997, Xia and Sun, 2002). CFD has become an integral part of the engineering design and analysis environment of many companies due to its ability to predict the performance of new designs or processes before they are ever manufactured or implemented (Schaldach *et al.*, 2000, Xia and Sun, 2002). Recently, CFD has been increasingly used to analyse the flow and performance of process equipment in food industry, such as baking ovens, refrigerated display cabinets, stirred tanks, spray dryers, heat exchangers and some other equipment (Xia and Sun, 2002; Norton and Sun, 2006; Sun, 2007). Considered to be a standard numerical tool, CFD cannot only predict the flow field, but also the heat and mass transfers. Additionally, phase changes (such as in freezing, melting and boiling), chemical reactions (such as combustion), mechanical movement (such as turbine, pistons) and even stress-strain behaviour of solid structures can be described. However, it is

only in recent years that CFD has been applied in food applications to assist in the understanding of the complex physical mechanisms governing the thermal, physical and rheological properties of food materials (Xia and Sun, 2002; Norton and Sun, 2006; Sun, 2007).

1.3.2 Performing CFD analysis

In order to perform CFD simulations, the state of the problem has to be comprehended using the scientific knowledge to express it mathematically. Subsequently, the CFD software will embody this knowledge and express the stated problem in scientific terms. CFD is a computer code that can solve fluid flow problems, consisting of three main parts (Fig. 1.8): (i) a pre-processor, (ii) a solver and (iii) a post-processor.

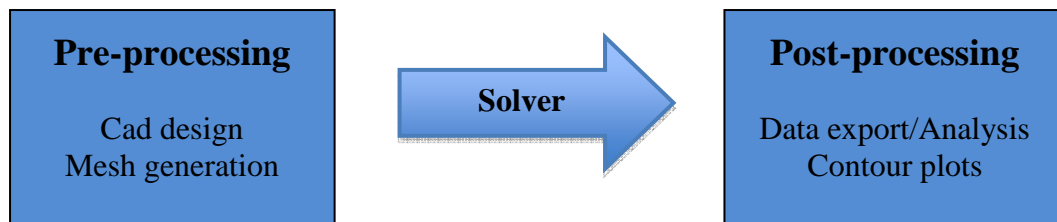


Figure 1.8 Steps for performing CFD analysis.

1.3.2.1 Pre-processing

In order to perform CFD simulations, the first step is the definition of the geometry of the problem domain, created by means of CAD and related programs such as Gambit (Ansys Inc., Canonsburg, PA). The domain is then divided into numerous cells, also known as control volumes or elements (meshing or grid generation). Before solving a problem, in addition to the geometry creation and grid generation, the boundaries of the domain and the necessary initial conditions have to be specified. These conditions together with physical properties of the fluid specify

the actual flow problem to be solved (Xia and Sun, 2002; Versteeg and Malalasekera, 2007; Sun, 2007).

1.3.2.2 Solving

When a mesh is completed, the solver, the actual computational part of the CFD, can be started. At this point the completed geometry can be imported into the solver program and the CFD simulations can be started using the given information from pre-processing. Among three numerical methods: finite difference, finite elements and finite volume, the latter, originally developed as a special finite difference formulation, is the most common technique used in CFD. The algorithm of the finite volume method consists of the following steps (Xia and Sun, 2002; Versteeg and Malalasekera, 2007; Sun, 2007):

- 1) Integration of the governing equations for fluid flow and heat transfer over the computational domain.
- 2) Discretisation, which converts the integral equations into a system of algebraic equations using finite difference type approximation.
- 3) Solving algebraic equations by an iterative method.

As mentioned above, the process usually requires the computer to solve many thousands of equations iteratively until acceptable convergence is achieved.

1.3.2.3 Post-processing

Once the model has been solved, the results are evaluated and analysed both numerically and graphically. In addition to line plots, the post-processor can create visualisation ranging from simple 2-D graphs to 3-D representations. There are as many ways of displaying the simulated data as there are data points, so it is important to select the data representation that is required to compare the different simulations with each other and with external data such as experimental data (Xia and Sun, 2002).

1.3.3 Overview of Computational Fluid Dynamics

The schematic diagram shown in Fig. 1.9 describes the process of solving a fluid flow problem to determine practical information with the use of governing equations. Considering a small control volume, as shown in Fig. 1.10, mass and energy are conserved and the rates of change of all components of momentum are equal to the corresponding components of the applied force. A total of five equations, including the conservation of mass, conservation of energy and three equations from Newton's second law of motion, combined with the equation of state, are used to solve all six unknown variables: pressure (p), density (ρ), temperature (T), and three velocity components (u , v , w). Those six unknown variables can subsequently be solved using six equations as functions of position and time with sufficient boundary conditions. Some other flow variables, such as flow rates, heat transfer rates, and forces can be obtained based on the six aforementioned physical variables.

In this section, an overview of the main key transport phenomena, convection (transport due to fluid flow) and diffusion (transport due to variation of flow variable) is presented. Some detailed theory of CFD code for specific problems will be presented when in the following chapters.

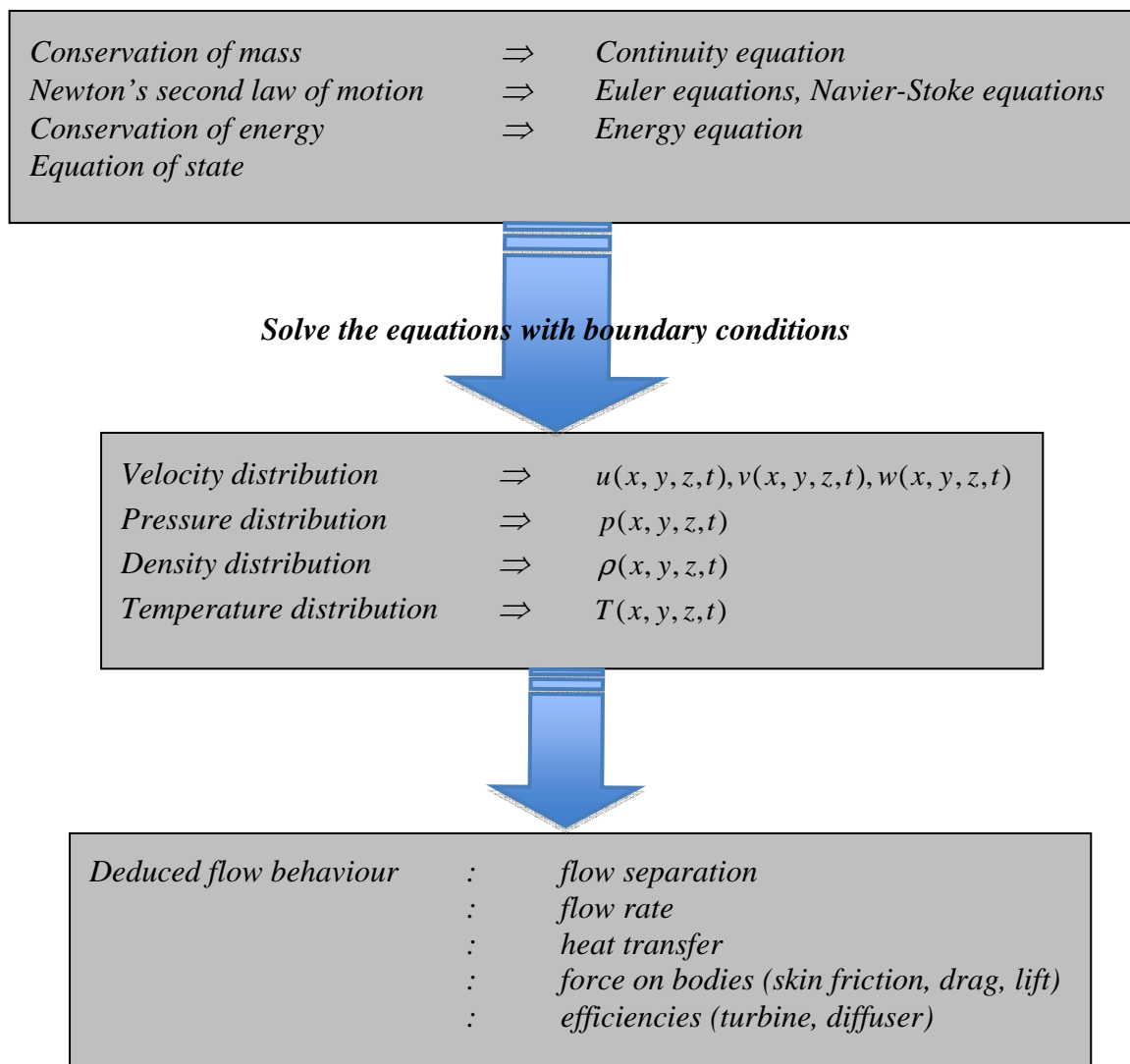


Figure 1.9 Overview of computational fluid dynamics (Fletcher, 1991).

1.3.3.1 Governing equations

The governing equations of fluid flow and heat transfer represent mathematical statements of the conservation laws of physics:

- 1) The law of conservation of mass (continuity)
- 2) The conservation of momentum (Newton's second law)
- 3) The conservation of energy (the first law of thermodynamics).

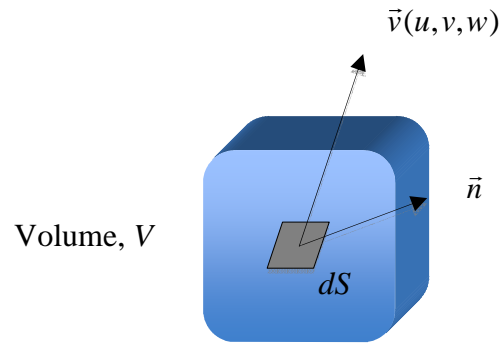


Figure 1.10 Control volume geometry.

By enforcing these conservation laws over an arbitrary control volume V (Fig.1.10), in space and time, the rates of change of mass and momentum within the control volume are equal to the mass flux across the surface S and the sum of forces acting on the rigid body or closed system, respectively. According to the first law of thermodynamics, the time rate of change of internal energy plus the kinetic energy is equal to the rate of heat transfer less the rate of work done by the system. The resulting equations can be written as

Conservation of mass equation:

$$\frac{\partial \rho}{\partial t} + \nabla \cdot (\rho \vec{v}) = 0 \quad (1.7)$$

Equation (1.7) is the mass-conservation or continuity equation, which can be written in Cartesian coordinates in most applications, as shown in equation (1.8):

$$\frac{\partial \rho}{\partial t} + \frac{\partial}{\partial x}(\rho u) + \frac{\partial}{\partial y}(\rho v) + \frac{\partial}{\partial z}(\rho w) = 0 \quad (1.8)$$

Conservation of momentum:

$$\rho \frac{D\vec{v}}{Dt} = \rho \vec{f} - \nabla p + \vec{\tau} \quad (1.9)$$

Equation (1.9) is called the *Navier-Stokes equation*. It can be written in Cartesian coordinates, as

$$\begin{aligned} \text{x - momentum: } \rho \frac{Du}{Dt} &= \rho f_x - \frac{\partial p}{\partial x} + \frac{\partial \tau_{xx}}{\partial x} + \frac{\partial \tau_{yx}}{\partial y} + \frac{\partial \tau_{zx}}{\partial z}, \\ \text{y - momentum: } \rho \frac{Dv}{Dt} &= \rho f_y - \frac{\partial p}{\partial y} + \frac{\partial \tau_{xy}}{\partial x} + \frac{\partial \tau_{yy}}{\partial y} + \frac{\partial \tau_{zy}}{\partial z}, \\ \text{z - momentum: } \rho \frac{Dw}{Dt} &= \rho f_z - \frac{\partial p}{\partial z} + \frac{\partial \tau_{xz}}{\partial x} + \frac{\partial \tau_{yz}}{\partial y} + \frac{\partial \tau_{zz}}{\partial z}. \end{aligned} \quad (1.10)$$

Conservation of energy:

$$\rho \frac{Dh}{Dt} - \frac{Dp}{Dt} = \Psi - \nabla \cdot \dot{q} \quad (1.11)$$

where the heat transfer rate due to heat conduction is related to local temperature, T , as

$$\dot{q} = -k \nabla T \quad (1.12)$$

and with h and Ψ as defined further.

In Cartesian coordinates, equation (1.11) can be expressed as

$$\rho \frac{Dh}{Dt} - \frac{Dp}{Dt} = \Psi + \frac{\partial}{\partial x} \left(k' \frac{\partial T}{\partial x} \right) + \frac{\partial}{\partial y} \left(k' \frac{\partial T}{\partial y} \right) + \frac{\partial}{\partial z} \left(k' \frac{\partial T}{\partial z} \right) \quad (1.13)$$

where Ψ is given by

$$\Psi = 2\mu \left[\begin{aligned} &\left(\frac{\partial u}{\partial x}\right)^2 + \left(\frac{\partial v}{\partial y}\right)^2 + \left(\frac{\partial w}{\partial z}\right)^2 + \frac{1}{2}\left(\frac{\partial u}{\partial y} + \frac{\partial v}{\partial x}\right)^2 \\ &+ \frac{1}{2}\left(\frac{\partial v}{\partial z} + \frac{\partial w}{\partial y}\right)^2 + \frac{1}{2}\left(\frac{\partial w}{\partial x} + \frac{\partial u}{\partial z}\right)^2 - \frac{2}{3}\nu\left(\frac{\partial u}{\partial x} + \frac{\partial v}{\partial y} + \frac{\partial w}{\partial z}\right)^2 \end{aligned} \right] \quad (1.14)$$

where ν is the fluid kinematic viscosity (m^2s^{-1}), and u , v , w are the velocity components in the x , y , z direction, respectively.

When using equation (1.14) with an ideal gas such as air, the internal energy e and enthalpy h can be related to the temperature by

$$\begin{aligned} e &= c_v(T - T_{ref}) \\ &\quad \text{and} \\ h &= c_p(T - T_{ref}) \end{aligned} \quad (1.15)$$

where c_v and c_p are the specific heats at constant volume and pressure, respectively. T_{ref} is the reference temperature. Hereby, the internal energy and enthalpy are calculated relative to their values at T_{ref} , which are set to zero.

1.3.3.2 Equations of state

The state of a substance in thermodynamic equilibrium can be described by just two state variables, the equations of state for pressure p and internal energy e are

$$\begin{aligned} p &= p(\rho, T) \\ &\quad \text{and} \\ e &= e(\rho, T) \end{aligned} \quad (1.16)$$

It is useful to note that, for a perfect gas,

$$p = \frac{n}{V}RT \quad (1.17)$$

In the flow of compressible fluids there are links between the energy equation and the continuity and momentum equations, which occur due to density variations as a result of pressure and temperature variations in the flow field. As a result, without the link between the energy, the continuity and momentum equations, the flow field can be solved by considering only the continuity and Navier-Stokes equations, whereas the energy equation only needs to be solved alongside the other if the problem involves heat transfer.

1.3.4 Turbulence models

Turbulent flows are characterised by fluctuating velocity fields, resulting in mixed-transported quantities such as momentum, energy, and species concentration, and the fluctuation of transported quantities as well. In most practical engineering calculations, fluctuations are computationally too expensive to simulate directly, resulting from their small scale and high frequency. Instead, the instantaneous (exact) governing equations can be time-averaged or otherwise manipulated to remove the small scales, resulting in a modified set of equations that are computationally less expensive to solve. However, the modified equations contain additional unknown variables, and turbulence models are needed to determine these variables in terms of known quantities (Zabaleta, 2007).

Unfortunately, there is no single turbulence model universally accepted as being superior for all classes of problems. Consequently, the choice of model has to be made based on considerations of the physics encompassed in the flow, the available computational resources, and the simulation time. To make the most

appropriate model selection for a specific problem, it is required to understand the capabilities and limitations of various models.

A turbulence model is a computational procedure to close the system of mean flow equations. For most engineering purposes, it is unnecessary to resolve the details of the turbulent fluctuations. Only the effects of the turbulence on the mean flow are usually sought. For a turbulence model to be useful in a general purpose CFD code, it must have wide applicability, be accurate, simple and economical to run (Versteeg and Malalasekera, 2007). Among the most common turbulence models, the k- ϵ model has been used due to its advantages (Versteeg and Malalasekera, 2007):

- simplest turbulence model for which only initial and/or boundary conditions need to be supplied
- excellent performance for many industrially relevant flows
- well established; the most widely validated turbulence model.

1.4 CFD in food industry

Applications of CFD, originally used in the automotive, aerospace, and nuclear industries, have extended into the food industry in order to model industrial processes with the enhancement of computing power and efficiency, and the availability of affordable CFD packages (Xia and Sun, 2002; Sun, 2007). CFD serves as a powerful design and analysis tool in many food industrial processes such as drying, mixing, cooking, chilling, sterilisation, and other application areas, as found in literature reviews (Xia and Sun, 2002; Norton and Sun, 2006; Sun, 2007).

Recently, food drying is an example of an industrial application in which CFD has been widely used in order to solve a problem such as non-uniformity of drying air in a chamber, which is a common problem encountered in a batch drying process.

Many attempts have been made to optimise and develop not only traditional drying methods such as tray and spray drying, but also new innovative drying techniques. Application of CFD for simulation of drying processes has been reviewed in Jamaledine and Ray (2010). Spray drying is another traditional drying technique in which food powders are derived in order to easily store, handle, and transport (Nijdam and Langrish, 2004). CFD has also been used to investigate the performance and the designs of spray dryers (Kuriakose and Anandharamakrishnan, 2010).

Applications of CFD have been found in other areas of the food processing industry, including coffee roasting (Fabbri *et al.*, 2011), membrane clarification of juice (Mirsaeedghazi *et al.*, 2011), forced convection cooling (Dehghannya *et al.*, 2010) and even food rheology (Ptaszek, 2010), and egg pasteurisation (Denys *et al.*, 2004).

1.5 CFD in fluidised bed coating process

Fluidised bed coating is a process in which multiphase flow is encountered. Due to the inherent complexity of multiphase flows from a physical as well as a numerical point of view, general CFD codes do not exist because of:

- the very complex physical phenomenon where many flow types occur; gas-solid, gas-liquid, etc.
- the undeveloped complex physical laws and mathematical treatment of phenomena occurring in the presence of two phases (interface dynamics, coalescence, break-up, drag, etc).
- the complex numerics for solving the governing and closure equations.

Up till now, CFD models have been used in order to describe multiphase flows based on two classical techniques: the Lagrangian technique and the Eulerian technique. In Eulerian models, both solid and gas phases are considered a continuum and empirical equations have to be applied to introduce fluid-particle

drag into the model (Goldschmidt *et al.*, 2004). Moreover, with regard to modelling granulation and/or coating, constitutive relations for particle-particle collisions, droplet-particle coalescence and granulation kinetics are required (Goldschmidt *et al.*, 2003, Ronsse, 2006). On the other hand, the Lagrangian models (also referred to as discrete particle models (DPM) or discrete element models (DEM)) calculate the motion of every individual particle without additional closure equations for the suspended particulate phase, taking collisions and external forces acting on the particles directly into account (Goldschmidt *et al.*, 2003). As a result of the more detail in description of particle motion, discrete element models show better consistency with experimental results. However, using Lagrangian models for (industrial) fluidised bed coating and/or granulation processes requires a high computational cost resulting from a large number of particles in the simulation (Graham and Moyeed, 2002; Goldschmidt *et al.*, 2003).

1.5.1 CFD modelling of gas-solid fluidised beds

As the basic principle in fluidised bed coating, gas-solid fluidised bed flow is reviewed based on the CFD modelling in this section.

Based on standard CFD, Pan *et al.* (2002) presented the very first Eulerian-Lagrangian simulations of a fluidised bed encountered in practical applications. Not only the bed expansion could be simulated, but also the slip velocity could be directly calculated. However, due to the severe computational effort required, this approach is seldom applied. Many researchers have attempted to formulate transport equations governing the evolution in time and physical space, resulting in reduced description of the flow, as found in several studies (Anderson and Jackson, 1967; Whitaker, 1969; Drew, 1971; Drew and Segel, 1971; Drew, 1983; Drew and Lahey, 1993; Gidaspow, 1994; Zhang and Prosperetti, 1994; Enwald *et al.*, 1996; Jackson, 1997; Zhang and Prosperetti, 1997; Jackson, 1998). However,

the intent is far more practical and aspires to formulate relations that should be good enough to satisfactorily describe the phenomena of interest.

Another CFD approach, Eulerian-Eulerian, is often favoured, because it is computationally less demanding. Owing to the vast number of particles involved in industrial plants, continuum modelling is likely to replace the discrete modelling in the future (Lettieri and Mazzei, 2009). Many researchers have successfully simulated monodisperse-fluidised beds by means of the Eulerian-Eulerian approach. Ding and Gidaspow (1990) investigated and qualitatively validated the simulated results of the bubble dynamics of Group B particles. Van Wachem *et al.* (1998) simulated bubbling gas-fluidised beds of Group B particles, using columns of various diameters and different superficial velocities. Pain *et al.* (2001) analysed the effect of an obstruction on the fluidisation quality with the use of simulated bubbling and slugging gas-fluidised beds. Gelderblomm *et al.* (2003) studied the bubbling and collapsing of particles in groups A, B and C, and validated the model-predicted results with published data. Lettieri *et al.* (2003) simulated the transition from bubbling to slugging and subsequent turbulent gas fluidisation of group B particles. Owoyemi *et al.* (2005) investigated the hydrodynamics of powders of group B, whereas Mazzei and Lettieri (2008) studied the expanding and contacting homogeneous fluidised beds and their transition to the bubbling regime. Recently, Vatani *et al.* (2011) have used CFD to model gas-solid heat transfers to investigate the influence of the inlet gas velocity and temperature on mass transfer of air to wet particles.

1.5.2 Fluidised bed coating process

Here again many attempts have been made to model the flow in the fluidised bed coating process with the use of two approaches: Eulerian (or continuum) and Lagrangian (or discrete element) models. In addition to both approaches, the population balance model has been introduced in the CFD community to describe

the flow in this process. For more details concerning the population balance model, the reader is referred to chapter 4.

Goldschmidt *et al.* (2003) investigated the key features of fluidised bed hydrodynamics, liquid-solid interaction and subsequently agglomeration in a fluidised bed spray granulation using a novel discrete model, computing the motion of every individual particle and droplet with the consideration of the gas phase as a continuum. In addition, the influence of fluidisation airflow rate, spray rate and pattern on powder product characteristics was demonstrated. Karlsson *et al.* (2009) developed the multiphase fluid dynamics combined with heat and mass transfer to model the drying and wetting conditions in a lab-scale Wurster bed coater. The model-predicted characteristics of circulation of particles and moisture behaviour in a system were compared with experimental data. Rajniak *et al.* (2009) developed models combining the theoretical and experimental techniques for analyzing particle growth in a fluidised bed granulator. The methodology combined the population balance of particle growths from different materials, a CFD model describing the gas-solid flow, a model of contact mechanics and granule formation, a calculation of successful collisions, and a well-controlled experimental study of the wet granulation. Fries *et al.* (2011) developed the coupled DEM-CFD model by combining the gas and particle dynamics with a simple model of particle wetting to study the fluid and particle dynamics in two configurations of fluidised bed granulator: top-spray and Wurster reactor, on the scale of individual particles. Wetting of particles was estimated based on the residence time distribution inside a biconical spray zone. It was found from their work that the Wurster coater had a narrower residence time distribution than that obtained using the top-spray coater, resulting in more homogeneous particle wetting.

Other approaches in modelling liquid-sprayed fluidised beds include combining population balance models with Eulerian models, as demonstrated by Tan *et al.*

(2004). Heinrich *et al.* (2005) developed a model taking into consideration the heat and mass transfer in liquid-sprayed fluidised beds used for granulation, coating and agglomeration. To describe the particle size distribution and the seeds formation, the model was coupled with a population balance model. Gryczka *et al.* (2009) used the CFD models to simulate the hydrodynamic behaviour in a novel spouted bed apparatus for spray granulation and coating. Turchiuli *et al.* (2011) used the population balance model to describe the particle size distribution evolution during the granulation process in a top-sprayed fluidised bed with the use of air temperature distribution relevant to the wetting zone.

It can be found in the literature reviews that process models still need to be developed in order to describe the fundamental process of top-spray fluidised bed coating. Consequently, the main objective of this current research is to numerically study the processes taking place in the fluidised bed coating by means of computational fluid dynamics method.

Chapter 2 Comparison and evaluation of interphase momentum exchange models for simulation of the solids volume fraction in tapered fluidised beds

Parts of this chapter are published in:

Duangkhamchan, W., Ronsse, F., Depypere, F., Dewettinck, K., Pieters, J.G., 2010. **Comparison and evaluation of interphase momentum exchange models for simulation of the solids volume fraction in tapered fluidised beds.** *Chemical Engineering Science* 65, 3100-3112.

Abstract

An Eulerian computational fluid dynamics (CFD) model with granular flow extension was used to simulate a gas-solid fluidised bed in a tapered reactor. Various drag coefficient models were evaluated, which are used to calculate the drag force, describing the momentum transfer between the gas and solid phases. Comparison and evaluation between time-averaged solids volume fractions obtained from experiments and from simulations with several drag coefficient models were made. The predicted results obtained by the different drag models were verified using experimental data of Depypere *et al.* (2009). Initial results using a 2-phase Eulerian model showed poor agreement with experimental results. However, extending the Eulerian model to include 3 solid phases – with different mean particle diameter per phase in order to account for the particle size distribution of the fluidised solid material – yielded good agreement with experimental results. Furthermore, quantitative analyses showed that the modified Gidaspow drag model gave the best agreement between CFD simulations and experimental data.

2.1 Introduction

Among the wide range of microencapsulation techniques, fluidised bed technology has been successfully used for the coating of particulate solids due to its excellent mixing capabilities and its optimal heat and mass transfer rates (Dewettinck and Huyghebaert, 1998; 1999; Ronsse *et al.*, 2007a-b). Moreover, this technology has proven to be applicable in different industries, e.g. the chemical, pharmaceutical, mineral and food industry, not only because it allows for a large number of unit operations to be performed within the same piece of equipment, either separately or sequentially (Depypere *et al.*, 2003), but it also tunes the effect of functional ingredients and additives (Depypere *et al.*, 2009). Due to the complex flow behaviour and the many interactions taking place in fluidised bed systems which are not fully understood, there is still a need for mathematical models to improve the fundamental understanding of the flow inside the fluidised bed reactor (Cruz *et al.*, 2006; Cornelissen *et al.*, 2007). Recently, Computational Fluid Dynamics (CFD), a powerful numerical tool for solving fluid flow problems, has been widely used in an attempt to model gas-solid fluidised beds using two different approaches: a discrete method (Lagrangian model) and a continuous approach (multifluid or Eulerian-Eulerian model). In the discrete phase method, the fluid phase is described by a locally averaged Navier-Stokes equation with the use of interphase forces for coupling the two phases. The multifluid model, on the other hand, is based on continuum mechanics which treat the two phases as interpenetrating continua (Taghipour *et al.*, 2005). Up to date, although many researchers have attempted to study the complex flow behaviour in gas-solid flow systems by means of CFD, they are still challenged to obtain accurate solutions of any multiphase flow problem where the concentration of at least one dispersed phase is a few percent or more (Gera *et al.*, 1998; Benyahia *et al.*, 2000; Du *et al.*, 2006a-b; Jiradilok *et al.*, 2006; Hidayat & Rasmuson, 2007). In gas-solid flow systems, a number of complex factors need to be modelled. Among these are the interfacial forces, electrostatic forces, particles properties, interparticle forces –

e.g. due to van der Waals forces – and interparticle collisions (Grace & Taghipour, 2004). As the primary effect on the hydrodynamic behaviour, the interfacial forces, which are used to describe the momentum transfer between the two phases, include drag force, lift force and virtual mass force (Du *et al.*, 2006a). When coupling the equations of the two phases and considering the density and particle size of solids used in typical fluidised bed coating applications, forces other than drag force are less significant due to the large difference in density between the two phases and can thus usually be neglected. Consequently, in most studies dealing with interfacial forces, only drag force is considered. However, due to the sensitivity of the model solution to the values of drag coefficients, the choice of drag coefficient models has to be taken into account in simulating gas-solid flows (Yasuna *et al.*, 1995). Du *et al.* (2006a) found that the selection of suitable drag models plays an important role in simulating two-phase flows. Among the different drag models, they concluded that the Gidaspow (1994) model gave the best agreement with experimental data. Cruz *et al.* (2002, 2006) showed that the drag force closure models available in the FLUENT CFD software were suitable for low density risers to predict the radial distribution of solids concentration and solids mass flux, while new models for high density systems had to be developed. Taghipour *et al.* (2005) calculated the momentum exchange coefficients using the Symlal-O'Brien, Gidaspow and Wen-Yu drag functions available in FLUENT. Agreement between the model predictions and experimental measurements on the time-averaged bed pressure drop, bed expansion, and qualitative gas-solid flow, was found for most operating conditions. Furthermore, Zimmermann and Taghipour (2005) modified the drag law of Symlal-O'Brien (1989), which is based on the measurements of the terminal velocities of particles in fluidised or settling beds, to match the minimum fluidisation conditions of the particles.

In this chapter, the simulation of gas-solid flow in a tapered fluidised bed coater by means of CFD associated with an Eulerian-Eulerian approach was investigated in order to select a suitable drag coefficient model. Various drag models both

available in FLUENT and proposed by researchers elsewhere were employed in the CFD simulations to assess the suitability of drag coefficient functions for modelling the hydrodynamics of the multiphase flow in tapered fluidised bed coaters. Finally, the results of the CFD simulation were compared with experimental results obtained with the Positron Emission Particle Tracking (PEPT) technique (Depypere, 2005; Depypere *et al.*, 2009).

2.2 Governing equations

For the current study, the Eulerian approach was used to treat the different phases as interpenetrating continua by incorporating the concept of phase volume fractions, and to solve the conservation equations for each of the two phases to obtain a set of equations which have a similar structure for each phase.

2.2.1 Conservation equations of mass and momentum

The conservation of mass of phase q ($q =$ either gas or solid) is described as

$$\frac{\partial}{\partial t}(\alpha_q \rho_q) + \nabla \cdot (\alpha_q \rho_q \vec{v}_q) = 0 \quad (2.1)$$

where α_q is the phase volume fraction, ρ_q the density and \vec{v}_q the velocity of phase q . The volume fractions of each phase are constrained by:

$$\sum_{q=1}^n \alpha_q = 1 \quad (2.2)$$

The following equation describes conservation of momentum for the fluid phase l :

$$\begin{aligned} \frac{\partial}{\partial t}(\alpha_l \rho_l \bar{v}_l) + \nabla \cdot (\alpha_l \rho_l \bar{v}_l \bar{v}_l) = & -\alpha_l \nabla \cdot p + \nabla \cdot \bar{\tau}_l + \alpha_l \rho_l \bar{g} + K_{ls}(\bar{v}_l - \bar{v}_s) + \\ & \dot{m}_{ls} \bar{v}_{ls} + (\bar{F}_l + \bar{F}_{lift,l} + \bar{F}_{vm,l}) \end{aligned} \quad (2.3)$$

In Equation (2.3), \bar{F}_l is an external body force, $\bar{F}_{lift,l}$ a lifting force, $\bar{F}_{vm,l}$ a virtual mass force and \bar{v}_{sl} is the slip velocity between the phases. Mass transfer from the fluid phase to the solid phase is characterised by \dot{m}_{ls} . K_{ls} denotes an interacting force between the phases, p is the pressure and $\bar{\tau}_l$ the fluid phase stress-strain tensor.

Analogous, the conservation of momentum for the solid phase s is expressed by adding the solid pressure term ($-\nabla p_s$) to the right side of Eq. (2.3). The solids pressure is derived by making an analogy between the random particle motion arising from particle-particle collisions and the thermal motion of molecules in a gas (Fluent Inc, 2006),

$$\begin{aligned} \frac{\partial}{\partial t}(\alpha_s \rho_s \bar{v}_s) + \nabla \cdot (\alpha_s \rho_s \bar{v}_s \bar{v}_s) = & -\alpha_s \nabla \cdot p - \nabla \cdot p_s + \nabla \cdot \bar{\tau}_s + \alpha_s \rho_s \bar{g} + K_{sl}(\bar{v}_l - \bar{v}_s) + \\ & \dot{m}_{sl} \bar{v}_{sl} + (\bar{F}_s + \bar{F}_{lift,s} + \bar{F}_{vm,s}) \end{aligned} \quad (2.4)$$

When coupling the equations of the two phases, the external body force, \bar{F} , the lift force, \bar{F}_{lift} , and the virtual mass force, \bar{F}_{vm} in Eqs. (2.3) and (2.4) were neglected in this study due to the large difference in density between the two phases. However, in order to close the solid phase momentum equation, constitutive equations which describe the solid phase stress are required. For more details concerning these equations, the reader is referred to the FLUENT user manual (Fluent Inc, 2006).

2.2.2 Interphase momentum exchange coefficient (drag coefficient) models

It can be seen in Eqs. (2.3) and (2.4) that momentum exchange between the two phases (drag force) can be represented by the product of the slip velocity ($\vec{v}_l - \vec{v}_s$) and the gas-solid exchange coefficient, K_{sl} ($K_{sl} = K_{ls}$) as expressed by

$$F_{drag} = K_{sl} (\vec{v}_s - \vec{v}_l) \quad (2.5)$$

In this study, different drag force models were used based on different exchange coefficient models. Besides the gas-solid exchange coefficient models available in FLUENT, namely the Wen-Yu model (1966), Symlal-O'Brien model (1989) and Gidaspow model (Gidaspow *et al.*, 1992), the other models proposed by Arastoopour *et al.* (1990) and Gidaspow (1994) were applied to close the conservative momentum equations.

2.2.2.1 Symlal-O'Brien drag model

Symlal & O'Brien, (1989) proposed the drag coefficient model which is based on measurements of the terminal velocities of particles in fluidised or settling beds:

$$K_{sl} = \frac{3}{4} \frac{\alpha_s \alpha_l \rho_l}{v_{r,s}^2 d_s} C_D \left(\frac{Re_s}{v_{r,s}} \right) |\vec{v}_s - \vec{v}_l| \quad (2.6)$$

where Re_s is the relative Reynolds number expressed by

$$Re_s = \frac{\rho_l d_s |\vec{v}_s - \vec{v}_l|}{\mu_l} \quad (2.7)$$

$v_{r,s}$ is the terminal velocity for the solid phase:

$$v_{r,s} = 0.5 \left(a - 0.06 \text{Re}_s + \sqrt{(0.06 \text{Re}_s)^2 + 0.12 \text{Re}_s (2b - a) + a^2} \right) \quad (2.8)$$

with

$$a = \alpha_l^{4.14} \quad (2.9)$$

and

$$b = 0.8 \alpha_l^{1.28} \quad (2.10)$$

for $\alpha_l \leq 0.85$, and

$$b = \alpha_l^{2.65} \quad (2.11)$$

for $\alpha_l > 0.85$.

2.2.2.2 Wen-Yu drag model

Wen and Yu (1966) presented a correlation for dilute systems ($\alpha_l > 0.8$):

$$K_{sl} = \frac{3}{4} C_D \frac{\alpha_s \alpha_l |\vec{v}_s - \vec{v}_l|}{d_s} \alpha_l^{-1.65} \quad (2.12)$$

where

$$C_D = \frac{24}{\alpha_l \text{Re}_s} \left[1 + 0.15 (\alpha_l \text{Re}_s)^{0.687} \right] \quad (2.13)$$

2.2.2.3 Gidaspow drag model

For dense systems, Gidaspow *et al.* (1992) combined the model of Wen-Yu (1966) for dilute phase calculation ($\alpha_l > 0.8$), as shown in Equations (2.12) and (2.13), with the Ergun (1952) model for dense phase calculation ($\alpha_l < 0.8$), as follows:

$$K_{sl,Ergun} = 150 \frac{\alpha_s (1 - \alpha_l) \mu_l}{\alpha_l d_s^2} + 1.75 \frac{\rho_l \alpha_s |\bar{v}_s - \bar{v}_l|}{d_s} \quad (2.14)$$

2.2.2.4 Modified Gidaspow model

Because of the discontinuity of drag functions found in Eqs. (2.12) and (2.14) at $\alpha_l = 0.8$, Gidaspow (1994) introduced a transition function which gives a rapid continuous transition from one regime to the other. This function is given by

$$\varphi_{sl} = \frac{\tan^{-1}[150 \times 1.75(0.2 - \alpha_s)]}{\pi} + 0.5 \quad (2.15)$$

Therefore, the gas-solid drag coefficient, K_{sl} , can be modified as (Gidaspow, 1994),

$$K_{sl} = (1 - \varphi_{sl}) K_{sl,Ergun} + \varphi_{sl} K_{sl,Wen-Yu} \quad (2.16)$$

Eq. (2.16) is further referred to as the ‘modified Gidaspow’ model.

2.2.2.5 Arastoopour drag model

In order to give continuous values over all ranges of solids volume fractions, Arastoopour *et al.* (1990) modified a pressure drop correlation proposed by Gibilaro *et al.* (1985) and used it as a gas-solid drag coefficient model, expressed as:

$$K_{sl} = \left[\frac{17.3}{\text{Re}_s} + 0.336 \right] \frac{\rho_l}{d_s} |\bar{v}_s - \bar{v}_l| \alpha_s \alpha_l^{-2.8} \quad (2.17)$$

2.3 Materials and methods

2.3.1 Numerical setup

Prior to performing CFD calculations, the half geometry of a laboratory-scale Glatt GPCG-1 fluidised bed (Glatt GmbH, Germany), as shown in Figure 2.1, was defined and a grid was generated using Gambit 2.2.30 (Ansys Inc., Canonsburg, PA). A hybrid hexahedral-tetrahedral meshing was done with a size of 0.005 m, based on a grid dependency test. Furthermore, mesh refinement was generated: boundary layers in the vicinity of the distributor and an increased number of nodes near the walls. The meshed geometry, containing 108,721 elements, is displayed in Figure 2.1.

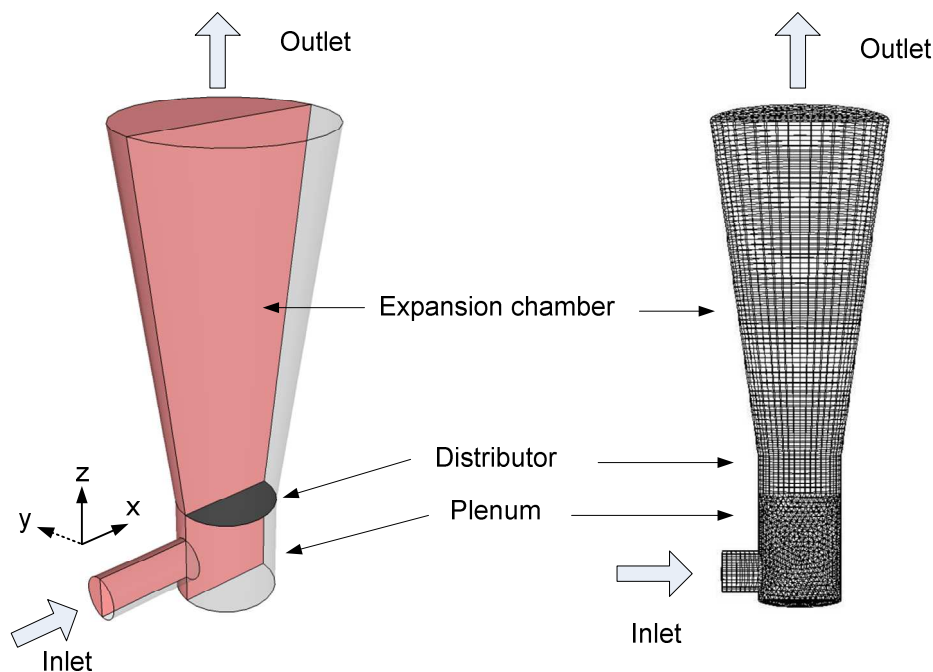


Figure 2.1 The modelled half geometry of a laboratory Glatt GPCG-1 fluidised bed reactor (left) and the corresponding mesh (right).

Two different models were used: the common two-phase Eulerian model and a 4-phase Eulerian model. The latter approach was used to account for the polydispersity of the solids, as used in the experimental validation (see Section

2.3.2). In the 4-phase model, gas was defined as the primary phase and three separate phases were defined as the solid phase with different particle size for each phase. The particle size used in each solid phase of the 4-phase model corresponded to the average size of the particles (i.e., those used in the experimental validation) with a diameter below the 20th, between the 20th and 80th, and above the 80th percentile, respectively. These values were chosen for the purpose not to disregard the effect of the significantly larger and smaller sized particles (i.e., corresponding to the right and left tail in the particle size distribution) in the modelled fluidised bed behaviour. The particle size distribution of the glass beads used in the PEPT-experiments is given in Figure 2.2, along with definition of the particle size classes used in the 4-phase model.

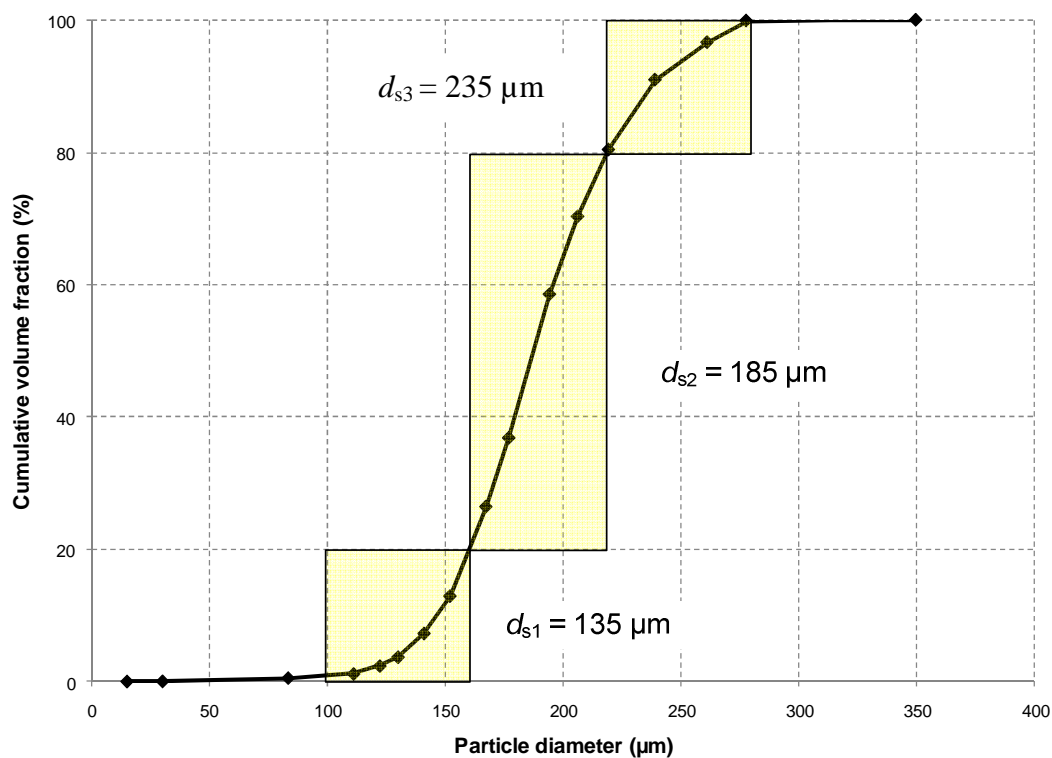


Figure 2.2 Particle size distribution of the glass beads used in the PEPT-measurements and definition of the 3 solid phases with their corresponding particle diameter in the four-phase model.

In the next step, the boundary conditions and the fluid and solid properties had to be specified. The air inlet was modelled as a velocity inlet, and the outlet was modelled as a pressure outlet. Furthermore, the walls were set as stationary boundaries at which the no-slip condition was applied, meaning that the gas velocity closest to the walls is equal to zero. The porous zone boundary condition was specified to model the air distributor for which values for the impermeability and inertial resistance were obtained by Depypere *et al.* (2004). The remaining model parameters and conditions are summarised in Table 2.1.

Table 2.1 The simulation model parameters and conditions

<i>Description</i>	<i>Value</i>
Particle density (kg m ⁻³)	2467
Gas density (kg m ⁻³)	1.225
Mean particle diameter (µm)	197 ^a
	135, 185, 235 ^b
Restitution coefficient ^c	0.9
Initial solids packing	0.64
Superficial gas velocity (m s ⁻¹)	1.00, 1.75
Vessel height (m)	0.56
Vessel bottom diameter (m)	0.14
Vessel top diameter (m)	0.30
Static bed height (m)	0.03
Inlet boundary condition	velocity
Outlet boundary condition	pressure

(^a) two-phase model, (^b) four-phase model

$$(\text{c}) \text{ restitution coefficient} = \frac{\text{velocity after collision}}{\text{velocity before collision}}$$

In the current study, the commercially available CFD software FLUENT 6.3.26, from ANSYS Inc. (Canonsburg, PA, US) was used to perform simulations using

the finite-volume method. FLUENT uses a computational grid where the governing equations describing fluid flow, the continuity equation, the set of Navier-Stokes equations, and any additional conservation equations such as the energy balance based on the multifluid Eulerian approach are solved. CFD simulations were performed using a single-precision, unsteady-state, first order implicit solver. For the solution of the gas/solid flow, a multiphase flow Eulerian model was applied together with the momentum exchange coefficients calculated using the different exchange-coefficient models (Symlal-O'Brien, Wen and Yu, and Gidaspow) available in FLUENT. In addition the drag coefficient models proposed by Arastoopour *et al.* (1990), Gidaspow (1994), the latter being called the modified Gidaspow model in this work, were applied through user-defined functions. Flow turbulence was simulated using the standard $k-\varepsilon$ model with standard wall functions, and first order upwind schemes were selected for the convection terms. The relation between velocity and pressure corrections was calculated using the phase-coupled SIMPLE algorithm. Finally, a time step of 0.0001 s with a maximum of 100 iterations per time step was chosen in order to improve convergence behaviour. On an Intel Pentium[®] Core i7 (2.67 GHz) equipped computer, simulating 15 seconds of the fluidisation process using the modelling procedure described above, on average took 4 to 5 days of simulation time.

According to the objective of this study, the contour maps of the fluidised bed voidage were processed in the mapping program Surfer v8 (Golden software, Inc., USA) using the triangulation with linear interpolation gridding method and the differences between model-predicted and measured (interpolated) voidage contours were evaluated using the sum of squared residuals (SSR). The SSR is a measure of the model's deviation from the experimentally measured solids volume fraction (Ronsse *et al.*, 2007a). It was calculated as

$$SSR = \sum (\alpha_{s,\text{exp}} - \alpha_{s,\text{sim}})^2 \quad (2.18)$$

The summation in Eq. (2.18) is performed on a per-pixel basis of the voidage contour plots (pixel size equals 0.001×0.001 m). Therefore, the SSR has no absolute reference value, but does allow for the direct and quantitative comparison of different model-predicted voidage contours against the experimentally measured voidage contours. Next to the SSR, the absolute mean error (e_{abs}) was calculated, according to

$$e_{abs} = \sqrt{SSR/n_{pix}^2} \quad (2.19)$$

where n_{pix} is the number of pixels in the contour plot which were used to calculate the SSR.

2.3.2 Experimental setup

For the validation of the model, the experimental data obtained by Depypere (2005) and Depypere *et al.* (2009) were used. In this research work, fluidisation experiments in a laboratory-scale Glatt GPCG-1 fluidised bed (Glatt GmbH, Germany) comprising a stainless steel tapered (8.1° inclination) vessel with a stainless steel woven wire Robusta 172 distributor (Spörl, Germany) at the base were conducted. The characteristics of this distributor are summarised in Table 2.2. The air flow rates in the fluidised bed were $55 \text{ m}^3 \text{ h}^{-1}$ and $97 \text{ m}^3 \text{ h}^{-1}$, which correspond to a superficial air velocity across the distributor of 1.00 m s^{-1} and 1.75 m s^{-1} , respectively. It should be kept in mind that flow rate measurements are usually characterised by uncertainties of about 20%. For the fluidisation experiments 0.75 kg of glass beads (Microbeads®, Sovitec, Belgium) were used (surface-weighted diameter, d_{32} : $196.54 \pm 0.64 \text{ }\mu\text{m}$; particle density: $2467 \pm 3 \text{ kg m}^{-3}$). In addition, using a 10-hPa differential pressure probe (Testo), the static

pressure at several bed heights located at 0.02 m increments above the air distributor were recorded in order to determine the expanded bed height.

Table 2.2 Air distributor characteristics (Depypere, 2005)

<i>Characteristic</i>	<i>Value</i>	<i>Remarks</i>
Warp mesh (wpi)	172	Number of wires per inch (wpi) in one direction
Weft mesh (wpi)	36	Number of wires per inch in the orthogonal direction
Absolute filter fineness (μm)	100	Diameter of the largest, hard spherical particles which can pass through the distributor (stationary flow conditions)
Distributor thickness (μm)	650	
$D_z(\text{m}^{-2})$	3.4×10^8	Porous zone impermeability
$C_z(\text{m}^{-1})$	3204	Porous zone inertial resistance

Depypere (2005) and Depypere *et al.* (2009) measured the motion of the glass beads (solids) inside the reactor vessel using Positron Emission Particle Tracking (PEPT). This technique allows 3-D movement of a single tracer particle to be followed in a non-invasive way. By tracking the particle location and movement over prolonged periods, time-averaged steady-state solids volume concentration (α_s) and voidage (α_l) profiles can be derived.

2.4 Results and Discussion

2.4.1 Introduction

In order to determine the time-averaged steady-state fluidised bed behaviour using the CFD model, the simulation time at which the voidage fluctuated around a near

steady-state value had to be determined. Subsequently, the simulation results from time zero until steady-state was reached, were discarded from the time-averaged bed voidage profile calculations. Figure 2.3 shows the model-predicted time-dependant bed voidage (α_i), averaged at heights of 1.7 cm, 7.0 cm and 12.2 cm above the air distributor, with an inlet air flow rate of $97 \text{ m}^3\text{h}^{-1}$. From Figure 2.3, it can be observed that the simulated values reached a near steady-state value after about 5 s. A 5% deviation was taken as steady-state criterion, as a trade-off between numerical accuracy and computational time. Based on this analysis, the time-averaged steady-state solids volume and bed voidage fraction for comparing modelling and experimental results were taken after 5 s.

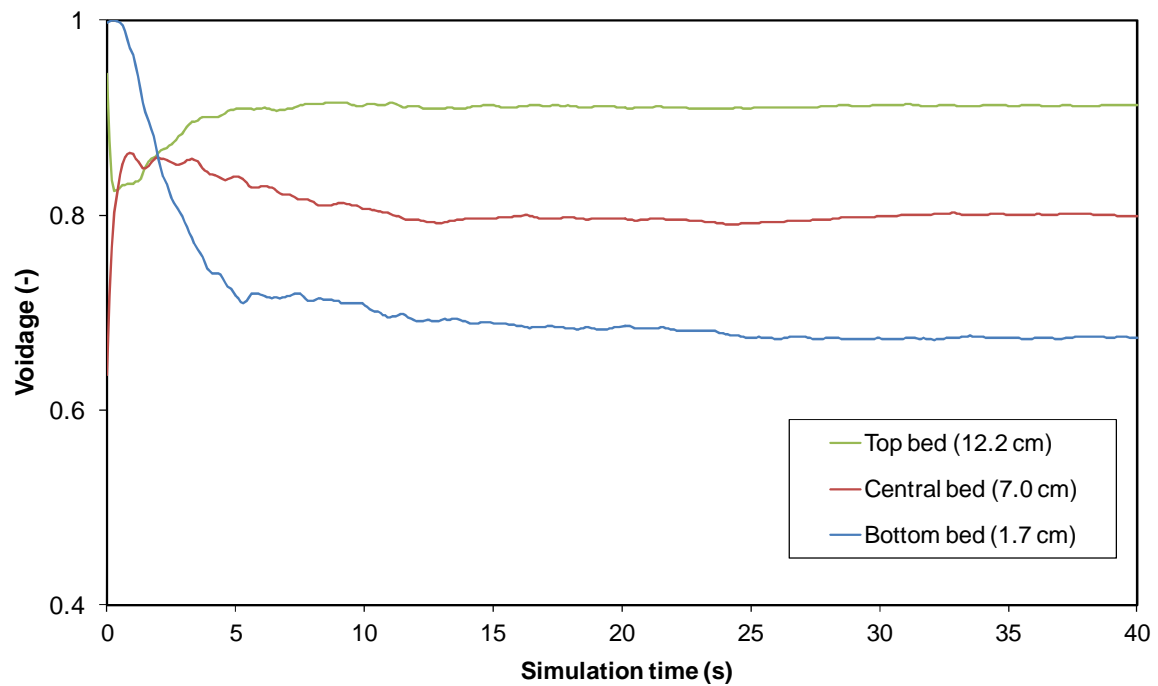


Figure 2.3 Simulated time-averaged voidages (α_i) as a function of length of simulated time in the bottom bed, the central bed and the top bed, taken at 1.7, 7.0 and 12.2 cm above the air distributor, respectively. Modelled inlet air flow rate was set at $97 \text{ m}^3\text{h}^{-1}$.

2.4.2 Voidage contours

2.4.2.1 Qualitative analysis

Predicted bed voidage profiles (α) using different drag coefficient models in two-phase flow simulations were plotted and compared with experimental results at fluidisation air flow rates of $55 \text{ m}^3\text{h}^{-1}$ and $97 \text{ m}^3\text{h}^{-1}$, as shown in Figures 2.4 and 2.5, respectively.

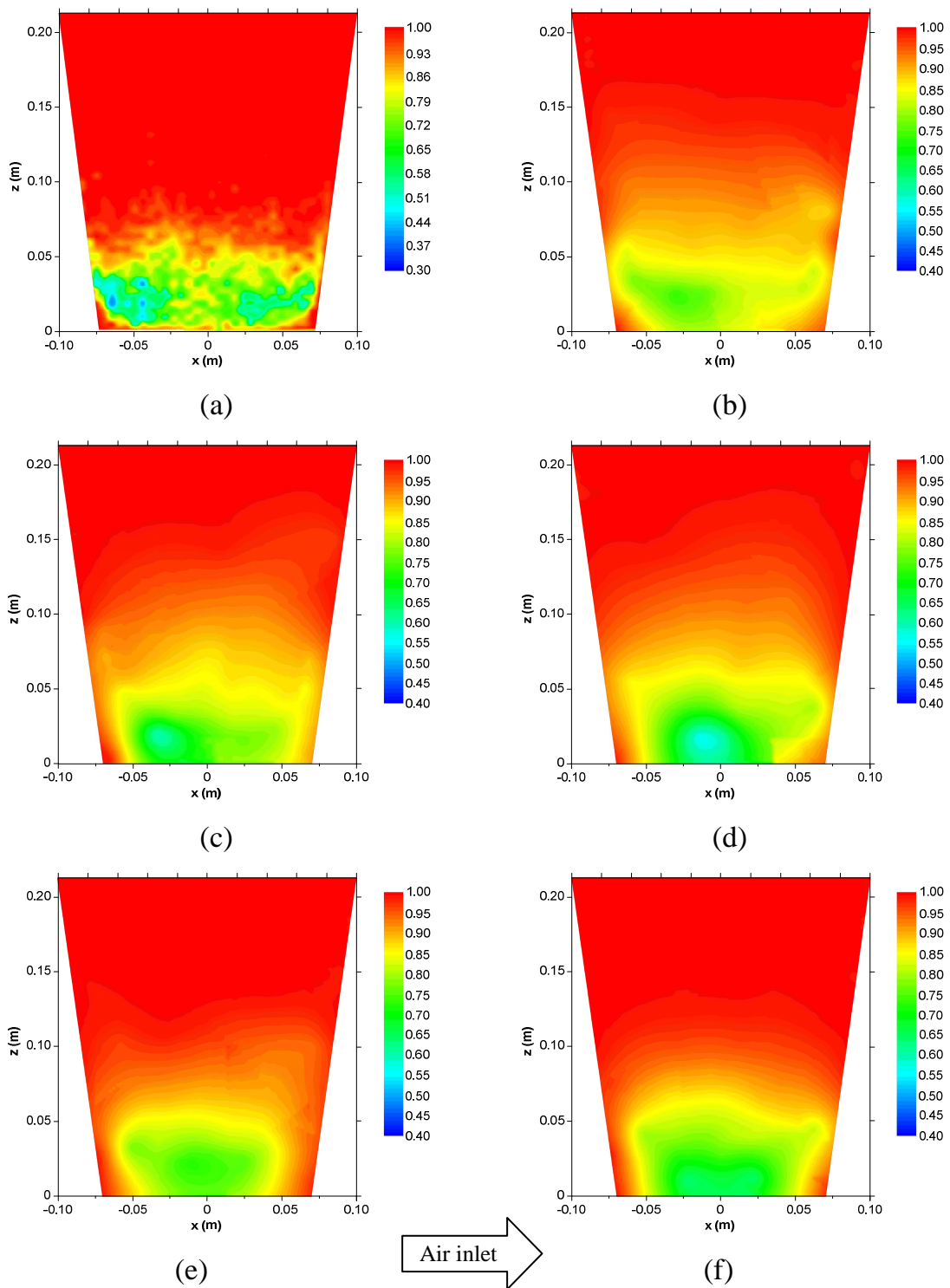


Figure 2.4 Model-predicted (2-phase) and experimental bed voidage (dimensionless) contour plots in the XZ plane ($y = 0$) for glass beads fluidised at $55 \text{ m}^3\text{h}^{-1}$ from (a) PEPT-experiment, (b) Wen-Yu model, (c) Symlal-O'Brien model, (d) Gidaspow model, (e) modified Gidaspow model and, (f) Arastoopour model.

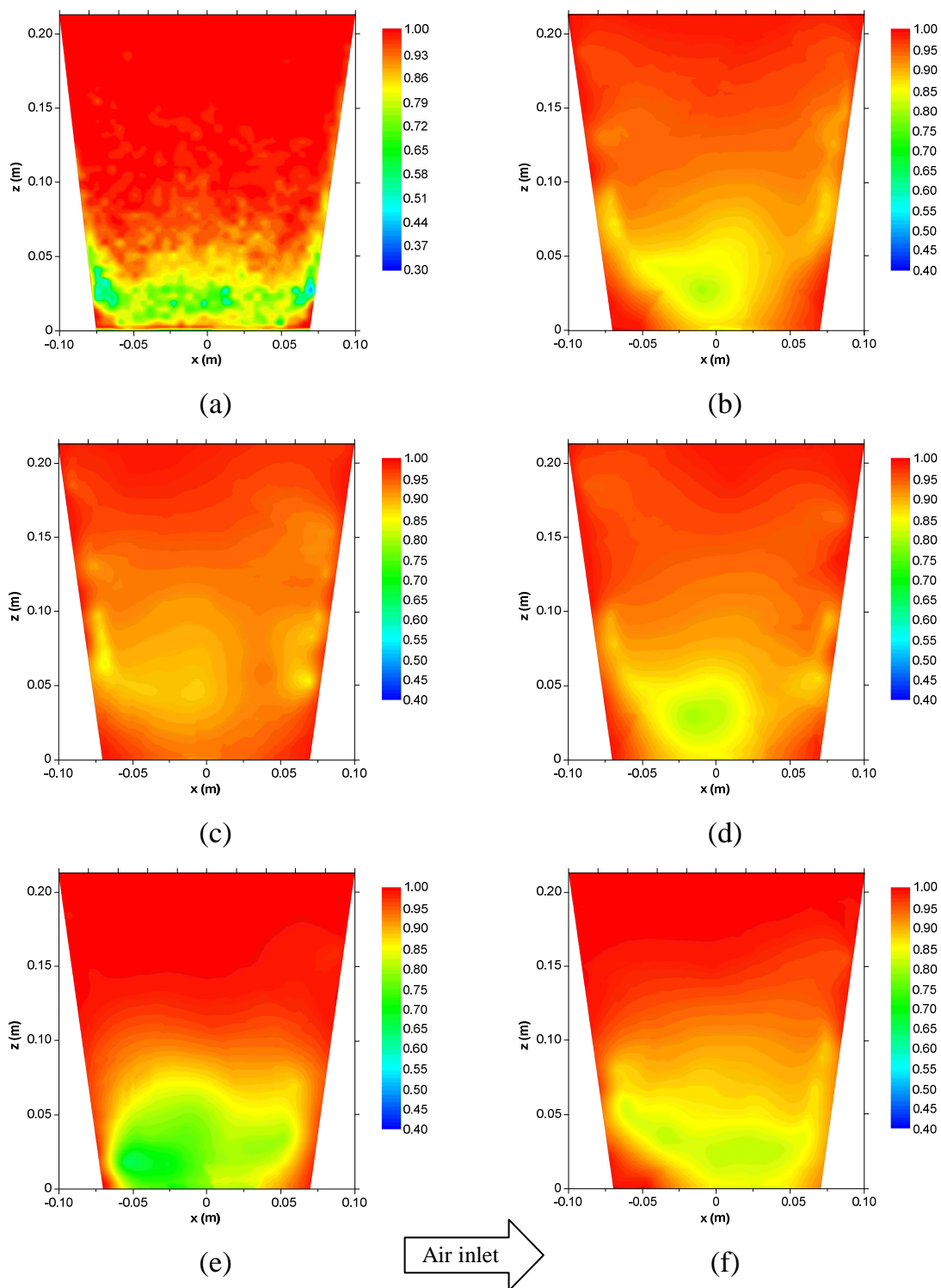


Figure 2.5 Model-predicted (2-phase) and experimental bed voidage (dimensionless) contour plots in the XZ plane ($y = 0$) for glass beads fluidised at $97 \text{ m}^3\text{h}^{-1}$ from (a) PEPT-experiment, (b) Wen-Yu model, (c) Symlal-O'Brien model, (d) Gidaspow model, (e) modified Gidaspow model and, (f) Arastoopour model.

From these figures, it is found that the model-predicted time-averaged voidage contours showed poor agreement with the experimental results. A possible explanation could be the effect of the width of the particle size distribution of the solids used in the experiments as opposed to the model, in which the solid phase is characterised by a single particle diameter. In order to study the effect of particle size distribution in the model, the simulations were repeated using the four-phase Eulerian model, in which the fluidisation gas was defined as the primary phase and three separate phases were defined for the solid phase. The diameter of the solids in each of the three phases were 135, 185 and 235 μm , respectively. These particle sizes correspond to the average size of the particles with a diameter below the 20th, between the 20th and 80th, and above the 80th percentile, respectively, from the particle mix used in the PEPT-experiments, as is also shown in Figure 2.2 (Depypere, 2005; Depypere *et al.*, 2009).

Simulation results from the four-phase model, expressed as time-averaged voidages (taken between 5 to 15 seconds of simulation time) using different drag coefficient models were plotted with the contour mapping software. Figures 2.6 and 2.7 demonstrate the contour plots of voidage profiles for glass beads fluidised at fluidisation air flow rates of 55 m^3h^{-1} and 97 m^3h^{-1} , respectively.

Due to the lateral position of the fluidisation air inlet in the plenum section of the Glatt-GPCG-1 equipment, as shown in Figure 2.1, the air flow pattern above the distributor was asymmetric. The air velocities on the right side of the XZ-plane were higher than those on the adjacent (left) side of the plenum air inlet as demonstrated by Depypere *et al.* (2004). This pattern can also be observed in the bed voidage profiles obtained by the PEPT experiments (Depypere, 2005; Depypere *et al.*, 2009), and are shown in Figure 2.7a where it can be seen that solids contacting the wall on the opposite side of the air inlet (right side) reach a higher position compared to those on the adjacent wall. The higher fluidisation air flow on the right side caused an inclined particle bed along the wall as shown in

the voidage profiles. This inclined particle bed could also be seen numerically using CFD simulations with the use of all drag coefficient models, as illustrated in Fig 2.7(b-f), although the majority of the tested drag models – with the exception of the modified Gidaspow model – tended to overestimate this bed inclination.

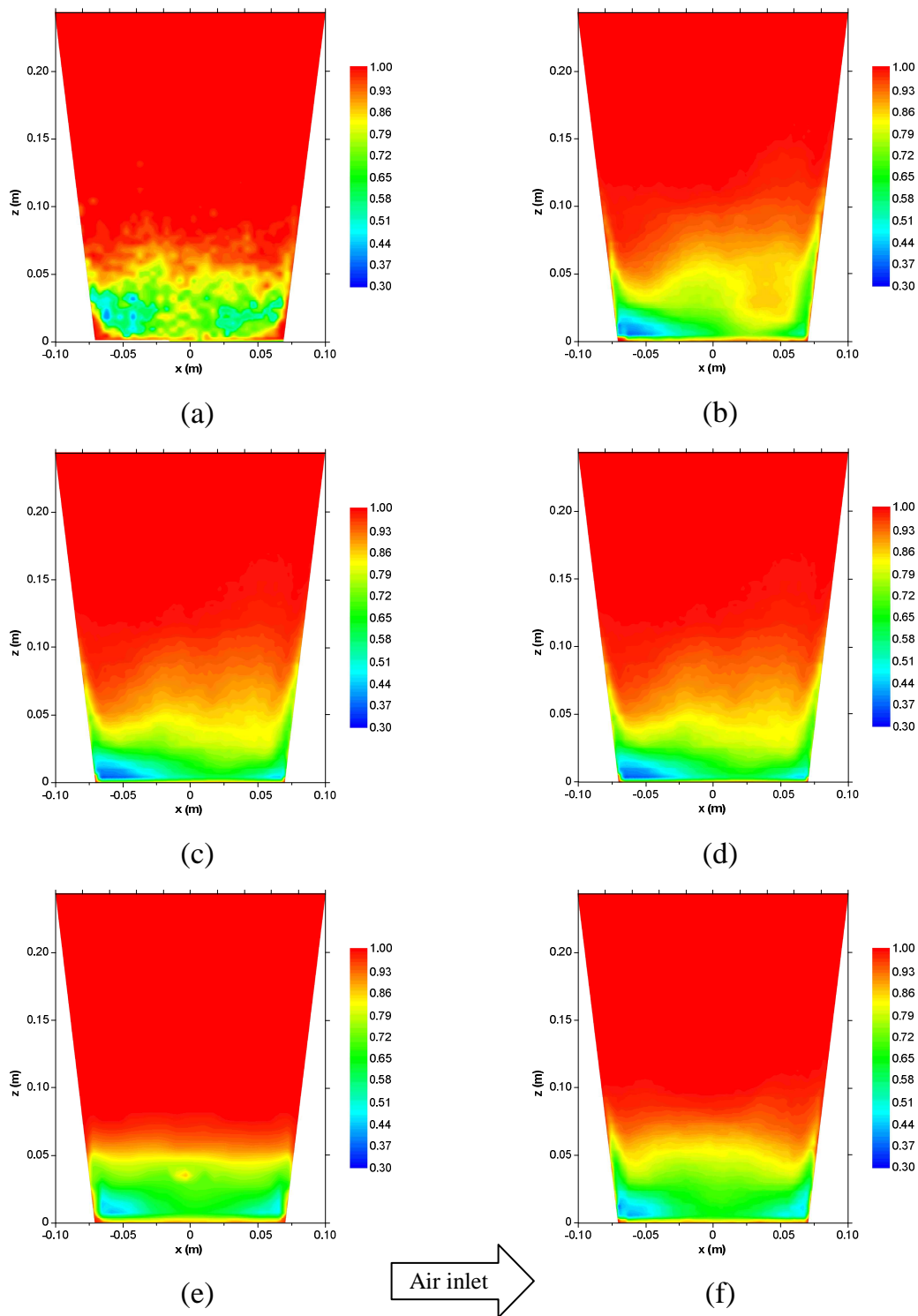


Figure 2.6 Model-predicted (4-phase) and experimental bed voidage (dimensionless) contour plots in the XZ plane ($y = 0$) for glass beads fluidised at $55 \text{ m}^3\text{h}^{-1}$ from (a) PEPT-experiment, (b) Wen-Yu model, (c) Symlal-O'Brien model, (d) Gidaspow model, (e) modified Gidaspow model and, (f) Arastoopour model.

When comparing the model-predicted versus the experimental voidage profiles, as shown in Figure 2.7, the use of the different drag models in the CFD modelling of the fluidised bed can bring about notably different prediction of drag forces acting on the particles. It can be observed that the results by the Arastoopour model, the Symlal-O'Brien model, the Gidaspow model and the Wen-Yu model gave rise to the presence of a very dilute region to the right side of the reactor just above the air distributor while a very dense region can be seen on the opposite side, which obviously differs from the experiment.

The discrepancy between the results of the Wen-Yu model and the experiments could be explained by the suitability of this closure for simulations involving dilute systems with void fractions not lower than 0.8. Additionally, since the Symlal-O'Brien model is based on the measurement of terminal velocities of particles in fluidised or settling beds which were used to determine the minimum fluidisation condition (see also Eqs. (2.6) to (2.8)), the calculated values of the momentum exchange were changed with the minimum fluidisation conditions (Zimmermann & Taghipour, 2005). Therefore, the discrepancy of voidages observed between predictions using the Symlal-O'Brien model and PEPT, as shown in Figure 2.7c may be caused by the variation of the minimum fluidisation conditions predicted in the Symlal-O'Brien drag model.

Although Gidaspow *et al.* (1992) combined the model of Wen-Yu (1966), which is suitable for dilute phase calculations ($\alpha_i > 0.8$), with the Ergun model (1952) for dense phase calculations ($\alpha_i < 0.8$), there is still a discontinuity of the drag function at $\alpha_i = 0.8$. Considering that a large fraction of the bed has a voidage of which the values are in the vicinity of $\alpha_i = 0.8$ – as can be seen from Figure 2.6a – the discrepancy between the modelling results from the Gidaspow model and the experimental PEPT results could be explained by this discontinuity of the drag function. Furthermore, Gidaspow (1994) attempted to avoid this problem of discontinuity by introducing a transition function which gives a rapid continuous

transition from dense to dilute regime around $\alpha_f = 0.8$ (modified Gidaspow model) and consequently, an improved agreement between experimental and model-predicted result can be seen in Figure 2.6e. Similar conclusions can be drawn from Figure 2.7, in which the comparison between the experimental and model-predicted voidage contour plots using a fluidisation air flow rate of $97 \text{ m}^3\text{h}^{-1}$, is given. Again, it can be seen that the simulation result based on the modified Gidaspow model gave the best agreement with the experimental results. In order to assess and evaluate which drag model is most suitable, quantitative analysis should be carried out (see Section 2.4.2.2).

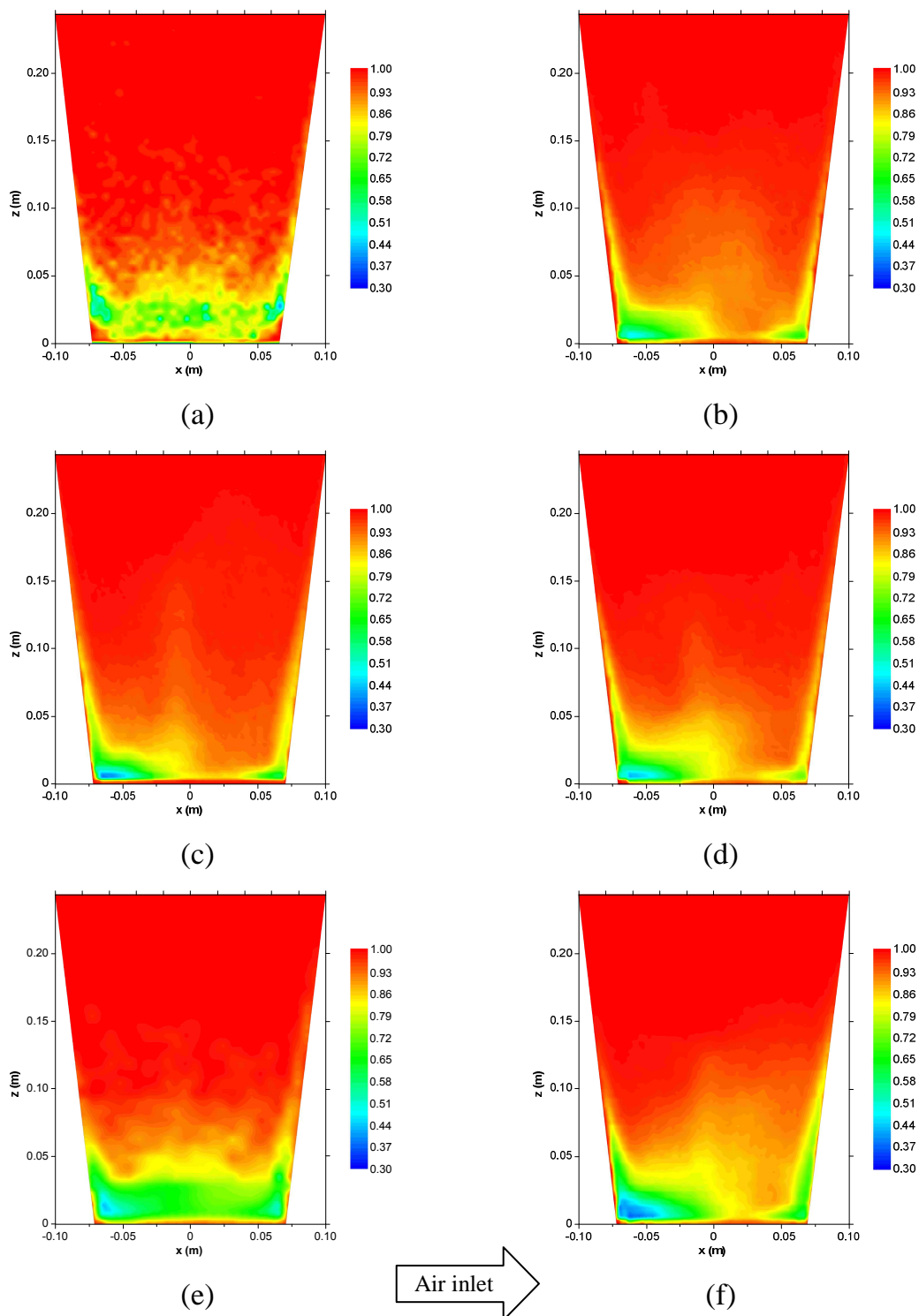


Figure 2.7 Model-predicted (4-phase) and experimental bed voidage (dimensionless) contour plots in the XZ plane ($y = 0$) for glass beads fluidised at $97 \text{ m}^3\text{h}^{-1}$ from (a) PEPT-experiment, (b) Wen-Yu model, (c) Symlal-O'Brien model, (d) Gidaspow model, (e) modified Gidaspow model and, (f) Arastoopour model.

In this study, a ‘dense region’ is defined as a dense zone ($\alpha_i \leq 0.60$) near the wall at the bottom of the bed – but not fully extending towards the air distributor – as shown in Figure 2.8. This dense region can be experimentally observed at both air flow rates, as shown in Figs 2.6a and 2.7a, but it cannot be distinguished in most of the model-predicted bed voidage profiles. Especially the two-phase Eulerian models (Figures 2.4b-f and 2.5b-f) fail to predict the near-wall dense region, while the four-phase Eulerian models (Figures 2.6b-f and 2.7b-f) distinctively predict the occurrence of this near-wall dense region. At high air flow rates, all four-phase model-predicted results showed this phenomenon at the near-wall bottom region of the bed, with bed voidages as low as 0.55-0.60. Again, the modified Gidaspow model (Figures 2.6e and 2.7e) yielded the best agreement with the PEPT-experiments.

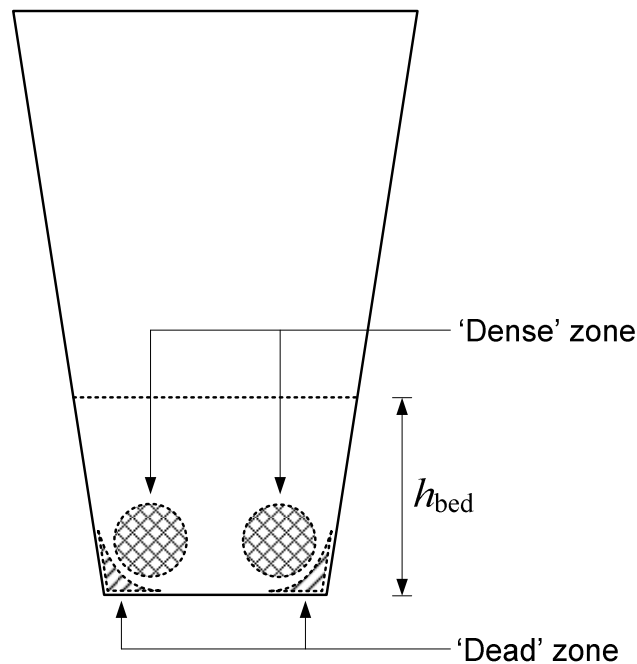


Figure 2.8 Definition of zones and regions in the fluidised bed.

2.4.2.2 Quantitative analysis

The results previously discussed reveal in a qualitative way that the choice of the drag model can considerably affect the simulated flow patterns. To quantitatively underpin the drag model selection, analysis of the SSR (sum of squared residuals)

– comparing the calculated spatial distribution of solids volume fraction with those from experiments – was carried out.

Table 2.3 presents the comparison of SSR for different drag coefficient models at high and low fluidisation air flow rates. From Table 2.3 it can be concluded that the modified Gidaspow model had the lowest SSR for both flow rates and approached closely the experimentally measured values, whereas the Wen-Yu model gave the worst results.

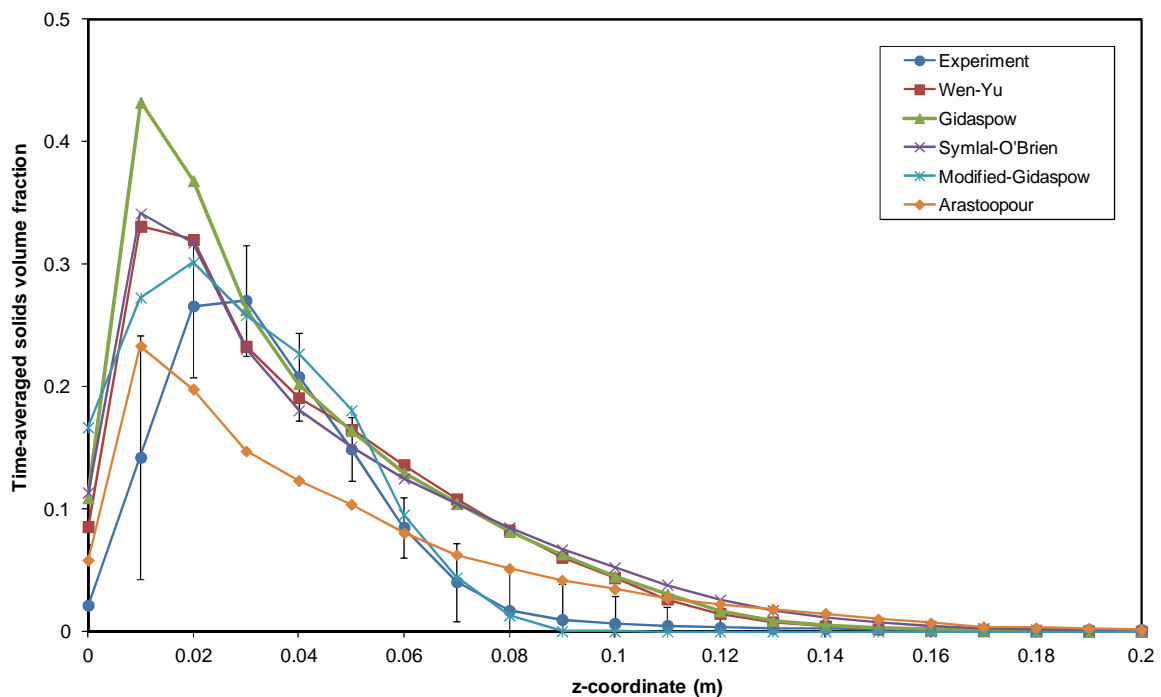
Table 2.3 Comparison of SSR and absolute mean error, e_{abs} , for different drag coefficient models (4-phase model)

<i>Drag coefficient models</i>	<i>SSR (high air flow)</i>	<i>SSR (low air flow)</i>	<i>Total SSR</i>	<i>e_{abs} (high air flow)</i>	<i>e_{abs} (low air flow)</i>
Wen-Yu	241	197	438	0.085	0.077
Symlal-O'Brien	168	204	372	0.071	0.079
Gidaspow	247	235	482	0.087	0.084
Arastoopour	175	153	328	0.073	0.068
Modified Gidaspow	113	122	235	0.059	0.061

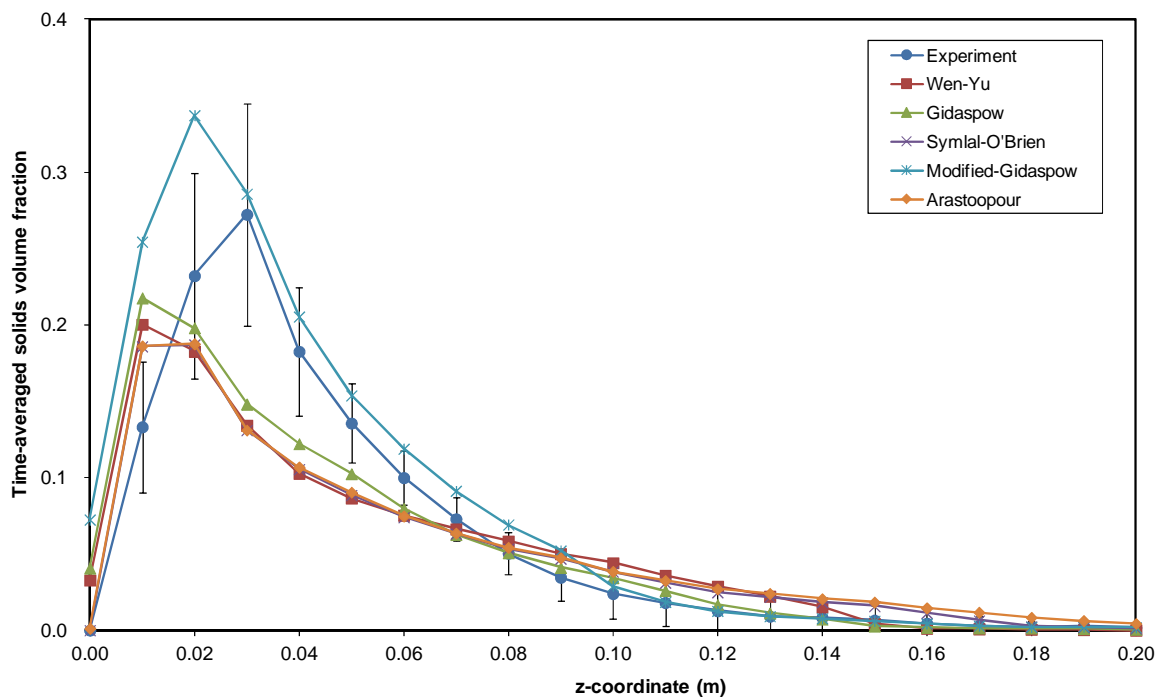
The total values of SSR were used in order to make a good choice of drag coefficient models for both fluidisation air flow rates. As a result, from the data in Table 2.3, it can be concluded that the modified Gidaspow model with a total SSR of 235 gave the best prediction of the solids volume fraction, followed by the Arastoopour and the Symlal-O'Brien model. Since the model of Gidaspow, which is appropriate for dense fluidised beds (Gidaspow *et al.*, 1992) and that performed rather poorly in this series of simulations (high SSR in Table 2.3), was modified with the use of the transition function in order to avoid the discontinuity of the drag coefficient at $\alpha_t=0.8$, the modified Gidaspow model performed significantly better. It was therefore considered the best choice of the drag coefficient model in this study.

2.4.3 Time-averaged solids volume fraction profiles

Model predicted values of time-averaged solids volume fractions as a function of the vertical position in the bed were compared with experimental data obtained from PEPT with two different fluidisation air flow rates (Depypere, 2005; Depypere *et al.*, 2009). Figures 2.9a and 2.9b illustrate these values as a function of position above the air distributor (z -coordinate) for various drag coefficient models with air flow rates of $55 \text{ m}^3\text{h}^{-1}$ and of $97 \text{ m}^3\text{h}^{-1}$. For both fluidisation air flow rates, all predicted solids volume fraction profiles show that the solids volume fraction decreased, after reaching a maximum, with increasing vertical position in the bed, illustrating a qualitative agreement with the experimental tendency. It can also be observed that at the position just above the air distributor ($z \leq 0.01 \text{ m}$ at $55 \text{ m}^3\text{h}^{-1}$ and $z \leq 0.03 \text{ m}$ at $97 \text{ m}^3\text{h}^{-1}$), lower particle concentrations can be found both experimentally and numerically. Even though the modified Gidaspow model is considered a better choice of drag model in this study, disagreement can be noticed at the height just above the air distributor ($z \leq 0.03 \text{ m}$, both flow rates). More specifically, the predicted solids volume fraction was over-estimated. This discrepancy could be explained by the presence of an annular dead zone at the bottom of the bed, in which particles do not reside, a phenomenon which tapered fluidised beds have in common with spouted beds (Stein *et al.*, 2000). The presence of this annular dead zone, whose position in the bed is shown in Figure 2.8, was observed in the PEPT-experiments, as shown in Figures 2.6a and 2.7a, but could not be reproduced using a 2- or 4-phase Eulerian model, regardless of the drag model used.



(a)

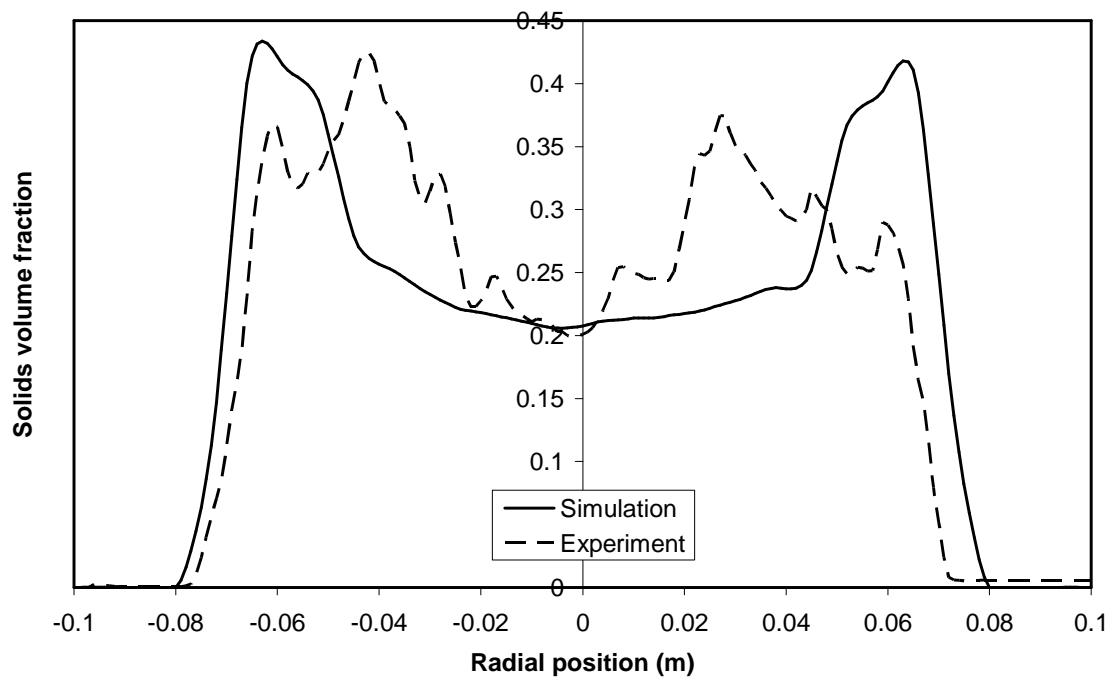


(b)

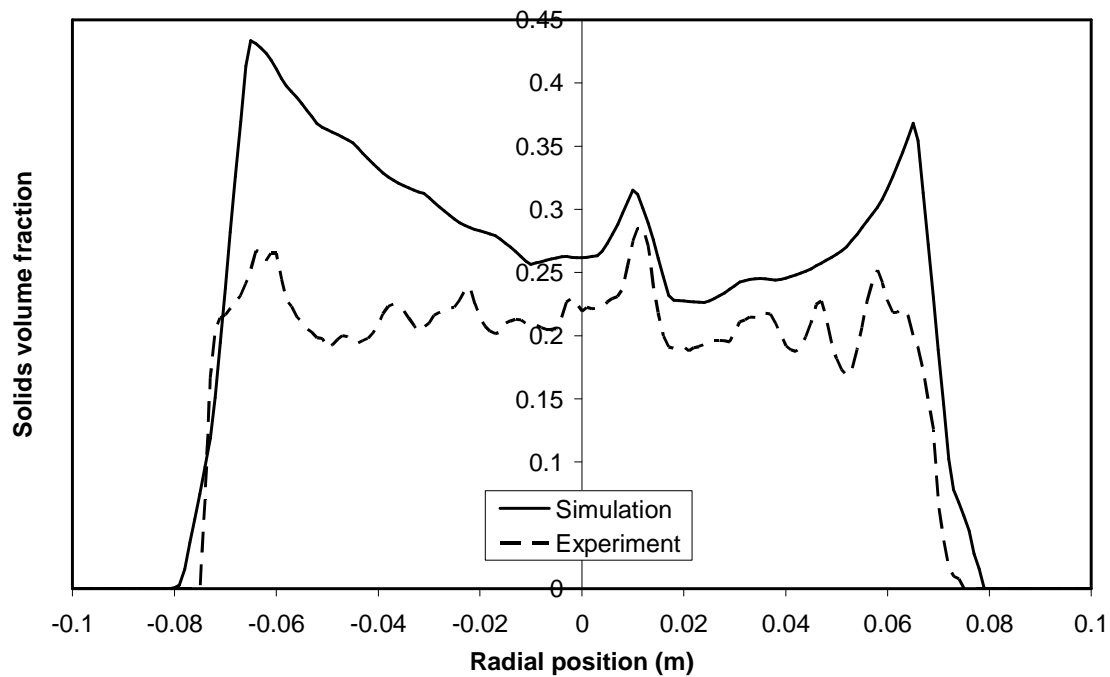
Figure 2.9 Comparison of time-averaged solids volume fraction (dimensionless) as a function of position above the air distributor between model-predicted (4-phase) and experimental results, (a) at low fluidisation air flow rate ($55 \text{ m}^3\text{h}^{-1}$), (b) at high fluidisation air flow rate ($97 \text{ m}^3\text{h}^{-1}$).

More details concerning the solids volume concentration just above the air distributor (volume integrated between $z = 0$ m and $z = 0.03$ m) are shown in Figures 2.10a and 2.10b, for low and high fluidisation air flow rates and simulated using the modified Gidaspow drag model. Clearly, the model-predicted solids concentrations were significantly higher than those of the experiments at the near-wall regions. Therefore, it was concluded that the dead zone could not be captured numerically using the modelling approach of this study.

However, as a result of increasing the number of dispersed phases from 1 to 3, resulting in the increase of transport equations to be solved, the computational load for solving this 4 phase model was higher than for the 2-phase model. It took on average two weeks for a simulation time of 15s, whereas this took only 4-5 days for the 2-phase model.



(a)



(b)

Figure 2.10 Experimental and model-predicted (4-phase), time-averaged solids volume fraction (dimensionless) from 0 – 3 cm above the air distributor as a function of radial position (x-coordinate) at (a) flow rates of $55 \text{ m}^3\text{h}^{-1}$ (low) and (b) of $97 \text{ m}^3\text{h}^{-1}$ (high).

2.5 Conclusion

In addition to the widely used interphase momentum exchange models available in FLUENT, including the Wen and Yu model, the Symlal and O'Brien model, and the Gidaspow model, the drag coefficient models proposed by Arastoopour *et al.* (1990) and Gidaspow (1994), built into an Eulerian two-fluid model, were compared and evaluated. The model-predicted values were validated against the PEPT results of Depypere (2005) and Depypere *et al.* (2009). The performance of the two-phase model was found to be poor. So, in order to include the effects of the width of the particle size distribution, a four-phase Eulerian model was proposed, effectively improving model accuracy with regards to the bed voidage and solids volume concentration profiles. The SSR (sum of squared residuals) was used to assess the simulation results obtained from the five different drag models and showed that the modified Gidaspow model gave the best prediction of solids volume fraction and bed voidage. However, discrepancy was observed at the bottom of the fluidised bed which can be explained by the presence of an annular dead zone, being a region in which particles do not reside, a phenomenon which tapered fluidised beds have in common with spouted beds.

Chapter 3 CFD study of solids concentration in a fluidised-bed coater with variation of atomisation air pressure

Parts of this chapter are published in:

Duangkhamchan, W., Ronsse, F., Dewettinck, K., Pieters, J.G., 2011. **CFD study of solids concentration in a fluidised bed coater with variation of atomisation air pressure.** *Powder Technology* 212, 103-114.

Abstract

The solids volume fraction inside a tapered fluidised bed coater was simulated with the use of an Eulerian computational fluid dynamics (CFD) model with atomisation nozzle sub-model. The drag force, describing momentum transfer between the gas and solid phases was calculated using the drag model proposed by Gidaspow (1994). In order to account for the particle size distribution of the fluidised solid materials, a 4-phase Eulerian model was used. The model-predicted results for different atomisation air pressures were verified using published experimental data (Depypere *et al.*, 2009). The model proved to be highly sensitive to changes in the fluidisation air flow rate with regard to the model-predicted solids volume distribution.

3.1 Introduction

In the previous chapter, to study the air flow pattern inside the GPCG-1 unit, gas-solid interaction was implemented in an Eulerian CFD model with granular flow extension. Comparison and evaluation of interphase momentum exchange models for simulation of solids volume fraction in the Glatt GPCG-1 fluidised bed coater with the absence of atomisation were carried out. In this work, the particle behaviour in the fluidised bed coater with the inclusion of atomisation at different pressures was investigated, by means of CFD associated with an Eulerian-Eulerian approach, in order to provide better qualitative and quantitative consistency of the simulation model with experimental data. Finally, comparison between the results from simulations and the experimental results obtained with the positron particle tracking (PEPT) technique was made (Depypere *et al.*, 2009).

3.2 Governing equations

As already discussed in the previous chapter, the substantial and prohibitive computational demands for large fluidised beds with several million particles exclude the use of a Lagrangian framework. Therefore, an Eulerian approach was used to treat the different phases as interpenetrating continua by incorporating the concept of phase volume fraction, and to solve the conservation equation for each phase to obtain a set of equations which have a similar structure for each phase. Currently, the kinetic theory of granular materials is used in both the dilute-phase modelling of circulating fluidised beds (Benyahia *et al.*, 2000; Arastoopour and Gidaspow, 1979; Agrawal *et al.*, 2001) and the dense phase modelling of bubbling fluidised beds (Ding and Gidaspow, 1990; Wirsum *et al.*, 2001; Peirano *et al.*, 2002; Soo, 1989).

As a result of the particle size distribution of the materials used in the validation (PEPT) experiments (Depypere *et al.*, 2009), polydispersity was taken into account

in order to provide better qualitative and quantitative consistency of model simulations with experimental data. In the previous chapter, a four-phase Eulerian model was built using a single gas phase as the primary phase and three separate solid phases with different particle sizes, for which an improvement in model accuracy with respect to bed voidage and solids volume fraction profiles was observed when compared to standard two-phase Eulerian models. Therefore, in this chapter again, the four-phase Eulerian model was used to investigate the bed voidage and solids concentration profiles in a fluidised bed coater with the presence of an atomisation nozzle operating at different air pressures.

3.2.1 Conservation equations of mass and momentum

In this chapter, the Eulerian approach was used to treat the different phases as interpenetrating continua by incorporating the concept of phase volume fractions, and to solve the conservation equations for each of the two phases to obtain a set of equations which have a similar structure for each phase. More details concerning the conservation equations of mass and momentum for each phase, the reader is referred to chapter 2.

3.2.2 Interphase momentum exchange coefficient (drag coefficient) models

3.2.2.1 The solid – solid momentum exchange coefficient

In practical fluidised bed applications, systems with monosized particles of equal densities are seldom found (Wu and Baeyens, 1998). Therefore, a more-than-2-phase model should be applied to simulate fluidisation phenomena by describing the different types of solid particles as distinct particulate phases. Hence, the momentum transfer between the particulate phases due to collisions should be taken into account using constitutive relations known as the solid – solid drag term (Symlal, 1987).

Unlike in dilute systems such as pneumatic conveyors, it is not possible to measure the solid-solid drag and develop empirical correlations in dense systems such as fluidised beds. Therefore, an expression for the solid-solid drag term has been derived based on the kinetic theory of granular flow (Symlal, 1987). Similarly, the momentum exchange between two solid phases can be represented by the product of slip velocity and the solid – solid momentum exchange coefficient.

The solid-solid (between solid phases s and m) momentum exchange coefficient is calculated using the Symlal-O'Brien symmetric model (Symlal, 1987):

$$K_{sm} = \frac{3(1 + e_{s,sm}) \left(\frac{\pi}{2} + C_{fr,sm} \frac{\pi^2}{8} \right) \alpha_s \rho_s \alpha_m \rho_m (d_s + d_m)^2 g_{0,sm}}{2\pi(\rho_s d_s^3 + \rho_m d_m^3)} \times |\vec{v}_s - \vec{v}_m| \quad (3.1)$$

The drag between particles found from the Symlal-O'Brien symmetric model has a strong influence on the settling rates of the closely packed particles. It assumes that momentum is exchanged through a collision of two particles. The model is dependent upon the size of the two particles as well as the radial distribution coefficient $g_{0,sm}$, which essentially is a function describing the distance between the spherical particles (Cooper and Coronella, 2005).

3.2.2.2 Sphericity coefficient

Over the years, many versions of the closure presenting the Eulerian multiphase momentum exchange have been developed in order to provide better qualitative and quantitative consistency of model simulations with specific experimental data. As a result of non-spherical materials used in the current work, the effect of sphericity coefficient of particles was taken into account (Sobieski, 2009a,b). Due to the non-spherical shape of the granulate particles, the diameter d_s seen in expressions of the interphase momentum exchange coefficient mentioned earlier

was modified by introducing the so-called coefficient of sphericity ϕ_s (for spheres $\phi_s = 1$) (Gomez and Milioli, 2006).

Therefore, the expressions of Wen and Yu (1966) and Ergun (1952) which were applied in the modified Gidaspow model (Gidaspow, 1994) and the solid-solid drag term (Eq. (3.1)) can be modified to Eqs. (3.2), (3.3) and (3.4), respectively:

$$K_{sl,Wen-Yu} = \frac{3}{4} C_D \frac{\alpha_s \rho_l |\vec{v}_s - \vec{v}_l|}{(\phi_s d_s)} \alpha_l^{-1.65} \quad (3.2)$$

$$K_{sl,Ergun} = 150 \frac{\alpha_s (1 - \alpha_l) \mu_l}{\alpha_l (\phi_s d_s)^2} + 1.75 \frac{\rho_l \alpha_s |\vec{v}_s - \vec{v}_l|}{(\phi_s d_s)} \quad (3.3)$$

$$K_{sm} = \frac{3(1 + e_{s,sm}) \left(\frac{\pi}{2} + C_{fr,sm} \frac{\pi^2}{8} \right) \alpha_s \rho_s \alpha_m \rho_m (\phi_s (d_s + d_m))^2 g_{0,sm}}{2\pi \phi_s^3 (\rho_m d_m^3 + \rho_s d_s^3)} \times |\vec{v}_s - \vec{v}_m| \quad (3.4)$$

$$Re_s = \frac{\rho_l (\phi_s d_s) |\vec{v}_s - \vec{v}_l|}{\mu_l} \quad (3.5)$$

3.3 Materials and methods

3.3.1 Numerical setup

In order to reduce the computational effort, the half geometry of a laboratory-scale Glatt GPCG-1 fluidised bed (Glatt GmbH, Germany), as shown in Figure 3.1, and also used by Depypere *et al.* (2009) to obtain the experimental data, was defined. The grid was generated using Gambit 2.2.30 (Ansys Inc., Canonsburg, PA) and exported into the solver program. A hybrid hexahedral–tetrahedral grid, containing 209,955 elements, with mesh refinement at near-wall regions in which turbulent flow was effected, was generated. The grid size was uneven in both the horizontal and the vertical directions such that the smallest cells were adjacent to the nozzle opening. The grid is displayed in Figure 3.1.

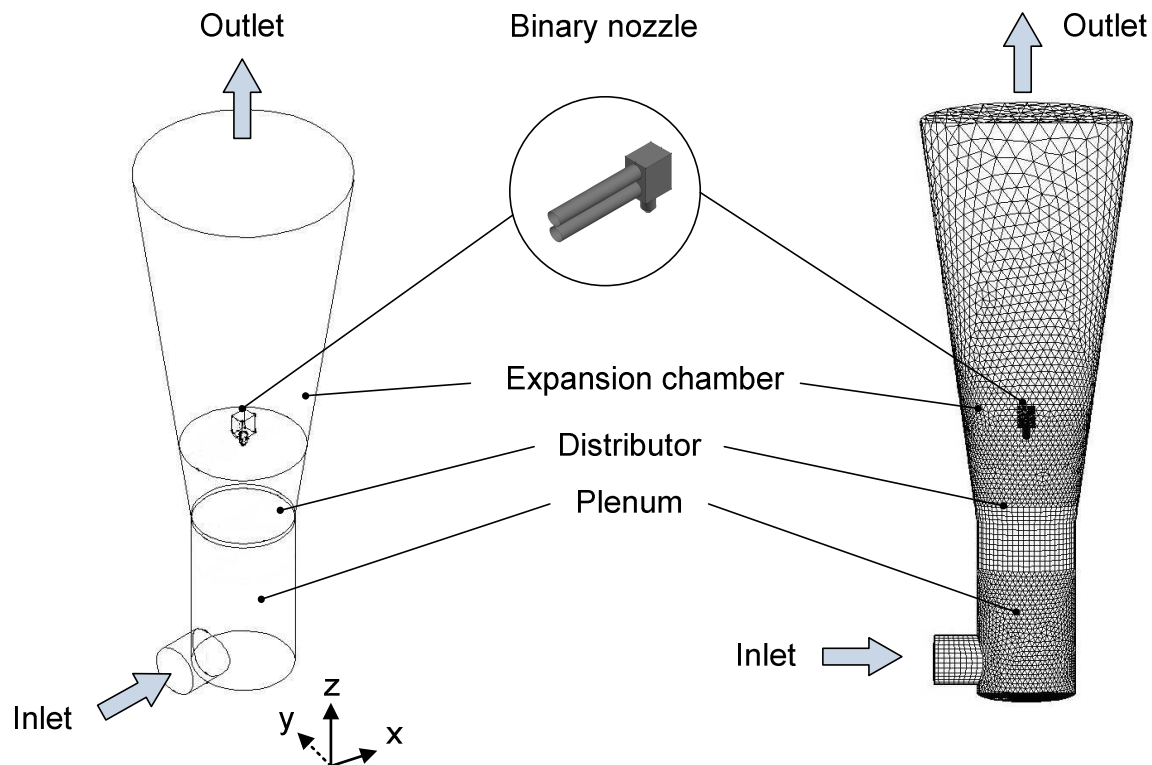


Figure 3.1 The modelled geometry of a laboratory Glatt GPCG – 1 fluidised bed reactor (left) and the corresponding half mesh (right).

In order to effectively improve model accuracy with respect to bed voidage and solids volume fraction profiles (See chapter 2), a four-phase Eulerian model was used to account for the polydispersity of the solids, used in the experimental validation. The system was described using a single gas phase as the primary phase and three separate solid phases with different particle size for each phase. The particle sizes of the sucrose/starch beads (“non-pareils”) used in each solid phase of the 4-phase model were 200 μm , 355 μm and 510 μm , corresponding to the average sizes of the particles (i.e. those used in the experimental validation) with a diameter below the 20th, between the 20th and 80th, and above the 80th percentile, respectively.

In the next step, the boundary conditions and the fluid and solid properties, given in Table 3.1, had to be specified. The nozzle was designated as a velocity inlet, where the direction of gas flow is normal to the surface. The velocities of

atomisation air used for the nozzle were measured by means of an anemometer (Testovent 4000, TESTOTERM N.V. (B), accuracy of $\pm 0.3 \text{ m s}^{-1}$) while blowing air at nozzle pressures of 1.5, 2, 3 and 4 bar through a cylindrical pipe with a diameter of 3 cm.

The nozzle velocities varying from 9.67 to 16.08 ms^{-1} , corresponding to atomisation air pressures of 1.5 to 4 bar, were specified. The air inlet was modelled as a velocity inlet, and the outlet was modelled as a pressure outlet. Furthermore, the walls were set as stationary boundaries at which the no-slip condition was applied, meaning that the gas velocity closest to the walls is equal to zero. The porous zone boundary condition was specified to model the air distributor for which values of the impermeability and inertial resistance were obtained by Depypere *et al.*, (2004). The remaining model parameters and conditions are summarised in Table 3.1.

In the current study, the commercially available CFD software FLUENT 6.3.26, from ANSYS Inc. (Canonsburg, PA, US) was used to perform simulations using the finite-volume method. CFD simulations were performed using a single-precision, unsteady-state, first order implicit solver. As in the previous chapter, for the solution of the gas/solid flow, a multiphase flow Eulerian model was applied together with the momentum exchange coefficients calculated using the modified Gidaspow model, which was applied through user-defined functions. Furthermore, the solid-solid interaction and the sphericity coefficient of non-spherical particles were included in the simulations. Flow turbulence was simulated using the standard $k-\epsilon$ model with standard wall functions, and first order upwind schemes were selected for the convection terms. The relation between velocity and pressure corrections was calculated using the phase-coupled SIMPLE algorithm. Finally, a time step of 0.001s with a maximum of 100 iterations per time step was chosen in order to improve convergence behaviour. On an Intel Core i7 (2.67GHz) equipped

computer, simulating 15s of the fluidisation process using the modelling procedure described above, on average took two weeks of simulation time.

Table 3.1 The simulation model parameters and conditions

<i>Description</i>	<i>Value</i>
Particle density (kg m ⁻³)	1459
Gas density (kg m ⁻³)	1.225
Mean particle diameter (µm)	200, 355, 510
Sphericity coefficient (-)	0.753
Restitution coefficient (-)	0.9
Initial solids packing (-)	0.6
Fluidisation gas flow rate (m ³ h ⁻¹)	55
Atomisation air pressure (bar)	1.5 - 4
Vessel height (m)	0.56
Vessel bottom diameter (m)	0.14
Vessel top diameter (m)	0.30
Static bed height (m)	0.03

3.3.2 Experimental setup

For the validation of the model predicted results, the experimental data obtained by Depypere *et al.* (2009) were used. In this research work, fluidisation experiments in a laboratory-scale Glatt GPCG-1 fluidised bed (Glatt GmbH, Germany) comprising a stainless steel tapered (8.1° inclination) vessel with a stainless steel woven wire Robusta 172 distributor (Spörl, Germany) at the base were conducted. The characteristics of this distributor are summarised in Table 2.2. The air flow rate in the fluidised bed was 55 m³h⁻¹, which corresponds to a superficial air velocity across the distributor of 1.00 m s⁻¹. Fluidisation experiments with the nozzle producing atomisation air at different levels of pressure (2, 3 and 4 bar) were conducted. When the nozzle was not in use, a small maintenance atomisation air pressure (1.5 bar) was applied to avoid particles obstructing the nozzle outlet.

For the fluidisation experiments 0.75 kg of sucrose/starch beads (Penwest Pharmaceuticals, United States) were used (surface-weighted diameter, d_{32} : $345 \pm 1.29 \mu\text{m}$; particle density: $1459 \pm 10 \text{ kg m}^{-3}$). The sphericity coefficient (ϕ_s) of the used particles was 0.753, as was determined by Depypere *et al.*, (2009).

Depypere *et al.* (2009) measured the motion of the non-pareils (solids) inside the reactor vessel using Positron Emission Particle Tracking (PEPT). This technique allows 3-D movement of a single tracer particle to be followed in a non-invasive way. By tracking the particle location and movement over prolonged periods, time-averaged steady-state solids volume concentration (α_s) and voidage (α_l) profiles can be derived. In this chapter, in order to enable qualitative and quantitative comparison between simulation and experimental results, the time-averaged occupancy plots for non-pareils were converted into more physically meaningful voidage plots. If the tracer motion is indeed typical of that within the bed, and the experimental time is long enough, time-averaged occupancy is equivalent to time-averaged density which in the case of granular materials, is directly related to void fraction. For every volume element (voxel) of the occupancy plot, the time-averaged density, ρ_{vox} , can be calculated from (Depypere *et al.*, 2009):

$$\rho_{vox} = \frac{t_{vox}}{t_{run}} \cdot \frac{M_{tot}}{V_{vox}} = O_{vox} \cdot \frac{M_{tot}}{V_{vox}} \quad (3.6)$$

in which t_{vox} is the total time the tracer spent in the voxel of interest, t_{run} is the total run time, M_{tot} is the total mass in the total region of interest (0.75 kg), V_{vox} is the volume of the voxel (in this case $5 \times 10^{-7} \text{ m}^3$) and O_{vox} is the voxel occupancy. From this time-averaged density, the voidage, α_l , can be calculated as,

$$\alpha_l = 1 - \frac{\rho_{vox}}{\rho_s} = 1 - \frac{O_{vox} \cdot V_{tot}}{V_{vox}} \quad (3.7)$$

where ρ_s is the particle density and ρ_t is the air density, which is sufficiently small that it can be neglected, and V_{tot} is the volume occupied by the solids in the total region of interest.

3.3.3 Validation

According to the objective of this study, the contour maps of the fluidised bed voidage were processed in the mapping program Surfer v8 (Golden software, Inc., USA) using the triangulation with linear interpolation gridding method and the differences between model-predicted and measured (interpolated) voidage contours were evaluated using the root mean square (RMS). The RMS is a measure of the model's deviation from the experimentally measured solids volume fraction. It was calculated as

$$RMS = \left(\frac{\sum (\alpha_{s,exp} - \alpha_{s,sim})^2}{N} \right)^{1/2} \quad (3.8)$$

From Eq. (3.8), the values based on each pixel of the simulated and experimental contour plots (pixel size equals 0.001 m x 0.001 m, with a total of N pixels) were used to calculate the RMS.

3.4 Results and Discussion

3.4.1 Steady-state results

In the model, the time at which the voidage in the bed fluctuated around a near steady-state value was determined using the CFD model. Subsequently, the simulation results from time zero until steady-state was reached were discarded from the time-averaged bed voidage profile calculation. As shown before, fluidised bed behaviour after 5 s was considered to be at steady state. Therefore, in this chapter, the time-averaged steady-state solids volume and bed voidage fraction for comparing model-predicted and experimental results were taken after 5 s.

3.4.2 Experimental validation

In order to enable qualitative comparison between simulation and experimental results with variation of atomisation air pressures, the model-predicted bed voidage contours at atomisation air pressures of 1.5, 2, 3 and 4 bar with the inclusion of solid-solid interaction and with the use of a sphericity coefficient of 0.753 were plotted and compared with experimental results, as shown in Figure 3.2.

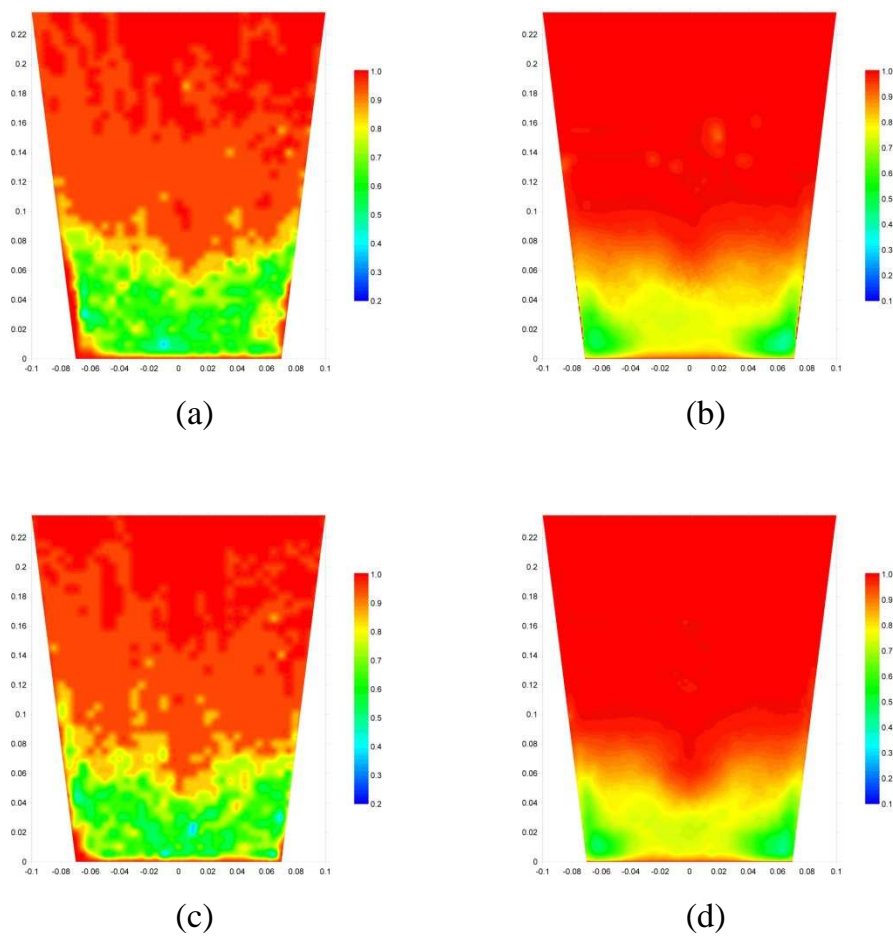


Figure 3.2 Comparison between PEPT results, from Depypere *et al.* (2009) and simulated, time-averaged steady-state voidage at different atomisation air pressures: (a) PEPT-1.5 bar, (b) simulation-1.5 bar, (c) PEPT-2 bar, (d) simulation-2 bar.

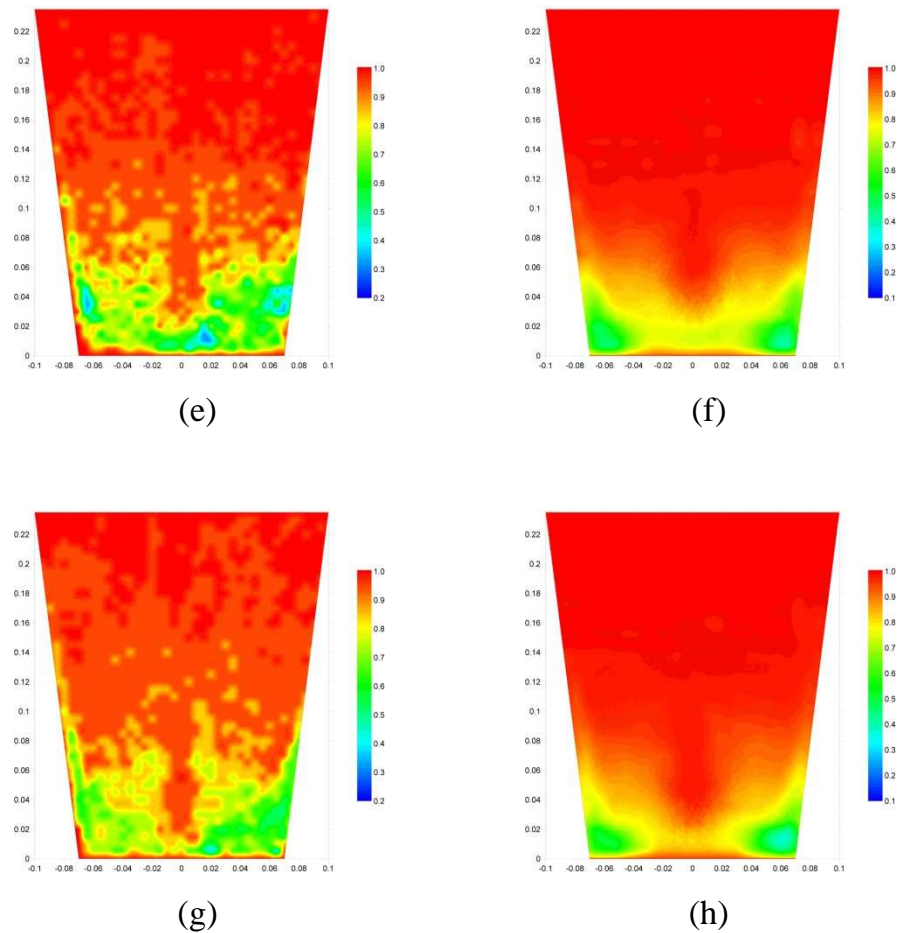


Figure 3.2 (continued) Comparison between PEPT results, from Depypere *et al.* (2009) and simulated, time-averaged steady-state voidage at different atomisation air pressures: (e) PEPT-3 bar, (f) simulation-3 bar, (g) PEPT-4 bar, (h) simulation-4 bar.

From these figures, the change of the time-averaged voidage with the increase of atomisation pressure can be observed. More specifically, the central part of the conical vessel which was occupied by a hollow atomisation cone, as seen obviously in the experiments, was enlarged with the increase of atomisation pressure resulting in a smaller radial zone between the nozzle atomisation cone and the reactor wall (Depypere *et al.*, 2009). However, when comparing the predicted results with the experimental voidage contours, as shown in Figure 3.2, the discrepancy in bed voidage can clearly be seen, especially at the bottom of the reactor. Dense regions ($\alpha_l \leq 0.6$) near the wall at the bottom of the bed – but not

fully extending towards the air distributor – can be observed from the simulations whereas these regions cannot be observed experimentally. This disagreement may be explained by the physical properties of the solid material (non-pareils) used in the experiments such as the shape of particles, which cannot be fully characterised in CFD models. Differences in bed void fraction, inversely related to effective particle sphericity, may be suggested as a possible explanation to describe the different solids particle concentrations upon increasing the nozzle atomisation pressure.

At the bottom centre of the conical reactor, where the particles have to be lifted against the counterforce of the atomisation air, non-pareils used as solid material in experiments may be easier and quicker transported to higher levels in the fluidised bed resulting in the larger air voids (Depypere *et al.*, 2009). Even though the sphericity coefficient can be defined in CFD models, it can only be employed to calculate the fluid-solid momentum exchange coefficient. The change in hydrodynamics caused by a different shape of the particles such as oval ones cannot be captured by CFD models. Another element that has to be taken into consideration is the sensitivity of the computational model to variations of certain boundary conditions. More specifically, the CFD model showed to be highly sensitive to changes in fluidisation air flow rate. Considering the uncertainty of the fluidisation air flow rate as a result of the measurement error in the experiments, this model sensitivity could also explain the observed discrepancy between the model and the experiment, as will be further detailed below.

3.4.3 Sensitivity of the model to the fluidisation air flow rate

In order to test the sensitivity of the CFD model to the fluidisation air flow rate or more specifically, to the superficial air velocity, a perturbation factor was introduced in the model with values of 5%-, 10%-, 15%-, and 20%-increased superficial velocity. All simulations were done with an atomisation pressure set to

2 bar and comparison with the experimental data was carried out. The correlation between the experimental average solids volume fraction and the model predicted values at different bed heights, operating at the aforementioned (adjusted) superficial air velocities, is presented in Figure 3.3. The linear regression coefficients and the root mean square (RMS) calculated using Eq. (3.8), based on the solids volume fraction, are shown in Table 3.2. From this table it can be concluded that the model with a perturbation factor corresponding to a 10% increase in superficial air velocity had the lowest RMS and approached closely the experimentally measured values, whereas the model with a perturbation factor corresponding to a 5% increase in superficial air velocity gave the worst results.

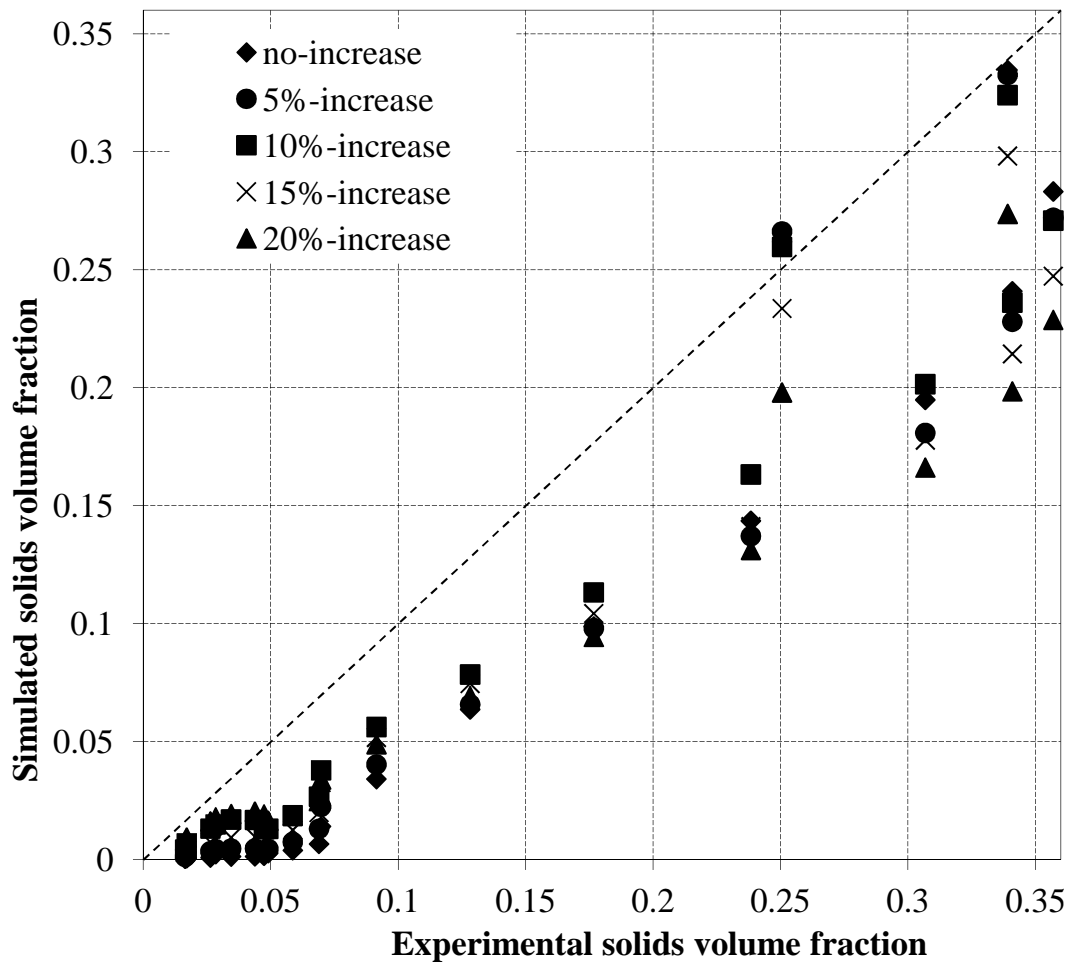


Figure 3.3 Correlation between experimental and simulated solids volume fraction, taken at different heights, using different perturbation factors for superficial air velocity at atomisation air pressure of 2 bar.

Table 3.2 Regression analysis between model-predicted and experimental solids volume fraction, including the root mean square (RMS).

Conditions	$\alpha_{s,exp} = a\alpha_{s,sim} + b$			
	Slope, a	Intercept, b	R ²	RMS
No – increased fluidisation air flow rate	0.8968	-0.0360	0.9330	0.079
5% - increased fluidisation air flow rate	0.8573	-0.0306	0.9167	0.085
10% - increased fluidisation air flow rate	0.8412	-0.0188	0.9443	0.076
15% - increased fluidisation air flow rate	0.7742	-0.0207	0.9417	0.084
20% - increased fluidisation air flow rate	0.6796	-0.0107	0.9488	0.083

The previous results indicate that using a perturbation factor corresponding to a 10% increase in superficial air velocity yielded the best comparison with the experimental data, when an atomisation air pressure of 2 bar was considered. In order to verify whether the improved agreement between simulation (with 10% perturbation of the superficial air velocity) and experimental results could also be observed at other atomisation air pressures, the model was resimulated with atomisation air pressures of 1.5, 3, and 4 bar. The resulting model-predicted time-averaged bed voidage contours, along with the experimental results (Depypere *et al.*, 2009) are shown in Figure 3.4, while Figure 3.5 shows the model-predicted values of the time-averaged solids volume fraction as a function of the vertical position above the air distributor with and without the 10% perturbation of the fluidisation air flow rate, compared with experimental data.

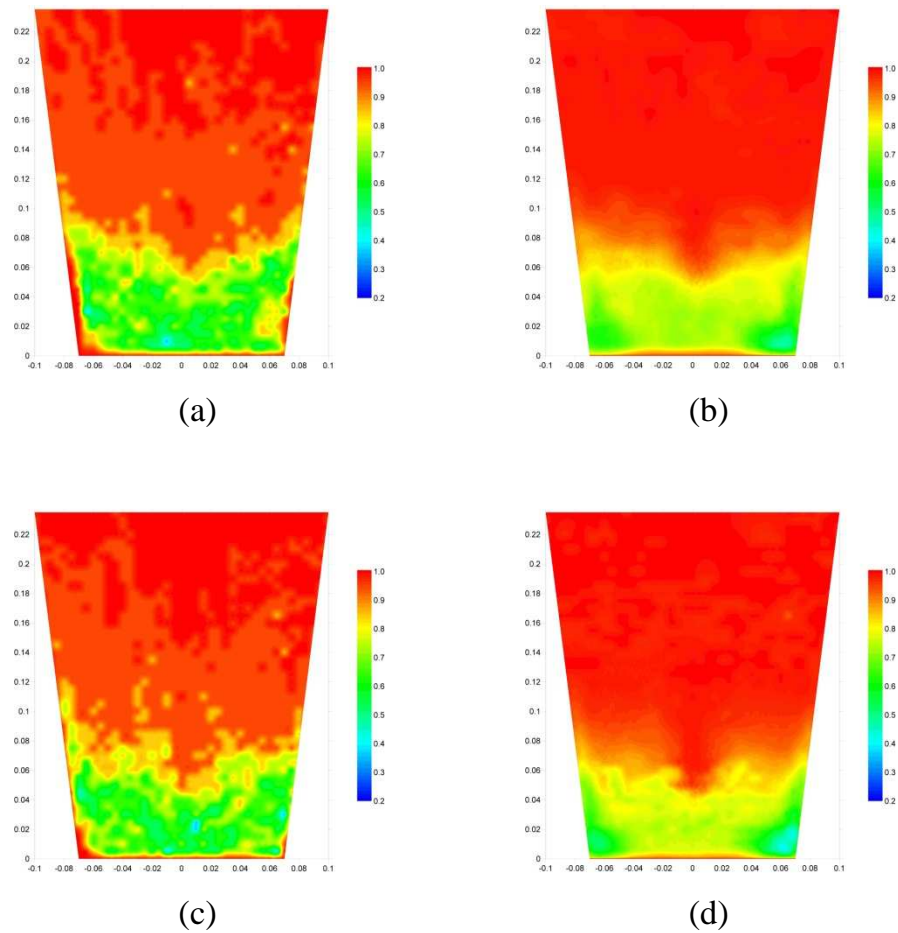


Figure 3.4 Comparison between PEPT (Depypere *et al.*, 2009) and simulated, time-averaged steady-state voidage at different atomisation air pressures and with a 10% increase of superficial air velocity: (a) PEPT-1.5 bar, (b) simulation-1.5 bar, (c) PEPT-2 bar, (d) simulation-2 bar.

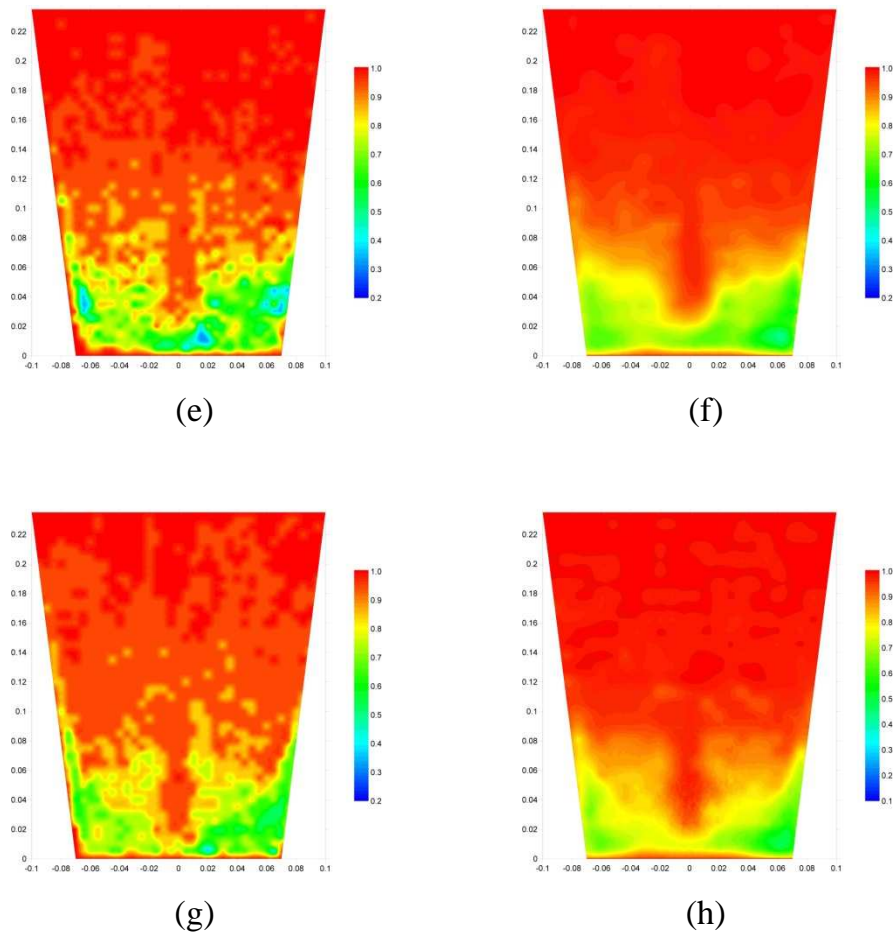
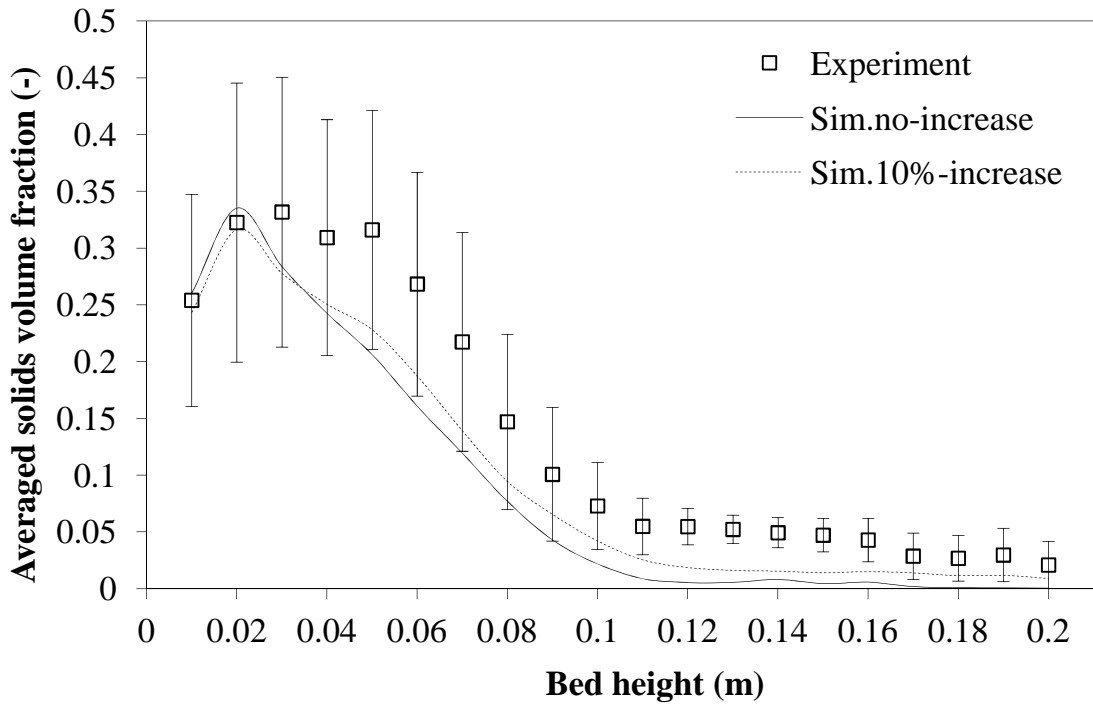
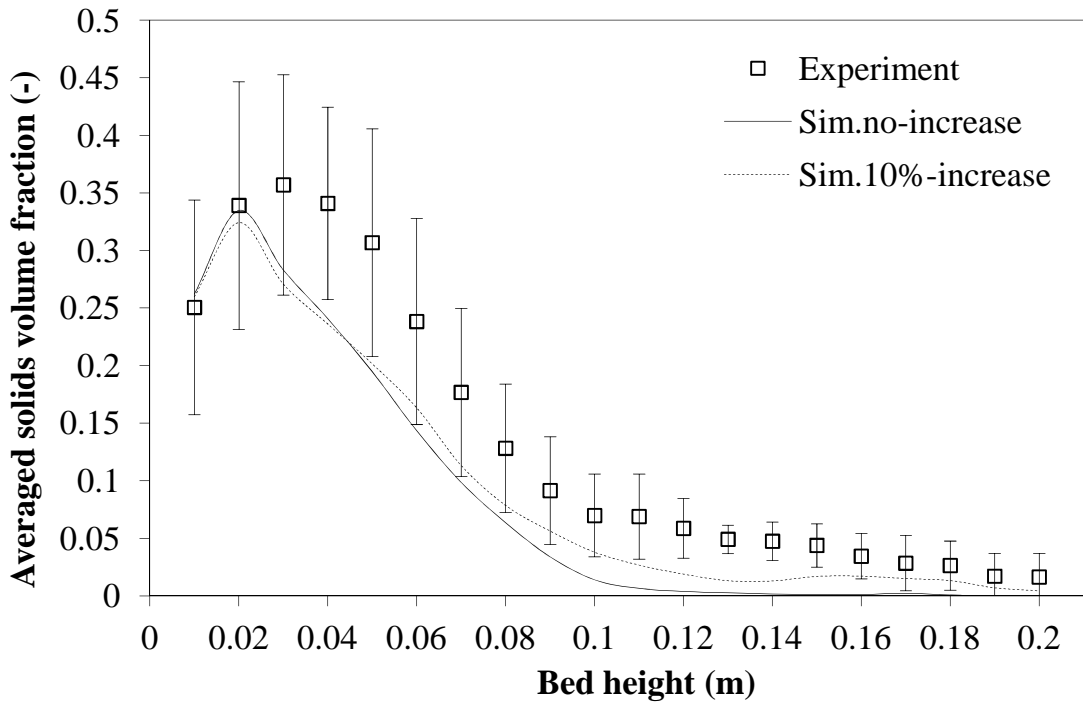


Figure 3.4 (continued) Comparison between PEPT (Depypere *et al.*, 2009) and simulated, time-averaged steady-state voidage at different atomisation air pressures and with a 10% increase of superficial air velocity: (e) PEPT-3 bar, (f) simulation-3 bar, (g) PEPT-4 bar, (h) simulation-4 bar.

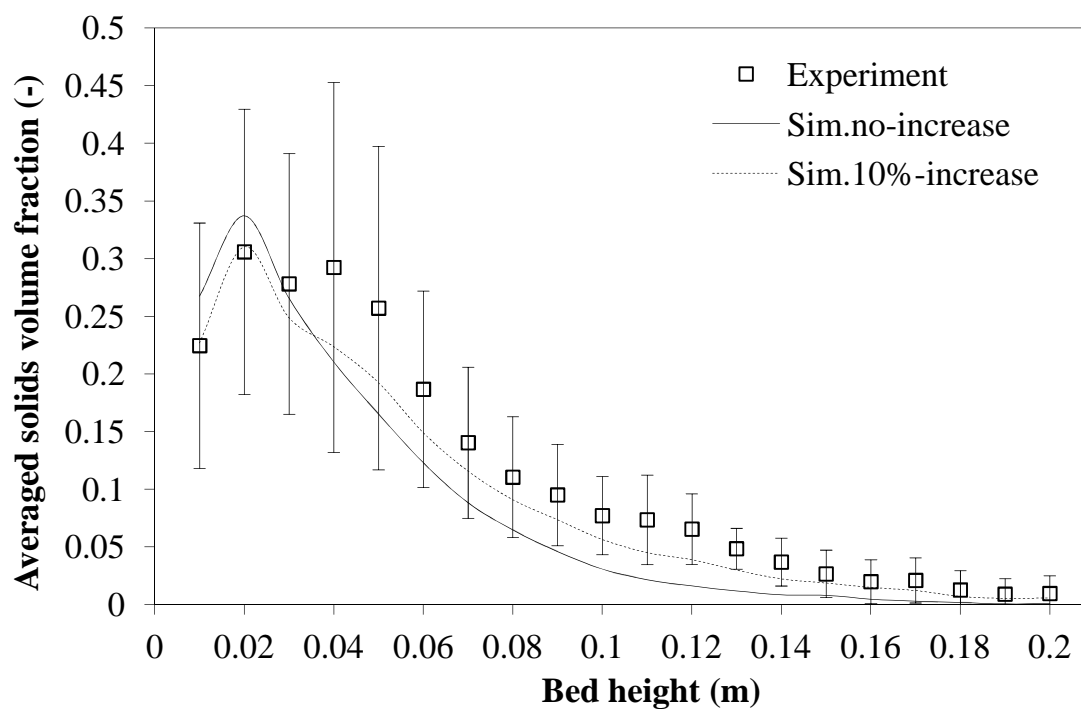


(a)

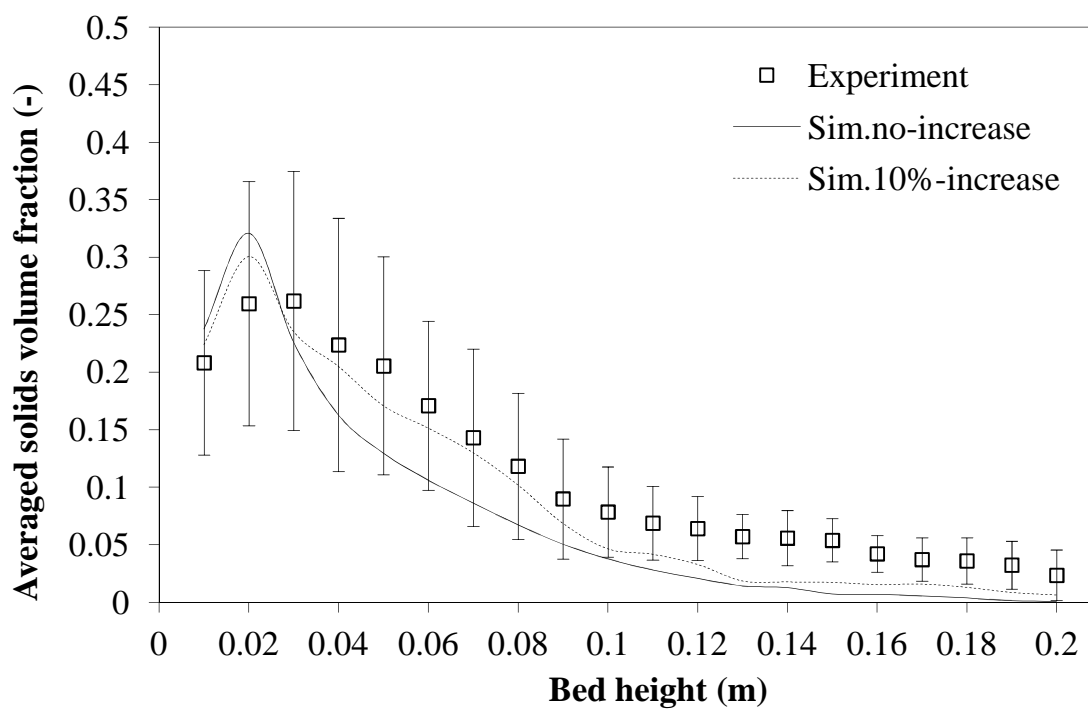


(b)

Figure 3.5 Comparison of time-averaged solids volume fraction as a function of vertical position above the air distributor with an atomisation air pressure of: (a) 1.5 bar, (b) 2 bar.



(c)



(d)

Figure 3.5 (continued) Comparison of time-averaged solids volume fraction as a function of vertical position above the air distributor with an atomisation air pressure of: (c) 3 bar, and (d) 4 bar.

From Figure 3.4, the change in solids concentration – more specifically the hollow cone below the atomising nozzle – with the increase in atomisation air pressure as seen in the experiments could also be observed using the Eulerian multiphase model, and to a much better extent than the results obtained from the simulations without a 10% perturbation factor of the superficial air velocity (as shown in Figure 3.3). In Figure 3.5, comparing the simulated results with a 10% increase in fluidisation air flow rate and the experimental data, improved agreement can be seen. For all studied atomisation air pressures, the solids volume fraction decreased as a function of position above the air distributor and reached a maximum at around $z = 0.02$ m, illustrating a qualitative agreement with the experimental tendency. However, a quantitative discrepancy, being a lower simulated particle concentration, can be found at the position above the nozzle ($z > 0.1$ m).

Furthermore, the model-predicted solids volume fraction averaged at different heights was plotted against the experimental solids volume fraction, as shown in Figure 3.6, and regression analysis was carried out. The linear regression coefficients and the root mean square (RMS), based on the time-averaged solids volume fraction, are demonstrated in Table 3.3. The values predicted by the model with the use of a correction factor to the superficial air velocity tended to deviate less from the experimental results, hence the lower RMS. It is also noticed that the RMS decreased with the increase of atomisation air pressure. As a result, it can be concluded that the model with the correction factor corresponding to a 10% increase in superficial air velocity operating at 4-bar atomisation with a RMS of 0.058 gave the best prediction, followed by the model operating at 3-bar, 2-bar and 1.5-bar atomisation.

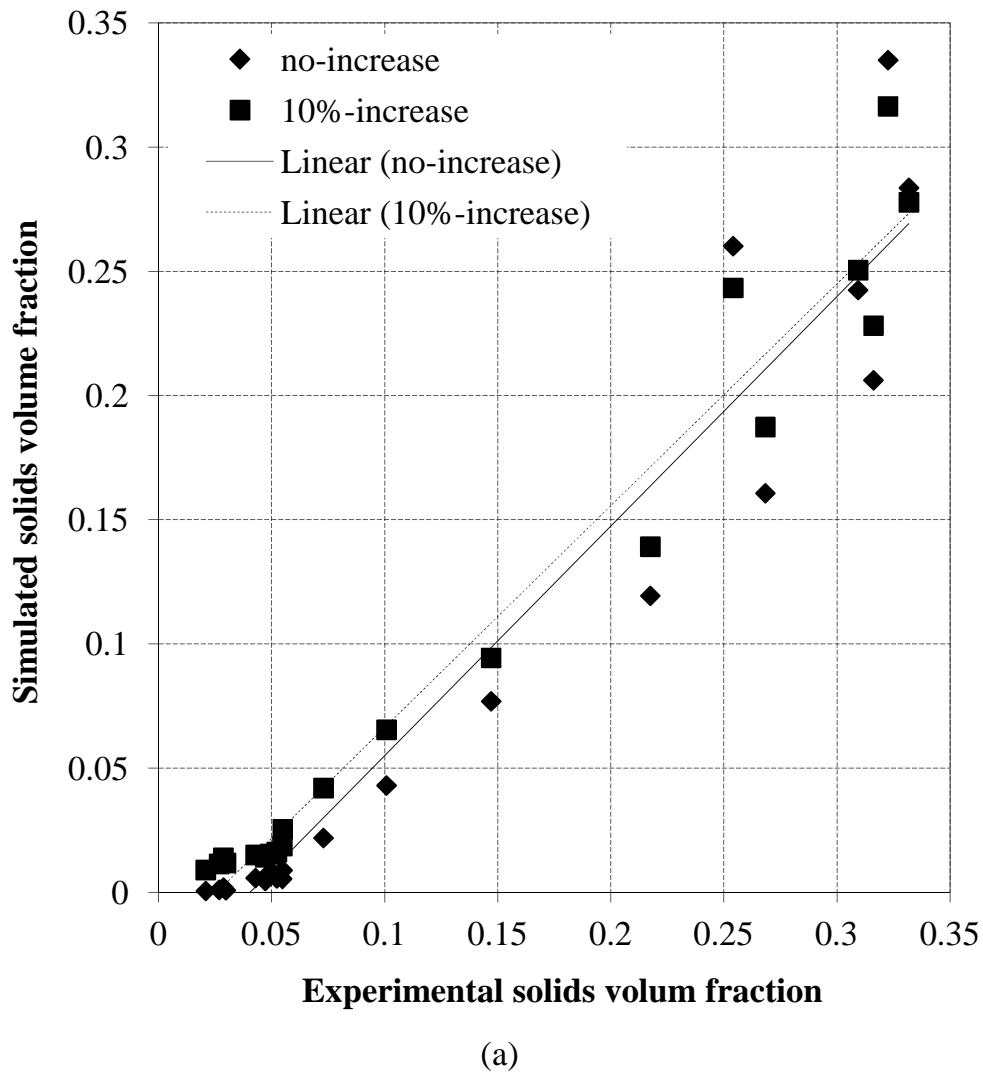
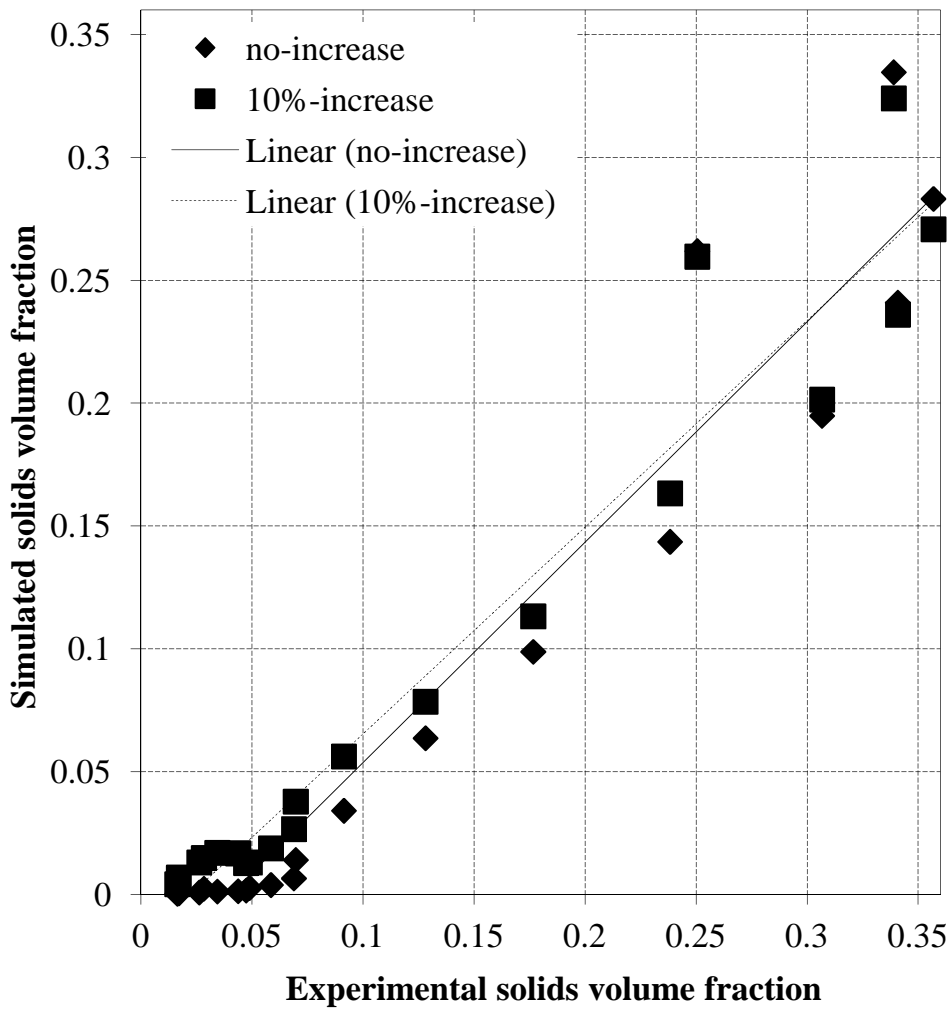
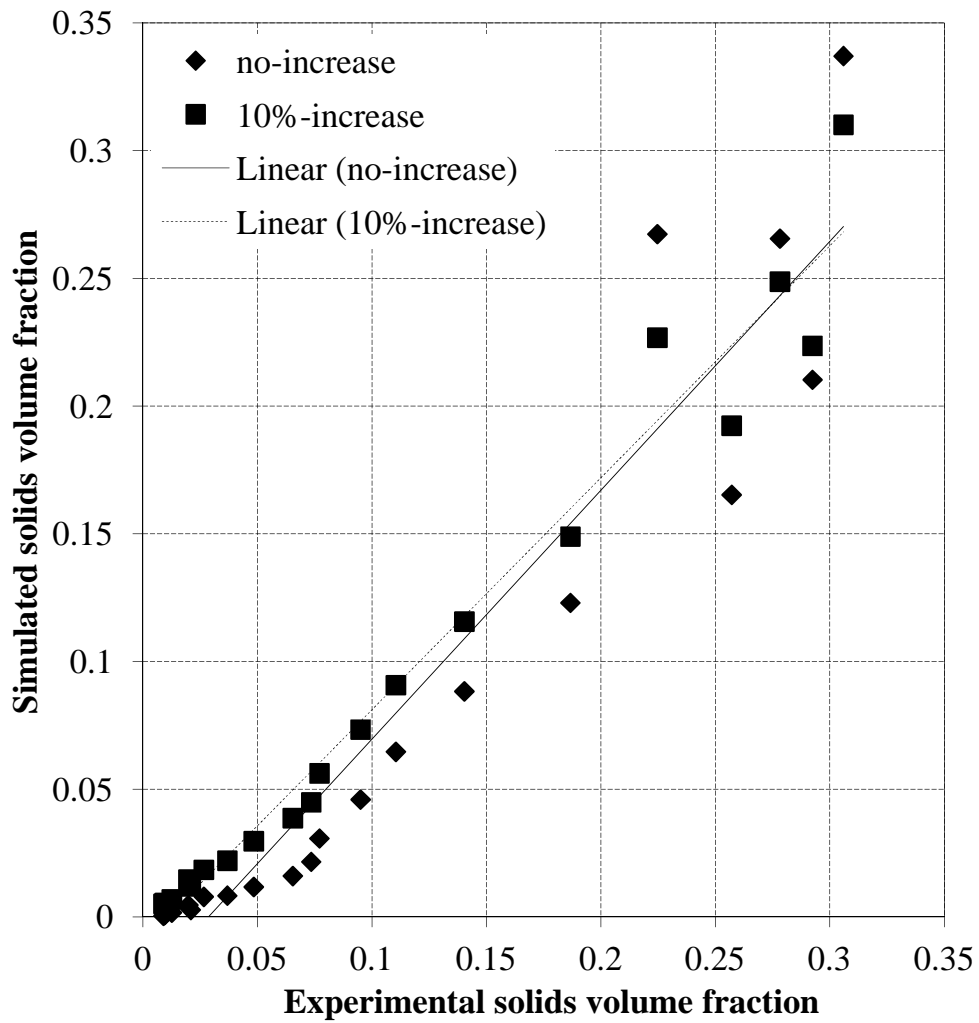


Figure 3.6 Correlation between experimental and simulated steady-state solids volume fraction with and without the use of 10%-increased superficial air velocity operating at (a) 1.5-bar (b) 2-bar (c) 3-bar and (d) 4-bar atomisation.



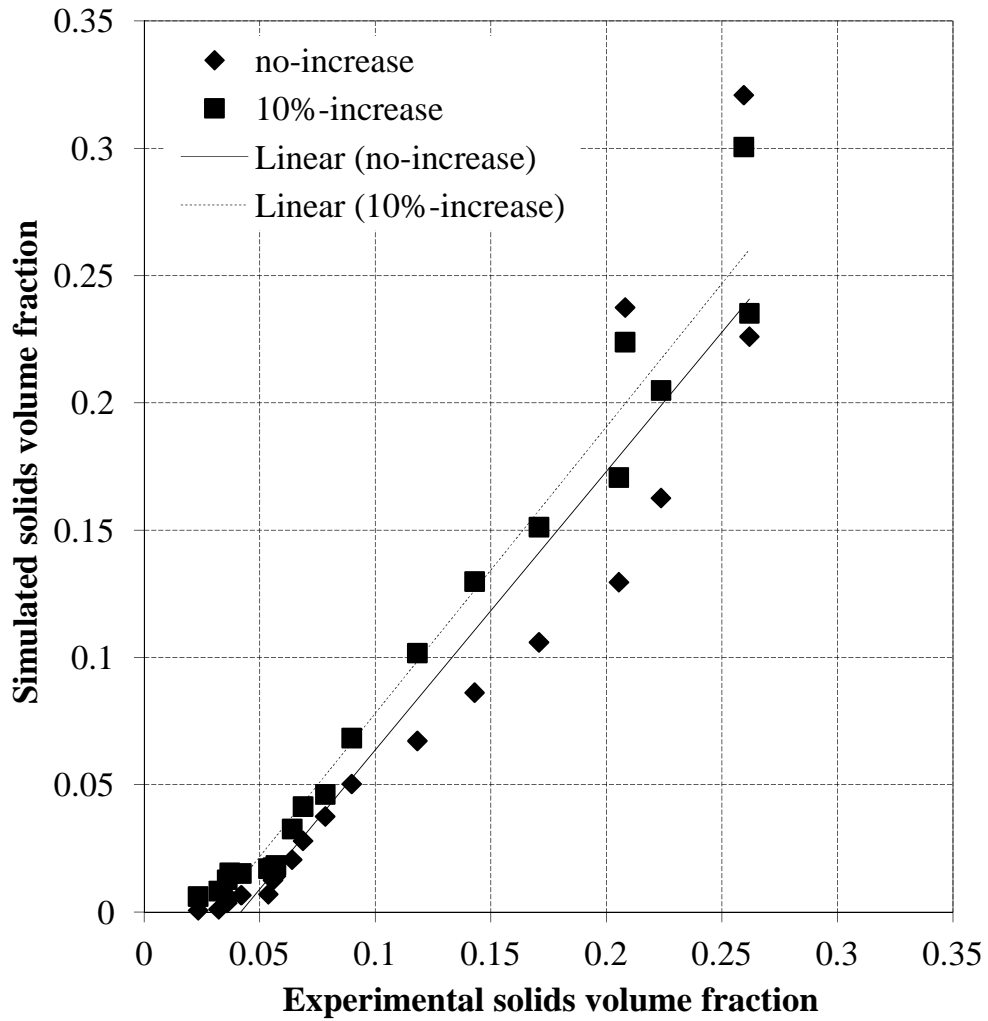
(b)

Figure 3.6 (continued) Correlation between experimental and simulated steady-state solids volume fraction with and without the use of 10%-increased superficial air velocity operating at (a) 1.5-bar (b) 2-bar(c) 3-bar and (d) 4-bar atomisation.



(c)

Figure 3.6 (continued) Correlation between experimental and simulated steady-state solids volume fraction with and without the use of 10%-increased superficial air velocity operating at (a) 1.5-bar (b) 2-bar(c) 3-bar and (d) 4-bar atomisation.



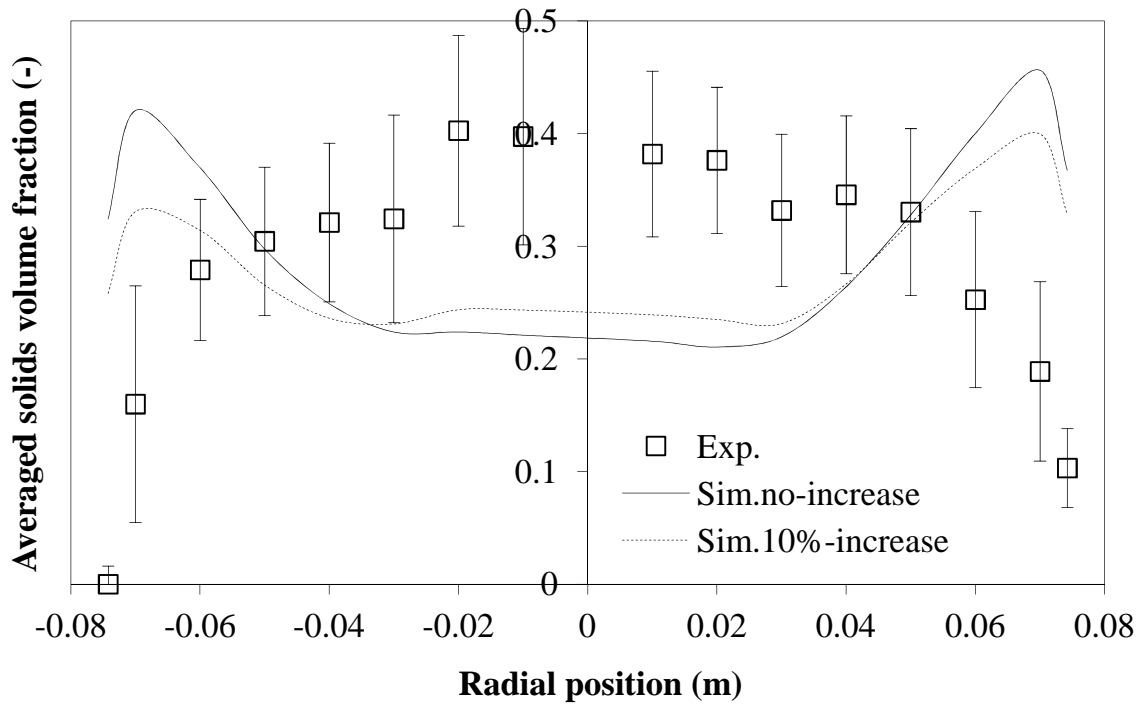
(d)

Figure 3.6 (continued) Correlation between experimental and simulated steady-state solids volume fraction with and without the use of 10%-increased superficial air velocity operating at (c) 3-bar (d) 4-bar atomisation.

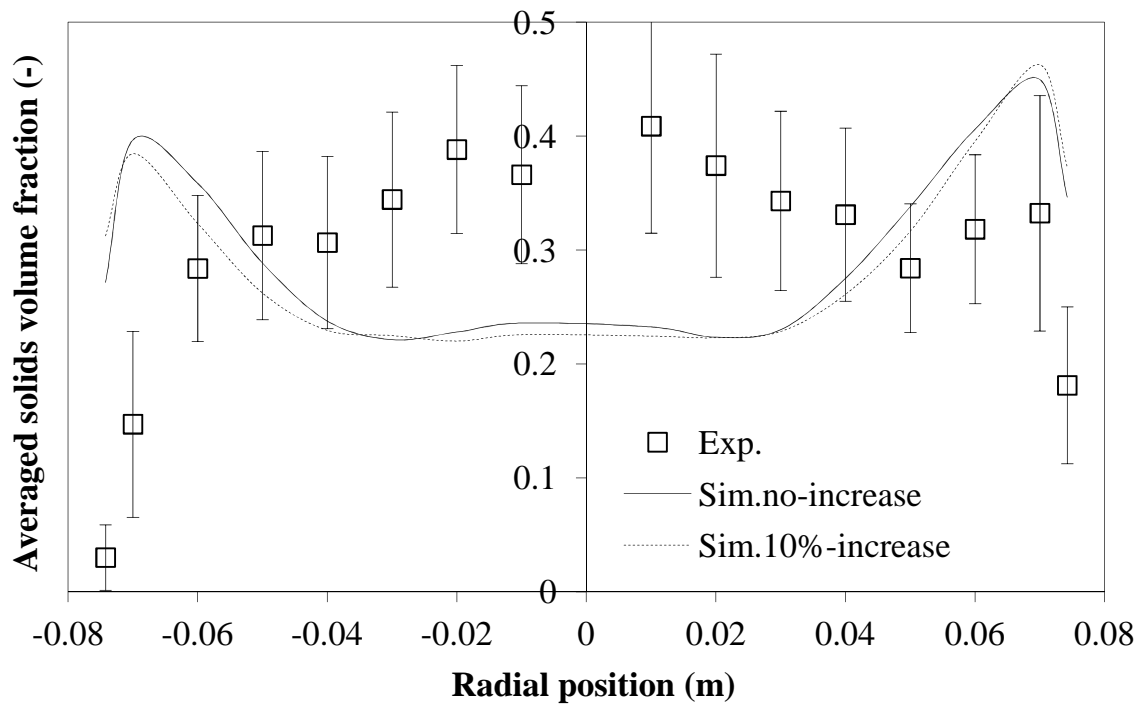
Table 3.3 Regression analysis between model-predicted, with and without a 10% increase in superficial air velocity, and experimental steady-state solids volume fraction, including the root mean square (RMS).

Atomisation pressure	$\alpha_{s,\text{exp}} = a\alpha_{s,\text{sim}} + b$							
	Slope, a		Intercept, b		R^2		RMS	
	no	10%	no	10%	no	10%	no	10%
1.5 bar	0.9240	0.8928	-0.0374	-0.0229	0.9273	0.9646	0.093	0.078
2 bar	0.8968	0.8412	-0.0360	-0.0188	0.933	0.9443	0.079	0.076
3 bar	0.9746	0.9085	-0.0278	-0.0098	0.0904	0.9689	0.080	0.062
4 bar	1.0936	1.1255	-0.0456	-0.0344	0.8984	0.9710	0.073	0.058

Even though the models with a 10% increase of the superficial air velocity gave better results, as shown in Figure 3.4 (a-h), dense zones at the bottom of the conical reactor between the air distributor and walls were still observed. Figure 3.7 (a-d) demonstrates more details concerning the solids volume concentration just above the air distributor (volume integrated between $z = 0$ m and $z = 0.03$ m). These figures present comparisons between the experimental time-averaged solids volume fraction and that of models with a 10% increase in superficial air velocity operating at different atomisation air pressures. It can be found from Figure 3.7 that the near-wall solids volume fraction of all atomisation pressures is over-predicted at the bottom bed region (0-3cm). This discrepancy was also observed numerically in the previous chapter in which fluidisation of glass beads was modelled in the same reactor geometry. Furthermore, it can also be noticed that the model-predicted time-averaged solids volume fraction in the centre at this height was lower than that of the experiments. The disagreement can be explained by the non-spherical shape of the granular material of which the implementation by means of the sphericity coefficient is insufficient to completely define its shape in the CFD model, thereby resulting in different model-predicted fluidisation behaviour.

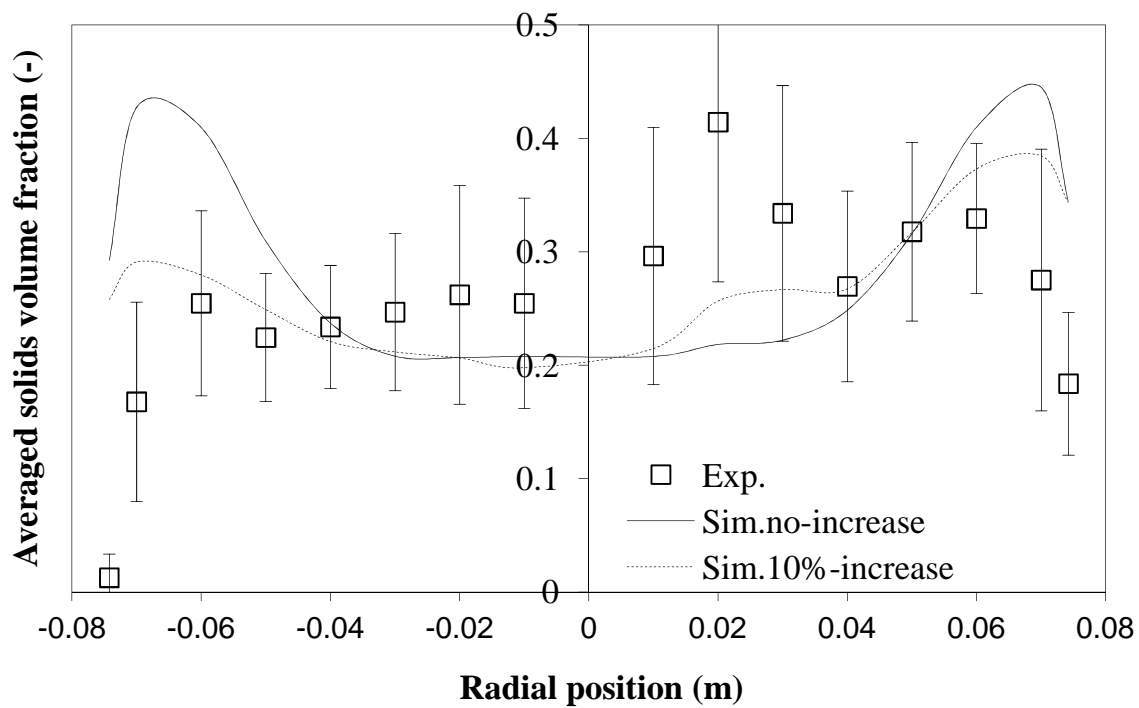


(a)

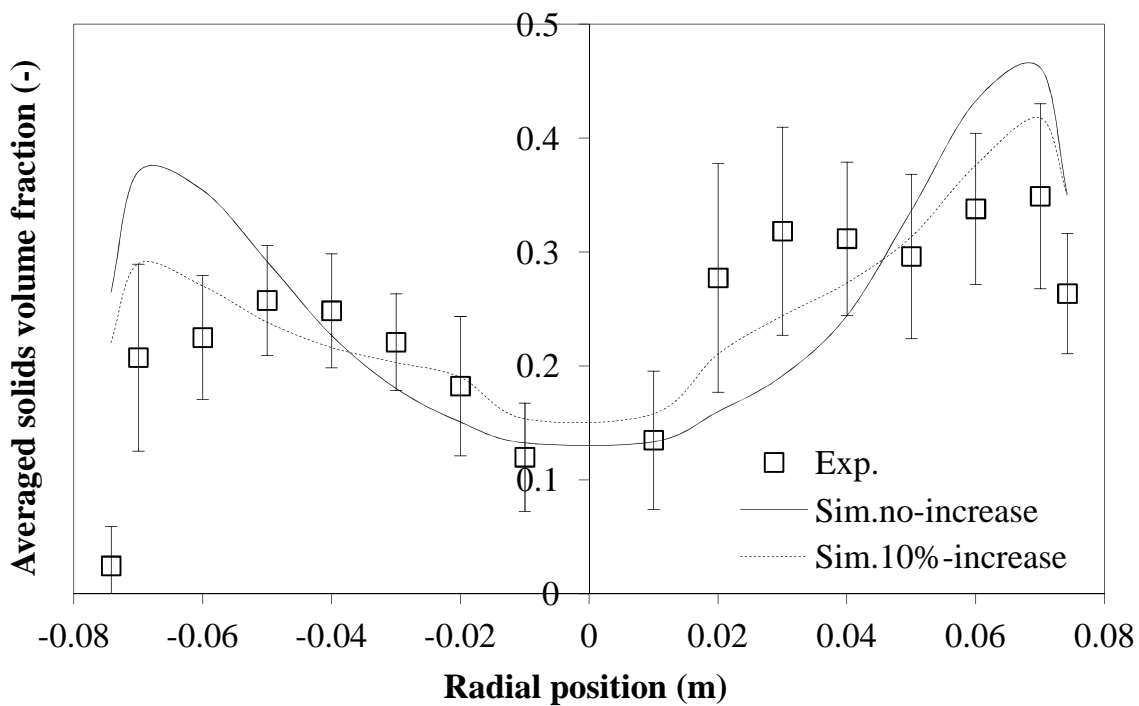


(b)

Figure 3.7 Experimental and model-predicted, time-averaged solids volume fraction from 0-3 cm above the air distributor as a function of radial position, with an atomisation air pressure of (a) 1.5 bar, (b) 2 bar.



(c)



(d)

Figure 3.7 (continued) Experimental and model-predicted, time-averaged solids volume fraction from 0-3 cm above the air distributor as a function of radial position, with an atomisation air pressure of (c) 3 bar and (d) 4 bar.

As seen in Figure 3.7 (a-d), it can also be observed that the models with the higher atomisation air pressures gave rise to better prediction of the time-averaged solids volume fraction at the bottom centre of the reactor. A possible explanation could be that with the nozzle operating at lower pressure, particles have a smaller circulation pattern with more radial than axial movement, which was also observed by Depypere *et al.* (2009).

Finally, for the sake of completeness, the comparison of the 4-phase model (as described in this study) and the more common 2-phase model (1 gas, 1 solid phase, single particle diameter) predicted solids volume fraction with the same flow conditions was made. As was also observed in the previous chapter, without the presence of an atomisation nozzle, the 4-phase Eulerian model yielded large improvement in model accuracy in polydisperse particle systems. From Figure 3.8, the same trend regarding model accuracy of the 4-phase model, now applied to a fluidised bed with an atomisation nozzle, was seen. The model-predicted time-averaged voidage contours showed poorer agreement with the experimental PEPT results in case of the 2-phase model (RMS = 0.093). When considering the voidage profile, displayed in Figure 3.8c, it appears that the 2-phase model predicted much higher voidages in the central bed region just above the air distributor. In contrast, the 4-phase model (Figure 3.8b) did not predict significantly higher voidages in this region and was therefore more in agreement with the experimentally measured voidage profile (Figure 3.8a). A possible explanation could be the effect of the width of the particle size distribution of the solids used in the experiments as opposed to the definition in the model, in which the solid phase is characterised by a single particle diameter for the case of the 2-phase model.

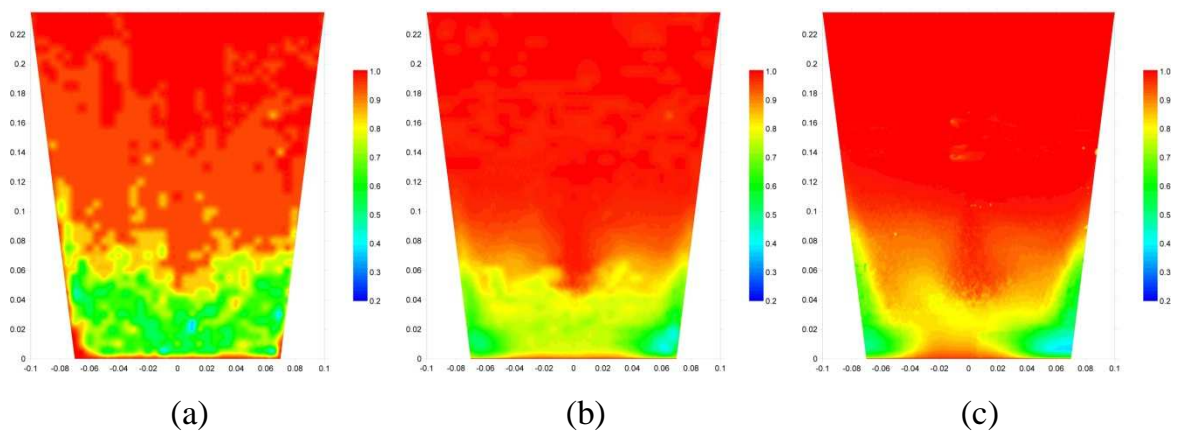


Figure 3.8 Comparison of the model-predicted bed voidage with 2-bar atomisation and 10% increase of the superficial air velocity: (a) PEPT result, (b) 4-phase model and (c) 2-phase model.

3.5 Conclusions

As a powerful numerical tool for solving fluid flow problems, commercially available CFD software, FLUENTTM 6.3.26, was used in an attempt to reproduce the important hydrodynamic aspect of a fluidised bed coater, by modelling four phases using an Eulerian interpenetrating fluids model. The non-spherical shape of solid particles was implemented in the model using the sphericity coefficient and the solid-solid interactions were taken into account. The model predicted solids concentrations and bed voidage profiles with the variation of atomisation air pressures, and the simulated results were qualitatively and quantitatively compared with experimental data obtained from Depypere *et al.* (2009).

Even though the model-predicted results showed good correlation with the experimental results, discrepancy between values from simulations and experiments could be seen. However, it has also been demonstrated that the model proved to be highly sensitive to changes in the fluidisation air flow rate. Therefore, a sensitivity analysis applying a positive perturbation factor to the superficial air velocity boundary condition was employed in the simulations. It was found that the model predicted results satisfactorily matched with the experimental data. It was established that the magnitude of this adjustment is within the range of the experimental error of the fluidisation air flow rate employed in the experiments. Furthermore, using a proper calibrated air flow rate – as a boundary condition – should allow to model the voidage and solids volume concentration profiles in the fluidised bed reactor with an acceptable accuracy, using the CFD model presented in this study.

Chapter 4 **CFD study of droplet atomisation using a binary nozzle in fluidised bed coating**

Parts of this chapter are published in:

Duangkhamchan, W., Ronsse, F., Depypere, F., Dewettinck, K., Pieters, J.G. (2012). **CFD study of droplet atomisation using a binary nozzle in fluidised bed coating**. *Chemical Engineering Science*, 68(1), 555-566.

Abstract

An Eulerian-Lagrangian computational fluid dynamics (CFD) model was employed to describe two-fluid atomisation in a tapered fluidised bed coater using the air-blast/air-assisted atomiser model. Atomisation was modelled both with and without the inclusion of the solids phase (i.e., gas-liquid and gas-solid-liquid multiphase modelling). In addition, a multi-fluid flow model (Eulerian-Eulerian framework) combined with a population balance model, used to compute the droplet size, was employed as an alternative approach for modelling the spray produced by a two-fluid nozzle. In this approach, the CFD solver couples the population balance equation along with the Navier-Stokes equations for predicting the droplet diameter and mass fraction distribution. Comparison between simulated spray pattern (gas-liquid model) and that experimentally visualised by means of UV illumination was made and good agreement was obtained. Parametric studies were done in order to investigate the effects of operating conditions on spray cone and liquid mass fraction inside the reactor. Furthermore, comparison of time-averaged fluidised bed behaviour with the inclusion of sprays obtained by both gas-solid-liquid multiphase modelling methods is presented.

4.1 Introduction

In order to control process efficiency in fluidised bed coating using a model-based approach, it is necessary to explore each phenomenon taking place in the system. In the previous chapters, momentum transfer between the gas and solid phases was modelled using various drag coefficient models, in order to evaluate the suitable drag model for the description of fluidised bed behaviour. Subsequently, the solids volume fraction was simulated including the effect of the release of compressed air by the two-fluid nozzle in order to provide qualitative and quantitative consistency of model simulations with experimental data. However, the liquid phase, being the sprayed droplets, was not yet included. Therefore, the next step – as outlined in this chapter – is the addition of the liquid phase to the existing fluidised bed CFD model.

To produce sprays in fluidised bed coating processes, pneumatic or two-fluid atomisation is frequently used. In the mechanism of the two-fluid atomisation, as shown in Fig.4.1, a high velocity gas impacts a liquid jet issuing from a nozzle orifice creating high shear forces over the liquid surface, leading to disintegration into spray droplets. The optimum frictional conditions resulting from high relative velocity between gas and liquid are generated by expanding the air to sonic or supersonic velocities before impacting the liquid (Hede *et al.*, 2008). When injected from the nozzle orifice, the liquid jet starts to make contact with the mixing zone, expanding radially and squeezed into a thin circular sheet (Zeoli and Gu, 2006). The term “liquid sheet” is used for both flat and cylindrical jets as common nomenclature (Hede *et al.*, 2008). For more details about the two-fluid atomisation, the reader is referred to Hede *et al.* (2008), Sridhara and Raghunandan (2010) and Varga *et al.* (2003).

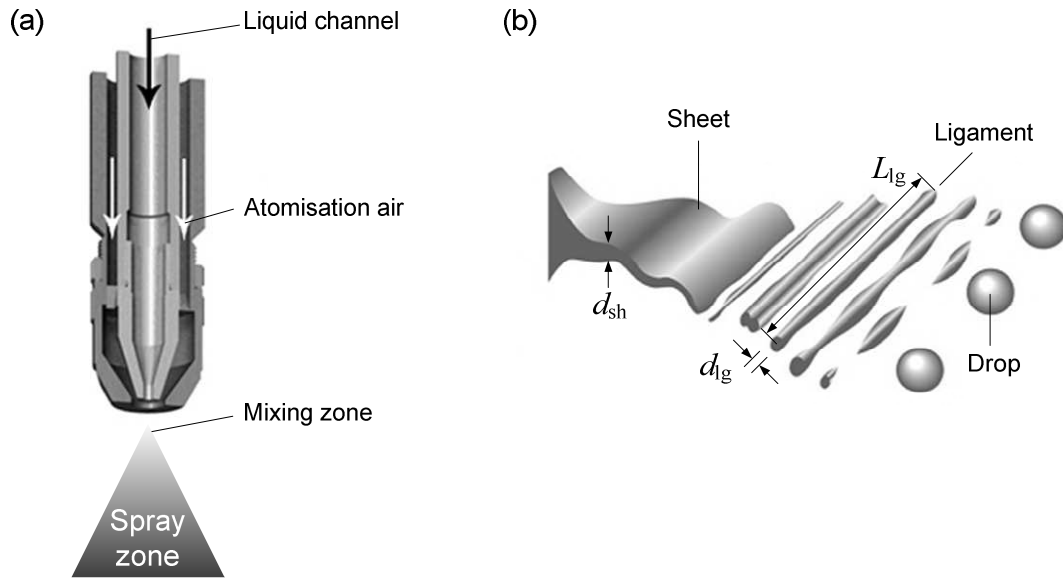


Figure 4.1 Schematic overview of the two-fluid nozzle (a) and the mechanism of droplet atomisation (b), adapted from Salman *et al.* (2007) and Spray Drying Systems Co. (2000).

Currently, to design and optimise the fluidised bed coating process, spray conditions and the operation of the two-fluid nozzle are identified as one of the most critical factors for the whole process and have to be trial-and-error tested in order to control spray characteristics, including droplet size distribution, droplets trajectories and spray cone angle (Hede *et al.*, 2008; Ronsse *et al.*, 2007b). Therefore, in order to reduce time consumption and costs of extensive experiments, many numerical approaches, for instance, Eulerian-Eulerian CFD, Eulerian-Lagrangian CFD, and population balance modelling, etc., have been developed as a powerful tool to comprehend or clarify the impact of different input variables on process efficiency and to research and design work (Ronsse *et al.*, 2007b).

During the last few decades, CFD has been widely adopted in many industrial uses. In spray application, various numerical methods, for instance, the volume of fluid (VOF) method and the discrete phase method (DPM), have been developed

to predict basic characteristics of spraying nozzles (e.g., spray angle and droplet size distribution) and to predict droplet trajectories. In the discrete phase method (Lagrangian framework), the droplet trajectory is calculated individually using the equation of motion, whereas the volume of fluid or multifluid method (Eulerian framework) is based on continuum mechanics which treat the two phases as interpenetrating continua (Taghipour *et al.*, 2005).

For instance, for studying the two-fluid atomisation, instead of using only experimental PIV to provide an instantaneous map of the entire velocity field, Hoeg *et al.* (2008) used Eulerian CFD models to investigate the flow pattern of gas and liquid jets issuing from a two-fluid nozzle. In that work, good agreement between model-predicted and experimental data was found. Furthermore, Zeoli and Gu (2006) used the discrete phase model to simulate the critical droplet breakup during atomisation producing fine spherical metal powders. To verify their model performance, the liquid metal was initialised to large droplet diameters varying from 1 to 5 mm. They found that the model could provide quantitative assessment for the atomisation process. Pimentel *et al.* (2006) improved the capability of CFD models to capture liquid atomisation mechanisms of the two-fluid nozzle associated with the measured droplet diameters to initialise the droplet size in the discrete phase model. Even though many researchers have attempted to model the droplet atomisation in various applications by means of CFD, as seen in Behjat *et al.* (2010), Fuster *et al.* (2009), Gianfrancesco *et al.* (2010), Kalata *et al.* (2009), Mezhericher *et al.* (2010), White *et al.* (2004) and Yamada *et al.* (2008), the two-fluid atomisation occurring in the fluidised bed coating process still needs to be explored, considering the fact that the liquid is atomised in the presence of the fluidised solid phase.

In addition to the two approaches for modelling multiphase flow problems mentioned previously, the population balance model combined with the CFD model has been introduced to the modelling community because of its minimum

level of computational complexity (Aly *et al.*, 2009). Moreover, the model can easily be coupled with the Eulerian-Eulerian model which eliminates the need for semi-empirical models employed in the Lagrangian framework (Aly *et al.*, 2009). Recently, the population balance model has been extensively used in liquid-liquid and gas-liquid systems for modelling droplets and bubbles (Aly *et al.*, 2010a, b). However, only few studies can be found in droplet atomisation problems, especially in fluidised bed coating systems. The atomisation process occurring in a plain jet air blast atomiser (two-fluid nozzle) was first investigated using the combination between a population balance model and a CFD Eulerian multi-fluid model by Aly *et al.* (2009). In that work, although the model obtained good agreement with experimental data, improvement still needed to be done. Therefore, Aly *et al.* (2010a, b) developed a new mathematical model for calculating droplet breakup frequency, instead of using a constant value, based on both drag and turbulence induced fragmentation stresses. Good agreement with the experimental data was achieved.

The main objective of this chapter is to present a CFD model of droplet atomisation of a two-fluid nozzle in the fluidised bed coating process, and to integrate with existing gas-solid CFD models for fluidised bed coating processes as described in the previous chapter. Furthermore, the alternative numerical approach to describe the two-fluid atomisation using population balance modelling combined with the Eulerian CFD framework was also demonstrated. Finally, the impact of process variables on spray characteristics and comparison of model-predicted distribution of voidage and liquid volume fraction obtained by two approaches were assessed.

4.2 CFD model description

4.2.1 Discrete phase model (DPM)

In addition to solving transport equations for the continuous phases (i.e., gas and solids), a discrete phase of droplets was simulated in a Lagrangian framework. The trajectories of these discrete phase entities were computed individually. The coupling between the phases and its impact on both the discrete phase trajectories and the continuous phase flow was included.

4.2.1.1 The Eulerian – Lagrangian approach

In the Euler-Lagrangian approach, the gas and solid phase are treated as continuous phases by solving the time-averaged Navier-Stokes equations, while the dispersed phase (liquid phase) is solved by tracking a large number of droplets through the calculated flow field. The discrete phase can exchange momentum with the fluid phase.

Continuous phase model

Each volume within the mesh is simultaneously solved in an Eulerian frame of reference to obtain the gas flow field with the use of general conservation equations, as summarised below and described in the previous chapters.

The conservation of mass of phase q ($q =$ either gas or solid) is described as

$$\frac{\partial}{\partial t}(\alpha_q \rho_q) + \nabla \cdot (\alpha_q \rho_q \vec{v}_q) = 0 \quad (4.1)$$

where α_q is the phase volume fraction, ρ_q the density and \vec{v}_q the velocity of phase q .

The following equation describes conservation of momentum for the fluid phase l :

$$\frac{\partial}{\partial t}(\alpha_l \rho_l \bar{v}_l) + \nabla \cdot (\alpha_l \rho_l \bar{v}_l \bar{v}_l) = -\alpha_l \nabla \cdot p + \nabla \cdot \bar{\tau}_l + \alpha_l \rho_l \bar{g} + K_{ls}(\bar{v}_l - \bar{v}_s) \quad (4.2)$$

In Eq. (4.2) $(\bar{v}_l - \bar{v}_s)$ is the slip velocity between the phases, where the subscript l denotes the fluid phase and s indicates the solid phase. K_{ls} denotes the drag force coefficient relevant to the phases l and s , p is the pressure and $\bar{\tau}_l$ the deviatoric effective stress tensor of fluid phase.

As described in chapter 3, the momentum transfer between the particulate phases due to collisions should be taken into account using constitutive relations known as the solid – solid drag term (Symlal, 1987).

The solid-solid (between solid phases s and m) momentum exchange coefficient is calculated using the Symlal-O'Brien symmetric model (Symlal, 1987):

$$K_{sm} = \frac{3(1 + e_{s,sm}) \left(\frac{\pi}{2} + C_{fr,sm} \frac{\pi^2}{8} \right) \alpha_s \rho_s \alpha_m \rho_m (d_s + d_m)^2 g_{0,sm}}{2\pi(\rho_s d_s^3 + \rho_m d_m^3)} \times |\bar{v}_s - \bar{v}_m| \quad (4.3)$$

Discrete phase model

The discrete phase model was solved in a Lagrangian frame of reference to simulate the spray pattern which is predicted by tracking the droplet trajectories by integrating the force balance on the particle (Newton's second law) (Behjat *et al.*, 2010; Pimentel *et al.*, 2006),

$$\frac{d\bar{v}}{dt} = \bar{f}_{drag} + \frac{\bar{g}(\rho_p - \rho_g)}{\rho_p} \quad (4.4)$$

where \vec{f}_{drag} is the drag force per unit particle mass,

$$\vec{f}_{drag} = \frac{3}{4} \cdot \frac{C_D \rho_g}{\rho_p d_p^2} \cdot |\vec{v}_g - \vec{v}_p| \cdot (\vec{v}_g - \vec{v}_p) \quad (4.5)$$

Here, \vec{v}_g is the gas phase velocity, \vec{v}_p is the droplet velocity, ρ_g is the gas density, ρ_p is the droplet density and d_p is the droplet diameter. C_D is the drag coefficient estimated using the correlation proposed by Morsi and Alexander (1972).

4.2.1.2 Air-blast/air-assisted atomiser model

Among the five atomiser models available in FLUENT, namely the plain-orifice, pressure-swirl, flat-fan, effervescent/flashing and air-blast/air-assisted atomiser models, the latter was found to be the suitable model for the two-fluid nozzle in this work due to its similar atomisation mechanism. The air-blast/air-assisted atomiser model predicts droplet formation in those atomisers where an additional air stream is used to accelerate the breakup of the liquid sheet formed by the nozzle into droplets (Figure 4.1).

In order to determine the sheet thickness, the effective mass flow rate, \dot{m}_{eff} , defined as

$$\dot{m}_{eff} = \frac{2\pi\dot{m}}{\Delta\theta} \quad (4.6)$$

is used. In this equation, $\Delta\theta$ is the difference between the azimuthal stop angle and the azimuthal start angle, which was 2π for the nozzle type considered in this study (circular liquid sheet). Here, \dot{m} is the liquid mass flow rate (kg s^{-1}) and hence, is

equal to \dot{m}_{eff} . Therefore, the thickness of sheet (mm), d_{sh} , produced by the air-blast/air-assisted atomiser can be approximated by relating the mass flow rate as

$$\dot{m}_{eff} = \pi \rho_l v_l d_{sh} (d_{inj} - d_{sh}) \quad (4.7)$$

where ρ_l is the liquid density (kg m^{-3}), v_l is the axial velocity component of the liquid at the nozzle orifice (m s^{-1}) and d_{inj} is the diameter of the liquid orifice. In Eq. (4.7), the effective mass flow rate is expressed as the liquid density (ρ_l) multiplied with the liquid velocity (v_l) and with the cross-sectional area of the circular liquid sheet with diameter ($d_{inj} - d_{sh}$) and sheet thickness d_{sh} .

Owing to the instability of the liquid sheet, the sheet breaks up and ligaments will be formed (Figure 4.1) whose length is given by

$$L_{lg} = C_{sh} \frac{v_{sh}}{\Omega} \quad (4.8)$$

where L_{lg} is the ligament length (mm), C_{sh} denotes a sheet constant assumed to be related to sheet break-up, v_{sh} is the total velocity of the liquid sheet and Ω is the maximum growth rate (s^{-1}) and is found by numerically maximising the dispersion relation based upon the growth of sinuous waves on the liquid sheet (Schmidt *et al.*, 1999). For short waves, the ligament diameter is assumed to be linearly proportional to the wavelength (resulting from the sheet break-up),

$$d_{lg} = \frac{2\pi C_{lg}}{K'} \quad (4.9)$$

where C_{lg} is the ligament constant, and K' is the wave number (m^{-1}) corresponding to the maximum growth rate, Ω . For more details concerning the air-blast/air-assisted atomiser model, the reader is referred to Ansys Inc. (2009b).

4.2.2 Multi-fluid flow model combined with population balance model (MFM-PBM)

In this approach, a conservation equation called the population balance equation is solved along with the Navier-Stokes equations in order to calculate the droplet diameter (Sauter Mean Diameter, SMD, which is commonly used to characterise droplets in spray modelling) and the subsequent transport throughout the atomisation process. The population balance equation is a statement of continuity that describes how the statistical distribution of one or more droplet-related variables changes with time and space (Peglow *et al.*, 2007). When the fraction of droplets with volume V at time t is given by the number density function $n(V, t)$, then the change in number of droplets with volume V as a result of larger droplets with volume V' , fragmenting into droplets with volume V and, the subsequent fragmentation of droplets with volume V into smaller droplets, is given in the population balance equation as (Ansys Inc., 2009a):

$$\frac{\partial}{\partial t} [n(V, t) + \nabla \cdot [\vec{v}_p n(V, t)]] = \int_{V'} g(V') \beta(V/V') n(V', t) dV' - g(V) n(V, t) \quad (4.10)$$

In the above equation, only droplet fragmentation or break-up was considered while droplet coalescence was assumed to be negligible since sprays in the fluidised bed coating process are considered to be dilute. Furthermore, droplet breakup was assumed to be binary, i.e. when a droplet with volume V' breaks up, it forms two new droplets with volume V and $(V' - V)$, respectively. The terms on the left hand side of Eq. (4.10) are the rate of change of the number density function and its convective derivative, respectively, while the terms on the right hand side represent the birth rate and the death rate terms resulting from droplet breakage (Ansys Inc., 2009a).

In Eq. (4.10) $g(V')$ is the breakage frequency, being the fraction of droplets of volume V' breaking per unit time (s^{-1}) and $\beta(V/V')$ is the droplet breakage kernel and expresses the probability by which a droplet with volume V originates from the binary fragmentation of a droplet with volume V' . Hence, the first term on the right hand side of Eq. (4.10),

$$\int_{V'} g(V') \beta(V/V') n(V', t) dV' \quad (4.11)$$

represents the rate of formation, or birth rate, of droplets with volume V from breakage of droplets with volume V' ($V < V' < \infty$). The second term on the right hand side of Eq. (4.10),

$$g(V) n(V, t) \quad (4.12)$$

expresses the rate at which droplets with volume V disappear from the system due to fragmentation in smaller droplets, hence the term death rate.

Many methods, like for instance the Monte Carlo method (Lasheras *et al.*, 2002; Ronsse *et al.*, 2007a), the discrete method (Aly *et al.*, 2009; Lasheras *et al.*, 2002), the quadrature method of moments (Marchisio *et al.*, 2003), and the direct quadrature method of moments (Madsen, 2006), are widely used in order to solve the population balance equations.

Due to the advantages of computing the droplet size distribution directly and the assumption of a small number of size intervals and the size distribution, in this work the discrete method (also known as the class method as referred to in this work) was used to discretise the droplet population into a finite number of size intervals, n . In the class method, assuming that aggregation is negligible for dilute

sprays, the population balance equation is written in terms of volume fraction of droplets with size class i (Aly *et al.*, 2010a,b; Aly *et al.*, 2009):

$$\frac{\partial}{\partial t}(\rho_p \alpha_i) + \nabla \cdot (\rho_p V_i \alpha_i) = \rho_p V_i (B_i - D_i) \quad (4.13)$$

where V_i is the size of droplets in size class i , ρ_p is the density of droplet phase and α_i is the volume fraction of droplet size class i defined as

$$\alpha_i = N_i V_i \quad ; i = 0, 1, \dots, n-1 \quad (4.14)$$

where N_i is the total number of droplets per size class, and is given by

$$N_i = \int_{V_i}^{V_{i+1}} n(V) dV \quad (4.15)$$

The droplet birth rate resulting from droplet breakage, B_i , and death rate term, D_i , in Eq.(4.13), are defined as

$$B_i = \sum_{j=1}^n g(V_j) \beta(V_i/V_j) N_j \quad (4.16)$$

$$D_i = g(V_i) N_i \quad (4.17)$$

In this study, breakage kernel and breakage frequency in the birth and death rate terms in Eqs. (4.16) and (4.17) were similar to those used in Aly *et al.* (2009): the breakage kernel corresponded to a case where equal droplet fragments are distributed to all daughter size bins, while a constant frequency of 2000 Hz – a number corresponding to the reciprocal of the mean characteristic time scale of turbulence eddies – was chosen for the breakage frequency. The breakage kernel used in Aly *et al.* (2009) was defined as:

$$\beta(V/V') = \frac{2}{V'} \quad (4.18)$$

In order to solve the number density function, the population balance equation is linked to the Eulerian CFD model via a two-way coupling procedure. In this procedure, the velocity v_i is calculated in the Eulerian framework and then substituted into the population balance equation in order to compute the mean droplet sizes (SMD) which are then returned to the Eulerian solver to calculate the phase interaction such as the momentum exchange. Heat and mass transfer were not taken into account in this work.

4.3 Materials and methods

4.3.1 Overview of the numerical method

In this work, in addition to the discrete phase model (DPM) which has been widely used to describe droplet atomisation, the basic class method of population balance model combined with the multi-fluid phase model (MFM-PBM) was used to simulate two-fluid atomisation. For both approaches, the 3-D geometry of a laboratory-scale Glatt GPCG-1 fluidised bed (Glatt GmbH, Germany) together with the two-fluid nozzle were meshed using Gambit 2.2.30 (Ansys Inc., Canonsburg, PA). A hybrid hexahedral-tetrahedral grid, containing 473,083 elements, was exported into the solver software, Ansys Fluent v.12 (Ansys Inc., Canonburg, PA). The grid is displayed in Fig. 4.2.

Flow turbulence was simulated using the standard $k-\epsilon$ model with standard wall functions, which has proven to result in good agreement with experimental data for this type of fluidised bed reactor geometry and solids material. First order upwind schemes were selected and the relation between velocity and pressure corrections was calculated using the phase-coupled SIMPLE algorithm.

In order to model the droplet atomisation and the interaction of the droplet phase with the gas and solid phases, the numerical setup was separated into four sections corresponding to two approaches as follows:

- modelling the droplet atomisation in a gas phase using the discrete phase model;
- modelling the droplet atomisation in a gas-solid flow by means of the discrete phase model combined with the multifluid flow model;
- modelling the droplet atomisation in a gas phase using the population balance model combined with the multifluid flow model;
- modelling the droplet atomisation in a gas-solid flow using the population balance model coupled with the multifluid flow model.

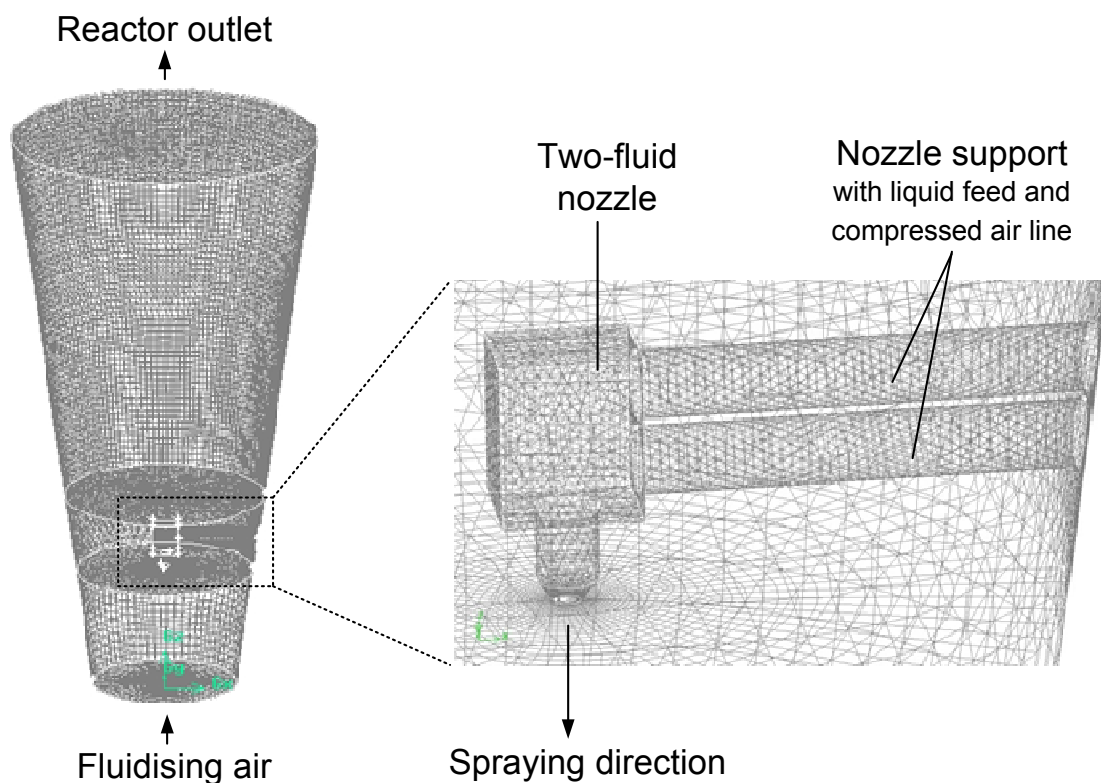


Figure 4.2 Meshed geometry of a conical Glatt GPCG-1 reactor together with the two-fluid nozzle.

4.3.2 Modelling the two-fluid atomisation using the DPM

4.3.2.1 Two-phase flow model (gas-liquid DPM model)

First, model parameters associated with the air-blast/air-assisted atomiser model were calibrated using published industrial data of the mean droplet diameter for the nozzle used in the Glatt GPCG-1 fluidised bed unit (Model 970-S1, Düsen-Schlick GmbH). In order to compare the calculated droplet sizes to the published industrial data, the spray injection (water) at atomisation air pressures of 1.0 and 3.0 bar was simulated in a stagnant-air cylinder geometry.

Multiple simulations using variation of spray sheet thicknesses (d_{sh}) of 0.4, 0.7 and 1.0 mm, sheet constants (C_{sh}) of 14, 15 and 16, and ligament constants (C_{lg}) of 0.5, 0.7 and 0.9, were performed. After calibration of the air-blast atomiser model, the model was employed to study the atomisation in the geometry of the laboratory-scale fluidised-bed unit and the impact of process variables on spray characteristics. The fluidisation air flow rates used before, namely 55, 76 and 97 $m^3 hr^{-1}$, were selected. Other process variables are presented in Table 4.1.

Table 4.1 Process variables used in this study (^a indicates reference scenario).

Process variables	Value
Fluidisation air flow rate, \dot{V}_f ($m^3 hr^{-1}$)	55, 76 ^a , 97
Atomisation air pressure, p_{at} (bar)	1.0, 2.0 ^a , 3.0
Liquid feed rate, \dot{m}_l ($\times 10^{-4} kg s^{-1}$)	0.5, 1.0 ^a , 1.5

4.3.2.2 Three-phase flow model (gas-solid-liquid DPM model)

A CFD model including all three phases and their interactions was developed to evaluate the impact of injection parameters on the performance of the fluidised bed coater. In this model, the water droplets were considered to be a separate phase in addition to the gaseous and solid particle phases in order to better describe the complex process of liquid spraying inside the fluidised bed reactor. Interactions between gas and solid (particle) phases were solved in the Eulerian-Eulerian framework, including the modified-Gidaspow drag coefficient, while the trajectories of injected droplets were simulated by solving the equations of motion of an individual dispersed phase (Lagrangian framework). For fluidisation, the properties of 1 kg of glass beads were used (Depypere *et al.*, 2009) which are listed in Table 4.2, along with the boundary conditions and simulation parameters.

Table 4.2 Boundary conditions and simulation parameters.

Descriptor	Value
Primary phase (continuous)	Gas
Secondary phase (continuous)	Glass beads
Discrete phase	Water droplet
Solids particle size, d_s (μm)	196.54
Solids density, ρ_s (kg m^{-3})	2467
Solids loading, M_s (kg)	1
Gas phase density, ρ_g (kg m^{-3})	1.225
Liquid phase density, ρ_p (kg m^{-3})	998
Reactor bottom diameter (m)	0.14
Reactor top diameter (m)	0.30
Reactor height (m)	0.56

4.3.3 Modelling the two-fluid atomisation using the MFM-PBM

4.3.3.1 Two-phase flow model (gas-liquid MFM-PBM model)

An unsteady pressure-based solver in Ansys Fluent v.12 was used with the Eulerian multiphase model coupled with the discrete population balance model in order to simulate water droplet atomisation through the two-fluid nozzle. Assuming that sprays are dilute, turbulence was modelled using the dispersed $k-\epsilon$ turbulence model. To be sure that the solution convergence behaviour was reached within each time step, a small time step of 10^{-5} s was chosen. The velocity boundary conditions for the water and atomising air are shown in Table 4.1. As the use of compressed air in the two-fluid nozzle produces droplets with a size ranging from 10 to 40 μm (Lefebvre, 1989), the droplet population was discretised into 7 size classes with a diameter ranging from 10 to 40 μm .

4.3.3.2 Three-phase flow model (gas-solid-liquid MFM-PBM model)

Instead of solving the motion of injected droplets separately in the Lagrangian discrete phase model, the gas, droplets and solid particles were treated as interpenetrating continua in the Eulerian framework. The gas phase was considered the primary phase, whereas the droplets and solid particle phases were the secondary phases. To track the droplet diameter in the Eulerian solver, the number density function was solved using the class population balance method. The details of this method were described in section 4.2.2.

4.3.4 Experimental spray visualisation

4.3.4.1 Measurement set-up

Spray visualisation experiments were performed in a transparent, polycarbonate reactor with similar dimensions to the Glatt GPCG-1 fluidised bed coating reactor. The tapered reactor had a bottom diameter of 0.14 m, a top diameter of 0.30 m and a total height of 0.56 m. The reactor shell material consisted of 5 mm thick polycarbonate. Fluidisation air was provided by a 2.2 kW high pressure centrifugal fan (Ventomatic CHT160-2T-3, Belgium) equipped with electronic frequency control (Figure 4.3). The volumetric air flow rate was measured between the fan and the reactor inlet by means of a 0.1 m diameter rotating vane flow meter (Airflow Developments, VMD20, UK).

The air distributor used in the fluidised bed reactor, consisted of a Robusta 172×36 wpi (wires per inch) wire mesh (Spörl KG, Germany). The pneumatic nozzle (Schlick Model 970-S1, Germany), normally used in the Glatt GPCG-1, was installed in the lower nozzle port of the transparent reactor. The spraying liquid was water with an added fluorescent dye, being sodium fluorescein salt (Sigma-Aldrich) and was transported to the pneumatic nozzle by means of a peristaltic pump (Watson-Marlow, 505 Du/RL, US).

The spray cone produced by the pneumatic nozzle was visualized by means of UV illumination, by directing a 400 W UV spotlight 0.5 m above the reactor outlet. Illumination through the open reactor outlet proved to be most efficient, as the polycarbonate reactor shell material had some UV absorbing capacity. The illuminated spray was recorded by a digital camera (Olympus i-Speed 1) at 60 frames per second (800 × 600 pixel size), and stored in an uncompressed video format (AVI).

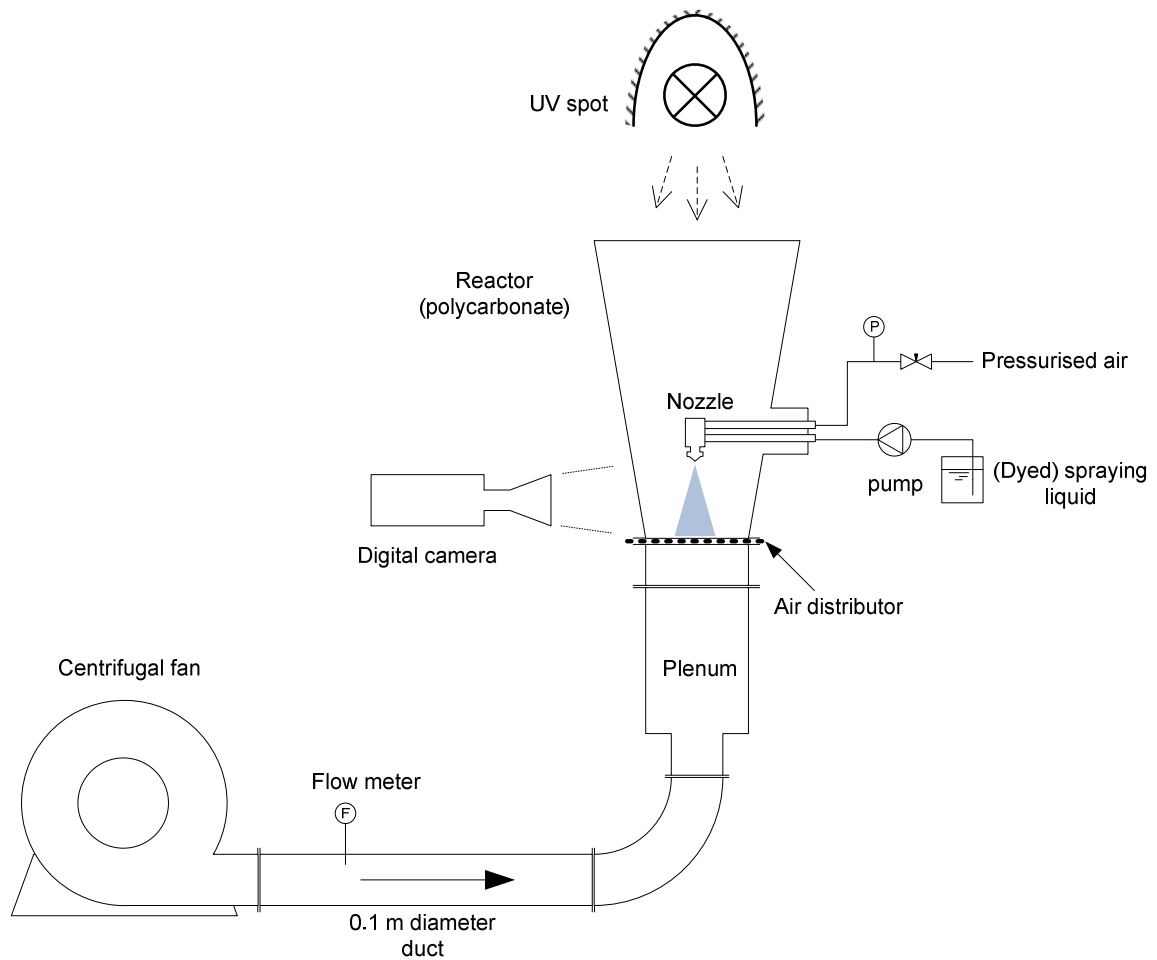


Figure 4.3 Spray visualisation setup.

4.3.4.2 Data processing

To visualise the spray cone, post-processing of the captured image data was necessary (i.e., contrast enhancement). The uncompressed frames captured by the video camera can be considered to be matrices holding the pixel intensity values (between 0 and 1), A_i , with subscript i indicating the frame number (i.e. 60 per recorded second of video) and having the dimensions of 800 by 600. As the recording was triggered at the moment of activating the peristaltic pump, an initial number of frames, b , was recorded without spray, i.e., before the development of the actual spray cone. Of these b frames, an average, A'_b , was calculated that served as a reference blank frame to be subtracted from the actual spraying frames,

$$A'_b = \frac{1}{b} \sum_{i=1}^b A_i \quad (4.19)$$

The actual frames to be used for visualisation were taken after the steady-state spraying cone had developed itself, and were denoted by frames A_i with $m \leq i \leq n$. The contrast enhancement of each of the frames during steady-state spraying consisted of two steps. First, the reference blank frame was subtracted from the spraying frame A_i resulting in A_i'' , and second, each frame matrix was multiplied with a scalar so the pixel with the highest intensity value in A_i reached unity (i.e. maximum intensity) – with the new resulting matrix denoted as E_i :

$$m \leq i \leq n \rightarrow \begin{cases} A_i'' = A_i - A'_b \\ E_i = x \cdot A_i'' \Leftrightarrow \max(E_i) = 1 \end{cases} \quad (4.20)$$

Finally, the average matrix of all E_i with $m \leq i \leq n$ was taken and used as the contrast-enhanced spray visualisation image,

$$E' = \frac{1}{n-m} \sum_m^n E_i \quad (4.21)$$

4.4 Results and Discussion

4.4.1 Air-blast/air-assisted atomiser model calibration

Several simulations with different spray injection setups were performed in order to calibrate the air-blast atomiser model as outlined in Section 4.3.2.1. The measured mean volume droplet diameters at 1.0 and 3.0 bar atomisation pressure (data supplied by Düsen-Schlick GmbH) were compared with simulated mean droplet sizes while the ligament constant, the sheet constant and sheet thickness were varied.

Figure 4.4 shows the simulated versus experimental mean droplet size at 3.0 bar atomisation pressure and using different values for the ligament constant, C_{lg} . From this figure, the spray injection characterised by using a ligament constant, C_{lg} , of 0.9, gave the best agreement with the experimental mean droplet diameter. With respect to variation of the sheet constant (C_{sh}) and the sheet thickness (d_{sh}), no significant differences in the model-predicted droplet diameter distribution were observed. Similar trends were seen from the simulation with 1.0 bar atomisation pressure and consequently, the following calibrated air-blast atomiser model parameters were used in subsequent simulations: ligament constant, $C_{lg} = 0.9$ and standard values for sheet constant, $C_{sh} = 15$ and sheet thickness, $d_{sh} = 0.7$ mm.

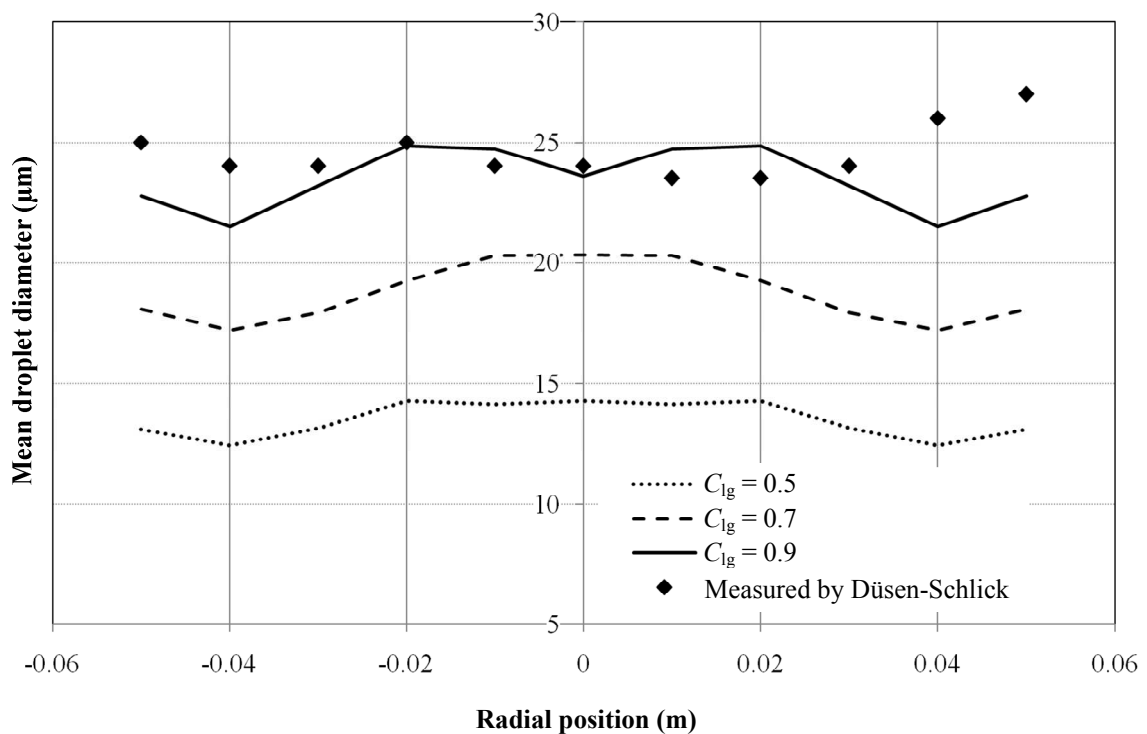


Figure 4.4 Effect of ligament constant, C_{lg} , on the model-predicted mean volume droplet diameter at 3 bar atomisation air pressure, compared against the experimental droplet size, as provided by Düsen-Schlick.

4.4.2 Two-phase (gas-liquid) model of droplet atomisation in the fluidised bed coater

4.4.2.1 Discrete phase model (gas-liquid DPM)

Using calibrated atomiser model parameters, the spray was modelled using DPM inside the geometry of a fluidised bed coater, as detailed in Table 4.2 and Figure 4.2. The effects of fluidisation air flow rate, atomisation air pressure and liquid feed rate – as outlined in Table 4.1 – on spray characteristics were simulated.

Figure 4.5 demonstrates the contour plots of droplet mass fraction at different atomisation air pressures. It can be seen that the spray pattern did not change with increasing atomisation air pressure. When considering the impact of fluidisation air flow rate, as detailed in Figure 4.6, higher flow rates were seen to reduce the diameter of the spray cone and lower the droplet mass fraction in the reactor. This can be explained by the fact that, at higher fluidisation air flow, droplets are easier lifted out of the conical vessel. However, it is important to stress that the DPM model in its current state did not include droplet evaporation (no energy equation). Consequently, the length of model-predicted droplet trajectories is likely to be overestimated compared to the actual process, where droplets are subjected to spray drying. This might also influence the shape of the trajectories. Finally, the effect of liquid feed rate on the droplet mass fraction distribution was simulated, as shown in Figure 4.7. It can be observed from this figure that at the higher liquid feed rate at the fixed atomisation air velocity and fluidisation air flow rate, more droplet mass fraction can be found, while less amount of droplet mass occurred at the lower feed rate. However, due to the higher amount of spray issuing from the nozzle in Figure 4.7c, the spray cone shape can obviously not be characterised. Therefore, the normalised contour plot of droplet mass fraction of Figure 4.7 was done in order to easily assess the effect of liquid feed rate on spray characteristics, as shown in Figure 4.8.

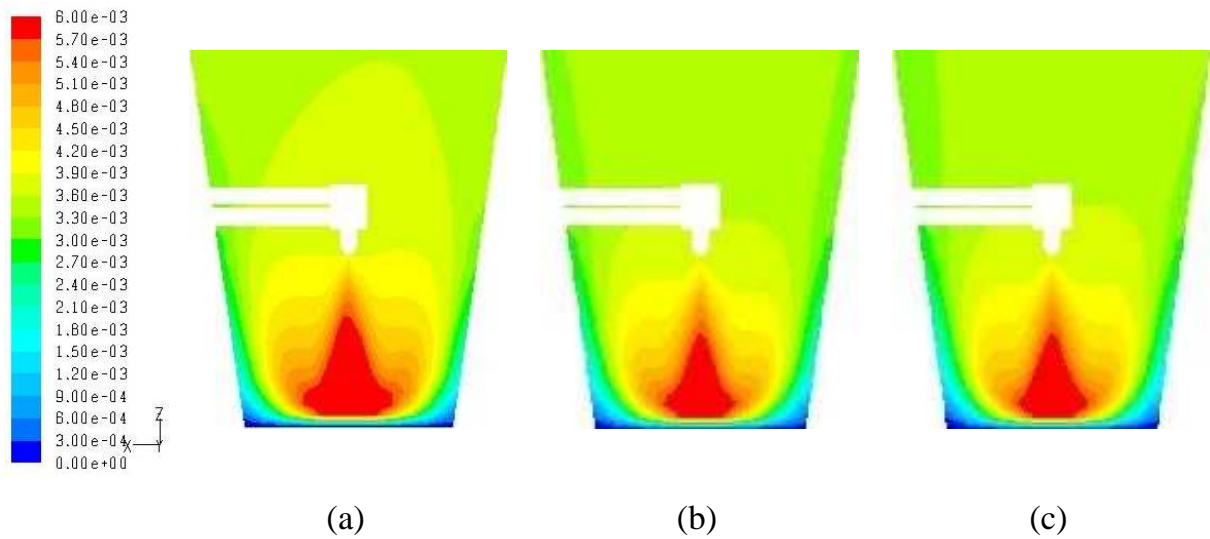


Figure 4.5 Contour plots of model-predicted (gas-liquid DPM) droplet mass fractions at fixed fluidisation air flow rate of $76 \text{ m}^3\text{h}^{-1}$ and liquid feed rate of $1 \times 10^{-4} \text{ kg s}^{-1}$, and at variation of atomisation air pressures: (a) 1.0 bar, (b) 2.0 bar (reference scenario, see Table 4.1) and (c) 3.0 bar.

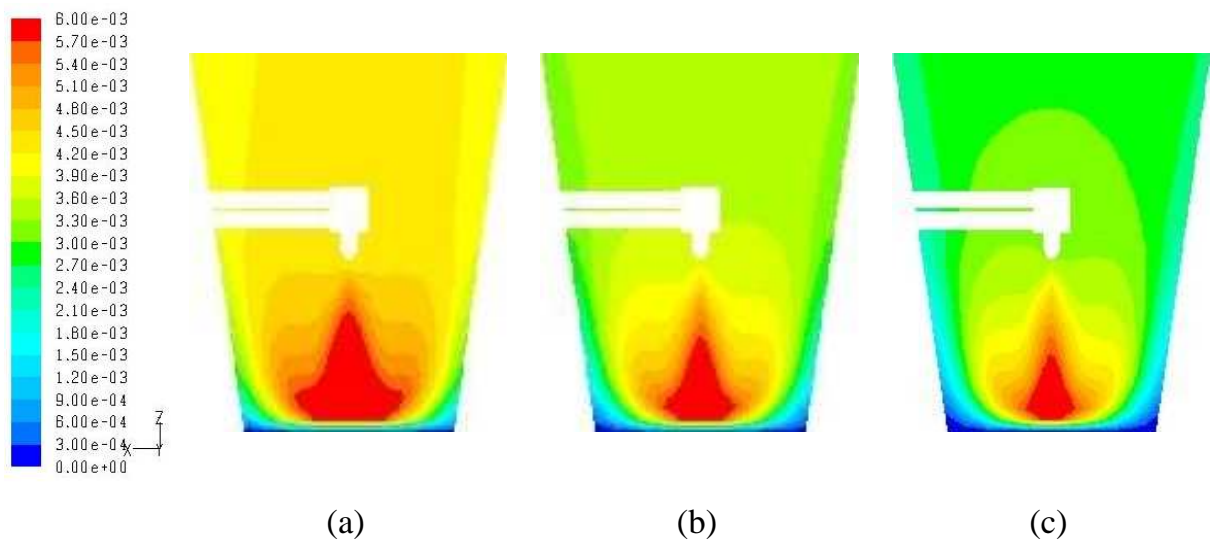


Figure 4.6 Contour plots of model-predicted (gas-liquid DPM) droplet mass fractions at fixed atomisation air pressure of 2 bar and liquid feed rate of $1 \times 10^{-4} \text{ kg s}^{-1}$, and at variation of fluidisation air flow rates: (a) $55 \text{ m}^3\text{hr}^{-1}$, (b) $76 \text{ m}^3\text{hr}^{-1}$ (reference scenario, see Table 4.1) and (c) $97 \text{ m}^3\text{hr}^{-1}$.

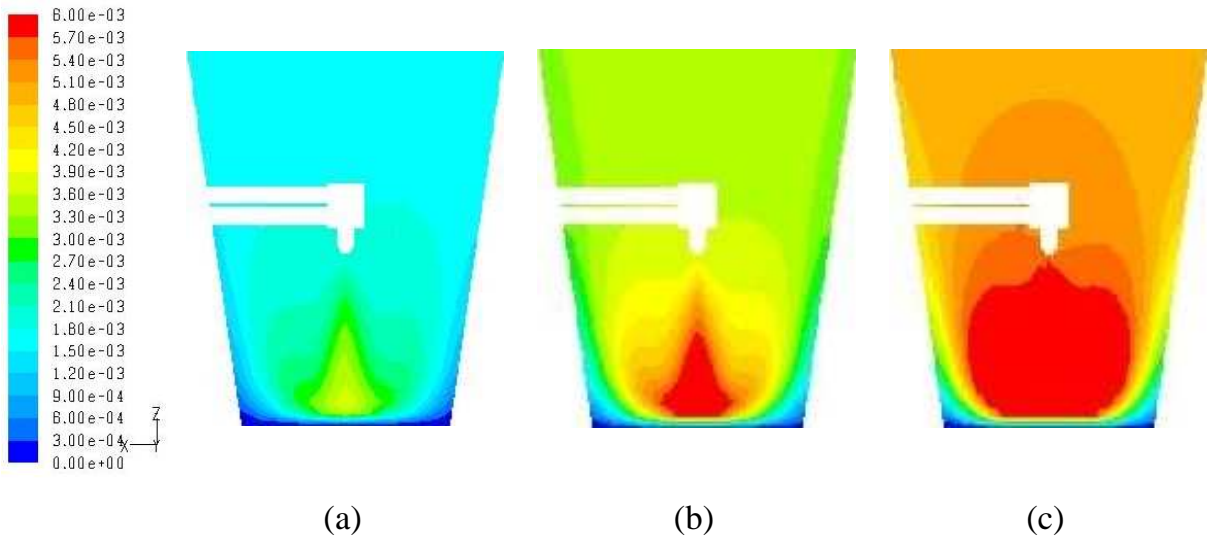


Figure 4.7 Contour plots of model-predicted (gas-liquid DPM) droplet mass fractions at fixed fluidisation air flow rate of $76 \text{ m}^3\text{h}^{-1}$ and atomisation air pressure of 2 bar, and at variation of liquid feed rates: (a) $0.5 \times 10^{-4} \text{ kg s}^{-1}$, (b) $1.0 \times 10^{-4} \text{ kg s}^{-1}$ (reference scenario, see Table 4.1) and (c) $1.5 \times 10^{-4} \text{ kg s}^{-1}$.

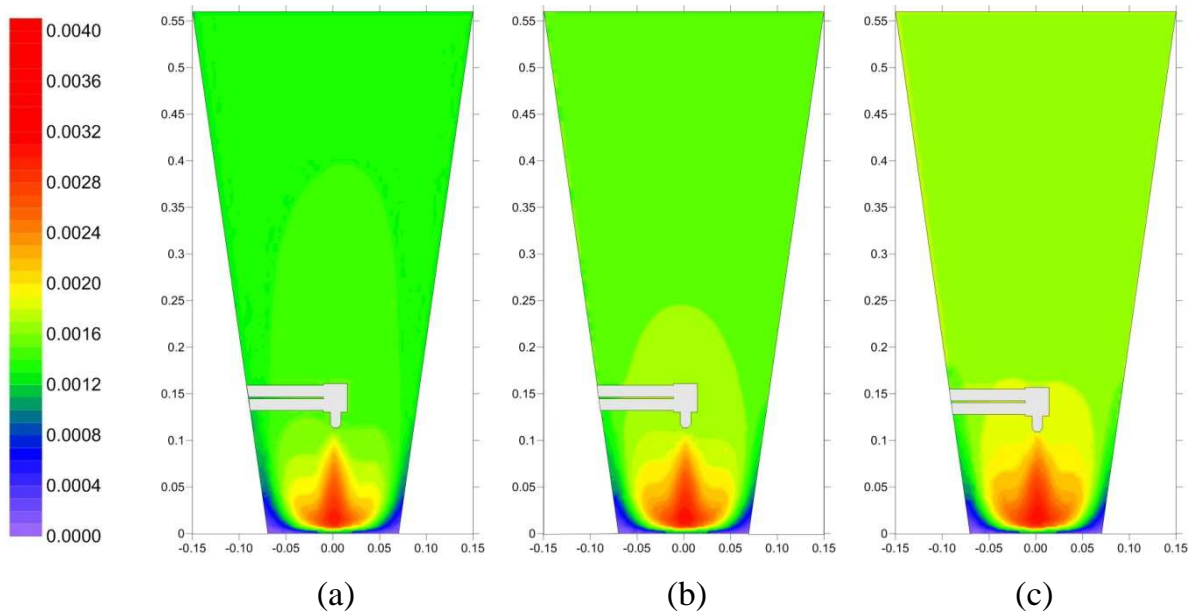


Figure 4.8 Normalised contour plots of model-predicted (gas-liquid DPM) droplet mass fractions at fixed fluidisation air flow rate of $76 \text{ m}^3\text{h}^{-1}$ and atomisation air pressure of 2 bar, and at variation of liquid feed rates: (a) $0.5 \times 10^{-4} \text{ kg s}^{-1}$, (b) $1.0 \times 10^{-4} \text{ kg s}^{-1}$ (reference scenario, see Table 4.1) and (c) $1.5 \times 10^{-4} \text{ kg s}^{-1}$.

It can be found from Figure 4.8 that even though the change in normalised droplet mass fraction was observed with the variation of liquid feed rates, the spray cone size did not change significantly.

4.4.2.2 Multi-fluid flow model combined with population balance model (gas-liquid MFM-PBM)

Figure 4.9 shows the distribution of the Sauter mean droplet diameter (SMD) and the droplet volume fraction in the geometry of the fluidised bed coater, as predicted by the MFM-PBM gas-liquid model with reference scenario conditions as outlined in Table 4.1. From this figure, it can be observed that the mean droplet sizes decrease continuously as the droplets depart from the liquid orifice of the two-fluid nozzle until they reach the air distributor. It can also be seen that the spray dispersion affects droplet diameter resulting in a decreasing droplet diameter with the higher spreading rate of spray.

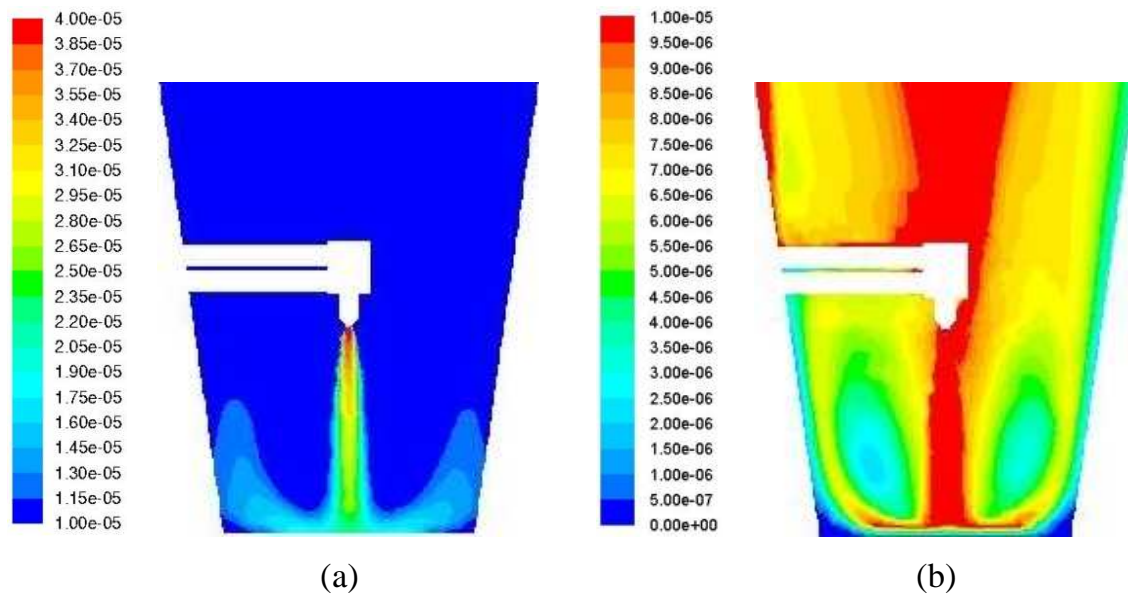


Figure 4.9 Simulated distribution of (a) the droplet Sauter mean diameter, in m and (b) droplet volume fraction using reference scenario conditions, as outlined in Table 4.1, as predicted by the gas-liquid MFM-PBM model.

Comparison of the droplet volume fraction as shown in Figure 4.9b with the droplet mass fraction from the DPM model gives a moderately good agreement (same order of magnitude when mass fraction is converted to volume fraction). The exception is a narrower diameter of the spray cone that was predicted by the MFM-PBM model. Furthermore, as the droplets were treated as a continuum in the MFM-PBM model, the droplet phase is seen to deflect from the air distributor at the bottom of the reactor (Figure 4.9b). This effect is not visible as such in the DPM results (Figure 4.5b), because in the discrete droplet tracking algorithm, tracking was ended when a droplet impacted on the boundaries of the reactor geometry.

Given these results, the MFM-PBM can be opted for as an alternative approach to model the atomisation of the two-fluid nozzle, considering advantages including minimum level of computational complexity, ease of coupling with the Eulerian-Eulerian CFD model and eliminating the need for semi-empirical models employed in the DPM model (Aly *et al.*, 2009).

Simulations with varying liquid feed rate, atomisation air pressure and fluidisation air flow rate were also performed. However, significant differences in droplet size distribution were not predicted by the MFM-PBM model with respect to process condition dependency. This observation is not consistent with both numerical and experimental studies reported in literature (Hede *et al.*, 2008; Lal *et al.*, 2010; Lebas *et al.*, 2009; Liao and Lucas, 2009; Liu *et al.*, 2006; Sridhara and Raghunandan, 2010). The possible explanation of this inconsistency is the assumption of a constant breakage kernel and breakage frequency in this study. In reality, breakage depends on droplet properties including size, as well as on local turbulences in the flow field. Consequently, improvement in model accuracy of the MFM-PBM model could be achieved when the breakage frequency and kernel are made dependent on (i.e. 'sensitised to') the droplet Weber and local Reynolds numbers (Aly *et al.*, 2009; Aly *et al.*, 2010a, b).

4.4.3 Spray pattern validation (gas-liquid two-phase flow)

Spray visualisation images combined with UV illumination as a function of atomisation air pressure are presented in Fig. 4.10. The effect of fluidisation air flow rate, varied within the interval outlined in Table 4.1, showed no observable difference in spray pattern. Regarding atomisation air pressure, higher air pressure not only resulted in a narrower spraying cone, but also resulted in a slightly asymmetric spraying cone, as shown in Fig. 4.10d. The asymmetry is likely due to the higher volume of expanding atomisation air (for $p_{at} = 3$ bar) in combination with the asymmetric construction of the reactor resulting from the one-sided nozzle support (at the right side of the nozzle, not shown in Fig. 4.10).

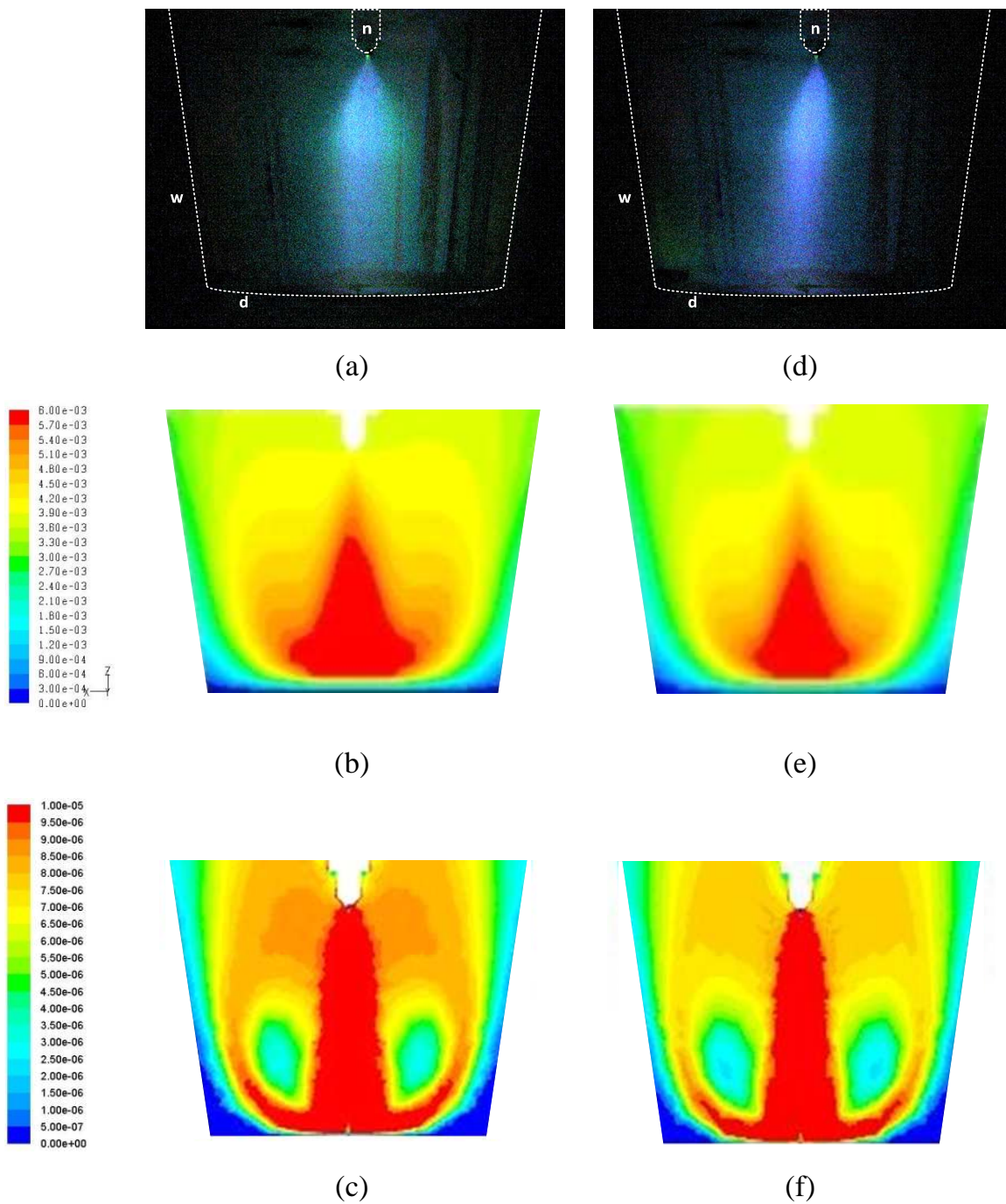


Figure 4.10 Comparison of the visualised spray pattern (a, d) with the gas-liquid DPM model-predicted mass fraction contours (b, e) and with the gas-liquid MFM-PBM model-predicted volume fraction contours (c, f). Results plotted for two atomisation air pressures: 1.0 bar (a-c) and 3.0 bar (d-e). Boundaries are indicated with ‘w’ for reactor walls, ‘d’ for air distributor and ‘n’ for nozzle.

When the experimental results are compared with the model-predicted spray patterns, a qualitative agreement is observed with the DPM or MFM-PBM predicted results. However, DPM gave better agreement compared to MFM-PBM including a wider spraying cone and much less deflection of the spray at the base of the reactor. As already stated in Section 4.4.2.2, as opposed to the MFM-PBM, the DPM can effectively account for droplet-wall collisions which correspond with the actual (experimental) process, where most of the droplets were seen to adhere onto the wire mesh air distributor at the base of the reactor.

4.4.4 Three-phase (gas-solid-liquid) model of droplet atomisation in the fluidised bed coater

4.4.4.1 Discrete phase model (gas-solid-liquid DPM)

Figure 4.11a shows the contour plot of the time-averaged steady-state voidage, taken over a simulated time period of 10s. The initial 5s of the simulated process were discarded to avoid the start-up fluidisation behaviour. As can be observed in Fig. 4.11a, in the central part of the conical vessel, the region under the nozzle is occupied by the hollow atomisation cone. In this zone, the solid particles have to be lifted by the fluidising air against the counterforce of the atomisation air resulting in an air void (see chapter 3), while a denser zone can be noticed in a radial area between the nozzle atomisation air cone and the reactor walls. It could be explained that particles move predominantly upwards in the centre to the above bed region (about 12 cm above the air distributor), then move radially towards the walls and downwards along the walls. This particle flow behaviour was confirmed by experimental results obtained by Positron Emission Particle Tracking (PEPT) (Depypere *et al.*, 2009). After moving downwards along the walls, in the bottom-bed region, re-circulating particles face an obstruction zone at the interface between spray cone and fluidising particles at the vessel centre, resulting from the

downwards pointing atomisation air cone (Depypere *et al.*, 2009), as shown in Fig. 4.12.

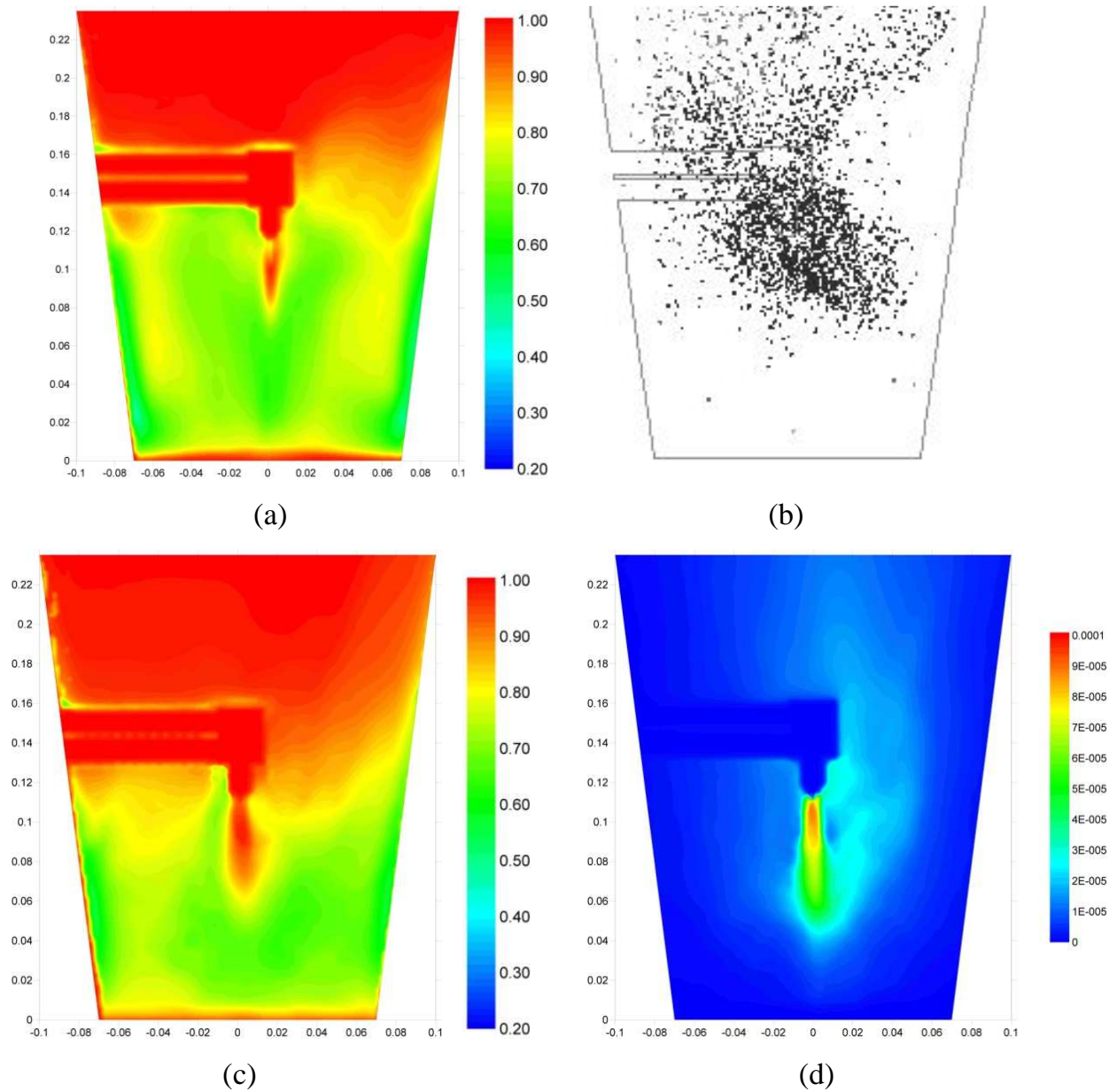


Figure 4.11 Comparison between (a) contour of gas-solid-liquid DPM model-predicted time-averaged steady-state voidage, (b) gas-solid-liquid DPM model-predicted droplet cloud at $t = 15$ s, (c) contour of gas-solid-liquid MFM-PBM model-predicted time-averaged steady-state voidage, (d) contour of gas-solid-liquid MFM-PBM model-predicted time-averaged steady-state liquid volume fraction.

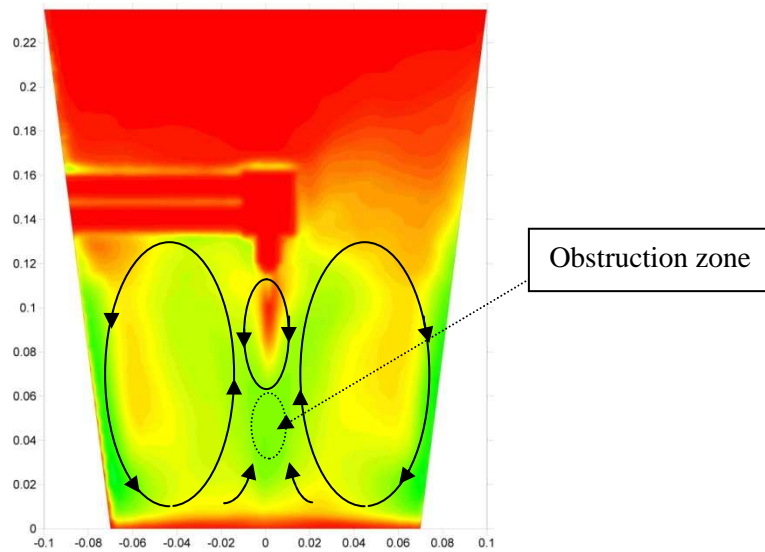


Figure 4.12 Schematic description of particle movements.

Fig. 4.11b, demonstrating the droplets tracked at 15s, confirms that the contacting between the droplets and the fluidising solids particles occurred at the central part of the vessel. The calculated droplet tracks revealed that droplets moved downwards along with the atomisation air cone until facing the counter-current fluidising solid particles. Considering the absence of phenomena including droplet evaporation and droplet/solids adhesion, the DPM algorithm continues to track the droplets until they exit the reactor at the top or impact one of the reactor geometry boundaries. In reality, the majority of the droplets adhere onto the fluidised particles, contributing to the layered growth of the coating wall around the individual core particles. Also, in an actual fluidised bed coating process, the majority – typically $\geq 70\%$ (Ronsse *et al.*, 2008) – of water in the coating solution is evaporated after the droplets have impacted the surface of the fluidised core particles. Only a minor fraction of the water is evaporated during droplet travel between the nozzle and the impacting particle surface. Consequently, there will be a minimal impact of the droplet size reduction as a result of droplet drying on the droplet dynamics (i.e. altered drag force, reduced droplet mass) and the resulting droplet trajectories.

4.4.4.2 Multi-fluid flow model combined with population balance model (gas-solid-liquid MFM-PBM)

Comparison between the gas-solid-liquid phase DPM and MFM-PBM model-predicted results is shown in Figure 4.11a-d. As can be seen in Fig. 4.11a and 4.11c, the model-predicted time-averaged steady-state voidage profiles of both models show a strong agreement. Also, when considering the model-predicted distribution of droplets within the fluidised bed (Figs. 4.11b and 4.11d), and specifically the penetration depth of the droplets in the bed, the MFM-PBM predicted results were consistent with those from the DPM predicted results.

4.5 Conclusions

As a powerful numerical tool for solving fluid flow problems, CFD was used to model the important hydrodynamic aspects of a fluidised bed coater, including the gas, liquid, and solid phases using two approaches: Eulerian-Lagrangian and combined Eulerian-Eulerian/population balance model. In the discrete phase model (DPM), the calibrated air-blast/air-assisted atomiser model was used as a suitable model for the two-fluid nozzle in the fluidised bed coating process in order to study the effects of process variables on spray flow and its mass distribution. It can be seen, in the gas-liquid DPM model, that the spray cone and liquid mass fraction changed with the variation of fluidisation air flow rate, atomisation air pressure and liquid feed rate. Furthermore, droplet atomisation was introduced in the fluidised bed using the DPM model (gas-solid-liquid model).

The population balance model combined with the Eulerian-Eulerian CFD model was also employed as an alternative approach to describe the two-fluid atomisation and the impact of process variables. The gas, droplets and solid particles were modelled by treating all phases as interpenetrating continua in the Eulerian framework, while the class population balance model was used to track the droplet diameter. The simulated results showed that even though this approach could be opted for instead of the DPM model to capture the two-fluid atomisation and interaction between phases, improvement of the population balance model such as more accurate breakage kernels (i.e. depending on Weber and Reynolds numbers) has to be carried out. When evolving from a gas-liquid to a gas-solid-liquid CFD model, consistency between the DPM and the population balance model in the Eulerian framework was shown to improve. Consequently the MFM-PBM approach was considered to be a viable alternative in the CFD modelling of gas-solid-liquid systems, including fluidised bed coaters.

Finally, given the absence of thermodynamics in the presented model, effects such as droplet evaporation could not be captured with the CFD model in its current state.

Chapter 5 **Conceptual study of heat and mass transfer in a fluidised bed coating process**

5.1 Introduction

In the previous chapters, all phases of the fluidised bed have been described and modelled using CFD. However, in order to describe the processes accurately, energy fluxes still need to be taken into account. Therefore, in this chapter, the energy equation will have to be introduced and energy exchanges between the phases will be studied. The same holds for the mass fluxes, mainly of water that can travel between the liquid and the gas phases, while in the liquid state it can contact the solids. The latter, however, is not in the scope of this PhD.

Up to date, many attempts have been made in order to describe heat and mass transfer in multiphase flow applications including liquid injection as shortly described in the following paragraphs.

Wang *et al.* (2004) described droplet evaporation, heat transfer due to droplet-solids collision and hydrodynamic interactions between phases by means of a hybrid Eulerian-Lagrangian model in a gas-solid suspension flow. The droplet flow field was captured by the Lagrangian method while the gas and solids flow fields were determined by the two-fluid Eulerian method. It was found that a layer of dense solids developed on the spray jet boundary, affecting the heat and mass transfer between the spray region and its surroundings. Werther and Bruhns (2004) developed a CFD model associated with submodels for heat and mass transfer considering the processes of liquid transport and evaporation in the vicinity of the point of injection to describe the injection of liquid reactants into fluidised bed reactors operating in the bubbling fluidised bed regime. Nayak *et al.* (2005) developed the Eulerian-Lagrangian CFD model to simulate droplet evaporation

resulting from heat transfer from solid particles in a gas-solid riser. This model related the evaporation rate of droplets to the rate of collisions of solid particles, specific heat capacities of solid and liquid, latent heat of vaporisation, relative velocity of gas and liquid and temperature of the three phases. Qureshi and Zhu (2006) simulated the gas-solid flow via an Eulerian two-fluid model, while tracking the spray via the Lagrangian trajectory approach describing the rapid spray evaporation. O'Rourke *et al.* (2009) presented a new model to simulate collisional transfer of mass, momentum and energy in gas-solid-liquid fluidised beds in a framework of the computational particle fluid dynamics numerical methodology. The model was capable of calculating spray injection and subsequent liquid spreading in gas-solid flows. Furthermore, the collisional liquid transfer model proposed by O'Rourke *et al.* (2009) was used by Zhao *et al.* (2009) in order to simulate liquid injection in dense-phase gas-solids fluidised beds. It was found from their work that with the use of the collision model taking into account liquid mass transfer, momentum exchange, and energy transfer between particles, the model predicted results were comparable to those of experiments. Behjat *et al.* (2010) developed a 3-D CFD model of a riser reactor to study hydrodynamics, heat transfer and evaporation of droplets into a gas-solid flow using an Eulerian-Lagrangian approach. It was found that not only the evaporating droplet caused higher local velocities of the gas and solid particles, but it also resulted in reduction of gas-solid flow temperature.

To complete the description of the fluidised bed coating process, developed in the previous chapters, heat transfer and droplet evaporation, which were until now disregarded, have to be taken into account. Consequently, the main objective of this work is to present a CFD model describing droplet evaporation and heat transfer in the fluidised bed coating process. However, collisions between the droplet and solid phase will not yet be included.

5.2 CFD model description

In this work, the movements of gas phase and solid phases were modelled in the Eulerian framework where the dispersed solid particles were treated as interpenetrating continua. The gas-solids flow fields and their interactions were obtained with the use of the general conservation equations, described before, while the discrete phase model was solved in a Lagrangian framework to simulate the spray pattern which was simulated by tracking the droplet trajectories by integrating the equation of droplet motion. The momentum exchange between liquid phase and continuous phases was considered via appropriate formulation of interphase coupling terms.

5.2.1 Heat transfer between gas and solid phases

In the Eulerian frame of reference, the conservation of energy is described using separate enthalpy equations for each phase with the assumption that the radiation component was negligible as a result of small temperature differences (Eriksson and Golriz, 2005):

Gas phase:

$$\frac{\partial}{\partial t}(\alpha_l \rho_l h_l) + \nabla \cdot (\alpha_l \rho_l \vec{v}_l h_l) = -\alpha_l \frac{\partial p_l}{\partial t} + \bar{\bar{\tau}}_l : \nabla \vec{v}_l - \nabla \cdot \vec{q}_l + \sum_{s=1, s \neq 1}^{N_s} Q_{ls} + Q_{ld} + \dot{m}_{ld} h_{ld} \quad (5.1)$$

Solid phase:

$$\begin{aligned} \frac{\partial}{\partial t}(\alpha_s \rho_s h_s) + \nabla \cdot (\alpha_s \rho_s \vec{v}_s h_s) = & -\alpha_s \frac{\partial p_s}{\partial t} + \bar{\bar{\tau}}_s : \nabla \vec{v}_s - \nabla \cdot \vec{q}_s + \sum_{s=1, s \neq 1}^{N_s} Q_{sl} \\ & + \sum_{s=1, s \neq m}^{N_s} Q_{sm} + \sum_{s=1}^{N_s} Q_{sd} \end{aligned} \quad (5.2)$$

where h_i is the specific enthalpy of phase i , Q_{ij} is the intensity of heat exchange between the i^{th} and the j^{th} phases, \dot{m}_{ij} is the mass flow rate transferred from the i^{th} phase to the j^{th} phase, and N_s is the number of solid phases. \vec{q}_i is the heat flux expressed by

$$q_i = -k'_i \nabla \cdot T_i \quad (5.3)$$

where k'_i is the thermal conductivity ($\text{Wm}^{-1}\text{K}^{-1}$) for the i^{th} phase.

The rate of energy transfer between phases, Q_{ij} , was assumed to be a function of the temperature difference

$$Q_{ij} = h_{c,ij} (T_i - T_j) \quad (5.4)$$

where $h_{c,ij}$ ($=h_{c,ji}$) is the heat transfer coefficient ($\text{kJ s}^{-1}\text{m}^{-2}\text{K}$) between the i^{th} phase and the j^{th} phase. Because the heat and mass transfer between solid phases and between a solid and the liquid phase were not taken into account, the last two terms in Eq. (5.2) were omitted. From Eq. (5.4) the heat transfer coefficient between the solid phase and the gas phase, $h_{c,sl}$ are related to the Nusselt number of the solid phase, Nu_s , by

$$h_{c,sl} = \frac{6k'_l \alpha_l \alpha_s Nu_s}{d_s^2} \quad (5.5)$$

where d_s is the solids diameter and k'_l is the thermal conductivity of the gas phase, whereas the Nusselt number can be determined from the correlation of Gunn (1978), applicable for a porosity of 0.35-1.0 and a Reynolds number of up to 10^5 :

$$Nu_s = (7 - 10\alpha_l + 5\alpha_l^2) \left(1 + 0.7 \text{Re}_s^2 \text{Pr}^{1/3}\right) + (1.33 - 2.4\alpha_l + 1.2\alpha_l^2) \text{Re}_s^{0.72} \text{Pr}^{1/3} \quad (5.6)$$

where Re_s is the relative Reynolds number based on the diameter of the solid phase and the relative velocity $|\vec{v}_l - \vec{v}_s|$, and Pr is the Prandtl number of the gas phase:

$$Pr = \frac{c_p \mu_l}{k'_l} \quad (5.7)$$

5.2.2 Heat and mass transfer models for the liquid phase

Two models corresponding to two different heat and mass transfer regimes (inert heating and vaporisation model) between discrete phase (droplet) and continuous phase (gas-solid), available in the CFD solver software, Ansys Fluent 12.0, were considered. The heat transfer from the gas phase to the droplet phase was computed by examining the change in thermal energy of a droplet as it passes through each control volume (Ansys Inc., 2009b).

5.2.2.1 Inert heating

For the liquid droplet, when its temperature is less than the vaporisation temperature, T_{vap} (K), of the droplet, which is a modelling parameter determining the onset of vaporisation, and/or when all the volatile mass of the drop is evaporated, the inert heating regime was considered. These conditions may be written as

$$T_d < T_{vap} \quad (5.8)$$

and

$$M_d \leq (1 - M_{v0})M_{d0} \quad (5.9)$$

where T_d (K) is the droplet temperature, M_{d0} is the initial mass of the droplet, M_d is its current mass and M_{v0} is the initial mass fraction of the volatile components.

When these conditions were satisfied, the following heat balance equation was used to relate the droplet temperature, T_d , to the convective heat transfer:

$$M_d c_d \frac{dT_d}{dt} = h_c A_d (T_l - T_d) \quad (5.10)$$

where c_d is the heat capacity of the droplet ($\text{J kg}^{-1}\text{K}^{-1}$), A_d the surface area of the droplet (m^2), T_l the local gas temperature (K), and h_c the heat transfer coefficient. In the case of a gas-liquid flow, the correlation of Ranz and Marshall (1952) can be used to calculate the heat transfer coefficient:

$$Nu = \frac{h_c d_d}{k'_l} = 2 + 0.6 Re_d^{1/2} Pr^{1/3} \quad (5.11)$$

Here Nu is the Nusselt number, d_d is the droplet diameter (m), k'_l is the thermal conductivity of gas ($\text{Wm}^{-1}\text{K}^{-1}$), Re_d is the relative Reynolds number and Pr is the Prandtl number.

5.2.2.2 Droplet vaporisation

When evaporation of liquid initiates, it is essential to consider the mass transfer as well as the heat transfer from the droplet surface. This regime of droplet vaporisation is initiated when the temperature of the droplet reaches the vaporisation temperature, T_{vap} (K), and continues until the droplet reaches the boiling point, T_{bp} (K), or until the droplet's volatile fraction is completely consumed:

$$T_d < T_{bp} \quad (5.12)$$

and

$$M_d > (1 - M_{v0})M_{d0} \quad (5.13)$$

The rate of vaporisation was modelled by relating the flux of droplet vapour into the gas phase to the difference of the vapour concentration between the droplet surface and the bulk gas as

$$N_i = K_C (C_{i,d} - C_{i,l}) \quad (5.14)$$

where N_i is the molar flux of vapour ($\text{mol m}^{-2}\text{s}^{-1}$), K_C the mass transfer coefficient (m s^{-1}), $C_{i,d}$ the vapour concentration at the droplet surface (mol m^{-3}) and $C_{i,l}$ the vapour concentration in the bulk gas (mol m^{-3}).

The concentration of vapour at the droplet surface was evaluated by assuming that the partial vapour pressure at the interface is equal to the saturated vapour pressure, p_{sat} , at the droplet temperature, T_d :

$$C_{i,d} = \frac{p_{sat,d}}{RT_d} \quad (5.15)$$

where R is the universal gas constant.

The concentration of vapour in the bulk gas was known from:

$$C_{i,l} = X_i \frac{p}{RT_l} \quad (5.16)$$

where X_i is the local bulk mole fraction of species i (water vapour in this case), p is the local absolute pressure, and T_l is the local bulk temperature in the gas. The mass transfer coefficient in Eq. (5.14) can be calculated from the Sherwood number correlation (Ranz and Marshall, 1952):

$$Sh = \frac{K_c d_d}{D_{l,m}} = 2.0 + 0.6 Re_d^{1/2} Sc^{1/3} \quad (5.17)$$

where $D_{l,m}$ denotes the diffusion coefficient of vapour in the bulk ($m^2 s^{-1}$) and d_d is the droplet diameter.

Sc is the Schmidt number expressed by

$$Sc = \frac{\mu_l}{\rho_l D_{l,m}} \quad (5.18)$$

To model heat transferred to the droplet, the droplet temperature is updated according to a heat balance relating the sensible heat change in the droplet to the convective and latent heat transfer between the droplet and the continuous phase with the assumption that radiative heat transfer to the droplet can be neglected for small temperature differences (Eriksson and Golriz, 2005):

$$M_d c_d \frac{dT_d}{dt} = h_c A_d (T_l - T_d) + \frac{dM_d}{dt} \lambda \quad (5.19)$$

Here λ denotes the latent heat ($J kg^{-1}$) and $\frac{dM_d}{dt}$ is the rate of evaporation ($kg s^{-1}$).

5.3 Numerical setup

Prior to the CFD calculations, the geometry of a laboratory-scale Glatt GPCG-1 fluidised bed coater (Glatt GmbH, Germany) together with a two-fluid nozzle (Schlick Model 970 S0) was defined and a 3-dimensional unstructured grid of tetrahedral-hexahedral cells, as shown in Fig. 5.1, was generated using Gambit 2.2.30 (Ansys Inc., Canonsburg, PA). In order to perform CFD simulations, the meshed geometry was imported into the solver, Ansys Fluent 12.0.

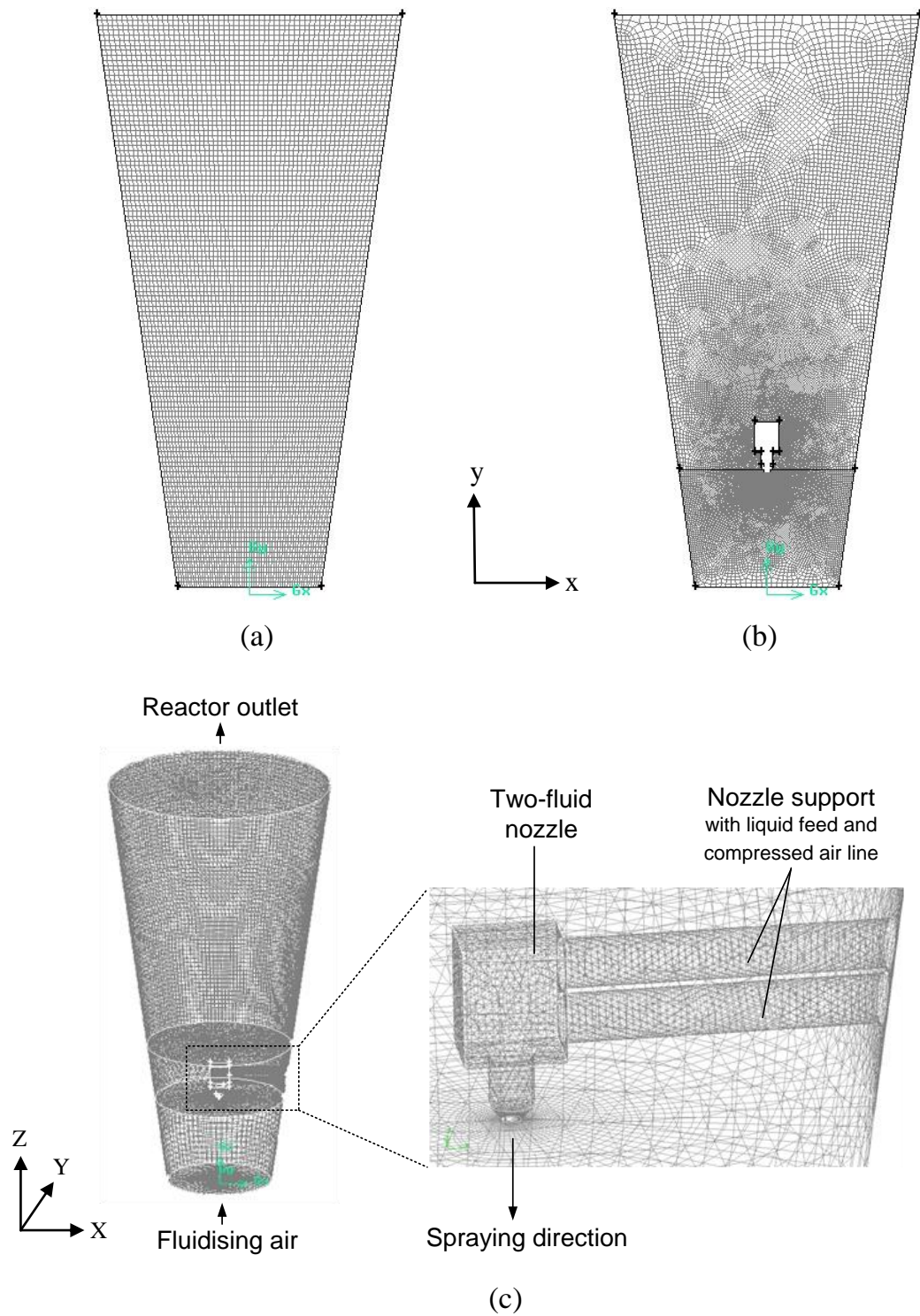


Figure 5.1 Meshed geometry of a conical reactor together with a two-fluid nozzle: (a) 2D without a nozzle, (b) 2D including the nozzle and (c) 3D including the nozzle.

Before solving, the boundary conditions, initial conditions and properties of all phases were specified. The fluidisation air inlet and the atomisation air from the two-fluid nozzle were modelled as a velocity inlet. In order to modify the reactor under-pressure, the air outlet was defined as a pressure outlet with radial pressure distribution and constant atmospheric pressure. At the walls, the no-slip boundary condition was applied for momentum equations.

CFD simulations were performed by means of the finite-volume code, Ansys Fluent 12.0, using a single-precision, unsteady-state and first order implicit solver, in order to model the fluidised bed in which three phases (gas, solid particles, droplets) were involved. To study the impacts of spray injection on the performance of the fluidised bed coater, the CFD model included all three phases and their interactions. For the solution of the gas/solids flow, a multiphase flow Eulerian model was applied to solve conservation equations of mass, momentum and energy. This approach treats each phase separately, and the coupling between phases was achieved through the drag force, heat transfer coefficient and mass source term, due to droplet evaporation. The momentum exchange coefficient (drag coefficient) was calculated using the modified Gidaspow model in which the drag model proposed by Gidaspow (1994) was modified in order to avoid the discontinuity of the drag function found at voidage of 0.8 (cfr. supra). The heat transfer coefficient was used to calculate the heat exchange between gas and solid phases with the use of the Gunn (1978) correlation, whereas heat transfers between solid and liquid phases and between solid phases were not taken into account in this work.

To avoid expensive time consumption for reaching the steady state (T_{ss}) starting from the initial condition, a method to accelerate the calculation of solid temperature in order to reach the steady-state point was taken into consideration. In this work, the initial solid temperature (T_0) was first specified as the inlet fluidisation air temperature instead of ambient temperature. From this point, the

solid temperature decreased constantly resulting from heat losses, meaning that the steady-state solid temperature was lower than the set-point value. Subsequently, the solid temperature was initiated with a lower value (T_1). If the solid temperature increased, the steady state point was examined at which the solid temperature was intermediate between higher and lower set point. This procedure was repeated until the solid temperature was almost constant. The steady-state acceleration method is outlined in Fig. 5.2.

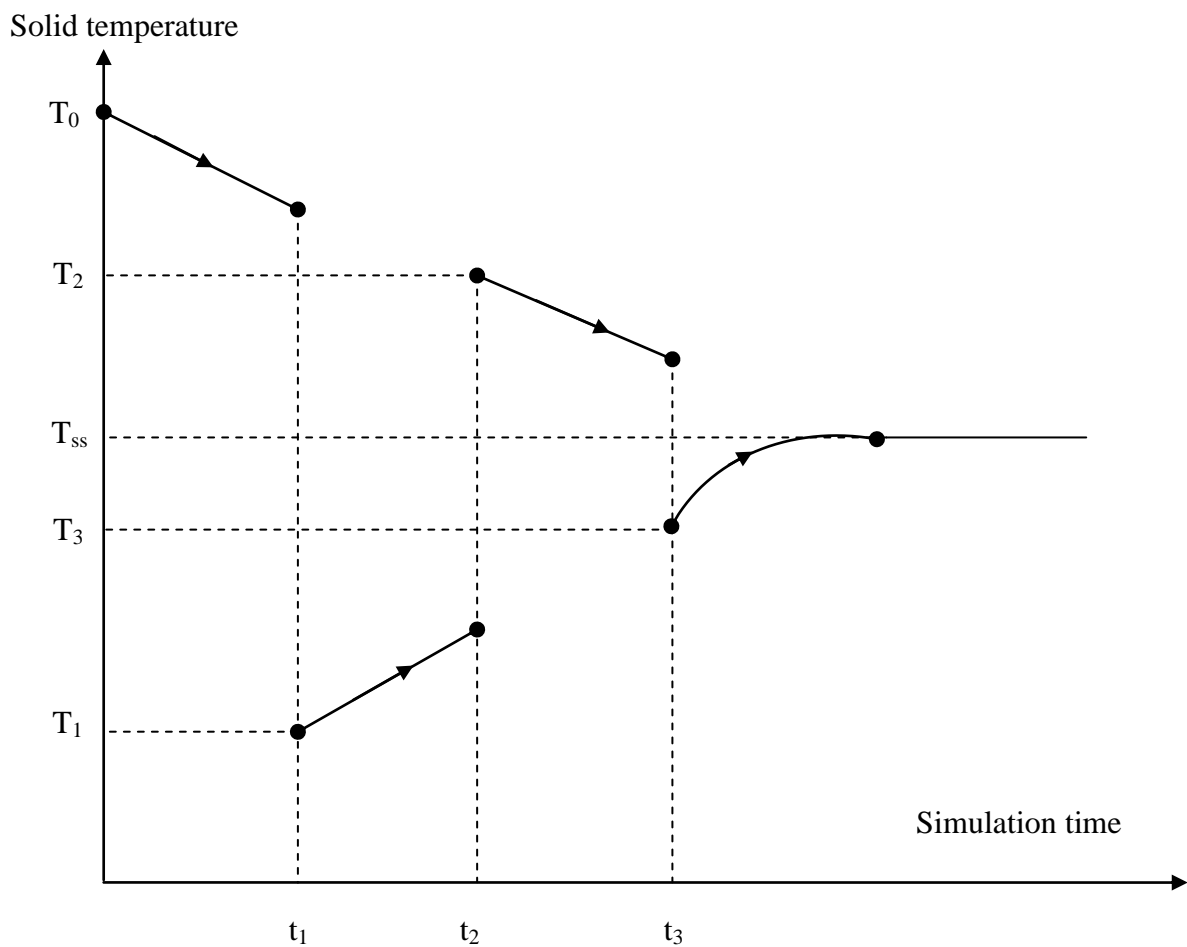


Figure 5.2 Procedure used to accelerate the calculation of solid temperature.

5.4 Simulation circumstances and validation

The four-phase Eulerian CFD model, using a single gas phase as the primary continuous phase and three separate solid phases with different particle sizes for each phase (cfr supra), was again employed to account for the polydispersity of solids used in the experimental validation. Furthermore, as discussed in chapter 3, not only the effect of the significantly different sized particles could be taken into account, but the adjustment in superficial air velocity boundary condition was also considered in the simulation in order to satisfactorily match the experimental data. Therefore, in this work, the adjusted fluidisation air flow rate (10% increased) was specified as an inlet boundary condition.

In this chapter, the numerical methods were categorised into four sections to study:

- expanded bed heights by means of near-wall gas temperature, compared to those obtained experimentally by static pressure and visual measurement (excluding the atomisation air)
- impact of atomisation air pressure on average bed temperature
- droplet evaporation in a gas flow field
- droplet evaporation in a gas-solids fluidised bed flow.

5.4.1 Expanded bed height determination

Two CFD simulations with different process variables were performed using a 2D meshed geometry (Fig. 5.1(a)) until steady-state behaviour was reached. In accordance with the measured expanded bed heights (Depypere, 2005; Depypere *et al*, 2005), 1 kg and 2 kg sucrose/starch beads, namely “non-pareils”, were used as solid phase materials fluidised at low fluidisation air flow rate ($40.3 \text{ m}^3\text{h}^{-1}$) and at high fluidisation air flow rate ($66.2 \text{ m}^3\text{h}^{-1}$), respectively, with the absence of atomisation air. In the models, the particle sizes used in each solid phase of the 4-

phase model were specified as 200 μm (20%), 355 μm (60%) and 510 μm (20%) (cfr. supra). The initial bed heights (static bed) were 7 cm and 12.6 cm for 1 kg and 2 kg of non pareils, respectively. The inlet air temperature was set to 50°C.

5.4.2 Effect of atomisation air pressure on average bed temperature

The atomisation air (excluding liquid injection) was supplied to the fluidised bed in order to study the impact of atomisation air pressure on bed temperature. In this section, 1 kg of glass beads were used for the solid phases with particle sizes of 135 μm (20%), 185 μm (60%) and 235 μm (20%). The remaining initial conditions, material properties and simulation parameters of section 5.4.1 and 5.4.2 are summarised in Table 5.1.

Table 5.1 Initial conditions, material properties and simulation parameters.

Boundary conditions and simulation parameters	circumstances	
	Temperature validation	Effect of atomisation air pressure
Primary phase	Gas	Gas
Secondary phase	Non-pareils	Glass beads
Mean solids particle size, d_{32} , μm	345 ^a	197 ^a
Solids particle density, kg m^{-3}	1459 ^a	2467 ^a
Solids particle loading, kg	1, 2	1
Gas density, kg m^{-3}	1.225	1.225
Fluidisation air flow rate, m^3hr^{-1}	40.3 ^b , 66.2 ^b	76
Atomisation air flow rate, m^3hr^{-1} corresponding to 2 and 4 bar	-	5.52, 7.64
Ambient temperature, °C	16.5	20

(^a) obtained by Depypere (2005), (^b) used for validation (Depyper, 2005; Depypere *et al.*, 2005).

5.4.3 Droplet evaporation

Not only temperature distribution affects the efficiency of the fluidised bed coating process, but humidity profiles also play an important role in the system. It is difficult to obtain detailed experimental insight into how these variables are distributed throughout the bed. Therefore, in addition to modelling heat transfer between gas and solid phases with and without the atomisation air in section 5.4.1 and 5.4.2, respectively, droplet evaporation without the presence of the fluidised bed was modelled by means of a Lagrangian approach in this section. The steady-state, single-precision, first order implicit solver was employed in order to solve a set of governing equations describing the droplet trajectories, heat transfer, vaporisation and interaction with the gas phase. In this section, water at 20°C was sprayed through the two-fluid nozzle with variation of water feed rates. Furthermore, various simulations were performed using the discrete phase model to study the influence of fluidisation air flow rate, atomisation air pressure and inlet air temperature on relative humidity and air temperature at the outlet of reactor.

5.4.4 Heat transfer in the fluidised bed coater with the inclusion of all phases

In this section, liquid injection was introduced through the two-fluid nozzle into the gas-solid flow in order to study the droplet evaporation in the fluidised bed coater. In order to study the impact of spray injection, the CFD model included all phases: gas, solid particles and droplets, and their interactions. Conservation equations of mass, momentum and energy were solved using the Eulerian framework, while the feed droplet flow and its evaporation were described by means of the Lagrangian approach. The single-precision, unsteady-state, first order implicit solver was employed to perform a case study of a CFD simulation for all phases involved in the process of fluidised bed coating.

As the major objective of this work, to investigate the heat and mass transfer in the system of fluidised bed coating including all phases (gas, solids and liquid), droplet evaporation was modelled together with gas-solid interaction using the overall CFD model. However, apart from difficulties in accurately simulating gas-solids flows, evaporation of injected droplets and subsequent agglomeration or layered growth mechanisms in the fluidised bed coating process is extremely demanding. Consequently, in this conceptual study of heat transfer in three-phase systems, the droplet collision and adhesion on solids particles resulting in particle growth mechanisms were not taken into account.

The bed or core material consisted of glass beads with a volume weighted averaged diameter of 365 μm (Sovitec Micropearl®) of which 0.75 kg were fluidised in the Glatt GPCG-1 fluidised bed coater. The particle sizes used in each solid phase of the 4-phase model were specified as 230 μm (20%), 330 μm (60%) and 430 μm (20%). The static bed height of 5.6 cm was determined from the geometry of the reactor, the bulk density of the glass beads and the total mass of glass beads initially in the bed. The bed material was initially assumed according to a procedure of accelerating the calculation of solid temperature (see section 5.3). The inlet fluidising air was specified at 50°C with a constant gas velocity corresponding to a mass flow rate of $9.38 \times 10^{-3} \text{ kg s}^{-1}$. Water at 20.7°C was used as the spraying liquid which was atomised into the bed by means of the two-fluid nozzle with a mass flow rate of 5.52 g min^{-1} , while the atomisation air pressure was specified as 2.5 bar. The heat transfer across the walls was supposed to be mainly governed by convection, although wall conduction (stainless steel AISI 304, 2.5 mm thickness, Depypere *et al.*, 2004) was also considered. An external free stream temperature of 20.7 °C was specified and the surface heat transfer coefficient was estimated from calculation of the Nusselt number (for free convection) to be $3.5 \text{ W m}^{-2}\text{K}^{-1}$ (Incropera and DeWit, 2002).

5.4.5 Experimental validation

The experimental results of the expanded bed heights obtained by Depypere *et al.* (2005) and the outlet air temperature obtained by Ronsse (2006) were used for validation.

5.4.5.1 Expanded bed height determination (Depypere *et al.*, 2005)

In order to validate the model-predicted expanded bed heights (section 5.4.1), the experimental results obtained by Depypere *et al.* (2005), were used. In that work, the experiments were carried out in the laboratory-scale Glatt GPCG-1 (Glatt GmbH, Germany) fluidised bed coater with a transparent polycarbonate insert in order to measure the expanded-bed heights by means of visual bed height determination, the static pressure method and the temperature method. Details concerning these experiments (Depypere *et al.*, 2005) are briefly described as follows:

- Visual method* - The expanded bed heights at different fluidisation conditions were measured visually by means of a digital camera.
- Pressure method* - Static pressures were measured along the tapered wall at regular intervals of 0.02m starting 0.02m above the air distributor. The expanded bed height was determined as the intersection of the second order polynomial pressure curve in the powder bed and the constant pressure line.
- Temperature method* - At the same heights used in the pressure method, wall temperatures were measured using K-type adhesive thermocouples.

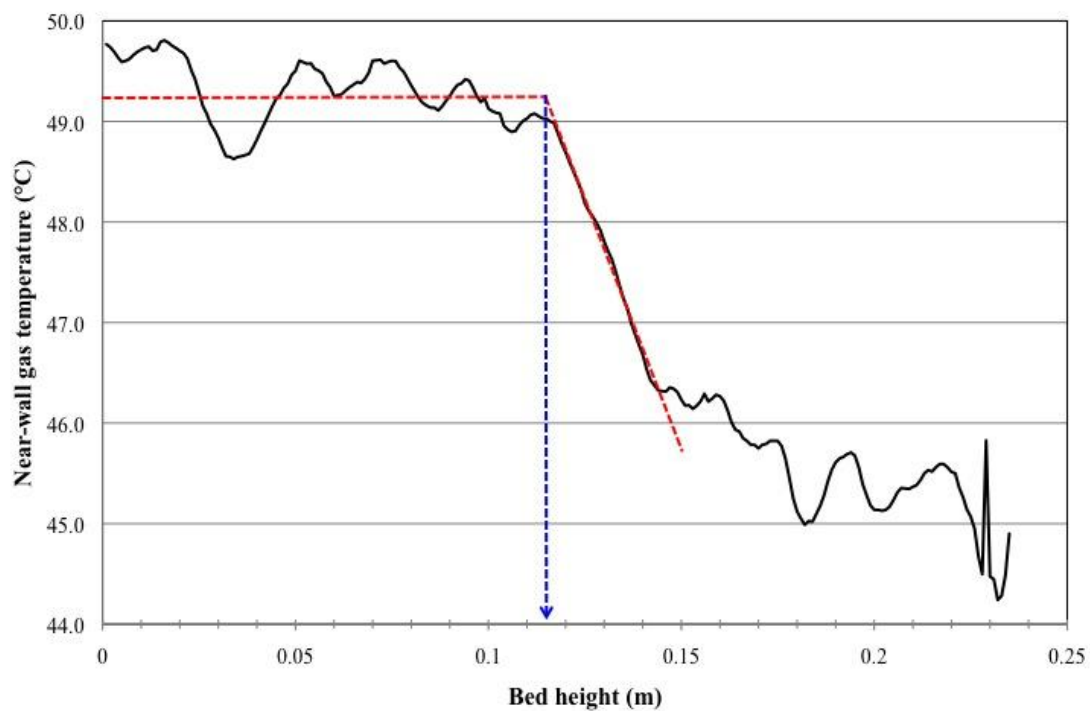
5.4.5.2 Outlet air temperature measurement (Ronsse, 2006)

The outlet air temperature for the operating conditions as described in section 5.4.4 was used for model validation. The air temperature was measured at the outlet of the Glatt GPCG-1 fluidised bed coater, with the AISI 304 stainless steel insert, by means of a stainless steel sheathed T-type thermocouple.

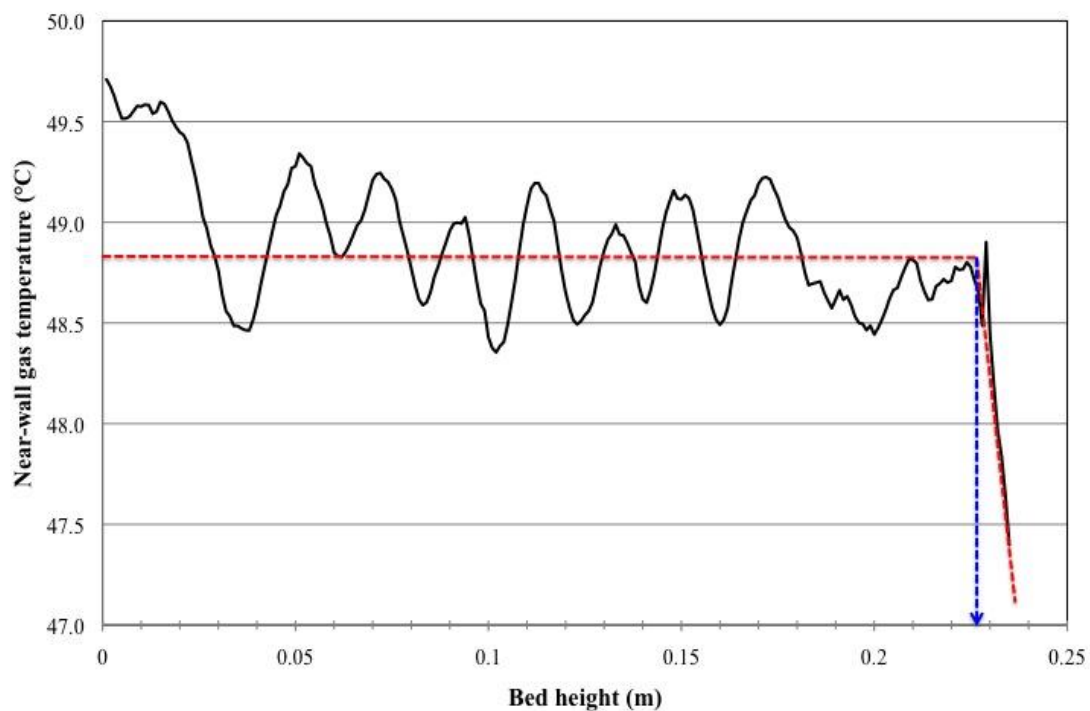
5.5. Results and discussion

5.5.1 Expanded bed height

In the experiments of Depypere *et al.* (2005), the expanded bed heights were experimentally determined by means of visual bed height determination, static pressure measurement and wall temperature measurement. In the present work, time-averaged near-wall gas temperatures were determined as a function of height above the air distributor for different operating conditions. Fig. 5.3 shows temperature profiles predicted using the CFD models with the operating conditions of 1 kg of non-pareils at low fluidisation air flow rate ($40.3 \text{ m}^3\text{h}^{-1}$) and 2 kg of non-pareils at high fluidisation air flow rate ($66.2 \text{ m}^3\text{h}^{-1}$).



(a)



(b)

Figure 5.3 Simulated near-wall gas temperature at: (a) low fluidisation air flow rate (1 kg of non-pareils) and (b) high fluidisation air flow rate (2 kg of non-pareils).

Figure 5.3 also illustrates the determination of the expanded bed height by means of the near-wall gas temperature for both operating conditions. The expanded bed height was determined as the intersection of the isothermal profile in the bed and the linear temperature decrease above the bed. It can be seen from Fig. 5.3 that for both cases, the gas temperature adjacent to the wall decreased rapidly at the height just above the air distributor (~4 cm above the air distributor). In this region, the hot fluidising air rapidly transfers heat to the bed resulting in a decrease in near-wall gas temperature. Above this height, well-mixed fluidisation causes the isothermal conditions, as can be seen in Fig. 5.3 by the constant temperature for 4 to 11 cm and for 4 to 22 cm for low and high fluidisation air flow rate, respectively. From Fig. 5.3, it can be concluded that the expanded bed heights obtained by CFD models using the intersection of a horizontal and an inclined regression line were approximately 11.5 cm and 22.6 cm at low and high fluidisation air flow rate, respectively, which are in a good agreement with results (11.5 cm and 20.0 cm, respectively) obtained by means of the visual method, (Depyper, 2005; Depypere *et al.*, 2005).

Furthermore, the static pressures from CFD simulations together with experimental results were plotted as a function of height above the air distributor, as shown in Fig. 5.4. It can be observed from this figure that the static gauge pressure in the fluidised bed as a function of height above the air distributor could be accurately described by a second order polynomial relationship. From the graphical representation of the gauge static pressure as a function of column height, the expanded bed height was determined as the intersection of a second order polynomial regression line and the constant pressure line.

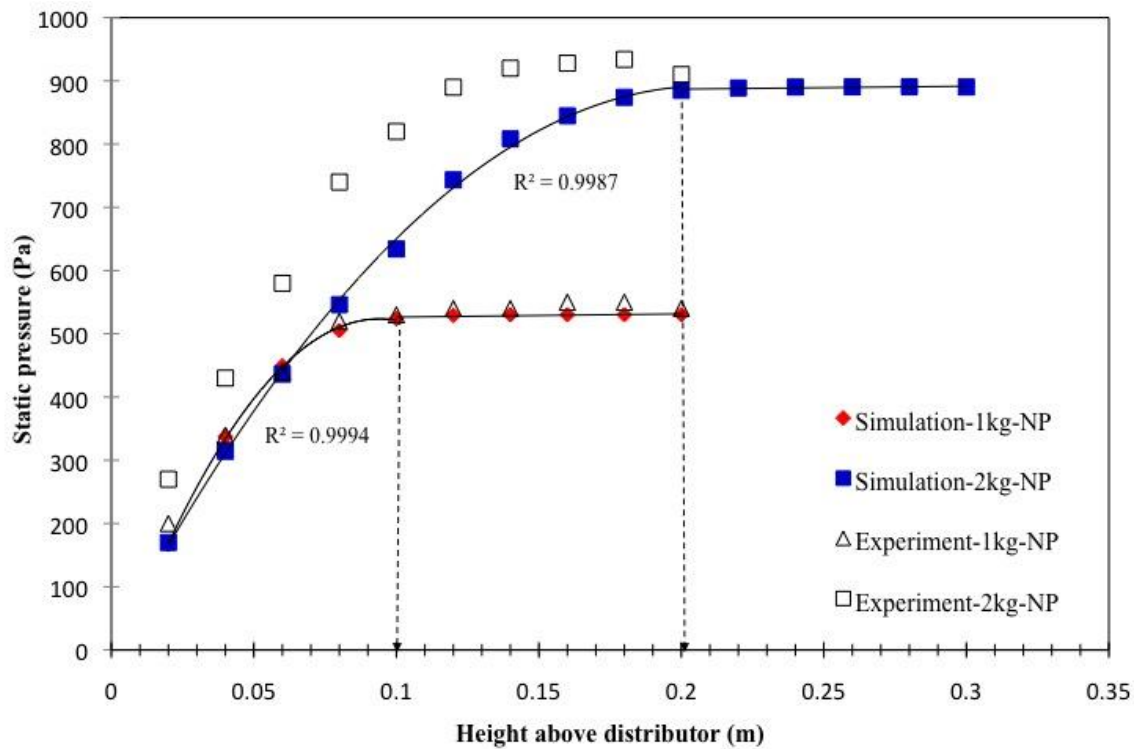


Figure 5.4 Comparison of model-predicted and experimental static pressure profiles as a function of the height above the air distributor.

To determine the intersection point, the pressure line was split into two lines: the second order polynomial line and the horizontal line. The point up to which the second order polynomial line has the maximum R^2 was considered the intersection point. Based on this analysis, for 1 kg of non-pareils fluidised at low flow rate and 2 kg of non-pareils fluidised at high flow rate, the expanded bed heights estimated using CFD simulations were 10.1 cm and 20.2 cm, respectively. Table 5.2 presents the comparison of the expanded bed heights using the different methods.

Table 5.2 Comparison of expanded bed heights between those obtained by CFD simulations and different experiments (Depypere *et al.*, 2005).

	Pressure method (cm)		Temperature method (cm)		Visual method (cm) (Depypere <i>et al.</i> , 2005)
	Exp. (Depypere <i>et al.</i> , 2005)	Sim.	Exp. (Depypere <i>et al.</i> , 2005)	Sim.	
1 kg	9.1	10.1	11.5	11.5	9.0±1.0
2kg	14.2	20.2	20.0	22.6	20.5±5.4

From the comparison of the expanded bed heights determined by different experimental methods with those obtained by the CFD model, as shown in Table 5.2, it was found that the simulated bed heights, determined using both the static pressure method and the temperature method, were in good agreement with experimental results using the visual method. However, when compared with the experimental results (14.2 cm) obtained by the pressure method, the model-predicted expanded bed height (20.2 cm) was over-estimated.

5.5.2 Effect of atomisation air pressure on bed temperature

In this section, the impact of atomisation air was described using the pressures of 2 and 4 bar (corresponding to $5.52 \text{ m}^3\text{hr}^{-1}$ and $7.64 \text{ m}^3\text{hr}^{-1}$, respectively) with an ambient temperature of 20°C , whereas fluidisation air flow rate and inlet fluidisation air temperature were kept constant at $76 \text{ m}^3\text{h}^{-1}$ and 60°C , respectively.

Fig. 5.5 demonstrates the simulated temperature contour plots of gas and solid phases at different atomisation air pressures. As found in this figure, solid temperature was high just above the air distributor, resulting from the rapid heat transfer from the hot fluidising air, as shown in the temperature contour plots of the gas phase in Figs. 5.5 (a) and (c) at 2 bar and 4 bar, respectively. It can also be

concluded from Fig. 5.5 that the additional volume of air released by the two-fluid nozzle resulted in a decrease in bed temperature, especially in the region near the nozzle, for both atomisation pressures. Furthermore, it can be concluded from Figure 5.5 that the bed temperature decreased with the increase of atomisation air pressure, resulting from the mixing of the process air with larger volumes of atomisation air.

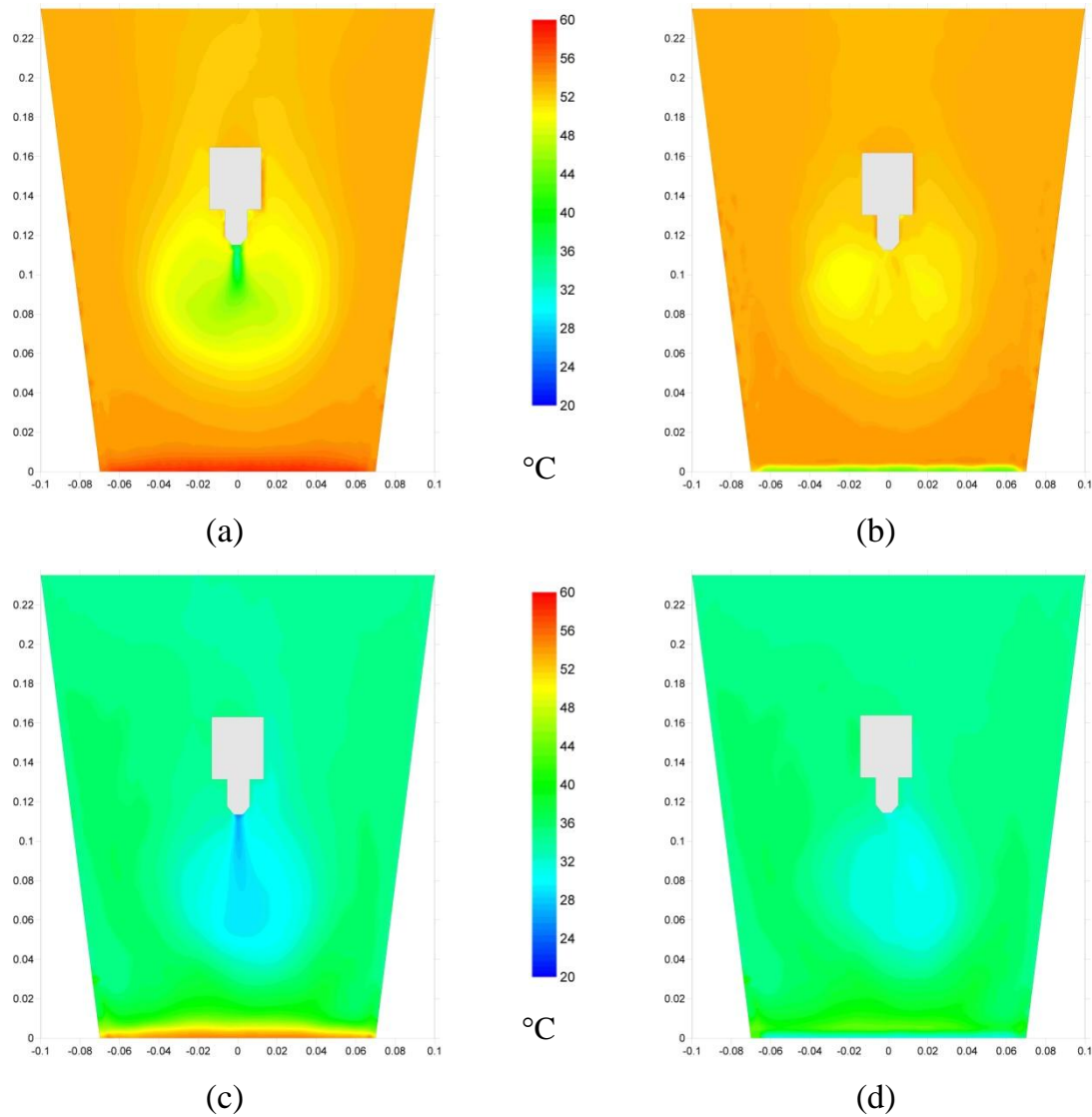


Figure 5.5 Model-predicted temperature contour plots of gas phase and solid phase at different atomisation air pressures: (a) gas at 2 bar, (b) solids at 2 bar, (c) gas at 4 bar and (d) solids at 4 bar. (coordinates in m)

5.5.3 Droplet evaporation

In this section, droplet evaporation in an empty reactor was modelled by means of the discrete phase model. Fluidisation air velocity, atomisation air pressure, inlet air temperature and liquid feed rate were varied to clarify their impact on the air temperature and relative humidity at the reactor outlet.

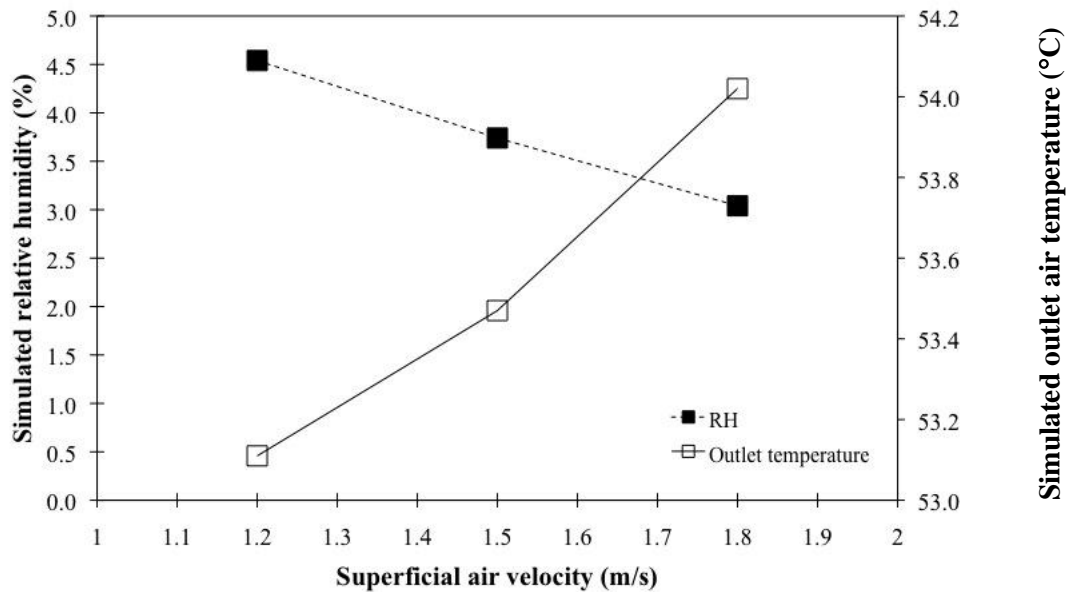


Figure 5.6 Model-predicted air relative humidity and temperature at the outlet of the reactor for different fluidisation air velocities.

To better understand the impact of fluidisation air velocity or flow rate, a series of simulations were performed with a variation of air velocity, ranging from 1.2 to 1.8 ms^{-1} . The model-predicted relative air humidity and temperature at the outlet were plotted as a function of fluidisation air velocity, as shown in Fig.5.6. It is clear that the outlet air temperature slightly increased when the fluidisation air velocity was higher, whereas the relative air humidity decreased.

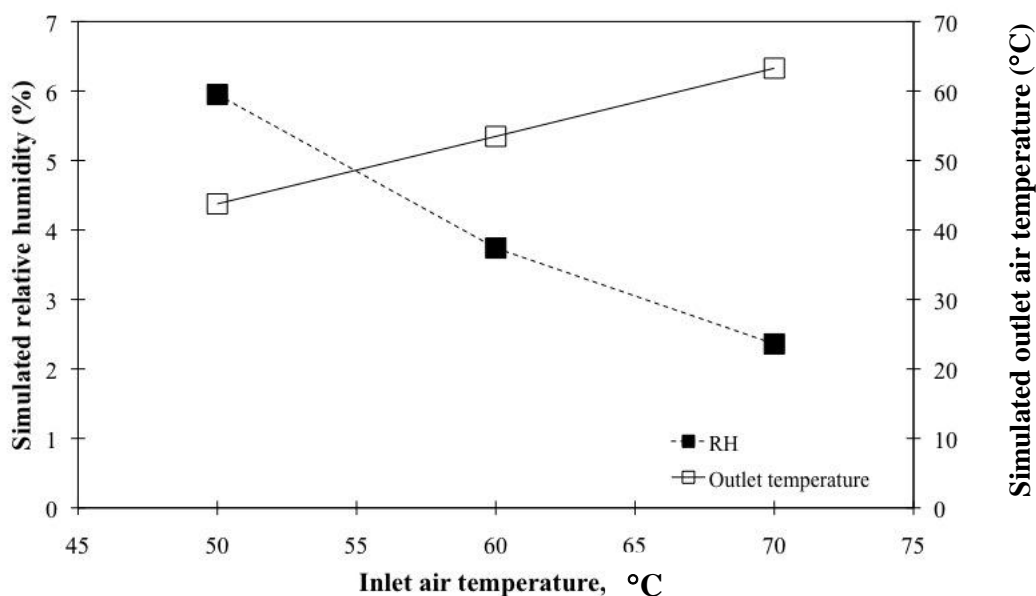


Figure 5.7 Model-predicted air relative humidity and temperature at the outlet of the reactor for different inlet air temperatures.

Figure 5.7 demonstrates the model-predicted relative humidity and temperature of the outlet air with inlet air temperatures varying from 50°C to 70°C. While all other variables were kept constant, the air temperature at the outlet was higher with increasing inlet air temperature. In contrast, the relative humidity at the outlet decreased when the inlet air temperature was higher. This effect can be explained by the drying kinetics of the sprayed liquid in the hot fluidising air. Additionally, simulations were performed with a liquid feed rate ranging from $0.5 \times 10^{-4} \text{ kg s}^{-1}$ to $1.5 \times 10^{-4} \text{ kg s}^{-1}$ in order to assess the effect of this variable on outlet air thermodynamics. As can be seen in Fig. 5.8, an increase in relative air humidity and a decrease in outlet air temperature were found when using higher liquid feed rate. This is to be explained by the higher amount of liquid spray with increasing the feed rate, as seen in Fig. 5.9, resulting in higher droplet evaporation.

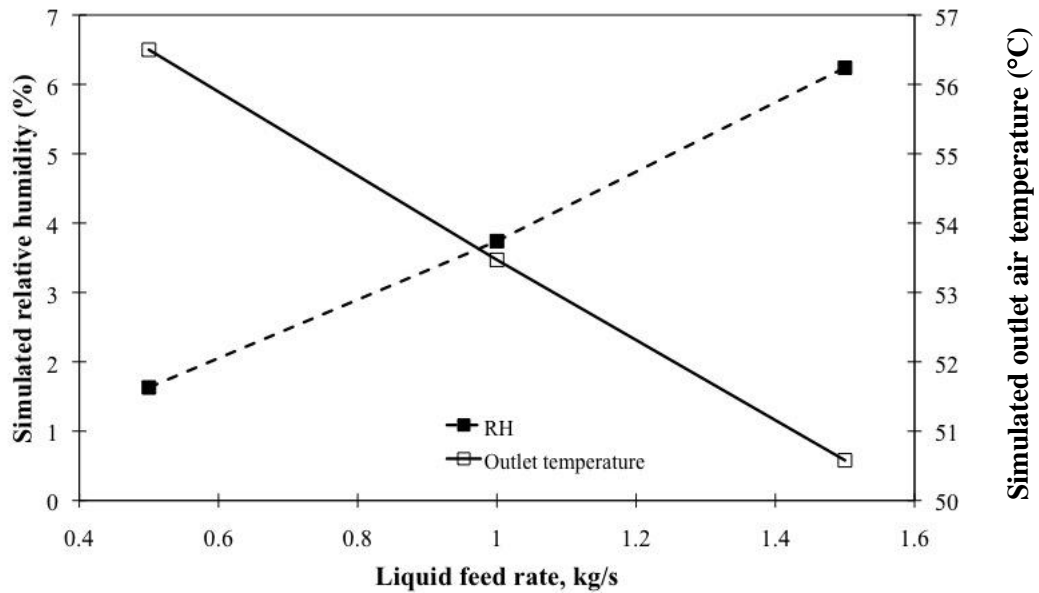


Figure 5.8 Model-predicted air relative humidity and temperature at the outlet of the reactor at different liquid feed rates.

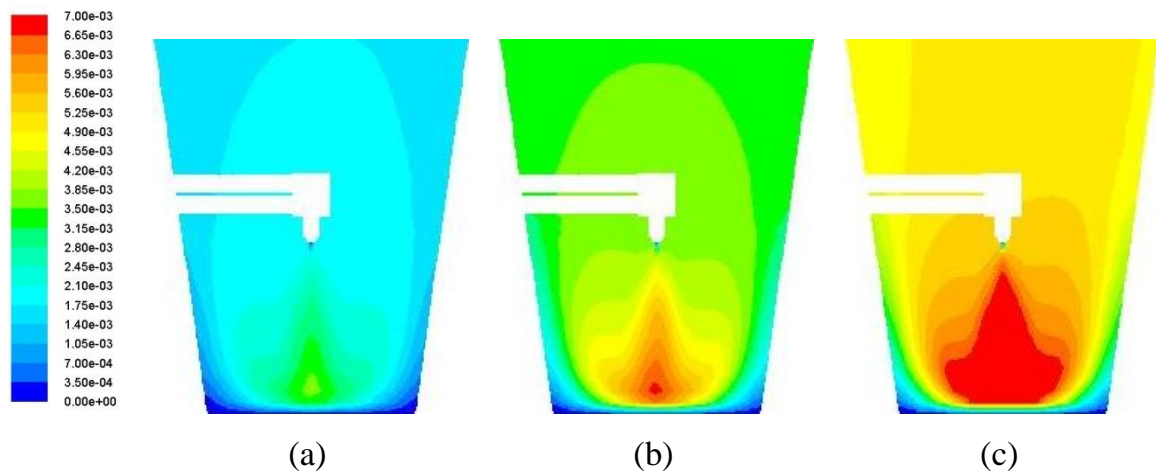


Figure 5.9 Simulated contour plots of liquid mass fraction ($\text{kg}_{\text{water}}/\text{kg}_{\text{mixture}}$) at: (a) $0.5 \times 10^{-4} \text{ kg s}^{-1}$, (b) $1.0 \times 10^{-4} \text{ kg s}^{-1}$ and (c) $1.5 \times 10^{-4} \text{ kg s}^{-1}$

To study the effect of atomisation air pressure on outlet air conditions, a series of simulations was performed with an atomisation air pressure ranging between 2 bar and 4 bar. All other variables were kept unchanged. Figure 5.10 illustrates the simulated air temperature and relative air humidity at the outlet at different atomisation air pressures. As can be seen from this figure, the relative air humidity slightly increased when the atomisation air was supplied at higher pressure, while

the outlet air temperature slightly decreased. The explanation is that the colder atomisation air, resulting from higher pressure, cools the air in the reactor.

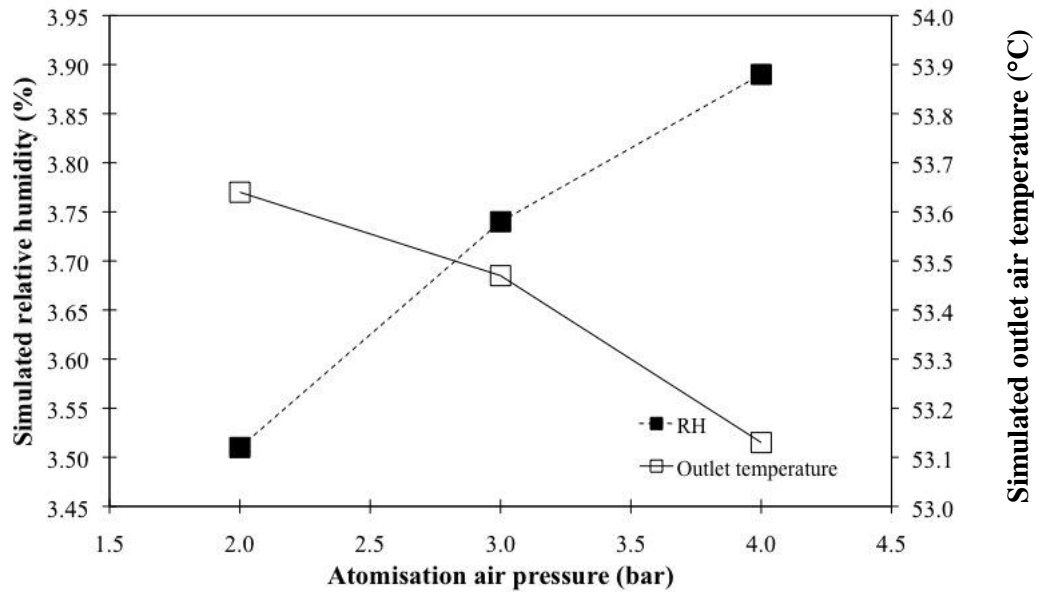


Figure 5.10 Model-predicted air relative humidity and temperature at the outlet of the reactor at different atomisation air pressures.

As expected it can be concluded from Figs. 5.6-5.8 and 5.10 that the outlet air temperature reacted inversely to the relative air humidity. This was also the case for the absolute humidity, as illustrated in Fig. 5.11.

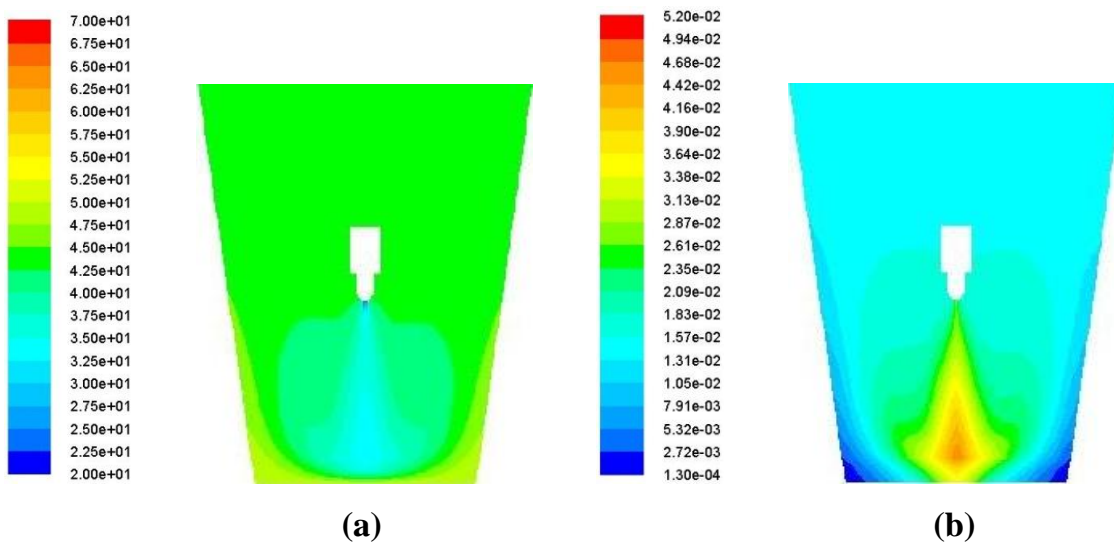


Figure 5.11 Simulated contour plots of (a) air temperature, °C and (b) absolute humidity, $\text{kg}_{\text{water}}/\text{m}^3_{\text{air}}$.

5.5.4 Results of droplet evaporation with the inclusion of a gas-solid fluidised bed

First, the time-averaged model-predicted voidage, taken for 10s after disregarding start-up behaviour of fluidisation, was illustrated in order to examine the bed in the conical fluidised bed vessel. As can be observed in Fig. 5.12, the voidage obtained by the model-prediction was consistent with the results described in chapter 2 and 3.

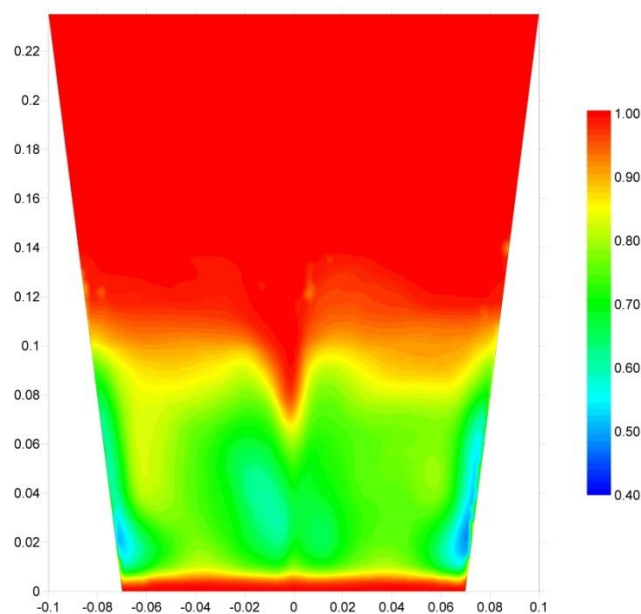


Figure 5.12 Time-averaged voidage contour plot from model prediction (coordinates in m)

Furthermore, the model-predicted temperature of gas and solids phases and absolute humidity (H_{abs}) averaged over a simulated time period of 10s after reaching heat transfer equilibrium (described in section 5.3) were plotted to demonstrate their distributions throughout the fluidised bed vessel, as shown in Figs. 5.13(a, b) and 5.14(a, b), respectively. The air and solid temperature contour plots ($^{\circ}\text{C}$), as shown in Fig. 5.13, revealed the existence of a low temperature region near the binary nozzle partly covering the top part of the bed. In this region, the temperatures of gas and solid phases were approximately $26\text{--}29^{\circ}\text{C}$ below the fluidisation inlet air temperature, with the lower air temperatures found right below

the nozzle, resulting from evaporation of the droplets. Away from the centre of this area, air temperature rose, leading to close isotherms corresponding to high temperature gradients. In the outer part of this region, isotherms were further away from one another delimiting a region where air temperature was high and almost constant, extending to the reactor wall. In Fig. 5.13, an important gradient was observed in the bottom part of the bed, situated just above the air distributor. In this narrow region, the particles coming down from the upper part of the bed absorbed heat from the entering hot air, resulting in rapid heat exchange described by the change in air temperature at the bottom of the bed.

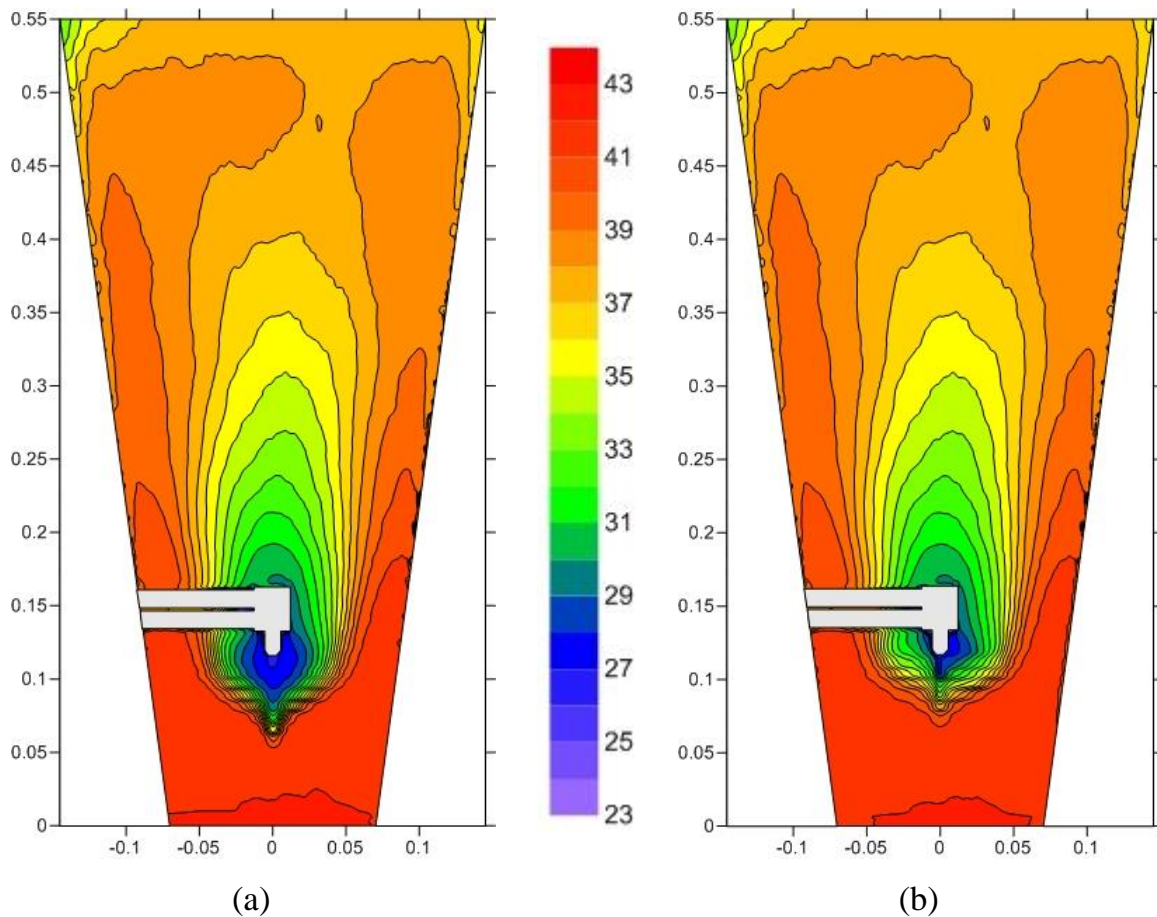


Figure 5.13 Time-averaged contour plots of (a) air temperature ($^{\circ}\text{C}$) and (b) solid temperature ($^{\circ}\text{C}$) from model prediction. (coordinates in m)

In addition, the absolute humidity predicted by the CFD model was demonstrated in Fig. 5.14, coloured by H_{abs} ranging from 0 to 20 g m^{-3} . From this figure, it can be seen that the high humidity region covers the top part of the bed near the nozzle, closely following the low air temperature region. According to the air temperature profiles (Fig. 5.13), this region has a shape resembling the one formed by the corresponding low air temperature region.

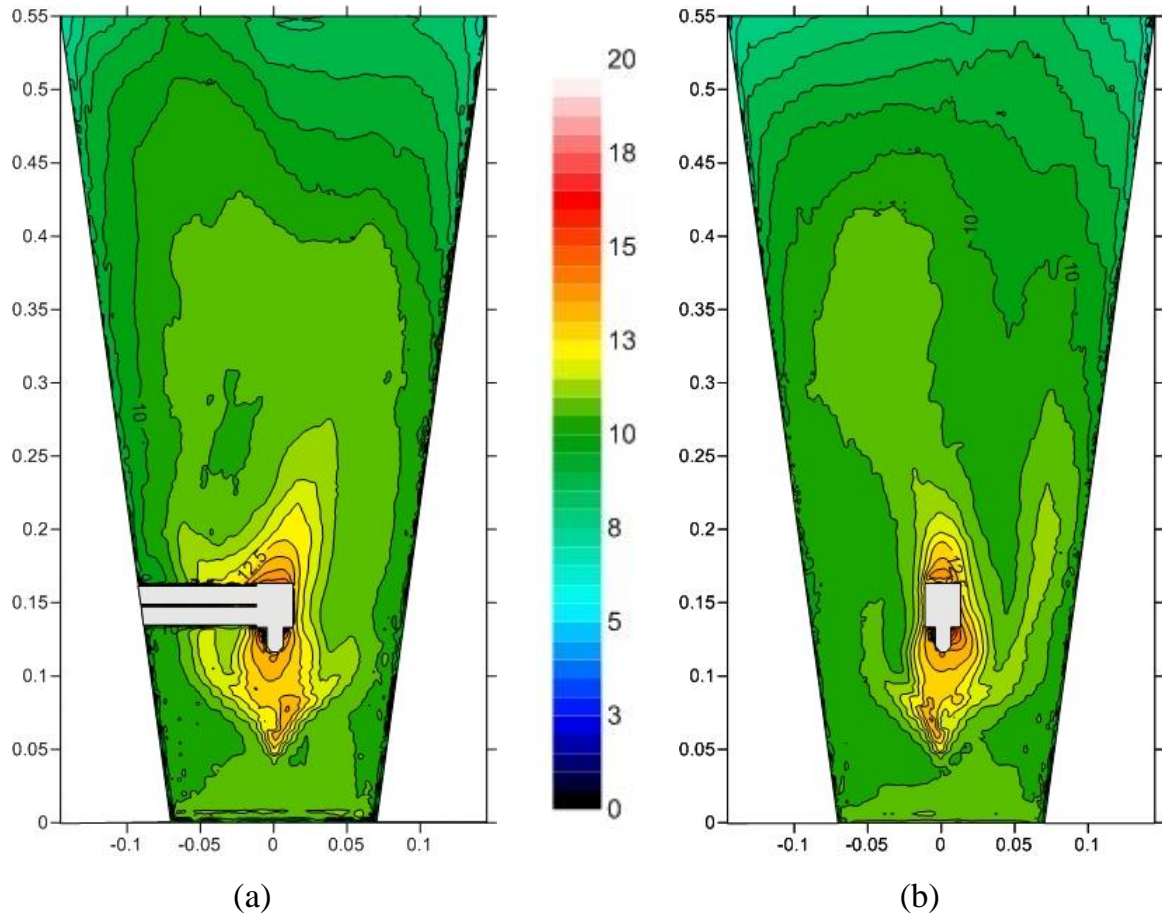


Figure 5.14 Time-averaged contour plots of absolute humidity (g m^{-3}) from model prediction in: (a) XZ-plane and (b) YZ-plane. (coordinates in m)

The model-predicted air temperature and absolute humidity distributions were consistent with the experimental observations carried out by Jimenèz *et al.* (2006), describing three thermal zones in the conical top-sprayed fluidised bed based on air temperature profiles. Based on air temperature and H_{abs} distributions illustrated

in Figs. 5.13 and 5.14, respectively, three thermal zones in the fluidised bed were considered:

- *The spray zone* characterised by a low air temperature and high humidity resulting from the sprayed water and its evaporation. This region is near the two-fluid nozzle at the top part of the bed.
- *The isothermal zone*, located near the wall and around the spraying zone. Due to the high heat transfer in fluidised beds, air temperature is homogeneous.
- *The heat transfer zone*, situated right above the air distributor. In this small area, the hot fluidising air temperature decreases as a result of the energy absorbed by the colder particles coming down from the upper part of the bed.

However, even though the CFD model gave acceptable qualitative agreement with the experimental tendency of three thermal zones observed by Jimenèz *et al.* (2006), discrepancy between the experimental outlet air temperature, $30.4 \pm 0.60^\circ\text{C}$, obtained by Ronsse (2006) and that predicted from the CFD model, approximately 37°C , could be seen. The explanation is most likely due to the underestimation of droplet evaporation in the reactor.

In the Eulerian-Lagrangian CFD model used in this section, the calculated droplets moved downwards along with the atomisation air stream until facing the counter-current fluidising solid particles. Due to the absence of phenomena including droplet deposition onto fluidised particles, the DPM algorithm continued tracking the droplets until they exited the reactor at the top, as shown in Fig. 5.15. In reality, the wet particles resulting from droplet adhesion onto their surface pass the coating zone several times with the appropriate circulation time, contributing to the layered growth of the wall around the individual core particles. In practice, the majority – typically $\geq 70\%$ (Ronsse *et al.*, 2008) – of water in the coating solution

is evaporated after the droplets have impacted and deposited on the fluidised solid surface. Conversely, in the current CFD model, the water droplets were evaporated during their flight throughout the reactor with short residence time, resulting in underestimation of latent heat transfer and consequently overestimation of the outlet air temperature. Therefore, in future work, the presence of droplet deposition onto the fluidised particles and the subsequent heat and mass transfer between fluidising hot air and wet particles should be taken into account, as described schematically in Fig. 5.16.

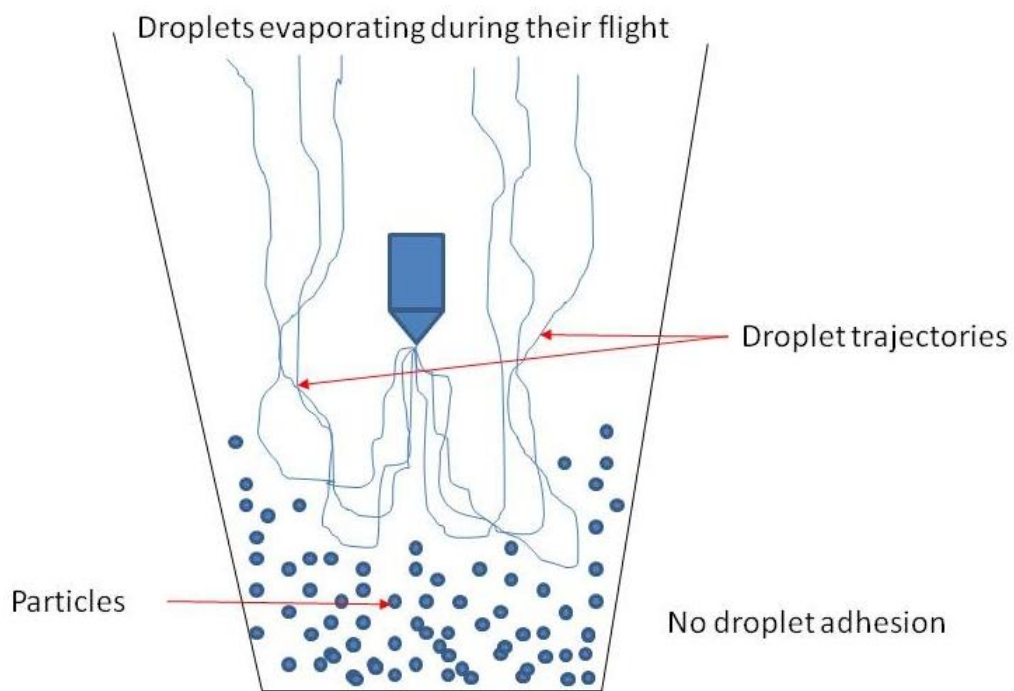


Figure 5.15 Droplet trajectories obtained from the current CFD model

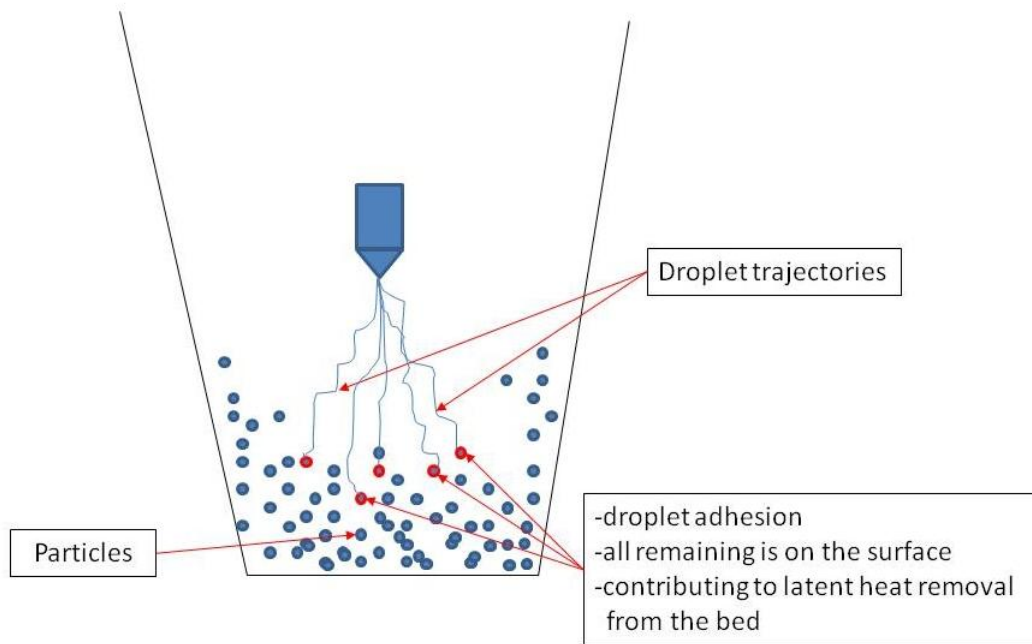


Figure 5.16 Interactions between phases included in the prospective CFD model

5.6 Conclusion

In this chapter, a combined Eulerian/Lagrangian modelling framework was provided for the top-spray fluidised bed coating process based on a 3D discretisation of the bed. The aim of this model was to describe a process including structured solids particle movement, droplets trajectories and their evaporation, temperature and humidity distribution in the fluidised bed coater. In order to describe the impact of process variables on the fluidised bed, thermodynamic properties such as temperature and humidity gradient, the main affecting variables (inlet air temperature, inlet air flow rate, liquid feed rate and atomisation air pressure) were taken into account. Moreover, simulated results were compared with the experimentally measured air temperature at the outlet. It was found that the model-predicted result was consistent with the experimental tendency. However, discrepancy between the measured outlet air temperature and that predicted by the CFD model could be seen. Stressing the fact that –as expected–, other mechanisms, for instance, droplet adhesion, heat and mass transfer between wet particles and hot fluidising air resulting in agglomeration and layered growth are to be taken into account in the future work.

6.1 Introduction

Microencapsulation is a process in which an active ingredient or mixture of ingredients is coated in order to improve or even provide totally new properties of products. Microencapsulation can be achieved with varying techniques, including fluidised bed coating which was originally developed for pharmaceutical applications. Although fluidised bed coating is increasingly applied in the food industry, its application in the food industry has to handle higher capacities with lower profit margin products, compared with the pharmaceutical industry. Therefore, to improve the economics in the food market, production costs and process optimisation of the fluidised bed coating have to be addressed.

To optimise the fluidised bed coating process, process models such as those using CFD, with adequate knowledge of phenomena occurring in the process, could be taken into consideration as a useful tool. CFD models could not only describe hydrodynamics of gas, solid and liquid in the system, but they can also clarify heat and mass transfer linked to the mechanisms of fluidised bed coating and the occurrence of side-effects and/or the quality of final products.

In order to understand the process fundamentals and to provide the insight of process control optimisation and reactor design using CFD, several aspects were studied in more detail.

6.2 Drag coefficient models and effect of particle size distribution

A CFD model with appropriate selection of a drag model used to calculate the interphase momentum exchange in the Eulerian two-fluid model was built to allow

the accurate prediction of gas/solid behaviour in tapered fluidised beds. In addition to the widely used drag models available in the CFD code software FLUENT, namely the Wen and Yu model, the Symlal and O'Brien model, and the Gidaspow model, the drag coefficient models proposed by Arastoopour *et al.* (1990) and Gidaspow (1994), were compared and evaluated using the SSR (sum of squared residuals). Among those drag models, it was found that the modified Gidaspow model (proposed by Gidaspow (1994)) gave the best prediction of solids volume fraction and bed voidage which agreed well with the PEPT results of Depypere (2005) and Depypere *et al.* (2009). Furthermore, a four-phase Eulerian model was proposed in order to include the effects of the polydispersity of the solids, effectively improving model accuracy with respect to the bed voidage and solids volume concentration profiles.

6.3 Effect of atomisation air on fluidisation behaviour

The effect of the release of compressed air – to assist in the atomisation of the coating solution – on the hydrodynamic behaviour of the fluidised bed was studied. An Eulerian interpenetrating fluids model was used in an attempt to describe the influence of the additional compressed air released from a two-fluid nozzle on solids hydrodynamics in the fluidised bed coater. To provide the consistency with the experimental results, the non-spherical shape of solid particles was implemented in the model using the sphericity coefficient, and the solid-solid interactions were taken into account. The model predicted solids concentrations and bed voidage profiles with the variation of atomisation air pressures showed good correlation with experimental data obtained from Depypere *et al.* (2009). However, discrepancy between values from simulations and experimental results could still be seen.

As the model was found to be highly sensitive to changes in the fluidisation air flow rate, a model with a positive perturbation factor for the superficial velocity

boundary condition provided a satisfactory match with the experimental data. Consequently, to model the voidage and solids volume concentration profiles in the fluidised bed coater, a properly calibrated air flow rate should be used as a boundary condition in the CFD model.

6.4 Hydrodynamics of the liquid spray in the gas/solid fluidised bed

The hydrodynamics of the liquid spray in the gas/solid fluidised bed were modelled by means of two CFD approaches: Eulerian-Lagrangian (the discrete phase model, DPM) and combined Eulerian-Eulerian/population balance model (the multi-fluid model/population balance model, MFM-PBM). The air-blast/air-assisted atomiser model calibrated using DPM was used as a suitable model for the two-fluid nozzle in the fluidised bed coating process in order to study the effects of process variables on spray flow and its mass distribution. It can be seen, in the gas-liquid DPM model, that the spray cone and liquid mass fraction changed with the variation of fluidisation air flow rate, atomisation air pressure and liquid feed rate.

Furthermore, as an alternative approach for modelling droplets in the gas-liquid system, the population balance model combined with the Eulerian-Eulerian CFD model was also employed to describe the two-fluid atomisation and the impact of process variables. In this approach, the gas, droplets and solid particles were modelled by treating all phases as interpenetrating continua, while the class population balance model was used to track the droplet diameter. The simulated results obtained using the MFM-PBM model showed the same trend in change of the spray characteristics as those found using the DPM model. However, when compared with the experimental results, the spray cone and liquid mass fraction predicted using the MFM-PBM model showed that even though this approach could be opted for instead of the DPM model to capture the two-fluid atomisation and interaction between phases, improvement of the population balance model such as a more accurate breakage kernel (i.e. depending on Weber and Reynolds

numbers) has to be carried out. In addition, the droplet atomisation was introduced in the fluidised bed using both the DPM and MFM-PBM models (gas-solid-liquid model). When evolving from a gas-liquid to a gas-solid-liquid CFD model, consistency between the DPM and the population balance model in the Eulerian framework was shown to improve. Consequently the MFM-PBM approach was considered to be a viable alternative in the CFD modelling of gas-solid-liquid systems, including fluidised bed coaters.

6.5 Heat and mass transfer in the fluidised bed coating process

The overall CFD model was concluded by adding the heat and mass transfer (i.e. evaporation of water used as the binder solution in the droplets) in a framework of Eulerian-Lagrangian provided for the top-spray fluidised bed coating process based on a 3D discretisation of the bed. The aim of this model was to describe a process including structured solids particle movement, droplets trajectories and their evaporation, temperature and humidity distribution in the fluidised bed coater. Solid-solid and solid-liquid interactions, however, were not taken into account.

Among several methods used to determine the expanded bed heights, the use of the gas near-wall temperature profile and static pressure profile as a function of bed height by means of CFD showed good agreement with the experimental results. The compressed air released from a two-fluid nozzle was introduced in order to describe temperature distribution of gas and solid phases. In the absence of sprays, a CFD model showed the influence of additional cold air release from the nozzle, resulting in lower gas and solid temperature with higher atomisation air pressures. Droplet evaporation was modelled by means of the discrete phase model with exclusion of fluidised solid particles. It could be concluded that the air temperature and relative humidity changed with the variation of fluidisation air velocity, atomisation air pressure, inlet air temperature and liquid feed rate. Finally, to describe the global aspect affecting the efficiency of fluidised bed coating, the

CFD model including structured solid particle movements (see chapters 2 and 3), droplet trajectories (see chapter 4) and their evaporation was developed. It was found that the model-predicted gas outlet temperature was over-estimated. Even though the simulated results agreed with experimentally observed tendencies including the identification of different thermal zones, the global CFD model still needs to be improved in order to provide quantitative model validation. As a result, disregarded mechanisms, including droplet adhesion to the surface of particles, heat and mass transfer between wet particles and fluidisation air and subsequent growth mechanisms need to be taken into account in the future work.

6.6 Future work

Compared with the multi-fluid CFD model (Eulerian-Eulerian approach), the discrete phase model (Eulerian-Lagrangian) offers a more natural way to simulate complex micro-level processes. Together with additional interactions between phases linking to growth mechanisms could be used as a prospective approach to provide model improvement. In the Eulerian-Lagrangian CFD model, the gas phase and the solid phases are treated as interpenetrating continua, whereas the liquid phase (droplet) is treated by solving equations of motion for all droplets in the system. Therefore, in the conceptual study of heat and mass transfer in the fluidised bed coating process (chapter 5), the CFD model did not describe interactions between the droplets and the fluidised particles resulting in the layered growth mechanism. A prospective approach to improve the global CFD model could be an Eulerian-Lagrangian model (DPM model) to describe in more detail phenomena such as heat and mass transfer and particle growth mechanisms by adding constitutive relations to take into account droplet-particle coalescence and their interactions via the user-defined functions. Constitutive relations based on interactions between the droplets and the fluidised particles are:

- frequency (f_c) of droplet-solid collision based on local solids volume concentration. If droplet adhesion occurs, then droplet tracking by the DPM model should be terminated.
- a variable that keeps track of the water on the solid phase and add a mass balance equation to the CFD model that includes the following terms:
 - o addition of water through droplets/solids adhesion
 - o evaporation of water from the solids surface, where the rate of mass transfer (evaporation) is based on the local Sherwood number and the local vapour concentration
- modification of the energy balance of the solids phase to include the latent heat removal from droplet evaporation.

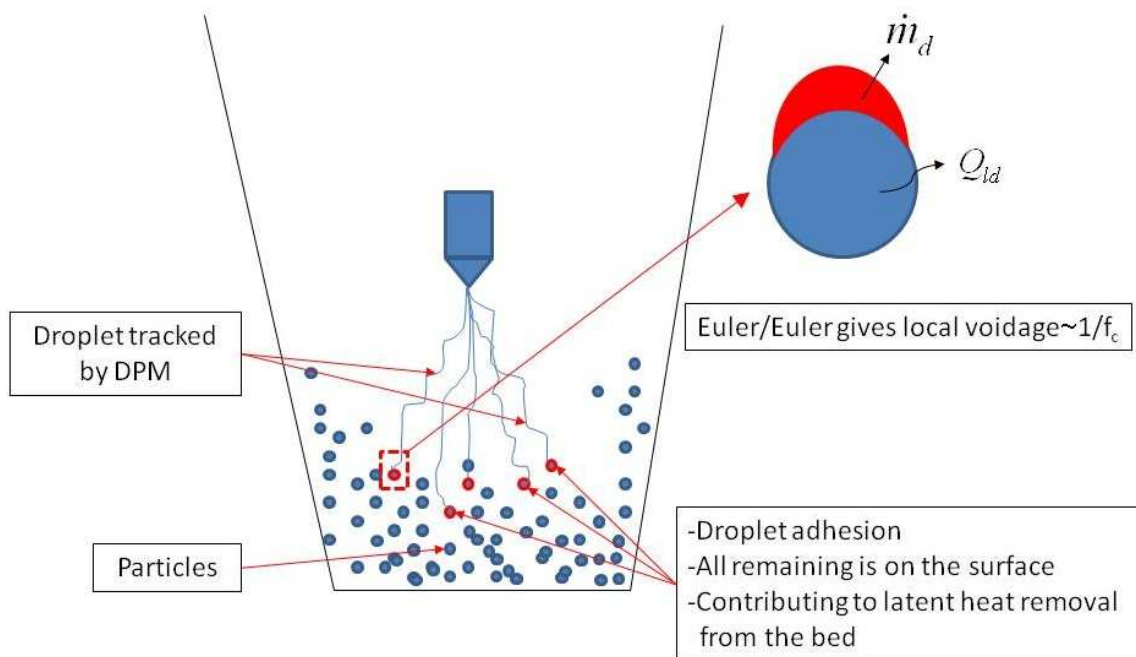


Figure 6.1 Mechanisms included in the prospective CFD model

References

Agrawal, K., Loezos, P., Symlal, M., Sundaresan, S., 2001. The role of meso-scale structures in rapid gas-solid flows. *Journal of Fluid Mechanics* 445, 151-185.

Aly, H.S., Eldrainy, Y.A., Lazim, T.M., Jaafar, M.N.M., 2010a. On the contribution of drag and turbulent stresses in the fragmentation of liquid droplets: A Computational Study. *CFD Letters* 2 (2), 97-105.

Aly, H.S., Eldrainy, Y.A., Saqr, K.M., Lazim, T.M., Jaafar, M.N.M., 2010b. A mathematical model for predicting spray atomisation characteristics in an Eulerian-Eulerian framework. *International Communications in Heat and Mass Transfer* 37, 618-623.

Aly, H.S., Lazim, T.M., Eldrainy, Y.A., Jaafar, M.N.M., 2009. Mathematical modelling of droplet atomisation using the population balance equation. *International Conference on Signal Processing Systems, ICSPS 2009*. Institute of Electrical and Electronics Engineers, New York, 955-959.

Anderson, T.B., Jackson, R., 1967. A fluid mechanical description of fluidised beds. *Equations of motion. Industrial and Engineering chemistry fundamentals* 6, 527-539.

Ansys Inc., 2009a. *Ansys Fluent 12.0 Population balance module manual*. Ansys Inc., Canonsburg, PA.

Ansys Inc., 2009b. *Ansys Fluent 12.0 User's guide manual*. Ansys Inc., Canonsburg, PA.

Apintanapong, M., Noomhorm, A., 2003. The use of spray drying to microencapsulate 2-acetyl-1-pyrroline, a major flavour component of aromatic rice. *International Journal of Food Science and Technology* 38, 95-102.

Arastoopour, H., Gidaspow, D., 1979. Analysis of IGT pneumatic conveying data and fast fluidisation using a thermo-hydrodynamic model. *Powder Technology* 22, 77-87.

Arastoopour, H., Pakdel, P., Adewumi, M., 1990. Hydrodynamic analysis of dilute gas-solids flow in a vertical pipe. *Powder Technology* 62, 163-170.

Arshady, R., 1993. Microcapsules for food. *Journal of Microencapsulation* 10, 413-435.

Arshdy, R., 1993. Microcapsules for food. *Journal of Microencapsulation*, 10, 413-435.

Bansode, S.S., Banarjee, S.K., Gaikwad, D.D., Jadhav, S.L., Thorat, R.M. 2010. Microencapsulation: A review. *International Journal of Pharmaceutical Sciences Review and Research*, 1(2), 38-43.

Barbosa-Canovas, G.V., Ortega-Rivas, E., Juliano, P., Yan, H. 2005. *Food Powders: Physical properties, processing and functionality*. Kluwer Academic/Plenum Publishers, New York, 372p.

Behjat, Y., Shahhosseini, S., Marvast, M.A., 2010. Modelling gas oil spray coalescence and vaporisation in gas solid riser reactor. *International Communications in Heat and Mass Transfer* 37, 935-943.

Benyahia, S., Arastoopour, H., Knowlton, T.M., Massah, H., 2000. Simulation of particles and gas flow behavior in the riser section of a circulating fluidised bed using the kinetic theory approach for the particulate phase. *Powder Technology* 112, 24-33.

Boh, B. and Sumiga, B., 2008. Microencapsulation technology and its applications in building construction materials. *RMZ-Materials and Geoenvironment* 55(3), 329-344.

Cooper, S., Coronella, C.J., 2005. CFD simulation of particle mixing in a binary fluidised bed. *Powder Technology* 151, 27-36.

Cornelissen, J.T., Taghipour, F., Escudie, R., Ellis, N., Grace, J.R., 2007. CFD modelling of a liquid-solid fluidised bed. *Chemical Engineering Science* 62, 6334-6348.

Cruz, E., Steward, F.R., Pugsley, T., 2006. New closure models for CFD modeling of high-density circulating fluidized beds, *Powder Technology* 169, 115-122.

Cruz, E., Steward, F.R., Pugsley, T.S., 2002. Modelling CFB riser hydrodynamics using Fluent, in: Grace, J.R., Zhu, J., de Lasa, H. (Eds.), *Circulating fluidised bed technology VII*, Canadian Society of Chemical Engineers, Ottawa, pp. 435-442.

Deasy, P.B., 1984. *Microencapsulation and Related Drug Processes*. New Yourk, Marcel Dedder Inc., 1-60.

Dehghannya, J., Ngadi, M., Vigneault, C., 2010. Mathematical modelling procedures for airflow, heat and mass transfer during forced convection cooling of produce: a review. *Food Engineering Reviews* 2 (4), 227-243.

Denys, S., Pieters, J.G., Dewettinck, K., 2004. Computational fluid dynamics analysis of combined conductive and convective heat transfer in model eggs. *Journal of Food Engineering*, 63(3), 281-290.

Depypere, F., 2005. Characterisation of fluidised bed coating and microcapsule quality: a generic approach. Ph.D. Thesis, Ghent University, Belgium.

Depypere, F., Dewettinck, K., Ronsse, F., Pieters, J.G., 2003. Food powder microencapsulation: principles, problems and opportunities. *Applied Biotechnology, Food Science and Policy* 1(2), 75-94.

Depypere, F., Pieters, J.G., Dewettinck, K., 2004. CFD analysis of air distribution in fluidised bed equipment. *Powder Technology* 145, 176-189.

Depypere, F., Pieters, J.G., Dewettinck, K., 2005. Expanded bed height determination in a tapered fluidised bed reactor. *Journal of Food Engineering* 67, 353-359.

Depypere, F., Pieters, J.G., Dewettinck, K., 2009. PEPT visualisation of particle motion in a tapered fluidised bed coater. *Journal of Food Engineering* 93(3), 324-336.

Desai, K.G.H., and Park, H.J., 2005. Recent developments in microencapsulation of food ingredients. *Drying Technology* 23, 1361-1394.

Dewettinck, K., Huyghebaert, A., 1998. Top-spray fluidised bed coating: Effect of process variables on coating efficiency. *Food Science and Technology* 31, 568-575.

Dewettinck, K. and Huyghebaert, A., 1999. Fluidised bed coating in food technology. *Trends in Food Science and Technology* 10, 163-168.

Di Felice, R., 1994. The voidage functions for fluid-particle interaction system. *International Journal of Multiphase flow* 20, 153-159.

Ding, J., Gidaspow, D., 1990. A bubbling fluidisation model using kinetic-theory of granular flow. *AIChE Journal* 36, 523-538.

Dixit, R. and Puthli, S. 2009. Fluidisation Technologies: Aerodynamic Principles and Process Engineering. *Journal of Pharmaceutical sciences* 98(11), 3933-3960.

Drew, D.A., 1971. Averaged field equations for two-phase media. *Studies in Applied Mathematics* L2, 205-231.

Drew, D.A., 1983. Mathematical modelling of two-phase flow. *Annual Review of Fluid Mechanics* 15, 261-291.

Drew, D.A., Lahey, R.T., 1993. Analytical modelling of multiphase flow. In *Particulate Two-Phase Flow*. Butterworth-Heinemann.

Drew, D.A., Segel, L.A., 1971. Averaged equations for two-phase flows. *Studies in Applied Mathematics* 50, 205. Einstein, A., 1906. Eine Neue Bestimmung der Molekuldimensionen. *Annual Physics* 19, 289.

Du, W., Bao, X., Xu, J., Wei, W., 2006a. Computational fluid dynamics (CFD) modeling of spouted bed: assessment of drag coefficient correlations. *Chemical Engineering Science* 61, 1401-1420.

Du, W., Bao, X., Xu, J., Wei, W., 2006b. Computational fluid dynamics (CFD) modeling of spouted bed: influence of frictional stress, maximum packing limit and coefficient of restitution of particles, *Chemical Engineering Science* 61, 4558-4570.

Duangkhamchan, W., Ronsse, F., Depypere, F., Dewettinck, K., Pieters, J.G., 2010. Comparison and evaluation of interphase momentum exchange models for simulation of the solids volume fraction in tapered fluidised beds. *Chemical Engineering Science* 65, 3100-3112.

Duangkhamchan, W., Ronsse, F., Dewettinck, K., Pieters, J.G., 2011. CFD study of solids concentration in a fluidised bed coater with variation of atomisation air pressure. *Powder Technology* 212, 103-114.

Duangkhamchan, W., Ronsse, F., Depypere, F., Dewettinck, K., Pieters, J.G., 2012. CFD study of droplet atomisation using a binary nozzle in fluidised bed coating. *Chemical Engineering Science* 68(1), 555-566.

Duesen-Schlick GmbH, Technical information 15/01, Duesen-Schlick GmbH, Coburg, Germany.

Dziezak, J.D., 1988. Microencapsulation and encapsulated ingredients. *Food Technology* 42, 136-151.

Enwald, H., Peirano, E., Almstedt, A.E., 1996. Eulerian two-phase flow theory applied to fluidisation. *International Journal of Multiphase Flow* 22, 21-66.

Ergun, S., 1952. Fluid flow through packed columns. *Chemical Engineering Progress* 48, 89-94.

Erikson, M., Golriz, M.R., 2005. Radiation heat transfer in circulating fluidised bed combustors. *International Journal of Thermal Sciences* 44(4), 399-409.

Fabbri, A., Cevoli, C., Alessandrini, L., Romani, S., 2011. Numerical modeling of heat and mass transfer during coffee roasting process. *Journal of Food Engineering* 105(2), 264-269.

Fanger, G.O., 1974. Microencapsulation: a brief history and introduction. In: Vandegaer, J.E. (ed.) *Microencapsulation Processes and Applications*. New York, Plenum Press, 1-20.

Fletcher, C.A.J., 1991. *Computational techniques for fluid dynamics*. Springer series in computational physics, vol.1, Berlin; New York: Springer-Verlag, 2nd edition.

Fluent INC., 2006, *Fluent 6 User Manual*, Fluent Inc.

Fries, L., Antonyuk, S., Heinrich, S., Palzer, S., 2011. DEM-CFD modeling of a fluidized bed spray granulator. *Journal of Chemical Engineering Science* 66, 2340-2355.

Fuster, D., Bague, A., Boeck, T., Moyne, L.L., Leboissetier, A., Popinet, S., Ray, P., Scardovelli, R., Zaleski, S., 2009. Simulation of primary atomisation with an octree adaptive mesh refinement and VOF method. *International Journal of Multiphase Flow* 35, 550-565.

Geldart, D., 1973. Types of gas fluidisation. *Powder Technology* 7, 285-292.

Gelderbloom, S.J., Gidaspow, D., Lyczkowski, R.W., 2003. CFD simulations of bubbling/collapsing fluidised beds for three Geldart groups. *AIChE Journal* 49(4), 844-858.

Gennadios, A., McHugh, T.H., Weller, C.L., Krochta, J.M., 1994. Edible coatings and films based on proteins. In: Krochta, J.M., Baldwin, E.A. and Nisperos-Carriedo, M. (eds.) *Edible coatings and films to improve food quality*. CRC Press, Boca Ralton, 201-278.

Gera, D., Gautam, M., Tsuji, Y., Kawaguchi, T., Tanaka, T., 1998. Computer simulation of bubbles in large-particle fluidised beds. *Powder Technology* 98, 38-47.

Gianfrancesco, A., Turchiuli, C., Flick, D., Dumoulin, E., 2010. CFD Modeling and Simulation of Maltodextrin Solutions Spray Drying to Control Stickiness. *Food Bioprocess Technology* 3(6), 946-955.

Gibbs, B.F., Kermasha, S.K., Alli, L., Mulligan, C., 1999. Encapsulation in the food industry: a review. *International Journal of Food Science and Nutrition* 50, 213-224.

Gibilaro, L.G., Di Felice, R., Waldram, S.P., Foscolo, P.U., 1985. Generalised friction factor and drag coefficient correlations for fluid-particle interactions. *Chemical Engineering Science* 40, 1817-1823.

Gidaspow, D., 1994. *Multiphase Flow and Fluidisation*. Academic Press, San Diego.

Gidaspow, D., Bezuruah, R., Ding, J., 1992. Hydrodynamics of circulating fluidised beds, kinetic theory approach, in: Proceedings of the 7th Engineering Foundation Conference on Fluidisation, Australia, Brisbane, 75-82.

Goldschmidt, M.J.V., Beeststra, R., Kuipers, J.A.M., 2004. Hydrodynamic modelling of dense gas-fluidised beds: comparison and validation of 3D discrete particle and continuum models. *Powder Technology* 142, 23-47.

Goldschmidt, M.J.V., Weijers, G.G.C., Boerefijn, R., Kuipers, J.A.M. 2003. Discrete element modeling of fluidized bed spray granulation. *Powder Technology*, 138, 39-45.

Gomez, L.C., Milioli, F.E., 2006. A numerical simulation analysis of the effect of the interface drag function on cluster evolution in a CFB Riser gas-solid flow. *Brazilian Journal of Chemical Engineering* 21, 569-583.

Gouin, S., 2004. Microencapsulation: industrial appraisal of existing technologies and trends. *Trends in Food Science and Technology* 15, 330-347.

Grace, J.R., Taghipour, F., 2004. Verification and validation of CFD models and dynamic similarity for fluidized beds. *Powder Technology* 139, 99-110.

Graham, D.I., Moyeed, R.A., 2002. How many particles for my Lagrangian simulations? *Powder Technology* 125, 179-186.

Greenblatt, H.C., Dombroski, M., Klishevich, W., Kirkpatrick, J., Garrison, W., Redding, B.K., 1993. Encapsulation and controlled release of flavours and fragrances. In: Kara, D.R., Stephenson, R.A. (eds.) *Encapsulation and controlled release*. The Royal Society of Chemistry, Cambridge, 148-162.

Gryczka, O., Heinrich, S., Jacob, M., Deen, N.G., Kuipers, J.A.M., 2009. Analysis of the fluidisation behaviour and application of a novel spouted bed apparatus for spray granulation and coating. In 9th International Symposium on Agglomeration, 22-26 June 2009, Sheffield, UK.

Gunn, D.J., 1978. Transfer to heat or mass to particle in fixed and fluidised beds. *International Journal of Heat and Mass Transfer* 21, 467-476.

Hede, P.D., Bach, P., Jensen, A.D., 2008. Two-fluid spray atomisation and pneumatic nozzles for fluid bed coating/agglomeration purposes: A review. *Chemical Engineering Science* 63, 3821-3842.

Heinrich, S., Blumschein, J., Henneberg, M., Ihlow, M., Peglow, M., Mörl, L., 2003. Study of dynamic multi-dimensional temperature and concentration distributions in liquid-sprayed fluidised beds. *Chemical Engineering Science* 58, 5135-5160.

Heinrich, S., Henneberg, M., Peglow, M., Drechsler, J., Morl, L. 2005. Fluidised bed spray granulation: analysis of heat and mass transfers and dynamic particle populations. *Brazilian Journal of Chemical Engineering*, 22(2), 181-194.

Hernandez, E., 1994. Edible coatings from lipids and resins. In: Krochta, J.M., Baldwin, E.A., Nisperos-Carriedo, M. (eds.) *Edible coatings and films to improve food quality*. CRC Press, Boca Raton, 279-304.

Hidayat, M., Rasmuson, A., 2007. A computational investigation of non-isothermal gas-solid flow in a U-bend. *Powder Technology* 175, 104-114.

Higgins, S., Carroll, Y.L., O'Brien, N.M., Morrissey, P.A., 1999. Use of micro encapsulated fish oil as a means of increasing n-3 polyunsaturated fatty acid intake. *Journal of Human Nutrition and Dietetics* 12(4), 265-272.

Hill, R.J., Koch, D.L., Ladd, J.C., 2001. Moderate Reynolds number flows in ordered and random arrays of spheres. *Journal of Fluid Mechanics* 448, 243-278.

Incropera, F.P., DeWit, D.P., 2002. *Introduction to heat transfer*, Wiley, New York, 892p.

Jackson, L.S. and Lee, K., 1991. Microencapsulation and the food industry. *Lebensmittel Wissenschaft und Technologie* 24(40), 289-297.

Jackson, R., 1997. Locally averaged equations of motion for a mixture of identical spherical particles and a Newtonian fluid. *Chemical Engineering Science* 52, 2457.

Jackson, R., 1998. Erratum. *Chemical Engineering Science* 53, 1955.

Jamaledine, T.J. and Ray, M.B., 2010. Application of Computational Fluid Dynamics for Simulation of Drying Processes: A Review. *Drying Technology* 28(2), 120-154.

Jiménez, T., Turchiuli, C., Dumoulin, E., 2006. Particles agglomeration in a conical fluidized bed in relation with air temperature profiles. *Chemical Engineering Science* 61, 5954-5961.

Jiradilok, V., Gidaspow, D., Damronglerd, S., Koves, W.J., Mostofi, R., 2006. Kinetic theory based CFD simulation of turbulent fluidisation of FCC particles in a riser. *Chemical Engineering Science* 61, 5544-5559.

Jyothi, N.V., Prasanna, M., Prabha, S., Ramaiah, P.S., Srawan, G., Sakarkar, S.N., 2009. Microencapsulation Techniques, Factors influencing encapsulation efficiency: A review. *The internet journal of Nanotechnology*, 3(1).

Kalata, W., Brown, K., Bade, K.M., Schick, R.J., 2009. Dimensional, thermal and evaporative Spray plume characteristics using Computational Fluid Dynamics, simulation versus empirical evaluation. *Spray Analysis and Research Services, A Service of Spraying Systems Co., Wheaton, USA.*

Karlsson, S., Rasmuson, A., van Wachem, B., Bjorn, I.N. 2009. CFD modeling of the Wurster bed coater. *AIChE Journal* 55(10) 2578-2590.

Kunii, D., Levenspiel, O., 1991. *Fluidisation Engineering* (2nd ed.). Butterworth-Heinemann, Stoneham, 491p.

Kuriakose, R., Anandharamakrishnan, C., 2010. Computational fluid dynamics (CFD) applications in spray drying of food products. *Trends in Food Science and Technology* 21, 383-398.

Lal, S., Kushari, A., Kapoor, J.C., Maji, S., 2010. Modelling of externally mixed air blast atomiser. *International Journal of Dynamics of Fluids* 6(1), 25-40.

Lasheras, J.C., Eastwood, C., Martinez-Bazaan, C., Montanes, J.L., 2002. A review of statistical models for the break-up of an immiscible fluid immersed into a fully developed turbulent flow. *International Journal of Multiphase Flow* 28, 247-278.

Lebas, R., Menard, T., Beau, P.A., Berlemont, A., Demoulin, F.X., 2009. Numerical simulation of primary break-up and atomisation: DNS and modelling study. *International Journal of Multiphase Flow* 35, 247-260.

Lefebvre, A.H., 1989. Atomisation and sprays. Hemisphere Publishing Corporation, Washington, DC.

Lettieri, P., Cammarata, L., Michale, G., Yates, J.G., 2003. CFD simulations of gas-fluidised beds using alternative Eulerian-Eulerian modelling approaches. *International Journal of Chemical Reactor Engineering* 1(1), 1-19.

Lettieri, P., Mazzei, L., 2009. Challenges and issues on the CFD modeling of fluidised beds: a review. *Journal of Computational Multiphase Flows*, 1(2), 83-131.

Liao, Y., Lucas, D., 2009. A literature review of theoretical models for drop and bubble breakup in turbulent dispersions. *Chemical Engineering Science* 64, 3389-3406.

Liu, H.F., Li, W.F., Gong, X., Cao, X.K., Xu, J.L., Chen, X.L., Wang, Y.F., Yu, G.S., Wang, F.C., Yu, Z.H., 2006. Effect of liquid jet diameter on performance of coaxial two-fluid airblast atomisers. *Chemical Engineering and Processing* 45, 240-245.

Lu, H., Gidaspow, D., 2003. Hydrodynamics of binary fluidisation in a riser: CFD simulation using two granular temperatures. *Chemical Engineering Science* 58, 3777-3792.

Lu, H., He, Y., Gidaspow, D., Yang, L., Qin, Y., 2003. Size segregation of binary mixture of solids in bubbling fluidised beds, *Powder Technology* 134, 86-97.

- Madsen, J., 2006. Computational and experimental study of sprays from the breakup of water sheets. Ph.D. Thesis, Faculty of Engineering and Science, Aalborg University, Esbjerg, Denmark.
- Marchisio, D.L., Pikturna, J.T., Fox, R.O., Vigil, R.D., 2003. Quadrature method of moments for population balance equations. *AIChE Journal* 49, 1266-1276.
- Mazzei, L., Lettieri, P., 2007. A drag force closure for uniformly dispersed fluidised suspensions. *Chemical Engineering Science* 62, 6129-6142.
- Mazzei, L., Lettieri, P., 2008. CFD simulations of expanding/contracting homogeneous fluidised beds and their transition to bubbling. *Chemical Engineering Science* 63, 5831.
- Mezhericher, M., Levy, A., Borde, I., 2010. Spray drying modelling based on advanced droplet drying kinetics. *Chemical Engineering and Processing: Process Intensification* 49, 1205-1213.
- Mirsaeedghazi, H., Emam-Djomeh, Z., Mousavi, S.M., Navidbakhsh, M., 2011. Modelling the membrane clarification of pomegranate juice with computational fluid dynamics. *European Food Research and Technology* 232(4), 671-677.
- Morsi, S.A., Alexzander, A.J., 1972. An investigation of particle trajectories in two-phase flow systems. *Journal of Fluid Mechanics* 55, 193–208.
- Nasr, G.G., Yule, A.J., Bendig, L., 2002. *Industrial sprays and atomisation – Design, analysis and applications*. Springer-Verlag, London, 501p.

Nayak, S.V., Joshi, S.L., Ranade, V.V., 2005. Modelling of vaporization and cracking of liquid oil injected in a gas-solid riser. *Chemical Engineering Science* 60, 6049-6066.

Nijdam, J.J., and Langrish, T.A.G., 2004. The effect of surface composition on the functional properties of milk powders. *Journal of Food Engineering* 77(4): 919-925.

Nisperos-Carriedo, M., 1994. Edible coatings and films based on polysaccharides. In: Krochta, J.M., Baldwin, E.A., Nisperos-Carriedo, M. (eds.) *Edible coatings and films to improve food quality*. CRC Press, Boca Raton, 305-336.

Norton, T. and Sun, D., 2006. Computational fluid dynamics (CFD) – an effective and efficient design and analysis tool for the food industry: A review. *Trends in Food Science and Technology* 17, 600-620.

O'Rourke, P.J., Zhao, P., Snider, D., 2009. A model for collisional exchange in gas/liquid/solid fluidised beds. *Chemical Engineering Science* 64, 1784-1797.

Owoyemi, O., Lettieri, P., Place, R., 2005. Experimental validation of Eulerian-Eulerian simulations of rutile industrial powders. *Industrial and Engineering Chemistry Research* 44(26), 9996-10004.

Pain, C.C., Mansoorzadeh, S., de Oliveira, C.R.E., 2001. A study of bubbling and slugging fluidised beds using the two-fluid granular temperature model. *International Journal of Multiphase Flow* 27, 527-551.

Pan, T.W., Joseph, D.D., Bai, R., Glowinski, R., Sarin, V., 2002. Fluidisation of 1204 spheres: simulation and experiments. *Journal of Fluid Mechanics* 451, 169-191.

Parviz, M., John, K., 1997. Tackling turbulence with supercomputers. *Scientific American* 1, 276.

Peglow, M., Kumar, J., Heinrich, S., Warnecke, G., Tsotsas, E., Mörl, L., Wolf, B., 2007. A generic population balance model for simultaneous agglomeration and drying in fluidised beds. *Chemical Engineering Science* 62, 513-532.

Peirano, E., Delloume, V., Johnsson, F., Leckner, B., Simonin, O., 2002. Numerical simulation of the fluid dynamics of a freely bubbling fluidised bed: influence of the air supply system. *Powder Technology* 122, 69-82.

Pimentel, R.G., de Champlain, A., Kretschmer, D., Stowe, R.A., Harris, P., Kurbatskii, K., 2006. Improved atomisation model for CFD codes. *Proceeding of the International Conference on Liquid Atomisation and Sprays Systems*, Kyoto, Japan.

Ptaszek, A., 2010. Rheological equation of state for shear-thickening food systems. *Journal of Food Engineering* 100:322-328.

Qureshi, M.M.R., Zhu, C., 2006. Crossflow evaporating sprays in gas-solid flows: Effect of aspect ratio of rectangular nozzles. *Powder Technology* 166(2), 60-71.

Rajniak, P., Stepanek, F., Dhanasekharan, K., Fan, R., Mancinelli, C., Chern, R.T., 2009. A combined experimental and computational study of wet granulation in a Wurster fluid bed granulator. *Powder Technology* 189, 190-201.

Ranz, W.E., Marshall, W. R., 1952. Evaporation from drops. *Chemical Engineering Progress* 48, 141-146; 173-180.

Richardson, J.F., Zaki, W.N., 1954. Sedimentation and fluidisation: Part 1. *Chemical Engineering Research and Design* 32a, 35-53.

Risch, S.J., Reineccius, G.A. (eds.), 1995. *Encapsulation and controlled release of food ingredients*. USA: American Chemical Society.

Ronsse, F., 2006. *Modelling heat and mass transfer in fluidised bed coating process*. Ph.D. Thesis, Ghent University, Belgium.

Ronsse, F., Pieters, J.G., Dewettinck, K., 2007a. Combined population balance and thermodynamic modelling of the batch top-spray fluidised bed coating process. Part I-Model development and validation. *Journal of Food Engineering* 78, 296-307.

Ronsse, F., Pieters, J.G., Dewettinck, K., 2007b. Numerical spray model of the fluidised bed coating process. *Drying Technology* 25, 1491-1514.

Ronsse, F., Pieters, J.G., Dewettinck, K., 2008. Modelling side-effect spray drying in top-spray fluidised bed coating processes. *Journal of Food Engineering* 86, 529-541.

Ronsse, F., Pieters, J.G., Dewettinck, K., 2009. Modelling heat and mass transfer in batch top-spray fluidised bed coating processes. *Powder Technology*, 190, 170-175.

Rosinski, S., Grigorescu, G., Lewinska, D., Ritzen, L.G., Viernstein, H., Teunou, E., Poncelet, D., Zhang, Z., Fan, X., Serpy, D., Marisony, I., Hunkeler, D., 2002. Characterisation of microcapsules: recommended methods based on round-robin testing. *Journal of Microencapsulation* 19(5), 641-659.

Salman, A.D., Hounslow, M.J., Seville, J.P.K., 2007. Handbook of Powder Technology, Vol. 11: Granulation. Elsevier Publishing, Amsterdam.

Schaldach, G., Berger, L., Razilov, I., Berndt, H., 2000. Comput simulation for fundamental studies and optimisation of ICP spray chambers. ISAS (Institute of Spectrochemistry and Applied Spectroscopy) Current Research Reports, Berlin, Germany.

Schmidt, D. P., Nouar, I., Senecal, P. K., Rutland, C. J., Martin, J. K., and Reitz, R. D., 1999. Pressure-swirl atomisation in the near field. SAE Transactions, Journal of Engines 108(3), 471-484.

Shah, N.P., Ravula, R.R., 2000. Microencapsulation of probiotic bacteria and their survival in frozen fermented dairy desserts. The Australian Journal of Dairy Technology 55(3), 139-144.

Shekhar, K., Madhu, M.N., Pradeep, B., Banij, D., 2010. A review on microencapsulation. International Journal of Pharmaceutical Sciences Review and Research, 5(2), 58-62.

Sobieski, W., 2009a. Switch function and sphericity coefficient in the Gidaspow drag model for modeling Solid-Fluid Systems. Drying Technology 27, 267-280.

Sobieski, W., 2009b. Momentum exchange in solid-fluid system modelling with the Eulerian multiphase model. Drying Technology 27, 653-671.

Soo, S.L., 1989. Average circulatory motion of particles in fluidised beds. Powder Technology 57, 107-117.

Spray Drying Systems Co., 2000. Engineer's guide to spray drying technology.

Sridhara, S.N., Raghunandan, B.N., 2010. Photographic investigations of jet disintegration in airblast sprays. *Journal of Applied Fluid Mechanics* 3(2), 111-123.

Stein, M., Ding, Y.L., Seville, J.P.K., Parker, D.J., 2000. Solids motion in bubbling gas fluidised beds. *Chemical Engineering Science* 55, 5291-5300.

Streeter, V.L. and Wylie, E.B., 1979. *Fluid mechanics*. McGraw-Hill, New York.

Sun, Da-Wen., 2007. *Computational Fluid Dynamics in Food Processing*. CRC Press, Taylor and Francis Group, 739p.

Symlal, M., 1987. The particle-particle drag term in multiparticle model of fluidisation, DOE/MC/21353-2373, DE87 006500.

Symlal, M., O'Brien, T.T., 1989. Computer simulation of bubbles in a fluidised bed. *AIChE Symposium Series* 85, 22-31.

Taghipour, F., Ellis, N., Wong, C., 2005. Experimental and computational study of gas-solid fluidised bed hydrodynamics. *Chemical Engineering Science* 60, 6857-6867.

Tan, H.S., Goldschmidt, M.J.V., Boerefijn, R., Hounslow, M.J., Salman, A.D., Kuipers, J.A.M., 2004. Building population balance model for fluidised bed melt granulation: lessons from kinetic theory of granular flow. *Powder Technology* 142, 103-109.

Teunou, E., Poncelet, D., 2002. Batch continuous fluid bed coating – review and state of the art. *Journal of Food Engineering* 53, 325-340.

Teunou, E., Poncelet, D., 2005. Experimental and computational study of gas-solid fluidised bed hydrodynamics. *Chemical Engineering Science* 60, 6857-6867.

Turchiuli, C., Jimenez, T., Dumoulin, E., 2011. Identification of thermal zones and population balance modeling of fluidised bed spray granulation. *Powder Technology* 208, 542-552.

van Wachem, B.G.M. and Almstedt, A.E., 2003. Methods for multiphase computational fluid dynamics. *Chemical Engineering Journal* 96, 81-98.

van Wachem, B.G.M., Schouten, J.C., Krishna, R., van Den Bleek, C.M., 1998. Eulerian simulations of bubbling behaviour in gas-solid fluidised beds. *Computers and Chemical Engineering* 22(1), 299–306.

Varga, C.M., Lasheras, J.C., Hopfinger, E.J., 2003. Initial breakup of a small-diameter liquid jet by a high-speed gas stream. *Journal of Fluid Mechanics* 497, 405-434.

Vatani, Z., Taghizadeh, M., Orouj, R., 2011. CFD Simulation of mass transfer around spherical particles in fluidised bed. *International Journal of Chemical Reactor Engineering*, 9, Article A53.

Vejahati, F., Mahinpey, N., Ellis, N., Nikoo, M.B., 2009. CFD simulation of gas-solid bubbling fluidised bed: A new method for adjusting drag law. *Canadian Journal of Chemical Engineering* 87, 19-30.

Versteeg, H.K., Malalasekera, W., 2007. An introduction to computational fluid dynamics: The finite volume method. Pearson Education Limited, England, 503p.

Wang, X., Zhu, C., Ahluwalia, R., 2004. Numerical simulation of evaporating spray jets in concurrent gas-solids pipe flows. Powder Technology 140, 56-67.

Wen, C.Y., Yu, Y.H., 1966. Mechanics of fluidisation. Chemical Engineering Progress, Symposium Series 62, 100-111.

Werther, J., Bruhns, S., 2004. 3-D Modelling of Liquid Injection into Fluidised Beds. International Journal of Chemical Reactor Engineering 2, Article A31, 1-35.

Whitaker, S., 1969. Advances in the theory of fluid motion in porous media. Industrial and Engineering Chemistry 61(12), 14-28.

White, T.R., Milton, B.E., Behnia, M., 2004. Direct injection of natural gas/liquid diesel fuel sprays. Proceeding of the 15th Australasian Fluid Mechanics Conference, Sydney, Australia.

Wilson, N. and Shah, N.P., 2007. Microencapsulation of vitamins. ASEAN Food Journal 14(1), 1-14.

Wirsum, M., Fett, F., Iwanowa, F., Lukjanow, G., 2001. Particle mixing in bubbling fluidised beds of binary particle systems. Powder Technology 120, 63-69.

Wu, S.Y., Baeyens, J., 1998. Segregation by size difference in gas fluidised beds. Powder Technology 98, 139-150.

Wurster, D.E., 1950. Means of applying Coating to tablets or like. *Journal of the American Pharmaceutical Association* 48(8), 451.

Xia, B. and Sun, D., 2002. Applications of computational fluid dynamics (CFD) in the food industry: a review. *Journal of Computers and Electronics in Agriculture*, 34, 5-24.

Yamada, H., Yoon, G., Okumiya, M., Okuyama, H., 2008. Study of Cooling System with Water Mist Sprayers: Fundamental Examination of Particle Size Distribution and Cooling Effects. *Building Simulation* 1(3), 214-222.

Yasuna, J.A., Moyer, H.R., Elliott, S., Sinclair, J.L., 1995. Quantitative predictions of gas-particle flow in a vertical pipe with particle-particle interactions. *Powder Technology* 84, 23-34.

Zabaleta, A.G., 2007. Computational fluid dynamics studies in heat and mass transfer phenomena in packed bed extraction and reaction equipment: special attention to supercritical fluids technology. Doctoral thesis, the Chemical Engineering Department, Universitat Politècnica de Catalunya, Spain.

Zank, J., Kink, M., Schlünder, E.-U., 2001. Particle growth and droplet deposition in fluidised bed granulation. *Powder Technology* 120, 76-81.

Zhang, D.Z., Prosperetti, A., 1994. Averaged equations for inviscid disperse two-phase flow. *Journal of Fluid Mechanics* 267, 185-219.

Zhang, D.Z., Prosperetti, A., 1997. Momentum and energy equations for disperse two-phase flows and their closure for dilute suspensions. *International Journal of Multiphase Flow* 23(3), 425-453.

Zhang, Y., Reese, J.M., 2003. A drag force in two-fluid models of gas-solid flows. *Chemical Engineering Science* 58(8), 1641-1644.

Zhao, P., O'Rourke, P.J., Snider, D., 2009. Three-dimensional simulation of liquid injection, film formation and transport, in fluidised beds. *Particuology* 7, 337-346.

Zeoli, N., Gu, S., 2006. Numerical modelling of droplet break-up for gas atomisation. *Computational Materials Science* 38, 282-292.

Zhou, L.X., 2009. Two-Fluid Models for simulating dispersed multiphase flows - a review. *Journal of Computational Multiphase Flows* 1, 39-56.

Zimmermann, S., Taghipour, F., 2005. CFD Modelling of the hydrodynamics and reaction kinetics of FCC fluidised-bed reactors. *Industrial and Engineering Chemistry Research* 44, 9818-9827.

Curriculum vitae

Wasan DUANGKHAMCHAN

Address: Faculty of Engineering, Maharakham University, Kantarawichai, Maharakham 44150, Thailand

Tel/Fax: +66 (0)43 754 316

E-mail: san_duang@yahoo.co.uk

Nationality: Thai

Date and place of birth: March 31, 1976, Maha Sarakham, Thailand

Education:

2007 - present: PhD in Applied Biological Sciences

Faculty of Bioscience Engineering, Ghent University, Belgium

(with a scholarship granted from Maharakham University Staff Development Fund of Maharakham University, Thailand, duration of 3 years)

2000 – 2003: MEng in Mechanical Engineering

Faculty of Engineering, Khon Kaen University, Thailand

Thesis title: The important factors for designing the spray dryer:
case study for roselle powder

1994 – 1998: BEng in Food Engineering

Faculty of Engineering, Kasetsart University, Thailand

Project title: Design and development of heat pump dryer

Professional experiences:

2005 – 2007: Lecturer, Faculty of Engineering, Mahasarakham University, Thailand

2003 – 2005: Lecturer, Faculty of Engineering, Kingmongkut's Institute of Technology Ladkrabang, Chumporn campus, Thailand

2000 – 2003: Teacher, Demonstration School of Mahasarakham University, Thailand

1998 – 2000: Service Engineer, Chapatech center Co., Bangkok, Thailand

Scientific publications:

A1 (Articles in international journals with peer review, listed in ISI - Web of Science):

1) Duangkhamchan, W.; Ronsse, F.; Depypere, F.; Dewettinck, K. & Pieters, J.G. (2010). Comparison and evaluation of interphase momentum exchange models for simulation of the solids volume fraction in tapered fluidised beds. *Chemical Engineering Science*, 65(10), 3100-3112.

2) Duangkhamchan, W., Ronsse, F., Dewettinck, K. and Pieters, J.G. (2011). CFD study of solids concentration in a fluidised-bed coater with variation of atomisation air pressure. *Powder Technology* 212(1), 103-114.

3) Duangkhamchan, W., Ronsse, F., Depypere, F., Dewettinck, K., Pieters, J.G. (2012). CFD study of droplet atomisation using a binary nozzle in fluidised bed coating. *Chemical Engineering Science*, 68(1), 555-566.

A2 (Articles in international journals with peer review, non-ISI):

Duangkhamchan, W., Ronsse, F., Braeckman, L., Pieters, J.G., Depypere, F. & Dewettinck, K. (2008). Computational study of the multiphase flow in the fluidised bed equipment. *Acta Horticulturae 802: Proceedings of the IV International Symposium on Applications of Modelling as an Innovative Technology in the Agri-Food-Chain: Model-IT*, 67-72

A3 (Articles in national journals with peer review):

1) Duangkhamchan, W., Ronsse, F., Dewettinck, K. & Pieters, J.G. (2011). Effect of atomisation air pressure on solids concentration in a fluidised-bed coater. *Communications in Agricultural and Applied Biological Sciences*, 76(1), 177-180

2) Duangkhamchan, W., Ronsse, F., Depypere, F., Dewettinck, K. & Pieters, J.G. (2008). Effect of maximum packing limit on granular flow pattern in the top-spray fluidised bed coater. *Communications in Agricultural and Applied Biological Sciences*, 73(1), 145-148

3) Duangkhamchan, W., Ronsse, F., Depypere, F., Dewettinck, K. & Pieters, J.G. (2007). A CFD model based on optimisation of fluidised-bed coating process for food ingredients. *Communications in Agricultural and Applied Biological Sciences*, 72(1), 183-187